MICROCELLULAR POLYMER PROCESSING AND THE DESIGN OF A CONTINUOUS SHEET PROCESSING SYSTEM

by

DANIEL FLANAGAN BALDWIN

B.S., Mechanical Engineering
Arizona State University
1988

S.M., Mechanical Engineering
Massachusetts Institute of Technology
1990

Submitted to the Department of Mechanical Engineering
in Partial Fulfillment of the Requirements for
the Degree of

DOCTOR OF PHILOSOPHY
IN MECHANICAL ENGINEERING

at the

MASSACHUSETTS INSTITUTE OF TECHNOLOGY

January 1994
(February 1994)

Signature of Author______________________________
Department of Mechanical Engineering
January 14, 1994

Certified by______________________________
Nam P. Suh
The Ralph E. and Eloise F. Cross Professor of Manufacturing and Head
Department of Mechanical Engineering
Committee Chairman and Thesis Advisor

Accepted by______________________________
Ain A. Sonin
Professor of Mechanical Engineering and
Chairman of the Departmental Graduate Committee
Department of Mechanical Engineering

(This page was intentionally left blank.)

MICROCELLULAR POLYMER PROCESSING AND THE DESIGN OF A CONTINUOUS SHEET PROCESSING SYSTEM

by

DANIEL FLANAGAN BALDWIN

Submitted to the Department of Mechanical Engineering on January 14, 1994
in Partial Fulfillment of the Requirements for the Degree of
Doctor of Philosophy in Mechanical Engineering

ABSTRACT

The goal of this research is the design, development, and experimental verification of a continuous processing system for the production of microcellular polymer sheets. Microcellular polymers are an innovative cellular polymer technology characterized by cell sizes on the order of 0.1 to 10 microns and cell densities on the order of 10^9 to 10^{15} cells per cubic centimeter. Due to their extreme cell densities and minute cell size, these materials require advanced process technologies which surpass the capabilities of conventional foam processes.

The continuous processing of microcellular sheets is based on three sub-processes which include the processing of the polymer matrix, the processing of the microcellular structure, and the processing the net shape. The creation of a microcellular structure is achieved by dissolving large gas concentrations into a polymer matrix and subjecting the saturated system to a rapid thermodynamic state change. This creates an unstable or supersaturated matrix which drives the nucleation of billions of microcells. Stable cells then grow as gas diffuses into the cells reducing the bulk density of the material. Based on these fundamental processing requirements, a hierarchical design strategy is used to synthesize the overall production system such that each of the processing functions is independently satisfied by a unique design parameter or process variable.

In order to develop the microcellular sheet processing system, a detailed batch processing characterization of amorphous and semi-crystalline polymers is performed. This characterization identifies viable process variables for continuous processing and demonstrates some of the fundamental processing differences of amorphous and semi-crystalline polymers. Based on the batch processing characterization, a detailed system design is presented. The basic concept of this design is the use of a plasticating extruder to process the polymer matrix, the use of staged pressure losses to produce a microcellular structure, and the use of a foaming/shaping die to produce the net dimensions. In satisfying the later two requirements, three of the critical continuous processing functions are addressed in detail: continuous nucleation, cell growth control, and shaping. Here the concepts of near-net shape nucleation and shaping of a nucleated polymer/gas solution flow are presented and experimentally verified. As an integral part of this development, various processing models and design criteria are developed to aid in the design process. In general, these models and criteria are found to agree well with the experimental results. Moreover, the results of the critical experiments verify the overall performance of the microcellular sheet extrusion system.

Thesis Supervisor: Nam P. Suh, Ph.D.
Title: The Ralph E. and Eloise F. Cross Professor of Manufacturing and Head of the Department of Mechanical Engineering

(This page was intentionally left blank.)

ACKNOWLEDGMENTS

First and foremost, I would like to extend my infinite gratitude to my advisor and mentor Professor Nam P. Suh. Through his guidance and encouragement, I feel I have grown and matured into a very competent researcher and engineer. Professor Suh has instilled in me the fundamental desire to be the very best. I will carry this with me for the rest of my life.

I am also indebted to the other members of my thesis committee. Professor David Hardt's suggestions and critiques of the manufacturing system and the design were very helpful. I also would like to thank Professor David Parks for the insightful discussions and suggestions concerning the processing of the polymer sheets. Professor Ioannis Yannas also deserves my debt of gratitude for his instrumental advice and critique regarding the viscoelastic behavior of the gas saturated polymer matrix. Moreover, I would like to thank all of my committee members for their invaluable assistance in my job search.

I would also like to thank Dr. Bruce M. Kramer and Dr. Maria Burka for their interest in this work, and the National Science Foundation, Grant Number CTS-9114738, for its generous support of this research. I am also indebted to the member companies of the MIT-Industry Microcellular Plastics Consortium, particularly Furukawa Electric Co., Ltd. and Axiomatic Incorporated for their support of this research. Other member companies have included Kraft General Foods Inc., Amoco Foam Products Co., Amoco Chemicals Co., Neste Inc., and Asahi Chemicals Co., Ltd.

One of the truly enjoyable parts of my work at the Laboratory for Manufacturing and Productively was my encounters with Professor Ernest Rabinowicz. His quick wit, one-liners, and delightful stories always made my day, not to mention his timely suggestions on research. I will certainly miss him, and wish to thank him for his friendship. I would also like to thank Professor Ernesto Blanco for his creative suggestions on dynamic seals for sheets. I am also grateful to Professor Ain Sonin and Professor Shahryar Motakef for their help with the fluid mechanics and heat transfer elements of this work. A special thanks goes to Professor E. (Ned) Thomas for his insightful comments and suggestions on the phenomenon of gas/solvent induced crystallization of polymers.

For those of you that didn't know, Doris Elsemiller is a saint. Without her patience, help and friendship, I would have never graduated. Thank you. I would also like to thank Ann Seaman; she always knew the right thing to say to calm me down and make me laugh. I am also deeply indebted to Leslie Regan, Joan Kravit, and Susan Melillo for all of their help and for teaching me the ropes here at MIT. They were nice enough to befriend a Westerner when I first got to Boston, and I hope our friendship continues. Leslie deserves a special thank you for all of her help in my job search.

Next I would like to thank all of my friends and colleagues at the Laboratory for Manufacturing and Productivity including Fred Cote, Gerry Wentworth, Kevin Spratt, Kevin Baron, Bob Cane, Dr. Greg Dillon, Sally Stiffler, Kathy Larson, Dorothy Cavignano, Melinda Green, Lynn Festa, and Dr. Nannaji Saka. Fred deserves a special thank you because he helped turn a theoretical engineer into a practical engineer while in the meantime taught me to be a skilled machinist. A great deal of this project centered around his help. I would also like to thank Gerry for his insightful technical advice and assistance in machining many of the dies used in this work. Kevin Spratt's wit always help to break the tension and lighten up the day. Greg also deserves a special thank you for all of this suggestions and comments on the materials aspects of this project. Finally, I would like to thank Sally Stiffler for her help in administrative issues and for her recommendations throughout my job search.

I would like to thank my colleagues in the Microcellular Plastics Research Group for their advice, comments, critical evaluations, and friendships over the past four years. Sung Cha always had a critical eye for the microcellular samples. Chul Park was always a formidable adversary, colleague, and friend. Our sometimes heated discussions concerning microcellular processing were always enlightening. Steve Nierlich was always good for FAC, and Julie Yang was very helpful with her suggestions and helpful comments. Derrick Tate and Ravi Patil deserve a special thank you for their help proofreading this thesis and for their being there whenever I needed someone to bounce and idea off of. I would also like to thank Torsten Herrmann for his comments and suggestions concerning extruders. I am also grateful to the undergraduate students which I had the pleasure of working with over the last four years including Dave Gustafson, Jeff Pfeifle, Semor Liao, Maria Yang, Scott Davie, and Eric Blau. I wish all of my MCP colleagues the best and look forward to continuing our friendships.

I would like to thank my family and friends for their support, love, and encouragement over these past four years. Particularly, I would like to thank my parents

Lionel and Kathleen, without whose love and encouragement I would have never had the courage to pursue this doctoral research. All I can say to my guardian angle, "The Lone Horseman" is we did it!

Finally and most importantly, I wish to thank my wife, Kristen, and my daughter, Kelsey, for their love, devotion, and trust in me. Through the last four years and the trials and tribulations of our life in Boston, we have grown together and strengthened as a couple and as a family. Kelsey was always very helpful at the computer. Thank you for always believing in me and picking me up when the research went bad. Kristen was truly a saint for putting up with me and reading about all "that plastic stuff." I think she's the real expert now. No one deserves the rewards of this degree more than you. It's now time to turn over a new chapter in our life together and as a family. I just want you to know that you made all of this possible.

TABLE OF CONTENTS

LIST OF FIGURES

LIST OF TABLES

NOMENCLATURE

A	interfacial surface area for a mixing domain or a nucleated cluster [m^2]
A	characteristic flow area [m^2]
A_i	surface area of a cluster containing i molecules [m^2]
A_{bp}	surface area of the bubble [m^2]
A_{ij}	surface area between constituents i and j [m^2]
B	half slit height [m]
c	instantaneous or local equilibrium concentration of gas molecules [kg(gas)/kg(polymer)]
c_o	initial uniform concentration of gas [kg(gas)/kg(polymer)]
c_1	concentration of gas at the surfaces [kg(gas)/kg(polymer)]
c_{eq}	equilibrium concentration of gas in a polymer [kg(gas)/kg(polymer)]
c_p	specific heat [J/kg K]
c_w	gas concentration at the cell wall surface [kg(gas)/kg(polymer)]
c_∞	initial equilibrium gas concentration [kg(gas)/kg(polymer)]
C_o	concentration of homogeneous nucleation sites [sites/m^3]
C_1	concentration of heterogeneous nucleation sites [sites/m^3]
d_b	average diameter of dispersed bubbles [m]
d_{max}	maximum diameter of elongated bubbles [m]
D	diffusivity of gas in a polymer matrix [m^2/s]
D	channel diameter [m]
D_c	average cell diameter or size [μm]
D_b	barrel diameter [m]
D_t	annulus diameter [m]
D_o	diffusivity coefficient [m^2/s]
e	width of screw flight [m]
E^*	complex dynamic tensile modulus = $E' + jE''$ [Pa]
E'	dynamic tensile storage modulus [Pa]
E''	dynamic tensile loss modulus [Pa]
E_f	tensile modulus of the foam [N/m^2]
E_m	tensile modulus of the polymer [N/m^2]
E_r	relaxation modulus [Pa]
ΔE_D	activation energy for diffusion [J]

ΔE_s	heat of solution [J]
f_o	frequency factor of gas molecules joining a homogeneous nucleus [1/s]
f_1	frequency factor of gas molecules joining a heterogeneous nucleus [1/s]
F	flux of gas or diffusing species
ΔF_k	Helmholtz free energy for critical cluster formation [J]
G	Gibbs free energy [J]
G_{ij}	Gibbs free energy of a mixture comprising constitutes i and j [J]
$G^0{}_i$	Gibbs free energy of constituent i in initial state [J]
ΔG^{*}_{het}	Gibbs free energy (activation energy barrier) for heterogeneous nucleation [J]
ΔG^{*}_{hom}	Gibbs free energy (activation energy barrier) for homogeneous nucleation [J]
ΔG_m	Gibbs free energy of mixing [J]
H	enthalpy [J]
H	depth of the screw channel [m]
ΔH	heat of fusion [J/kg]
ΔH_m	enthalpy of mixing [J]
I_o	amplitude of the incident radiant energy flux [J/m^2 s]
J	growth rate of nucleated clusters
k	thermal conductivity [J/m s K]
k_m	thermal conductivity of the polymer melt [J/m s K]
K_s	Henry's law constant [kg(gas)/kg(polymer)Pa]
K_{sa}	Henry's law solubility coefficient for an amorphous polymer [kg(gas)/kg(polymer)Pa]
K_{sc}	Henry's law solubility coefficient for a crystalline polymer [kg(gas)/kg(polymer)Pa]
K_{so}	Henry's law constant at reference conditions [kg(gas)/kg(polymer)Pa]
k	Boltzmann's constant [J/K]
l	half thickness or characteristic length over which gas diffuses [m]
L	length of metering zone [m]
L	characteristic flow length [m]
L	flow channel length [m]
m	factor in power law constitutive equation [Pa s^n]
m_f	power law coefficient for the nucleated polymer/gas solution [Pa s^n]
m_g	mass of the gas phase [kg]
m_p	mass of the polymer [kg]
m_s	mass of the gas remaining in solution [kg]

m_T	total mass of the gas [kg]
$\dot{m}_p$	polymer mass flow rate [kg/s]
M_t	mass of gas in polymer after time t [kg]
M_∞	initial mass of gas in polymer [kg]
n	distribution of nucleated clusters
n_i	number of clusters containing i molecules
n_i	mole fraction of constituent i
n_b	average number of gas molecules in a cluster
n	exponent in power law constitutive equation
N	screw speed [rpm]
N	microcell nucleation rate [cells/cm^3 s]
N_f	cell density relative to foamed material [cells/cm^3]
N_{hom}	homogeneous nucleation rate [cells/m^{3}s]
N'_{hom}	homogeneous nucleation rate during mixed mode nucleation [cells/m^{3}s]
N_{het}	heterogeneous nucleation rate [cells/m^{3}s]
N_T	total nucleation rate [cells/m^{3}s]
p	hydrostatic or thermodynamic pressure [Pa]
p_{sat}	gas pressure used during polymer saturation [Pa]
p_g	gas pressure in a cell or bubble [Pa]
p_∞	pressure of the polymer far from the cells [Pa]
Δp	difference in the pressure of the gas in the cluster and the ambient nucleation pressure [Pa]
Δp	pressure used to saturate the polymer with gas [Pa]
P_i	gas supply pressure to metering system [Pa]
P_b	barrel pressure at the gas injection port [Pa]
P_{barrel}	pressure at the barrel venting port [Pa]
P_{exit}	pressure at the foaming die exit [Pa]
P_g	pressure of the gas phase in the cells [Pa]
P_{go}	pressure of the gas phase upstream of the shaping channel [Pa]
P_{head}	pressure at the head of the screw [Pa]
P_n	pressure at the nucleation device [Pa]
P_s	shaping pressure at the foaming die inlet [Pa]
ΔP	pressure differential across metering zone [Pa]
ΔP	pressure loss along the flow channel (P_{inlet} - P_{outlet}) [Pa]
ΔP_{nuc}	effective pressure change driving nucleation [Pa]
r	gas bubble or cell radius [m]

r	radial coordinate relative to the center of the cell or flow channel [m]
r^*	critical radius of a stable cluster or nucleus [m]
q_{rad}	radiation heat transfer component [J/m^2 s]
q_z	melting rate per length along the melting zone [J/s m]
Q	volumetric flow rate [m^3/s]
Q_g	gas volumetric flow rate [m^3/s]
R	average radius of a cell [m]
R	nozzle or channel radius [m]
Re_n	Reynolds number for a non-Newtonian power law flow
R_p	flow resistance of porous material [Pa/m^3/s]
R_o	radius of critical nuclei [m]
$\dot{R}$	radial velocity of the cell surface [m/s]
$\ddot{R}$	radial acceleration of the cell surface [m/s^2]
R	universal gas constant [J/gmole K]
R	universal gas constant/molecular weight of the gas [J/kg K]
s	striation thickness [m]
S	entropy [J/K]
ΔS_m	entropy of mixing [J/K]
ΔS_{comb}	combinatorial entropy of mixing [J/K]
ΔS_{nc}	non-combinatorial entropy of mixing [J/K]
t	time or characteristic time [s]
$\tan\delta$	dynamic tensile loss tangent = E''/E'
Δt_n	characteristic nucleation time in the presence of cell growth [s]
Δt_d	characteristic diffusion time [s]
T	absolute temperature [K]
T_b	barrel temperature [K]
T_{die}	temperature of the die or the die lips [K]
T_{exit}	flow temperature at die exit [K]
T_{final}	final temperature of adiabatic expansion [K]
T_g	glass transition temperature [K]
T_m	temperature of melt [K]
T_m	melting temperature [K]
T_n	temperature of the solution at post nucleation [K]
T_{so}	temperature of solid bed core [K]
v_{exit}	specific gas phase volume at the die exit [m^3/kg]
v_{final}	specific gas phase volume after expansion [m^3/kg]

$v_{g/p}$	specific volume of the gas phase relative to the polymer mass [m^3/kg]
v_m	specific volume of the polymer/gas system [m^3/kg]
v_r	radial velocity component of the polymer or polymer/gas interface [m/s]
v_z	velocity along the z coordinate from the channel entrance [m/s]
$\bar{v}$	average flow velocity [m/s]
V	characteristic mixing volume [m^3]
V_b	volume of the cluster or nucleus [m^3]
V_{bx}	velocity of the polymer melt along screw axis [m/s]
V_f	volume fraction of voids or cells
V_j	velocity magnitude of the polymer film shear flow [m/s]
V_g	total volume of the gas phase
V_m	molar volume of a mixture [m^3/gmole]
W	width of the screw channel [m]
W	width of the slit [m]
We	Weber number (ratio of shear to surface forces)
W_s	shaft work performed on the system [J]
x	coordinate along the thickness direction [m]
X	width of the solid bed [m]
Δz	incremental distance along the flow channel (L/N) [m]

α	total entrance angle [rad]
α_i	rate molecules leave a cluster containing i molecules [1/s]
β	monochromatic extinction or absorption coefficient [1/m]
β_i	rate molecules join a cluster containing i molecules [1/s]
χ	mass fraction of crystalline polymer
δ	complex modulus phase angle [rad]
δ	characteristic spacing between stable nuclei [m]
δ	screw/barrel clearance [m]
δ_i	solubility parameter of constituent i
ε	tensile strain [m/m]
ϕ_i	volume fraction of constituent i
ϕ_2	volume fraction of polymer
Φ	ratio of the volume of material in the cell wall to that in the cell struts
Φ_v	volume fraction of gas phase
γ	stretching ratio of the gas component
γ_{bp}	surface energy of the polymer/bubble interface [N/m]

γ_{ij}	surface tension of interface between phases i and j [N/m]
$\dot{\tilde{\gamma}}$	rate-of-strain tensor [1/s]
$\dot{\tilde{\gamma}}$	rate-of strain tensor [1/s]
$\dot{\gamma}_w$	shear rate at the wall [1/s]
η	non-Newtonian viscosity [Pa s]
η_g	dynamic viscosity of the gas [Pa s]
η_p	dynamic viscosity of the polymer [Pa s]
μ	dynamic viscosity of the fluid [Pa s]
μ_f	viscosity across the screw flight [Pa s]
θ	wetting angle of the polymer-additive-gas interface [rad]
θ_b	screw helix at the barrel [rad]
Θ	wide angle x-ray scattering diffraction angle [degrees]
ρ_c	cell density relative to unfoamed material [cells/cm^3]
ρ_f	density of the foam [kg/m^3]
ρ_p	density of polymer [kg/m^3]
ρ_m	polymer melt density [kg/m^3]
σ	tensile stress [N/m^2]
τ	characteristic time [s]
τ_w	wall shear stress [N/m^2]
τ_{ij}	shear stress in the j plane along i [N/m^2]
τ_{ii}	normal compressive stress component along the i-th coordinate [N/m^2]
$\tilde{\tau}$	compressive stress tensor [N/m^2]
Ω	probability that a given state will exist

<u>subscripts</u>

1	gas or solvent
2	polymer
b	gas molecule cluster or bubble
g	gas
i	number of gas molecules in a cluster
k	critical number of gas molecules in a cluster
p	polymer
s	solid second phase particle

CHAPTER 1

INTRODUCTION

1.0 Prologue

The development of advanced materials and manufacturing systems is an integral component in strengthening the international competitiveness of American industry. The market for advanced materials is expected to grow at an annual rate of 10% throughout the decade. As new advanced materials are developed and brought into the marketplace, the demand for new and innovative manufacturing systems intensifies. The issues arising in the design and development of manufacturing systems encompass two broad fields of industrial and academic pursuits. First, a broad knowledge of manufacturing and processing is needed including forming, shaping, liquid and melt processing, surface processing, material addition, material removal, joining processes, and economic justification. Secondly, detailed scientific knowledge of physical systems is needed such as fluid dynamics, thermodynamics, solid mechanics, materials science, mass transport, tribology, and kinematics. Only through the integration of broad manufacturing process knowledge and basic scientific knowledge can competitive manufacturing systems be developed.

In this thesis, the design, development, and experimental verification of an advanced polymer processing system for the production of microcellular sheets is presented as a case study of manufacturing system design. The design of manufacturing systems is a complex task requiring engineering expertise in numerous disciplines as illustrated by the engineering and technological problems encountered in microcellular sheet processing. The problems include real time gas/polymer solution formation, microcell nucleation, premature cell growth, cell over-expansion, cell collapse, cell morphology control, sheet shaping, sheet dimensional stability, sheet surface finish, as well as the significant problem of system start-up and transient effects.

Microcellular polymers are an innovative cellular polymer technology characterized by cell sizes on the order of 0.1 to 10 microns and cell densities on the order of 10^9 to 10^{15} cells per cubic centimeter. Due to their extreme cell densities and minute cell size, these materials require advanced process technologies which surpass the capabilities of conventional foam processes.

The continuous processing of microcellular sheets developed in this work is based on three sub-processes which include the processing of the polymer matrix, the processing of the microcellular structure, and the processing the net shape. The creation of a microcellular structure is achieved by dissolving large gas concentrations into a polymer matrix and subjecting the saturated system to a rapid thermodynamic state change. This creates an unstable or supersaturated matrix which drives the nucleation of billions of microcells. Stable cells then grow as gas diffuses into the cells reducing the bulk density of the material. Based on these fundamental processing requirements, a hierarchical design strategy is used to synthesize the overall production system such that each of the processing functions is independently satisfied by a unique design parameter or process variable.

In order to develop the microcellular sheet processing system, a detailed batch processing characterization of amorphous and semi-crystalline polymers is performed. This characterization identifies viable process variables for continuous processing and demonstrates some of the fundamental processing differences of amorphous and semi-crystalline polymers. Based on the batch processing characterization, a detailed system design is presented. The basic concept of this design is the use of a plasticating extruder to process the polymer matrix, the use of staged pressure losses to produce a microcellular structure, and the use of a foaming/shaping die to produce the net dimensions. In satisfying the latter two requirements, three of the critical continuous processing functions are addressed in detail: continuous nucleation, cell growth control, and shaping. Here the concepts of near-net shape nucleation and shaping of a nucleated polymer/gas solution flow are presented and experimentally verified. As an integral part of this development, various processing models and design criteria are developed to aid in the design process. In general, these models and criteria are found to agree well with the experimental results. Moreover, the results of the critical experiments verify the overall performance of the microcellular sheet extrusion system.

1.1 Objectives of Research

Since their invention over a decade ago, microcellular plastics have received considerable attention from both an industrial standpoint and a fundamental research and development perspective. However, there is a great deal about the processing and physical interactions of these innovative materials which are not yet understood.

The objectives of this research are two-fold. First, the research seeks to design, develop, and experimentally verify a processing system for the continuous production of microcellular thermoplastic sheets. In order for this process technology to be successfully scaled to industrial levels, a second goal of this research is to build upon the scientific knowledge base underlying the continuous processing of microcellular polymers. Throughout this research, a deliberate attempt is made to develop a generic microcellular processing technology that will have a wide applicability to a variety of industrial processes. Through the advanced development of this generic technology, numerous applied processes can be developed to meet the needs of specific product applications.

Since the polymer processing technology and system detailed in this thesis is intended to have industrial applications, it is important to first set the framework of conventional polymer foam processes as a basis of comparison.

1.2 Conventional Polymer Foam Process Technology

Conventional polymer foams or cellular polymers are commonly made from thermoplastics, thermosets, and elastomers. These lightweight materials were originally developed for their thermal and mechanical properties, but more recently have found applications as a result of their unique dielectric properties. The most common foams include polyurethanes, polystyrene, poly(vinyl chloride), polyethylene, polypropylene, phenolics, urea-formaldehyde resins, silicones, natural rubber, and synthetic rubber. Polymer foams can be classified into two morphological categories: open-cell and closed-cell. Open-cell foams have a co-continuous, three-dimensional network of voids and polymer. Closed-cell foams have discrete bubbles randomly dispersed throughout a polymer matrix (e.g., typical microcellular foams are closed cell). Conventional polymer foams can be further classified based on five processing techniques; the first four are the predominant commercial foam processes.

(1) Cellular polymers processed by dispersing gases into the polymer matrix (polymerized, partially polymerized, or in solution) by mechanical mixing, frothing, whipping, agitation, or bubbling.

(2) Polymer foams in which gas bubbles are formed within the polymer matrix, generally a melt or a mixture, by heating and/or decreasing the pressure of a gas or volatile liquid and polymer solution. This is commonly called a physical blowing agent technique.

(3) Polymer foams in which gas bubbles are created in the polymer matrix as a result of the decomposition of a second phase material in the polymer which generates gases and bubble formation. This is called a chemical blowing agent technique.

(4) Polymer foams in which gas bubbles are created in the polymer matrix as a result of a chemical reaction of a second phase material in the polymer which creates gaseous by-products. This is also called a chemical blowing agent technique.

(5) Cellular polymers processed by first forming a polymer/solvent solution and phase separating out the solvent forming a precursor consisting of a discrete or co-continuous network of polymer and solvent. The precursor is subsequently dried to extract the solvent leaving a cellular polymer matrix.

Conventional polymer foams typically have cells ranging in size from 100 μm to 2 mm and have relative densities ot 0.7 to 0.8 for structural applications and less than 0.25 for insulation applications. The following sections present a representative cross section of conventional polymer foam process technologies while comprehensive reviews of conventional cellular polymers and conventional polymer foam technology are presented by Berins (1991), Gibson and Ashby (1988), Hilyard (1982), and Suh and Webb (1985).

1.2.1 Polyurethane Foam Processing

Polyurethane foams are made in rigid and flexible forms depending on the polyol and polyisocyanate constituents and the processing conditions. Typically, polyurethane foams are produced using chemical blowing agents or physical blowing agents. The chemically blown foams uses a secondary reaction of isocyanate and water (added to the polyol) which yields a intermediate carbonic acid that decomposes to form carbon dioxide. The carbon dioxide serves as a blowing agent for the foaming process. The physical blowing agent technique uses the volatilization of a low boiling point fluid to produce gas and provide for expansion. In this case, volatilization of the fluid occurs during the exothermic reaction of the polyol and isocyanate which increases the fluid temperature to achieve boiling of the volatile fluid.

Polyurethane foam processing requires the pumping and the metering of proper ratios of polyol, isocyanate, blowing agent, and additives. The pressurized, metered flow is thoroughly mixed to promote a uniform chemical reaction and foaming process. The reacting solution is formed into shape by pouring the mixture into a cavity, spraying it onto a surface, injecting it into a mold, or casting it onto a conveyer. The foam expansion is stabilized during cross-linking as the polymer viscosity and the stiffness increase. A critical step in polyurethane foam processing is the mixing of the constituents. This is accomplished by mechanical mixing techniques commonly used in pouring and casting processes or by high Reynolds number impingement mixing commonly used in spraying and injection processes. For example, automotive parts such as glove compartments and fascias use impingement mixing as part of a reaction injection molding (RIM) process. RIM foams typically have a sandwich-like structure consisting of a solid unfoamed surface and a low-density cellular core. Typically, the sandwich structure improves mechanical properties over standard polyurethane foams.

1.2.2 Latex Rubber Foams

Latex rubber foams are produced using a carefully metered mixture of rubber latex (i.e., comprised of a stabilized emulsion with rubber particles), a soap solution, an antioxidant, a vulcanizing or cross-linking agent, and a foam stabilizer (such as Na_2SiF_4). The process consists of agitating the mixture to promote random phase distributions followed by an aeration step typically accomplished using a rotating set of intermeshing teeth which whip air, carbon dioxide, or nitrogen into the liquid dispersion forming a froth. The mixture is heated using steam to vulcanize the rubber latex while it is molded into shape. Once molded, the remaining water is squeezed out of the part and the part is dried. The processing of latex rubber foams is very similar to that of plastisol foam processing.

1.2.3 Plastisol Foam Processing

Plastisol foams are commonly used as carpet backing, air filters, gaskets, vinyl flooring, weather-stripping, and artificial leather. Plastisols are vinyl dispersions consisting of fluid suspensions of fine-particle-size poly(vinyl chloride) resins in small amounts of volatile liquid plasticizer or diluent systems. Plastisols generally include particulate PVC resins, plasticizers, stabilizers, fillers, and pigments. A frequently used plasticizer in plastisols is di-2-ethylhexyl phthalate (DOP). There are two processing techniques used to produce plastisol foams: (1) a chemical blowing process and (2) a mechanical frothing process. Chemical blown plastisol foams are processed using an emulsion of PVC, a plasticizer, and a chemical blowing agent. The metered mixture is transferred under pressure into a mold so that the mold is completely full. The mold is held under pressure and heated resulting in the fusion of the plastisol and the reaction of the blowing agent forming a gaseous product. Under pressure, the gas disperses in the melt as small bubbles. Parts are then cooled and demolded followed by a secondary heating process to expand the part to the desired density. A second plastisol foam molding process consists of injecting the mixture into a low pressure mold at high temperatures. The high temperatures result in plastisol fusion and the decomposition of the blowing agent which expands the material to fill the vented mold. Both molding processes produce low-density, closed-cell foam components.

Additional plastisol foam processes include spread coating and calendering processes. For spread coating, a thin plastisol coating is applied to a release paper and partially fused in an convection oven. The product is coated a second time with a plastisol containing a blowing agent. The film is then processed through a higher temperature oven to fuse the plastisol and expand the blowing agent for foaming. The paper backing is then removed from the foam using winding rolls. In the calendering process, the plastisol and blowing agent are blended at temperatures promoting dissolution of the plasticizer in the PVC resin. The mixture is transferred into a Banbury mill which forms a homogeneous mass of vinyl compound. The compound is fed into an extruder and is subsequently processed through calender rolls to obtain an expandable sheet. The sheet can then be laminated with vinyl films and passed through an oven to expand the sheet to form a low-density foam having an integral skin.

Yet another plastisol foam processing method uses a mechanical frothing process to disperse a fine bubble structure in a plastisol emulsion containing surfactants. Rotating sets of intermeshing teeth can be used to whip air, CO_2, or N_2 in the liquid plastisol. The frothed mixture can then be cast into shape and cured to fuse the plastisol matrix creating an open cell foam structure. Open cell plastisol foam can also be created by fusing the plasticized PVC particles using excess plasticizer. The plasticizer remaining in the dispersion is then removed or dried yielding a relatively weak open-cell PVC matrix.

1.2.4 Expanded Polystyrene Foams

Expanded polystyrene foams are commonly used as insulation panels, flotation devices, insulated coolers, protective packaging, and insulated food and beverage containers. Expandable polystyrene resins (EPS) are prepared either by allowing a blowing agent (i.e., typically pentane, isopentane, hexane, or other halocarbons) to penetrate PS particles at elevated temperatures or by polymerizing the styrene monomer in the presents of a blowing agent such that the blowing agent is dispersed in the polymerized

PS particles. Expanded polystyrene foams are produced in two forms: (1) mold expanded polystyrene (MEPS) used for insulation and consumer goods and (2) loosed-filled polystyrene foam used for insulation and protective packaging.

The processing of MEPS parts involves first expanding polystyrene beads to an intermediate density using steam. Next, the partially expanded beads are aged to allow stabilization and drying. Finally, the beads are molded in a steam heated mold resulting in the expansion of the beads and in the fusion of beads to form a shaped part. The molding step plays a major role in determining the mechanical performance and appearance of the final part. To insure a uniform fusion process, the molds are commonly evacuated of air using a vacuum. Next, a low pressure steam heating is used to soften the beads, and finally, a high pressure steam heating is used to fuse the beads. The molded parts are then cooled to promote a stable structure.

Loose-filled EPS is produced by either processing an expandable polystyrene shape created during polymerization (such as a hollow shell or peanut) or extruding an expandable polystyrene preform (such as a figure eight). The expandable preforms are then expanded using multiple steam heating steps resulting in a low-density loose-filled material.

1.2.5 Thermoplastic Structural Foams

Another conventional foam processing technology is that of structural foams. Structural foams are characterized as having integral high density skins, a cellular core, and a sufficiently high strength-to-weight ratio to be utilized in load-bearing applications. A number of thermoplastic structural foam materials are produced including ABS, acetal, acrylic, polystyrene, polyethylene, nylon, vinyl, polycarbonate, polyphenylene oxide, polypropylene, polysulfone, thermoplastic polyester, and various glass-reinforced resins.

One common technique for producing thermoplastic structural foams is a modified injection molding process. Advantages of structural foam molding are the reduction of sink marks in thick sections, the increase in strength-to-weight ratio performance, and the reduction in tooling costs due to lower mold pressures. There are three widely used industrial structural foam molding process: low-pressure, high-pressure, and gas-assisted injection molding processes (Berins, 1991; Hilyard, 1982; Hobbs, 1976; Suh and Webb, 1985). These techniques produce foams characterized by non-uniform cell size distributions ranging from 50 to 500 microns. For a comprehensive review of thermoplastic structural foam molding, the reader is referred to Throne (1977).

Low-pressure foam moldings are processed using either physical or chemical blowing agents. The physical blowing agent process involves first extruding a polymer and injecting a blowing agent, such as nitrogen, into a molten polymer stream. The polymer and blowing agent system is mixed and pumped into an accumulator where it is held under pressure. Once filled, the accumulator is further pressurized and a nozzle valve opened. The back pressure of the accumulator forces the mixture into a mold maintained at low pressure. The mold is only partially filled and the foam expands to fill the mold cavity. The molds require low clamp forces, thus the term low-pressure foam molding; however, the resulting parts generally have a poor surface finish due to the surface cells which collapse during foam expansion creating a characteristic swirl pattern.

In contrast, the low-pressure chemical blowing agent process is accomplished in much the same manner as conventional injection molding. In this process, the chemical blowing agent is either compounded into the plastic pellets, mixed with the plastic pellets, or supplied as a blowing agent/resin concentrate. The moldings are processed using conventional injection molding equipment with minor modifications such as injection boosters for rapid injection rates. In this process, a metered short shot is rapidly injected into mold partially filling the cavity. During injection, the blowing agent decomposes due to heating and releases gas in the polymer melt. The polymer then expands filling the mold. In both low-pressure foam molding processes, the resulting parts have a swirl surface pattern yielding a poor surface finish and a non-uniform cell size distribution yielding poor mechanical performance. These effects can be reduced using a mold pressurized with an inert gas during the filling process (i.e., counter-pressure). The counter-pressure minimizes the expansion of the gas/polymer mixture at the flow front thereby reducing the collapse of surface cells and promoting even expansion pressures and uniform cell structures.

High-pressure foam molding is a less common process and is accomplished by injecting a high-pressure polymer/blowing agent mixture into a mold. This is accomplished using systems similar to low-pressure foam molding. In high pressure molding, the injected shot completely fills the mold. The mold can also be counter pressurized to enhance the surface finish of the final product or an integral unfoamed skin can be co-inject over the foam core. Foam expansion is accomplished by expanding the mold cavity volume (i.e. removing the mold pressure at a controlled rate) by outwardly displacing the mold segments and removing the counter-pressure. In this way, the density of the final product can be controlled accurately and consistently. However, it is difficult to achieve uniform expansions of complicated shapes unless multi-segment molds are used. The cell size distribution achieved by high pressure molding is generally better than that of the low-pressure foam molding.

A final process for producing structural foam moldings is gas-assisted injection molding. Gas-assisted injection molding is a process for manufacturing hollow parts. The basic concept is to inject inert gas into the polymer melt during or post molding. Since the gas does not immediately mix with the polymer, it tends to form continuous channels through the hotter, less viscous, sections of the molded plastic (i.e. the center sections). The gas maintains pressure throughout the molding cycle thus reducing sink marks, promoting a good surface finish, and producing a lower density part with a high strength-to-weight ratio.

1.2.6 Thermoplastic Foam Extrusion

There are a number of extrusion processes used for the continuous production of foamed sheets and profiles. These processes are commonly used to produce polystyrene, polyolefin, and poly(vinyl chloride) foams. Typical applications include production of sandwich panel cores, insulation panels, artificial wood panels, window and door frames, building siding, and fence posts.

One of the first polystyrene foam extrusion processes involved extruding a high pressure solution of a physical blowing agent and molten polymer through an orifice onto a moving belt at ambient temperature and pressure. The blowing agent vaporizes at low pressures causing the polymer matrix to expand. The expansion process is stabilized by the viscosity and elasticity of the polymer matrix which increases during cooling. Typical blowing agents used are fluorocarbons. Cellulose acetate foams are extruded using a similar process.

The majority of cellular polyolefins including polyethylene and polypropylene are extruded using chemical blowing agents. One of the first commercial processes developed for high density polyethylene foam was a wire coating process for insulation of electrical conductors. In this case, a mixture of polyethylene and a chemical blowing agent are extruded over a wire. During extrusion, the mixture is heated and the blowing agent decomposes, liberating gas. Relatively low die pressures are used to prevent expansion of the foam prior exiting the die. Upon exiting the die, the polyethylene coats and expands around the wire creating an insulated conductor. The expansion process is stabilized by the rapid crystallization of the polyethylene matrix.

Low density polyethylene (LDPE) foams can also be extruded by blending, under pressure, a polyethylene melt and a physical blowing agent (e.g., a halogenated hydrocarbon gas). The process uses either two sequential extruders or a two-stage extruder. The blending process is accomplished in the first extruder for sequential extrusion or in the first stage of a two-stage extruder. The second extruder or extruder stage is used to stabilize and meter the mixture. Under close temperature control, the mixture is extruded through a die and onto a conveyer at atmospheric pressure. Upon emerging from the die, the polymer/gas system expands forming a foamed sheet. Similar to the wire coating process, the expansion is stabilized by the rapid crystallization of the LDPE matrix.

Cross-linking is another technique used for manufacturing stable low-density polyethylene foams. Since low-density polyethylene has very low melt viscosity, it is commonly crosslinked prior to foaming yielding a stiffer polymer matrix with a higher viscosity. This helps stabilize the foaming process. Cross-linking is accomplished using radiation for thin cross-sections or chemical reaction for thick cross-sections. In chemical cross-linking processes, precise proportions of low density polyethylene, cross-linking agent (e.g., dicumyl peroxide), blowing agent (e.g., azodicarbonamide), and other additives are extruded into a sheet. The sheet then passes through a two-stage oven. In the first stage, the sheet is heated to a temperature activating chemical cross-linking. In the second stage, the sheet is heated to a higher temperature resulting in the decomposition of the blowing agent and the expansion of the foamed sheet. The sheet is then post-processed to impart surface finish and dimensional control. In an irradiation cross-linking process, the extrusion process takes a similar form except an irradiation step (e.g., using an electron beam) is substituted for the first heating stage, and no chemical cross-linking agent is used.

Yet another foam extrusion process is used for poly(vinyl chloride) resins. Closed cell rigid PVC foams can be extruded using volatile plasticizers such as acetone. The extrusion process incorporates a two-stage extruder where the volatile plasticizer is injected in the decompression section of the screw and mixed into the polymer melt. The second extruder stage is used to meter the flow and increase the temperature resulting in the volatilization of the plasticizer under pressure. The material is then passed through an orifice to a low pressure where expansion takes place. Stabilization of the foam occurs as the material is cooled.

For higher density structural foams, foam extrusion processes typically use a controlled expansion technique. One common process is the Celuka process. This process incorporates two sequential or tandem extruders; although, a two-stage extruder can be used. A dry mixture of polymer pellets and a nucleating agent is fed into the first extruder. After the mixture has been melted in the first extruder's compression zone, a high pressure physical blowing agent (typically a low molecular weight fluorocarbon or hydrocarbon) is injected into the polymer melt along the extruder barrel. The polymer/blowing agent melt is intensely mixed in the metering zone of the first extruder. The mixture flows into the second extruder which provides further mixing and meters the flow. At the exit of the extruder is a die (typically a annular or a sheet profile) which performs the primary shaping of the sheet. At the exit of the die, the expanding sheet is surface cooled using a gas jet cooling ring. While the sheet expands, it is drawn over or through a mandrel to hold shape and stabilize expansion. Commonly used resins for this process include polystyrene, PVC, and polyolefins.

1.2.7 Comparison with Microcellular Processing

Microcellular polymer processing differs considerably from conventional foam processing, and indeed conventional processes cannot be used to produce microcellular structures. In general, microcellular processing requires large concentrations of inert gas such as carbon dioxide or nitrogen. Concentrations can be ten times that of conventional foam processing. Conventional processes are not capable of achieving such high gas concentrations in single phase polymer/gas solutions. In addition, microcellular processing requires the nucleation of at least three orders of magnitude more cells compared with conventional foams. This requires nucleation rates beyond the capability of conventional processes (as is shown in chapter 8). Finally, microcellular processing requires the controlled growth of cells having a final sizes 100 times smaller than conventional foams. At this scale, the growth of cells can occur in less than one hundredth of a second which requires cell growth control techniques beyond that of conventional foam processing.

A final important aspect of the microcellular sheet processing system, as developed in this work, is the independent control of the major processing functions including polymer/gas solution formation, microcellular nucleation, cell growth, and sheet shaping. In conventional industrial processes, many of these functions are coupled in that no set of process variables or design parameters exist for independently satisfying these major functions.

1.3 Thesis Overview

This thesis begins with an introduction and review of microcellular plastics technology presented in chapter 2. This comprehensive review looks at the innovations and advances in microcellular plastics technology since its invention in the early 1980's. Chapter 2 first explores recent advances in microcellular materials technology followed by a review of existing process technology. This chapter concludes with a discussion of the relatively unique mechanical properties exhibited by these innovative materials. To provide a foundation for the development of a continuous sheet processing system, chapter 3 presents the fundamental principles of microcellular processing. First, the fundamentals of polymer/gas solution formation are explained. Next, the principles of microcellular nucleation and a general discussion of phase separation mechanisms are presented. Since the design of a continuous processing system is a major portion of this thesis, chapter 4 briefly introduces to the axiomatic design principles which are utilized throughout this work as a framework for the system design.

In order to develop the microcellular sheet processing system, a detailed batch processing characterization of amorphous and semi-crystalline polymers is presented in chapter 5. This characterization identifies viable process variables for the continuous process and demonstrates some of the fundamental processing differences between amorphous and semi-crystalline polymers.

The design of the continuous microcellular sheet processing system begins with a presentation of three conceptual designs in chapter 6. In chapter 7, these system concepts are compared based on various system design criteria. One of the conceptual system designs is then discussed in detail. The system design is fashioned in a hierarchical structure using the axiomatic design principles. The basic strategy of the design is to use a plasticating extruder to process the polymer matrix, a staged pressure losses to produce a microcellular structure, and a foaming/shaping die to produce the net dimensions.

In chapter 8, the design and analysis of continuous microcellular nucleation systems is presented. Chapter 8 introduces a new concept for continuous nucleation called near-net shape nucleation and provides experimental verification of various nucleation system designs. Moreover, various design criteria are developed to evaluate the relative performance of continuous nucleation devices. The critical processing functions of shaping and cell growth control are addressed in chapter 9. Here the concept of shaping of a nucleated polymer/gas solution flow is presented and experimentally verified using various foaming die designs. The design of these dies is based on a processing model for predicting the pressure loss and volumetric flow rate in nucleated polymer/gas solution flows. The overall performance of the microcellular sheet extrusion system is verified using a series of critical experiments presented in chapters 8 and 9. Finally, in chapters 10 and 11, the conclusions of this work and the recommendations for future research are presented.

CHAPTER 2

REVIEW OF MICROCELLULAR PLASTICS TECHNOLOGY

2.0 Introduction

In the early 1980's, an important process for making a new class of polymeric materials called microcellular plastics was invented at the Massachusetts Institute of Technology under the sponsorship of the MIT-Industry Polymer Processing Program with continued research support from the MIT-Industry Microcellular Plastics Consortium (Martini-Vvedensky et al., 1984). In many cases, these innovative materials have superior thermal, mechanical, and electrical properties when compared to the neat polymer (i.e., the unmodified polymer prior to microcellular processing), and are often found to have improved performance relative to conventional structural foams. Moreover, microcellular processing technology has advantages over many conventional polymer foam processes because it uses environmentally sound gases as blowing agents, rather than hydrocarbons, chlorofluorocarbons (CFCs), hydrochlorofluorocarbons (HCFCs), or toxic chemical blowing agents.

The MIT process consists of first forming a polymer/gas solution followed by the inducement of a rapid thermodynamic instability which simultaneously nucleates a very large number of microvoids (Martini-Vvedensky et al., 1984; Cha et al., 1992; Colton and Suh, 1992; Suh et al., 1993). This can be done at room temperature as well as at higher temperatures (Cha and Suh, 1992). A scanning electron microscope (SEM) micrograph of a typical microcellular polymer cross section is shown in Figure 2.1. The sample shown has an average cell diameter (or cell size) of 10 µm and a cell density of 10^9 cells/cm^3 which translates into a specific gravity of approximately 0.5. Notice the uniform cell structure across the core which is typical of these materials. After microcellular processing, transparent polymers become an opaque white and have a glossy surface finish. The glossy surface finish is due to a characteristic unfoamed surface layer, typically one to five cell diameters in thickness (Martini et al., 1982; Martini-Vvedensky et al., 1984; Hardenbrook et al. 1988). A model for predicting this integral skin thickness has been proposed by Kumar and Weller (1991b).

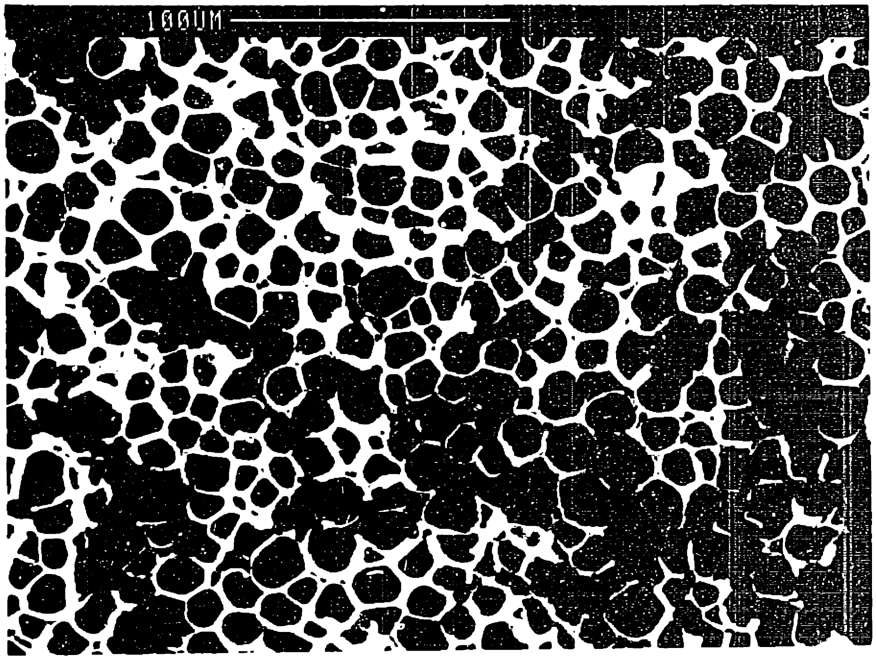

Figure 2.1: Scanning electron microscope micrograph of a typical microcellular poly(ethylene terephthalate) fracture surface.

This chapter is intended to provide an introduction to these innovative materials for a general audience, as well as, an overview of the current state of the technology with respect to research and development. First, some general background and history are presented followed by a discussion of the recent advances in microcellular materials technology. Next, a review of the current microcellular processing technology is presented. Finally, the mechanical properties exhibited by these unique materials is discussed. In the next chapter, the fundamental physical phenomena underlying microcellular processing are presented.

Microcellular plastics are characterized by cell sizes in the range of 0.1 to 10 micrometers, cell densities in the range of 10^9 to 10^{15} cells per cubic centimeter, and specific density reductions in the range of 5 to 98 percent. Typically, microcellular plastics exhibit high impact strength (i.e., up to a five-fold increase over the neat plastic), high toughness (i.e., up to a five-fold increase over the neat plastic), high stiffness-to-weight ratio (i.e., three to five times larger than the neat plastic), high fatigue life (i.e., up to a fourteen-fold increase over the neat plastic), high thermal stability, low dielectric constant, and low thermal conductivity. Microcellular plastics technology has been applied to most polymers including amorphous thermoplastics, semi-crystalline thermoplastics, liquid crystal polymers, elastomers, and thermosets.

The process technology for microcellular plastics was developed at MIT to address material cost and performance requirements of the Eastman Kodak Company. Kodak desired to reduce material consumption without adversely affecting the mechanical performance of a high volume plastic product. The rationale was the nucleation of voids smaller than the pre-existing flaws in the processed plastic (i.e., for the Kodak products, the flaws were carbon black particles 10 μm in size). The creation of microvoids results in a reduction in material consumption and cost without compromising the mechanical performance since failure will tend to initiate at the pre-existing flaw rather than at the nucleated microvoids.

The first stage of microcellular polymer processing involves dissolving an inert gas, such as nitrogen or carbon dioxide, under high pressure (i.e., the saturation pressure) into a polymer matrix to create a solution having a high gas concentration (typically 3 to 20 percent gas by weight). The equilibrium gas concentration, c_{eq}, can be expressed as a thermodynamic function of temperature, T, and pressure, p, as given by equation (2-1).

$$dc_{eq} = dc_{eq}(p,T) = \left(\frac{\partial c_{eq}}{\partial p}\right)_T dp + \left(\frac{\partial c_{eq}}{\partial T}\right)_p dT \qquad (2\text{-}1)$$

The next phase of microcellular processing is the rapid nucleation of billions of microvoids. Rapid nucleation promotes the even distribution of the dissolved gas, precipitating from the polymer matrix, over a multitude of cells. Nucleation is initiated by inducing a large thermodynamic instability. The thermodynamic instability is accomplished by quickly changing the solubility of gas in the polymer matrix. As seen in Figure 2.2 for typical processing ranges, the solubility of gas increases with pressure and decreases with temperature. The thermodynamic state must change quickly due to the competing phenomena of cell nucleation and cell growth. Without a rapid thermodynamic state change, the nucleation of cells occurs over a finite length of time, and the gas in solution will preferentially diffuse to cells which have already nucleated, rather than nucleating additional voids. Thus, the overall cell density is reduced compared with rapid thermodynamic state changes. In general, gradual thermodynamic state changes result in large cells and non-uniform cell size distributions which is the case for conventional foam processing. To promote the large cell densities characteristic of microcellular polymers, homogeneous cell nucleation is preferred over heterogeneous cell nucleation, but is not always possible. This follows since cells will preferentially nucleate at the limited number of high energy interfaces such as additive particles, crystalline phases, contaminants, and pigments.

The final phase of microcellular processing is the growth of stable nuclei. To allow growth of nucleated microvoids and to decrease the bulk density of the material, the polymer/gas solution is typically heated to near its glass transition temperature. This lowers the polymer's flow strength and allows the cells to grow as gas diffuses into the cells. The temperature of the foaming process (i.e., the foaming temperature) can be used to control the rate of cell growth. Higher temperatures enhance cell growth because of the lower flow strength of the polymer and because of the higher gas diffusivity. Cell growth subsides when the system temperature is lowered to a critical value such that the polymer matrix is stiff enough to suppress further expansion and/or the gas has completely diffused out of solution.

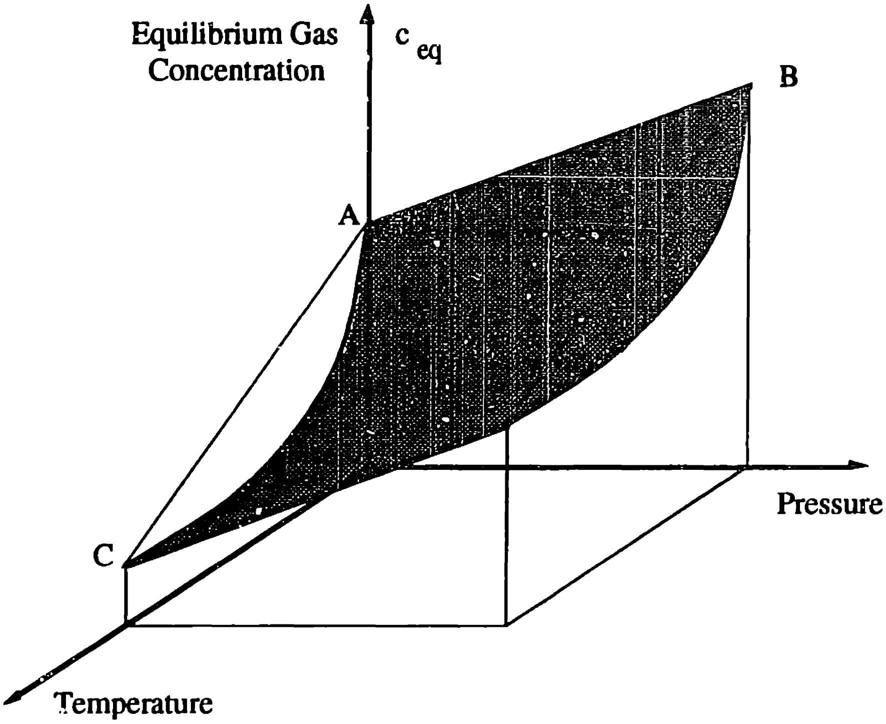

Figure 2.2: Typical equilibrium gas concentration in polymers as a function of temperature and pressure.

2.1 Advances and Potential Impact of the Technology

The initial development of microcellular plastics centered around styrenic resins and was performed by Martini (1981). Since it inception, advances in microcellular plastics technology have resulted in new generations of materials including supermicrocellular and, in the near future, ultra-microcellular plastics. Moreover, microcellular plastics technology has been applied to new polymer/gas systems including amorphous thermoplastics, semi-crystalline thermoplastics, and thermosets. Such material innovations will undoubtedly lead to numerous commercial applications of microcellular polymers.

2.1.1 Advances in the Material Technology

Supermicrocellular Plastics

The development of supermicrocellular plastics and the supporting process technologies represent a significant advancement in microcellular material technology (Cha et al., 1992). To produce supermicrocellular plastics, supercritical fluids such as carbon dioxide are used for the formation of the polymer/gas solution (by definition, a fluid is in a supercritical state when the temperature is higher than the critical temperature and the pressure is higher than the critical pressure). As with the original microcellular technology, a thermodynamic instability is used to initiate microvoid nucleation and cell growth occurs as the gas/supercritical fluid diffuses into the cells from solution.

Supermicrocellular plastics are characterized by cells on the order of 0.1 to 1.0 μm and cell densities on the order of 10^{12} to 10^{15} cells/cm^3 (Cha et al., 1992; Suh et al., 1993). Characteristic cell morphologies of some supermicrocellular polymers are shown in Figure 2.3 (Suh et al., 1993). In addition to the initial work at MIT, an early study of microcellular poly(methyl methacrylate) foamed using supercritical carbon dioxide is reported by Goel and Beckman (1992). Although supermicrocellular plastics have extremely small cell sizes, high volume expansions can be achieved due to the large cell densities produced in these materials. Therefore, density reductions can range from 5 to 98 percent.

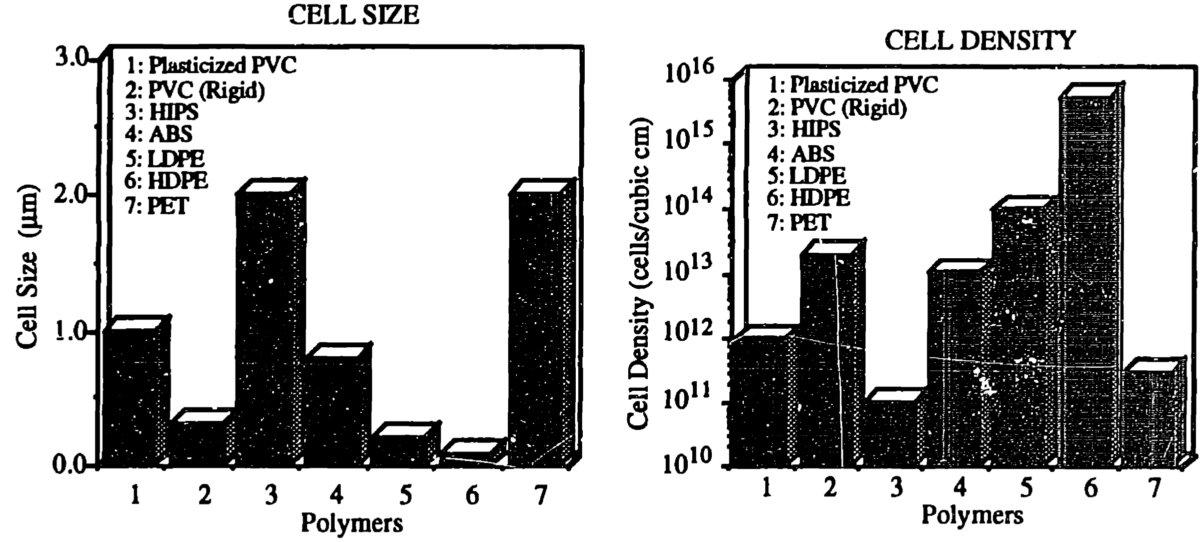

Figure 2.3: Characteristic cell morphologies of supermicrocellular polymers.

Using supercritical fluids for saturation, provides two advantages over microcellular processing using gas. The first advantage is a reduction in the saturation time, and the second advantage is an increase in the nucleated cell density. The saturation time can be reduced by increasing the saturation pressure and the saturation temperature. High saturation temperatures reduce the saturation time by increasing the diffusivity. Based on an order-of-magnitude estimate, the saturation time is approximately halved by a 10 °C increasing in the saturation temperature. Tne reduction in solubility associated with the higher temperatures can be compensated for by increasing the saturation pressure. This is possible because there is no limiting value of the saturation pressure in the supercritical state (i.e., no limiting vapor pressure). The second advantage of supercritical fluids is an increase in the nucleated cell density. The higher nucleated cell density follows from the higher saturation pressures which can be achieved in the supercritical state. Processing at higher saturation pressures results in a greater thermodynamic instability (i.e., a larger solubility change), leading to larger nucleated cell densities.

Ultra-microcellular Plastics

The extension of supermicrocellular technology into the next generation of microcellular materials has been proposed by Suh et al. (1993). This new class of microcellular material is called ultra-microcellular plastics and is characterized by extremely small cell sizes (on the order of 0.01 to 0.1 micrometers) and very large cell densities (on the order of 10^{18} to 10^{15} cells/cm^3). Ultra-microcellular plastics are currently under development at MIT. Development of ultra-microcellular plastics may result in many important industrial applications because of the superior properties attainable with such a microstructure. Potential areas of application include medical, industrial, and consumer products. Among the uses envisioned are optically transparent foams, enhanced electrical and thermal insulation materials, high impact strength plastics, energy saving transparent-window glazing, and "dye-able" plastic sheets.

A unique characteristic of ultra-microcellular plastics is its potential as a transparent material. By definition, the cell size of ultra-microcellular plastics is smaller than the wavelength of visible light (between 0.4 to 0.7 micrometers). Thus, the majority of light will transmit through the ultra-foamed polymer without being reflected provided that the cell density is not too large. The feasibility of producing such a transparent material is supported by microporous aerogels exhibiting varying degrees of transparency (LeMay et al., 1990, Pekala et al., 1992).

Low Temperature and Semi-Solid State Foaming

Changes in polymer viscoelastic behavior due to the presence of high gas concentrations have led to another advance in microcellular material technology. By forming high gas concentration solutions, it is possible to process microcellular polymers at low-temperatures (i.e. at temperatures considerably below the glass transition temperature, T_g, of the neat polymer) such that the polymer is in a semi-solid state. Kumar and Weller (1991a) report microcellular polycarbonate foamed at 60 °C which is 90 °C below the T_g of neat PC. Moreover, Cha and Suh (1992) report on the room-temperature microcellular foaming of plasticized poly(vinyl chloride) (PVC), poly(methyl methacrylate) (PMMA), and glycol modified poly(ethylene terephthalate) (PETG). The patent by Cha et al. (1992) also outlines a process by which this unique class of microcellular polymers can be formed into a three-dimensional shape without thermal processing. In general, low temperature microcellular processing is attributed to the large glass transition temperature depressions which can result from the presence of dissolved gas. Glass transition temperature depressions during microcellular processing of poly(ethylene terephthalate) have been reported by Baldwin et al. (1993). Baldwin et al. report T_g depressions as high as 75 °C during the microcellular processing of poly(ethylene terephthalate) using carbon dioxide.

Developments in Semi-Crystalline Polymers

Significant advances in microcellular materials have been made in the area of semi-crystalline thermoplastics, including a recent patent of Colton and Suh (1992). Colton and Suh (1992) report successful application of the microcellular technology to polypropylene, nucleated polypropylene, and an ethylene/propylene copolymer using nitrogen as the foaming agent. The process utilized by Colton and Suh (1992) involves saturation and foaming a polymer at temperatures above the melting point (i.e., in an amorphous state). Colton (1989) has also presents a study of the nucleation characteristics of the same polymer systems showing results paralleling amorphous thermoplastics.

Baldwin and Suh (1992) have reported producing semi-crystalline microcellular poly(ethylene terephthalate) (PET) and nucleated poly(ethylene terephthalate) (CPET) using carbon dioxide. In contrast to Colton and Suh, the process utilized by Baldwin and Suh (1992) involves saturation and foaming below the melting point (i.e., in a semi-crystalline state). More recently, Baldwin et al. (1992, 1994) have discussed some of the unique aspects of processing semi-crystalline resins compared to amorphous resins. The authors present experimental results indicating predominantly heterogeneous nucleation in crystalline polymers and further propose that the cell growth mechanisms differ in the crystalline systems due to their viscoelastic behavior (see chapter 5). Application of supermicrocellular processing to semi-crystalline polymers has been reported by Cha et al. (1992) and Suh et al. (1993). The authors discuss supermicrocellular processing of low and high density polyethylene (LDPE and HDPE) and PET using supercritical carbon dioxide. Yet another significant advancement in semi-crystalline microcellular polymers is the extrusion of microcellular polypropylene filaments reported by Park and Suh (1992a) using nitrogen and carbon dioxide.

Investigation of New Polymer/Gas Systems

Although the initial research involved only polystyrene and nitrogen systems, microcellular processing has been demonstrated in a number of new polymer/gas systems. Kumar and Weller (1991ab) have reported on the batch processing of microcellular polycarbonate using carbon dioxide. Kumar and Weller's study also presents a characterization of the batch processing variables. Cha et al. (1992) report on the successful implementation of the supermicrocellular foaming process on PVC and PETG using supercritical carbon dioxide while Goel and Beckman (1992) report on PMMA foamed using supercritical carbon dioxide. In addition, Suh et al. (1993) reports the application of supermicrocellular processing to impact grade polystyrene (HIPS) and acrylonitritle-butadiene-styrene (ABS). Kumar et al. (1992) have also reported on the production and batch processing characteristics of microcellular PVC. Both supermicrocellular and microcellular processing have also been applied to a number of other thermoplastics including PMMA, styrene-acrylonitrile (SAN), polymethylpentane (TPX), and PC.

Microcellular Thermosets

Microcellular technology has also been applied to short fiber reinforced polyester composites as reported by Youn and Suh (1985) and by Youn (1984). Such microcellular composites represent another significant extension of microcellular material technology namely into thermosetting polymers. Microcellular thermosets may have wide applicability in sheet molding compound (SMC) and bulk molding compound (BMC) applications, allowing for reduced-weight without significant mechanical property degradation compared with similar composites filled with solid particles.

2.1.2 Additional Microcellular Polymer Technologies

There are other microcellular polymer technologies which have been developed in addition to the materials and processes discussed in this chapter. LeMay et al. (1990) review various low-density microcellular material technologies developed at U.S. Department of Energy National Laboratories. These technologies use either phase separation of polymer or polymer-like solutions or replication of sacrificial pore networks. Both techniques produce liquid-filled precursors which are dried to form a microcellular morphology, typically an open cell structure. The microcellular materials developed include aerogels (Pekala et al., 1992), carbons (Aubert and Sylwester, 1991), and various polymers systems (Aubert and Clough, 1985; Young, 1987; Williams and Wilkerson, 1990). The creation of microcellular polymers using phase separation is also reported by Jackson and Shaw (1990), who discuss a microcellular technology for "rigid rod" polymers using a thermally-induced phase separation process producing open cell morphologies.

Literature is also rich with various cellular polymer technologies for polyurethane systems which are commonly termed microcellular. A recent patent by Stone et al. (1990) discloses various blowing agents for polyurethane foams including the use of supercritical carbon dioxide. Some representative articles include Harasin (1985) who presents an introduction to reaction injection molding technology including applications in polyurethane foam processing, Andrew and Smith (1987) who describe a study illustrating the effects of catalysts and surfactants in polyurethane foam processing, and Kogelnik et al. (1992) who discuss the use of cellular polyurethane elastomers as damping components.

Finally, there exist extensive technologies for producing microporous materials consisting of a three-dimensional open network of micropores. One process for producing amorphous polytetrafluoroethylene (PTFE) foamed films is presented by Tang and Kong (1991) for creating 0.1 to 0.2 μm pores in 150 μm PTFE films. This process consists of sintering polymer particles to form a microporous network. Gore (1980) describes a material and process where a porous PTFE matrix is generated using common PTFE pasted-forming technology followed by stretching of the dried, un-sintered paste to form a fibril structure that interconnects a matrix of solid nodes. Cellulose is yet another microporous material.

While these microcellular and microporous materials are of great commercial and technical interest, they are not the focus of this chapter and will not be addressed further.

2.1.3 Potential Impact of the Technology

In high-volume plastic products, such as pens, shavers, packaging, syringes, interior automobile components, food packaging, etc., the raw material costs account for up to 70 percent of the total manufacturing cost. Any savings in material consumption per unit can result in enormous overall cost savings. Microcellular plastics technology can reduce material weight, and hence consumption, by as much as 80 percent, without compromising structural properties to a large extent. This has the potential to provide manufacturers with a tremendous competitive advantage.

History has repeatedly shown that substantial competitive advantages arise from new material innovations, thus the impact of microcellular plastics technology on the manufacturing sector can be tremendous. Microcellular plastics exhibit high impact strength, high toughness, high stiffness to weight ratio, high fatigue life, high thermal stability, low dielectric constant, and low thermal conductivity. With such unique properties, there are seemingly infinite new and innovative applications of the materials including micro-technology insulation, telecommunications wire insulation, electric and dielectric insulation, fuel cells, and biomedical materials. Additional applications include aerospace and automotive parts which benefit from microcellular plastics' high specific strength and acoustic dampening properties, sporting equipment where weight reduction and energy absorption are critical, cold-weather clothing made from microcellular fiber fabrics for insulation, molecular grade filters for separation processes, and surface modifiers for low friction applications.

Moreover, the process technology used to produce microcellular plastics utilizes environmentally safe gases such as carbon dioxide and nitrogen as blowing agents. Thus, as environmental protection laws eliminate the use of CFCs and HCFCs as blowing agents for conventional polymer foam processing, microcellular processing technology can be used to replace these existing technologies.

As with many new technologies, the advanced development of microcellular plastics will lead to new scientific discoveries. For example, the formation of solutions where gas is the solvent and the polymer the solute creates many interesting questions about intermolecular forces, thermodynamics of solutions, kinetics of dissolution, and permeation of gases through polymeric solids. It also raises many technological issues which need to be answered to implement these non-conventional polymer processing techniques in large-scale production. As the underlying physical phenomena become better understood and experience working with these new materials becomes widespread, the unique characteristics of polymer/gas systems will become more apparent and innovative processing techniques will emerge. For example, one may be able to take advantage of the plasticizing effect of gas to process polymers historically difficult or impossible to process using conventional melt processing.

It is worth mentioning that many of the existing microcellular plastic processes as well as certain variations are currently being implemented in industry. Eastman Kodak developed a variation of the MIT process that is expected to give Kodak a major competitive advantage in its product over its Japanese competitors. The new product is scheduled to be introduced to the market in the near future. Another active microcellular plastics group in industry is at the Axiomatics Corporation in Woburn, MA. Axiomatics has recently purchased a microcellular patent license and has set up an internal R&D program dedicated to the development of microcellular processing technology. In addition, Microcellular Plastics Technology, Inc. in New London, NH is reportedly commercializing Kodak's initial microcellular processing patents (Gaspari, 1993).

2.2 Process Technologies

Early work in cellular polymer processing utilizing dissolved gases to nucleate voids dates back to the 1920's. Pfleummer (German Patent #249,777) discloses the development of a unicellular rubber process using high pressure nitrogen as a blowing agent (Collias and Baird, 1992). In 1942, Alderson of the E.I. du Pont de Nemours Company patented a process for producing cork-like products using ethylene as a blowing agent to produce polyethylene foams having cell sizes on the order of 25 to 100 μm. Using a process similar to Pfleummer, Gent and Tompkins (1969) present an experimental study of the formation and growth of microbubbles in crosslinked elastomers using dissolved gases as physical blowing agents. While these processes are similar to MIT's microcellular processing technology, they differ substantially in a number of ways. These conventional methods do not achieve either the level of supersaturation nor the control over nucleation necessary for producing microcellular plastics. In general, conventional processes result in non-uniform cell nucleation and large cell sizes. The MIT process circumvents these problems by (1) saturating the polymer with relatively large uniform gas concentrations to promote large cell densities and small cell sizes and (2) rapidly inducing a thermodynamic instability to insure uniform nucleation of voids.

To facilitate the transfer of microcellular polymer technology from research and development into commercial use, a number of process technologies have been developed, including a major part of this research, that integrate the creation of a microcellular structure with shaping operations in a viable manner. Recent work has focused on the design of continuous and semi-continuous processes. Current processes for making microcellular plastics include batch processes, a sheet extrusion process, a mono-filament extrusion process, a room-temperature forming and foaming process, and a modified thermoforming process.

Many of the developed process technologies are intended to be generic in nature. That is, the technologies were developed to have wide applicability for industrial processing requirements. The generic nature of the current processes, including the sheet processing system presented in this thesis, allows them to be tailored to specific applications. Moreover, the physical processing knowledge gained with each generation of technology will help promote flexibility and robustness in future generations.

2.2.1 Batch Processing

Batch microcellular processing of pellet, sheet, and pre-formed parts is an effective means for producing samples for laboratory testing, materials characterization, and critical process variable evaluation. Although, the cycle times are too long for most commercial production, the precise control of process variables and the repeatability of process results are definite advantages of batch processing. Additional advantages include the simplicity of the process, the relatively well understood nature of the process, and the potential for processing pre-formed three-dimensional parts provided that certain precautions are taken to preserve the formed shape. In general, there are two basic batch processing techniques used in microcellular processing.

Martini et al. (1982) and Martini-Vvedensky et al. (1984) describe the original microcellular batch processing technique which involves three steps. First, a polymer is placed in a pressure chamber and exposed to a high-pressure gas for a fixed saturation time at ambient temperature. Next, a thermodynamic instability is induced by reducing the pressure, removing the polymer from the chamber, and rapidly increasing the temperature. The rapid decompression and temperature increase result in a solubility drop forming a supersaturated state. The supersaturation provides a driving force for nucleation of billions of microvoids. Heating the polymer/gas system above the glass transition temperature, also promotes cell growth by diffusion of gas into nucleated cells and relaxation of the polymer matrix.

Alternatively, the batch process can be carried out at elevated temperatures as disclosed by Colton (1989) and Colton and Suh (1992). In this case, the sample and chamber are heated during the pressurized saturation time. When the pressure is released and the system quenched, a foamed microstructure is produced. The advantages of this high temperature process variation are increased gas diffusivity and reduced saturation time both of which lead to uniform temperature profiles across the part during foaming helping to promote a uniform microcellular morphology. However with this process, the initial gas concentration available for foaming is less because gas solubility decreases with increasing temperature (see equation 3-7). The high temperature processing is preferable for some semi-crystalline polymers. For example, the gas saturation and foaming of polypropylene should be done near the melting point, T_m, because it is difficult to dissolve gas into the crystallites (Colton and Suh, 1992; Colton, 1989).

2.2.2 Continuous Melt Processing

The first continuous microcellular polymer extrusion processing concepts were proposed by Waldman (1982) and further disclosed by Martini-Vvedensky et al. (1984), while a similar process was patented by Hardenbrook et al. (1988) of the Eastman Kodak Company. The Hardenbrook et al. patent describes a process where a web (i.e., a sheet) of plastic material, impregnated with an inert gas, is quenched using a complex die arrangement to form a saturated web of unfoamed material. Next, the surface gas is diffused out of the web in a controlled manner to promote an integral skin. The saturated web is then re-heated at a station external to the extruder to induce foaming. During the foaming step, the temperature and duration of the foaming process are controlled to produce the desired cell morphology. The process is designed to produce a foamed plastic web with an integral unmodified skin.

The significant limitation of this process is that only thin profiles (on the order of 0.020 inches in thickness) can be processed due to the limits of thermal cycling in producing thick walled microcellular webs. Yet another complication with this process is the use of potentially invasive lubricants and coolants in the die system which can degrade the sheet properties and surface finish. In addition, the die configuration used in the Kodak process is quite complicated and expansive. In contrast, the process developed in this work uses a relatively simple die arrangement having considerably lower capital costs. Moreover, the process developed here decouples cell nucleation, cell growth, and sheet shaping. A final difference between the process of this work and the Kodak process is that a staged pressure cycle is used to control microcellular processing in this work while the Kodak process uses a thermal cycle. In general, pressure cycles are far easier to control then thermal cycles.

Recently, Park and Suh (1992a, 1993) and Park et al. (1993) discuss the polymer/gas solution formation and nucleation aspects of an extrusion process for microcellular and supermicrocellular polymer mono-filaments. In order to make use of microcellular polymer technology in a continuous manner, Park and Suh (1992a, 1993) discuss two major process steps: (1) continuous formation of a polymer/gas solution and (2) microvoid nucleation by thermodynamic instability in the polymer/gas solution. The main strategy for this process was to integrate these two steps in the extrusion process in such a way that the overall process was de-coupled. The basic process is shown in Figure 2.4 and proceeds as follows.

Polymer/gas solutions are produced continuously in the extruder barrel by injecting a metered amount of gas such as carbon dioxide or nitrogen into a stream of molten polymer. The gas flow is metered by varying the injection pressure of the gas as it passes through a porous material which restricts the flow rate. The metered gas is then delivered to an extrusion barrel where it is mixed with the molten polymer to form a two-phase mixture.

The gas then diffuses into the polymer melt in a convective diffusion device (see section 3.2) which intensely mixes the materials, resulting in the formation of a single-phase solution. Once the single-phase solution is formed, the pressure is rapidly lowered to induce a thermodynamic instability thus promoting a high rate of bubble nucleation. The pressure drop is accomplished using a filament die or nozzle. Typical pressure-drop rates used in this process are above 0.9 GPa/s. The nucleated filament emerges from the die and expands nearly instantaneously. No external cell growth control is needed since the microcellular filament quenches rapidly at ambient temperatures due to its small diameter.

2.2.3 Forming Processes and Operations

Three forming and/or molding processes have been discussed in literature for producing three-dimensional microcellular parts. Kumar and Suh (1990) and Kumar (1988) were the first to develop a forming process for creating three-dimensional microcellular parts. The basic idea of their modified thermoforming process is to pre-saturate a polymer sheet with gas. The sheet is then subjected to a thermocycle where it is first heated to a forming temperature (above the glass transition temperature). At that point cell nucleation occurs, and the part is vacuum/pressure formed into a mold. Next, the formed part is heated to a foaming temperature (above the forming temperature) where cell growth occurs. Finally, the microcellular foamed part is cooled and removed from the mold. In general, this process is limited to those polymer/gas systems having relatively slow cell growth rates (i.e., styrenic resins processed with nitrogen) such that cell nucleation and part forming can be accomplished prior to cell growth. If cell growth occurs at nearly the same temperature required for forming then highly elongated cell structures result in the formed part.

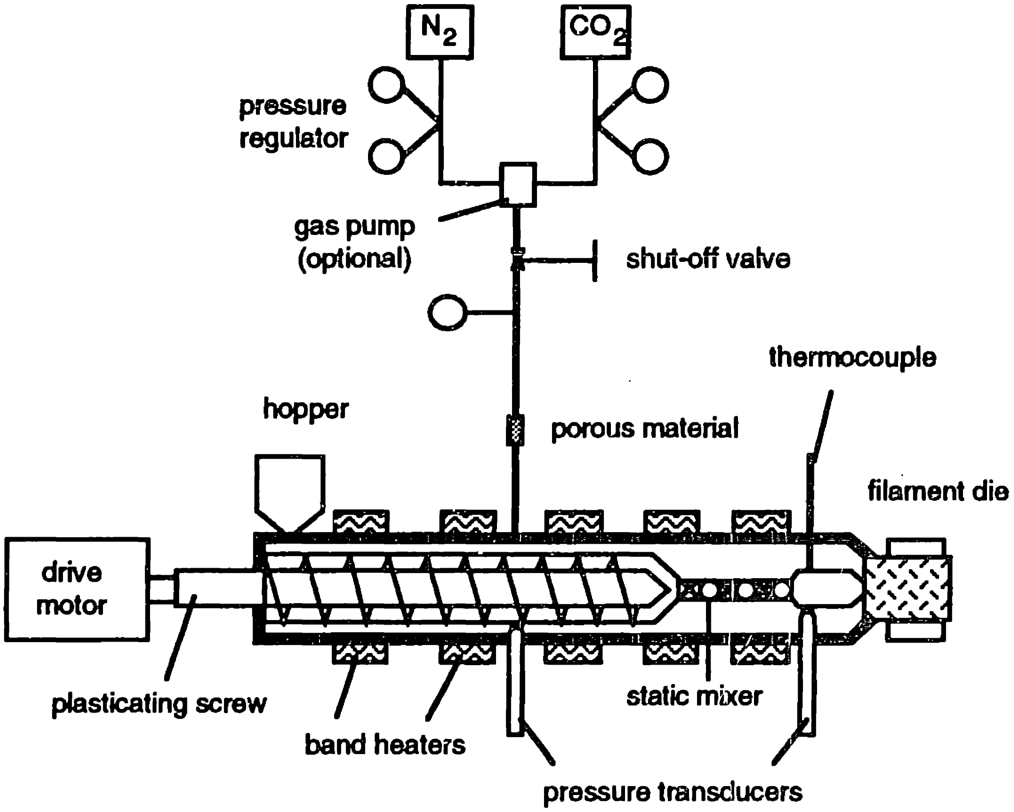

Figure 2.4: Schematic of the mono-filament extrusion process. (Park, 1993)

A room-temperature or semi-solid-state forming and foaming process is disclosed by Cha et al. (1992) for creating three-dimensional plastic parts. The basic idea is to take advantage of the plasticizing effect of the gas to form and foam polymers at low or room-temperature (see section 2.1.1). The process consists of saturating a polymer sheet with a gas while fixtured over a mold. Once the sheet is saturated, resulting in significant plasticization of the polymer matrix, the gas pressure on both sides of the sheet is lowered to allow cell nucleation to occur under pressure. Next, the gas pressure on the female mold side is removed and/or a matching mold plug is depressed, causing the sheet to form to the mold surface. Slowly, the remaining gas pressure is removed allowing cell growth to occur, resulting in a three-dimensional microcellular plastic part having uniform cell structures. This process is limited to polymers which foam at low or room-temperatures and experience significant plasticization during gas saturation.

A third molding process proposed by Clark and Seeler (1991) encompassed sintering microcellular foam parts as an alternative to injection molding. The potential advantages of sintering and foaming loose-packed granular polystyrene, compared with injection molding, are independent control of mold filling and foaming along with shorter saturation times. Unfortunately, gas desorption occurs rapidly with the small granular polymers leading to low density reductions. In addition, such sintered microcellular parts have low densities at the surface, as opposed to high density integral skins typical of microcellular foams, resulting in poor mechanical performance since bending stresses are greatest at the surface (Clark and Seeler, 1991).

While the process technologies for microcellular plastics have progressed rapidly over the past decade with the advent of forming processes, extrusion processes, and continuous solution formation systems, there are a number of significant processing issues which need to be addressed. These include, molding and injection molding technology, scaling of the existing processes to industrial processes, stability and robustness of existing processes, and identification of markets supporting the high value added processes. Next, lets look at the unique mechanical properties exhibited by microcellular plastics.

2.3 Material Property Characterization

Early studies by Martini (1981) showed that while microcellular polystyrene has strengths below the neat polymer, its specific strength was considerably higher. Later, Waldman (1982) characterized microcellular foamed impact grade polystyrene in an effort to predict the conditions which produce microcellular structures and to understand the relationship between structure and mechanical properties. Results indicated higher specific strengths compared to the neat polymer. In addition, the specific strength was found to reached a maximum at a 30% void fraction with an average cell size of 8 μm. Fracture toughness measurements showed a four-fold increase over the neat polymer. Moreover, notched Charpy impact tests and Gardner drop tests were performed to determine the contributions of craze initiation and crack blunting in fracture mechanisms. The notched Charpy impact tests showed a 200% improvement in crack propagation resistance believed to be the result of crack tip blunting at the microcells; the falling weight tests had a wide variation in values attributed to surface defects and non-uniform skin thickness.

Since these early studies, a number of investigations have been performed to ascertain the material properties of microcellular plastics. These studies include investigations of the flexural properties, the tensile modulus, the toughness, the fatigue life, and the viscoelastic behavior.

2.3.1 Flexural Properties of Microcellular Composites

A preliminary flexural property study of microcellular polyester composites was performed by Youn and Suh (1985) with further details presented by Youn (1984). This study compared the flexural properties of a sheet molding compound (SMC) and a microcellular composite having a 42% lower density. The flexural strength of the microcellular composite was shown to be nearly equal to the SMC. The specific strength was nearly 78% larger for the microcellular composite, and the flexural toughness of the microcellular composite was three times that of the SMC.

2.3.2 Tensile Modulus and Theoretical Developments

In 1991, Kumar and Vander Wel proposed a model for predicting the tensile modulus of microcellular foam based on the Gibson and Ashby (1982, 1988) model for closed-cell foam materials. From Gibson and Ashby (1982), the ratio of the foam tensile modulus to that of the polymer matrix is given by

$$\frac{E_f}{E_m} \approx \Phi^2 \left(\frac{\rho_f}{\rho}\right)^2 + (1 - \Phi)\left(\frac{\rho_f}{\rho}\right) \tag{2-2}$$

where E_f is the tensile modulus of the foam, E_m is the tensile modulus of the polymer, ρ_f is the foam density, ρ is the polymer density, and Φ is the ratio of the volume of material in the cell walls to that in the cell struts. Equation (2-2) accounts for the bending of the cell struts and stretching of the cell walls and neglects contributions from the compressibility or incompressibility of the fluid within the cells. Because the distribution of material in the cell walls decreases as the relative density decreases, Kumar and Vander Wel proposed that Φ is proportional to the relative density of the foam, i.e.,

$$\Phi \propto \frac{\rho_f}{\rho} \ . \tag{2-3}$$

With this assumption the relationship between foam modulus and relative density is given by:

$$\frac{E_f}{E_m} \approx \left(\frac{\rho_f}{\rho}\right)^4 - \left(\frac{\rho_f}{\rho}\right)^2 + \left(\frac{\rho_f}{\rho}\right) \ . \tag{2-4}$$

This equation was found to be in good agreement with experimental data for microcellular polycarbonate processed with carbon dioxide (Kumar and Vander Wel, 1991). In accordance with equation (2-4), the tensile modulus of the microcellular polycarbonate decreased with relative density to a greater extent then predicted by the rule of mixtures. Kumar and Vander Wel also showed that the microcellular polycarbonate has relative moduli comparable to structural foams.

In 1992, Weller and Kumar presented two micro-mechanical models for predicting the effective tensile modulus of microcellular polymers. The first was a dilute model based on Eshelby's equivalent inclusion method and Eshelby's solution for an ellipsoidal inhomogeneity in an infinite matrix. This model assumes that the concentration of voids is dilute enough that interactions among the voids may be neglected. A second model combines Eshelby's equivalent inclusion method and Mori-Tanaka's mean field theory as derived by Taya and Chou (Weller and Kumar, 1992) to predict the effective stiffness of an elastic body containing ellipsoidal inhomogeneities. Using available experimental data, the authors show that the dilute model over predicts the experimental data while the Mori-Tanaka's model agrees well between relative densities of 0.50 and 0.90 where the spherical void assumption holds.

2.3.3 Effects of Microcellular Processing on Toughness

In 1992, Collias and Baird studied the tensile properties of microcellular PS, SAN, and PC processed with nitrogen, in an attempt to determine the effect of various microcellular processing steps on the fracture toughness. Tests were performed on samples with three processing histories: (1) supersaturated with nitrogen, (2) heated in an oil bath at temperatures comparable to microcellular processing, and (3) microcellular processed. For PS, the results show a slight increase in ultimate strength and a substantial increase in the elongations at yield and break for the supersaturated polystyrene compared to the neat PS and compared to saturated polystyrene allowed to desorb nitrogen for three days. An increase in toughness over the neat polymer was also found for PS samples allowed to desorb gas for three days. The toughness for the thermally processed PS samples was equal to the neat polymer. Microcellular PS was found to have lower ultimate strength and elastic modulus, but higher elongations at yield and break compared to the neat polymer. The same series of experiments was carried out with samples of SAN. The supersaturated material experienced an increase in toughness which was not present after five days of desorption. Microcellular SAN showed no improvement in tensile properties compared to the neat polymer. In addition, neither the supersaturated nor the microcellular polycarbonate showed any increase in tensile properties compared to the neat polymer.

2.3.4 Fatigue Properties

Seeler and Kumar (1992, 1993) have investigated the fatigue of microcellular polycarbonate. In general, they found that the fatigue life increased with increasing relative density. Microcellular polycarbonate was also found to be less notch sensitive than solid polycarbonate at low stress amplitudes, but the notch sensitivity exceeded that of the solid material at high stress amplitudes. In this study, the fatigue life of microcellular polycarbonate was compared to the as-received sheet, samples thermally processed similar to microcellular processing, and samples which were saturated with gas and desorbed. The authors report that saturation of solid polycarbonate with carbon dioxide decreases tensile strength by 20 percent and increases fatigue life up to 10 times (similar to annealing metal which also decreases tensile strength and increases fatigue life). Below the maximum tensile stresses of 40 MPa, the fatigue life of microcellular polycarbonate having a relative density of 0.897 was approximately equal to that of unprocessed polycarbonate. Above this relative density, fatigue life increased up to 17 times that of the as-received material (Seeler and Kumar, 1993, 1992).

2.3.5 Viscoelastic Behavior

Shimbo et al. (1992, 1993ab) investigated the viscoelastic behavior and mechanical properties of microcellular poly(ethylene terephthalate) (PET) and a polyolefin nucleated PET (CPET). Using dynamic mechanical analysis, the authors found that the storage moduli of the microcellular PET and CPET relieve at a slower rate at temperatures near T_g compared to the neat polymer. Moreover for CPET, this effect was enhanced by increasing cell size. The microcellular CPET having varying cell size was also reported to follow the time-temperature correspondence principle at low strain amplitudes (i.e., approximately .0015 m/m presumably in the linear range). The authors surmise that microcellular CPET samples having varying cell sizes and constant cell densities, may be used to estimate the viscoelastic behavior microcellular CPET having the same cell density but arbitrary cell sizes. Shimbo et al. (1993a) also report semi-crystalline microcellular CPET having tensile strengths equal to the neat CPET and a 16% lower density. In addition, they found that the specific strength of the microcellular CPET exceeded the neat polymer and increased with increasing cell size.

Kumar et at. (1993) have studied the linear and nonlinear viscoelastic behavior of microcellular polycarbonate processed with carbon dioxide. This research also focused on predicting the creep in neat polycarbonate based on Schapery's single integral theory of nonlinear viscoelastic behavior. The eventual hope of the authors is to combine Schapery's theory with a micro-mechanical model (section 2.3.2) to predict non-linear viscoelastic behavior in microcellular polycarbonate. The authors report that microcellular polycarbonate samples with relative densities of 0.97 and 0.83 exhibited nonlinear viscoelastic/viscoplastic behavior over the strains studied based on creep and recovery experiments. Compared to neat polycarbonate, creep in microcellular polycarbonate initiated at lower stresses, and creep strains exhibited greater viscoplastic response. In addition, it was possible to subject microcellular polycarbonate to creep strains exceeding the tensile strain at creep rupture for neat polycarbonate. This implies that the microcellular polycarbonate shows a higher strain to failure then is possible in the neat polycarbonate (Kumar et al., 1993).

Finally, it is worth noting that some morphology characterization techniques for microcellular polymers are emerging. Aubert (1988) has proposed a method of objective characterization of open cell microcellular foams. Although the characterization is for open cell materials, it seems to have applicability to the characteristic closed cell microcellular foams discussed in this chapter. Ramesh et al. (1992) briefly discuss a digital image analysis technique for analyzing SEM micrographs of microcellular polymers. Moreover, Garbini (1992) discuss a proposed sensor and error analysis of an impedance based sensor for non-destructive characterization of core void fraction and skin thickness in microcellular foams.

2.4 Summary

The innovative new class of polymeric materials called microcellular plastics seem to possess the potential to substantially impact the use and manufacture of polymer products and polymer foams. These materials posses superior thermal, mechanical, and electrical properties which can expand the application of foamed polymers into new areas. In current structural foam applications, microcellular materials can reduce material consumption and costs without substantial performance loss. Additionally, microcellular plastics processing technology has advantages over conventional foam processes because it uses environmentally safe gases as blowing agents, rather than hydrocarbons, CFCs, HCFCs, or toxic chemical blowing agents.

With many unique properties, microcellular plastics have a large number of potential applications in high value-added products. These include aerospace and automotive parts which could benefit from microcellular plastics' high specific strength and acoustic dampening properties, sporting equipment where weight reduction and energy absorption are critical, cold-weather clothing made from microcellular fabrics, molecular grade filters for separation processes, and surface modifiers for low friction applications.

Since its initial development, microcellular plastics technology has been applied to new polymer/gas systems including amorphous thermoplastics, semi-crystalline thermoplastics, liquid crystal polymers, elastomers, and thermosets. Moreover, microcellular plastics technology has been advanced into new generations of materials and processes including supermicrocellular plastics, low-temperature microcellular processing, mono-filament extrusion, and with this research a new microcellular sheet extrusion process.

As with many new technologies, the advanced development of microcellular plastics will lead to new scientific discoveries. For example, the formation of solutions where gas is the solvent and the polymer the solute creates many interesting questions about intermolecular forces, thermodynamics of solutions, kinetics of dissolution, and permeation of gases through polymeric solids. It also raises many technological issues such as non-conventional processing techniques, mixing of gases and polymers, etc.

In the next chapter, the fundamentals of microcellular processing are presented. This chapter includes a discussion of the basic theory underling polymer/gas solution formation, microcellular processing, and cell growth.

CHAPTER 3

FUNDAMENTALS OF MICROCELLULAR POLYMER PROCESSING

3.0 Introduction

Now that a brief introduction to microcellular plastics has been given along with recent material advances and potential applications, it is useful to explore further the critical processing steps common to all microcellular processing and develop the theoretical fundamentals of each processing step. First the formation of gas/polymer solutions will be discussed, followed by microcellular nucleation (a form of phase separation) and cell growth. The theoretical treatment of this chapter will be used throughout the remainder of the thesis.

3.1 Formation of Gas/Polymer Solutions

Mixing plays a dominant role in the formation of a gas and polymer solution for microcellular polymer processing, and can take two forms. The first is spontaneous simple mixing where under proper conditions gas molecules diffuse into the polymer matrix creating what appears to be a molecular level dispersion. Such a dispersion is considered to be a single phase solution. The second is a dispersive mixing where gas is injected into a molten polymer and mixed by breaking down large gas bubbles into smaller bubbles and shearing these bubbles to promote diffusional mixing. In both cases, the formation of solutions and mixing can be understood from a macroscopic point of view in terms of thermodynamics. The following thermodynamic discussion is treated in detail by Flory (1953), Gutowski and Suh (1982), and Young and Lovell (1991).

3.1.1 Basic Thermodynamics of Mixing

At a given thermodynamic state, the system consisting of a polymer and a gas will try to minimize its free energy until equilibrium is reached. If the formation of a solution by mixing of the constituents lowers the system free energy, a solution will form spontaneously. Otherwise, the constituents will remain in separate phases and no spontaneous mixing will occur. By definition, the Gibbs free energy is given by:

$$G \equiv H - TS \tag{3.1-1}$$

When two constituents are mixed, the Gibbs free energy of mixing, ΔG_m, is given by the difference of the free energy of the mixture and the total free energy of the individual constituents and is described by equation (3.1-2). Under the conditions of constant temperature T and pressure p, the Gibbs free energy of mixing is given by equation (3.1-3) where ΔH_m and ΔS_m are the enthalpy and entropy of mixing, respectively.

$$\Delta G_m = G_{12}(T,p,n_1,n_2) - G_1^0(T,p,n_1) - G_2^0(T,p,n_2) \tag{3.1-2}$$

$$\Delta G_m = \Delta H_m - T\Delta S_m \tag{3.1-3}$$

Mixing and solution formation occurs only if the free energy of the system decreases, that is $\Delta G_m < 0$. Therefore, spontaneous mixing will occur provided that the enthalpy of mixing is negative and/or the entropy of mixing is positive and sufficiently large. In many cases, the Flory-Huggins theory can be used to approximate the Gibbs free energy of mixing for polymer and solvent solutions (Flory, 1953; Gutowski and Suh, 1980; Young and Lovell, 1991) although this detailed discussion is not given here.

A large enthalpy of mixing is characteristic of systems in which the constituents chemically react and/or bond at the molecular level. Enthalpy contributions also occur due to general intermolecular interactions. If $\Delta H_m > 0$, then mixing is endothermic; if $\Delta H_m < 0$, then mixing is exothermic; and if $\Delta H_m = 0$, then mixing is athermic. Flory-Huggins theory accounts for the enthalpy of mixing by approximating the Gibbs free energy of contact interactions between molecules. However, for dilute polymer solutions, the enthalpy of mixing can be estimated using the solubility parameter approach as given by equation (3.1-4) where V_m is the molar volume of the mixture, ϕ is the volume fraction of the polymer or solvent, and δ is the solubility parameter of a constituent and equal to the square root of the cohesive energy density (i.e., a parameter that characterizes the strength of attraction between molecules). The solubility parameter approximation holds at ambient temperature for systems of non-polar molecules, negligible hydrogen bonding, and negligible charge transfer interactions. The solubility parameter approach is typically used as a guide to miscibility, and within its limiting assumptions, can be used to estimate the enthalpy of mixing (i.e., predicting values greater than or equal to zero only).

$$\Delta H_m = V_m\phi_1\phi_2(\delta_1 - \delta_2)^2 \qquad (3.1\text{-}4)$$

The extent to which the enthalpy of mixing contributes to microcellular processing is not known at this time. In general, the enthalpy of mixing comprises contributions from secondary bonding between gas and polymer molecules such as hydrogen bonding and from chemical reactions between gas and polymer molecules. Researchers are currently studying the issue of secondary bonding during microcellular processing.

Spontaneous mixing will occur during athermic mixing, such as for ideal solutions, provided that $T\Delta S_m \geq 0$ also called entropic mixing. Historically, the entropy of mixing has been viewed as having two contributions: (1) a combinatorial component due to geometric rearrangement of molecules and (2) a non-combinatorial component due to the entropy of specific molecules in a given environment. † The entropy of mixing can then be written as

$$\Delta S_m = \Delta S_{comb} + \Delta S_{nc} \qquad (3.1\text{-}5)$$

where ΔS_{comb} is given by Boltzmann's equation such that $\Delta S_{comb} = k \text{ in } (\Omega)$ and Ω is the probability that a given state will exist. Substituting in equation (3.1-5), equation (3.1-3) can be rewritten as:

$$\Delta G_m = \Delta H_m - T(\Delta S_{comb} + \Delta S_{nc}) \qquad (3.1\text{-}6)$$

At low temperatures, the enthalpy term dominates the mixing process and can be estimated for some systems using equation (3.1-4). At moderate temperatures, the entropy term dominates mixing through the combinatorial component. As the system progresses to a randomly distributed configuration, the combinatorial entropy increases such that $\Delta S_{comb} > 0$. However, as the temperature is increased further, the non-combinatorial entropy component can dominate due to entropy contributions from intermolecular contacts and volume changes upon mixing. Both of these situations can reduce the available vibration states of the molecules thereby reducing the non-combinatorial entropy such that $\Delta S_{nc} < 0$. Thus at sufficiently high temperatures, mixing will worsen do to ΔS_{nc} contributions and two phase mixtures will prevail. Based on equation (3.1-6), it appears that the mixing of a gas and polymer to form a single phase solution is best performed at moderate temperatures such that the mixing process is driven by combinatorial entropy effects.

---

† In some ways, the term non-combinatorial entropy is a misnomer since all entropy contributions are ultimately related to geometric distributions and thus are combinatorial.

In some microcellular processing systems particularly melt processing, solution formation is accomplished by dispersive mixing accompanied by diffusion of gas into the polymer matrix. Both dispersive mixing and gas diffusion increase ΔS_{comb}. The most notable example of such a system is the continuous polymer/gas solution formation system developed by Park and Suh (1992a) which is discussed in section 2.5. In this case, the constituents have finite surface energy, γ, over a surface area, A, resulting from the injected gas bubbles in the polymer melt. Another common element in dispersive mixing systems is shaft work, W_s, which is done on the system. In the extrusion process, the shaft work is input through the screw rotation. Under constant temperature and pressure conditions, mixing will occur provided that the Gibbs free energy of mixing is less than or equal to interfacial energy and shaft work contributions and takes the form of equation (3.1-7) (Suh, 1986). From equation (3.1-7), it is clear that mixing can be enhanced by mechanical shaft work to overcome the interfacial energy barrier which suppresses spontaneous mixing. It is also important to note that mechanical mixing will tend to disperse the constituents into smaller domains thus increasing the overall interfacial energy of the system. From equation (3.1-7), one can see that mixing will occur if the Gibbs free energy is less than the interfacial energy increase resulting from extensive mixing associated with the mechanical shaft work. [§]

$$dG_m \leq d(\gamma_{bp} A) - \delta W_s \qquad (3.1\text{-}7)$$

3.1.2 Solution Formation in Microcellular Polymer Processing

Batch Processing

During batch processing, polymer/gas solution formation is accomplished by saturating a polymer under a high pressure gas. In this case, the solution formation is governed solely by gas diffusion into the polymer matrix (i.e., simple mixing). As the gas molecules diffuse into the solid polymer matrix, the polymer/gas system proceeds from a highly ordered state composed of two discrete phases (the gas phase and the polymer matrix phase) to a state of greater disorder where the two constituents are co-mingling at the molecular scale. Therefore, the diffusion process increases the entropy of the system and lowers the overall free energy of the system. Since the diffusion process is critical to understanding polymer/gas solution formation in microcellular batch and continuous

---

[§] Extensive mixing involves the shearing of the constituents which tends to increase the interfacial surface area-to-volume ratio of the mixture.

processing, it is worthy of some additional discussion. The following discussion is adapted from the extensive mathematical treatment of diffusion by Crank (1975).

In mid 1800's, Fick recognized that, like conduction heat transfer, diffusion is due to the random motions of molecules. Fick's first law states that the rate of diffusion (i.e., the transfer of gas through a unit area of a section) is proportional to the concentration gradient normal to the section (equation 3.1-8). Fick's second law gives the rate of change of concentration with respect to time (equation 3.1-9).

$$F = -D\,\nabla c \qquad (3.1\text{-}8)$$

$$\frac{\partial c}{\partial t} = \nabla \bullet (D\,\nabla c) \qquad (3.1\text{-}9)$$

In equations (3.1-8) and (3.1-9), c is the gas concentration, D is the diffusivity, and F is the gas flux. For some isothermal systems, the diffusivity can be assumed constant; however, in many polymer/gas systems, D depends strongly on concentration. Various solutions to equation (3.1-9) and methods of determining the diffusion coefficient from experimental data are found in Crank (1975). For the sorption of gas by an infinite plane sheet of thickness $2l$, with constant diffusivity, the solution to equation (3.1-9) is given by

$$\frac{c - c_0}{c_1 - c_0} = 1 - \frac{4}{\pi}\sum_{n=0}^{\infty}\frac{(-1)^n}{2n+1}\exp\left(\frac{-D(2n+1)^2\pi^2}{4l^2}t\right)\cos\frac{(2n+1)\pi x}{2l} \qquad (3.1\text{-}10)$$

where the sheet is initially at uniform concentration c_0, and the surfaces $x = \pm l$ are held at c_1 for time $t > 0$. If Henry's law is assumed to hold true for the polymer/gas system then the surface concentration is given by, $c_1 = K_s\,p_{sat}$ where p_{sat} is the saturation gas pressure (see equation 3.1-14). The ratio of the total amount of diffusing gas dissolved in the sheet after time t (M_t) to the equilibrium value (M_∞) is determined by integrating equation (3.1-10) over the sheet thickness, and is given by

$$\frac{M_t}{M_\infty} = 1 - \sum_{n=0}^{\infty}\frac{8}{(2n+1)^2\pi^2}\exp\left(\frac{-D(2n+1)^2\pi^2}{4l^2}t\right). \qquad (3.1\text{-}11)$$

Equations (3.1-10) and (3.1-11) serve as useful approximations for many systems encountered in microcellular processing. Extensions of the above solutions to more complicated cases, which are also encountered in microcellular processing, such as sorption causing the sheet to swell or concentration dependent diffusivities, are discussed in Crank (1975).

Continuous Processing

Diffusion processes encountered in batch microcellular processing are typically slow, resulting in long cycle times. Thus a critical step in continuous microcellular plastics processing is the creation of polymer/gas solutions at industrial rates. Solution formation in continuous processing can be accomplished in one of the following ways: (1) saturating pellets and extruding at high processing rates, (2) injecting gas into the polymer melt and promoting mixing to form a single phase solution, or (3) extruding a precursor such as a filament or sheet which is then saturated with gas before post-processing into the net shape. Recently, a continuous solution formation process implementing gas injection was developed by Park and Suh (1992a) with additional refinements presented by Park (1993). In this case, solution formation is achieved through two processes: (a) dispersive mixing of a supercritical fluid/gas and molten polymer and (b) diffusion of the supercritical fluid/gas into the polymer. In Park and Suh's system, real time solution formation is achieved by intense mixing of the polymer/gas system, decreasing the mean gas diffusion distance. The result is an increase in the solution formation rate and processing rate. At this point, it is worth exploring the embodiments of the continuous solution formation system presented by Park and Suh (1992a) since this technology is utilized in the microcellular sheet processing system developed in this work.

In general, continuous processing of microcellular plastics involves two solution formation steps: creation of the two-phase mixture in a polymer melt, and completion of the dissolution process using various mixing techniques to form a high-gas-concentration single phase polymer/gas solution. Figure 3.1 shows the morphology change of the polymer and gas phases during the process. Initially, a soluble amount of gas is injected into a polymer melt forming a two-phase polymer/gas mixture. The injected gas bubbles are then broken into small bubbles creating a fine bubble dispersion, followed by stretching via shear mixing to form high-aspect-ratio stretched bubble structures. Since the mean diffusion distance over which the gas must diffuse is decreased substantially, the gas diffuses into the polymer matrix forming a single-phase solution in real time.

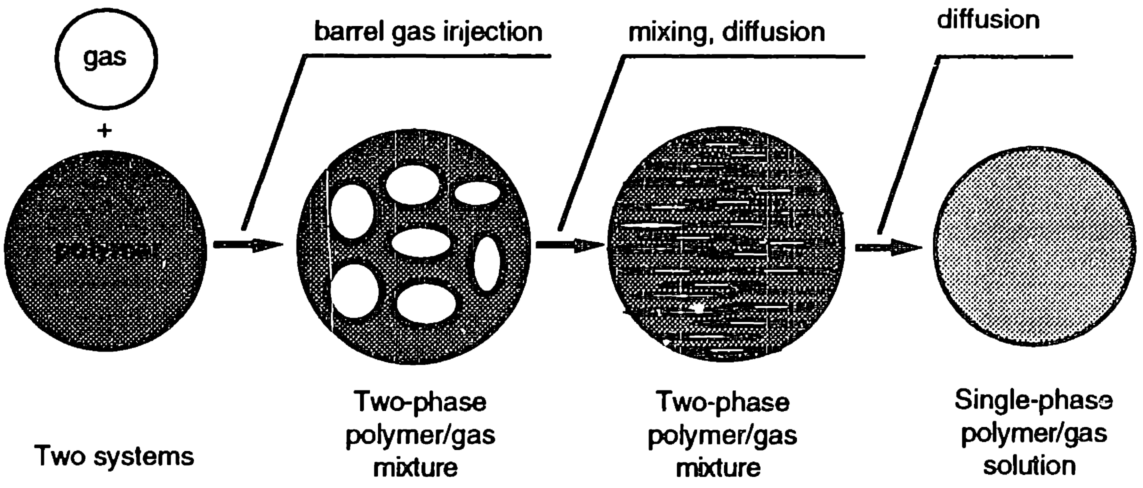

Figure 3.1: Morphology change of a polymer melt and gas system during a continuous solution formation process.

The basic strategies for rapid solution formation are increasing the diffusion coefficient and inducing convective diffusion (a form of laminar mixing). Since the diffusion coefficient increases as the temperature increases, the rate of gas diffusion is enhanced by processing the mixture at elevated temperatures. Convective diffusion results in an increase in the interfacial area per unit volume, a reduction of the diffusion distance, and a redistribution of the local gas concentration profile in polymer matrix.

Convective diffusion enhances the diffusion rate by bringing polymer melt with a low gas concentration into contact with a source of high gas concentration (i.e., the injected gas bubbles). Two convective-diffusion techniques are used by Park (1993) in the continuous process. One technique employs the shearing action of the extrusion screw to draw small bubbles of gas into the molten polymer shear field. The mixing action of the shear field continuously disperses the gas bubbles uniformly throughout the polymer matrix. A second convective diffusion technique was to enhance mixing effectiveness through laminar reorientation of the mixture by introducing various mixing sections in the extrusion process. Park and Suh (1992a) and Park (1993) present an approximate model for determining the time necessary for polymer/gas solution formation in continuous melt processing which is summarized in the following.

The theory of mixing for highly viscous fluids describes the growth of interfacial areas in different types of shear flows. The interfacial area per unit volume, A/V, a key parameter in quantifying mixing, is related to the striation thickness, s, by equation

(3.1-12) where the striation thickness is defined by the average distance between interfaces of the same component in the mixture.

$$s \equiv \frac{2}{A/V} \qquad (3.1\text{-}12)$$

Based on equation (3.1-12), the theory of laminar mixing can be used to derive the striation thickness in shear flow. Using developments of Mohr et al. (1957) and Kim et. al. (1972), the striation thickness in shear flow is given by

$$s \approx \frac{d_b}{\Phi_v \gamma} \qquad (3.1\text{-}13)$$

where d_b is the average diameter of the dispersed bubbles, Φ_v is the volume fraction of the gas, and γ is the mean stretching ratio of the gas component. Since the striation thickness is the average distance between gas and polymer interfaces, it follows that the average time necessary for the gas in the bubbles to diffuse into the polymer melt, during convective diffusion can be estimated from equation (3.1-14).

$$\tau \approx \frac{s^2}{D} \qquad (3.1\text{-}14)$$

In general, the diffusivity D is temperature, pressure, and gas concentration dependent (Durril and Griskey, 1966 and 1969; Koros and Paul, 1980; Newitt and Weale, 1948, Van Krevelen, 1976); however, it can be approximated as:

$$D = D_o \exp\left(-\frac{\Delta E_D}{RT}\right) \qquad (3.1\text{-}15)$$

where D_o is a reference diffusivity and ΔE_D is the activation energy for diffusion.

In order to estimate the striation thickness, the bubble stretching ratio, defined by equation (3.1-16), is taken to be the mean stretching ratio of the gas component, γ, which holds provided the stretching ratio is not to large (i.e., where molecular relaxation and surface tension instabilities can dominate).

$$\gamma = \frac{d_{max}}{d_b} \qquad (3.1\text{-}16)$$

In equation (3.1-16), d_{max} is the maximum diameter of elongated bubbles in the shear field which was experimentally estimated by Park and Suh (1992a).

According to Park and Suh (1992a), the dispersed bubble size can be estimated by assuming the mixing behavior of a gas in a polymer melt follows dispersive mixing theory for shear flow. When the shear stretching exceeds the critical value of the Weber number, We (i.e., given by equation 3.1-17) disintegration of the bubbles takes place due to surface tension effects forming a finer dispersion of bubbles.

$$We = \frac{\dot{\gamma} d_b \eta_p f(q)}{2 \gamma_{bp}} = \frac{\text{shear forces}}{\text{surface forces}} \qquad (3.1\text{-}17)$$

where

$$f(q) = \frac{19\,q + 16}{16\,q + 16} \quad \text{and} \quad q = \frac{\eta_g}{\eta_p} \qquad (3.1\text{-}18)$$

In equations (3.1-17) and (3.1-18), $\dot{\gamma}$ is the shear rate in the mixture, η_p is the dynamic viscosity of polymer matrix, η_g is the dynamic viscosity of gas, and γ_{bp} is the surface tension of the polymer/gas interface.

Using available literature data for the critical Weber number, equations (3.1-17) and (3.1-18) can be used to estimate the average bubble diameter, d_b. The stretching ratio of the gas bubble and the striation thickness can then be estimated using equations (3.1-16) and (3.1-13), respectfully. Finally, using available data for the diffusivity via equation (3.1-15), the time required for solution formation can be estimated from equation (3.1-14). Based on an order-of-magnitude analysis, Park (1993) estimates that the formation of a polystyrene solution containing 10 % carbon dioxide can be completed in one minute at a melt temperature of 200 °C.

Furthermore, Park and Suh (1992a) demonstrated that continuous solution formation can be achieved in an extrusion system without substantially degrading the processing rates of the extruder. They emphasize that only a soluble amount of gas should be injected into the polymer melt because excessive gas would result in the formation of undesirable voids and non-uniform cell structures. Park (1993) estimates the soluble amounts of CO_2 and N_2 in many thermoplastic melts (i.e., at 200 °C and 4000 psi) to be on the order of 10% and 2% by weight, respectively.

The equilibrium concentration of gas in a polymer is an important consideration in microcellular processing. Generally, the equilibrium concentration is expressed as a function of temperature and pressure (Durril and Griskey, 1966 and 1969; Koros and Paul, 1980; Lundberg et al., 1966; Newitt and Weale, 1948; Van Krevelen, 1976; Veith et al., 1966; Weinkauf and Paul, 1990) as indicated in equation (2-1). Henry's law, equation (3.1-19) valid for dilute solutions, can be used to estimate the equilibrium concentration of gas in a polymer as a function of pressure. In general, Henry's law predicts that the partial pressure of an ideal solute is proportional to the mole fraction in the solution. Henry's law constant is temperature dependent and is typically given by an Arrhenius relation, equation (3.1-20). Combining equations (3.1-19) and (3.1-20), an approximate relation for the equilibrium solubility of gas in a polymer is given by equation (3.1-21). Note that equation (3.1-21) predicts the general shape of the equilibrium concentration surface in Figure 2.2.

$$c_{eq} \approx K_s \, p_{sat} \tag{3.1-19}$$

$$K_s \approx K_{so} \exp\left(-\frac{\Delta E_s}{R\,T}\right) \tag{3.1-20}$$

$$c_{eq} \approx K_{so} \, p_{sat} \exp\left(-\frac{\Delta E_s}{R\,T}\right) \tag{3.1-21}$$

It should be noted that Henry's law is only an approximate relation which holds for some polymer/gas systems over a limited temperature and pressure range. Numerous other relations exist describing the partial pressure of a solute and the concentration in solution such as the Langmuir equation and elements of the Flory-Huggins theory (Comyn, 1985; Koros and Paul, 1980). Nevertheless, Henry's law is a convenient relation for estimating the equilibrium concentration of gases in polymers over the temperature and pressure ranges typically used in microcellular processing.

Another significant consideration of high gas concentration solutions found in microcellular processing is the effect of dissolved gases on the viscoelastic behavior of polymers. For many polymer/gas systems, the glass transition temperature has been shown to be a strong function of the gas concentration (Baldwin, et al. 1993 and 1992; Chiou et al., 1985; Condo et al., 1992; Koros and Paul, 1980; Wang et al., 1982). In general, an increase in dissolved gas concentration decreases the glass transition temperature. Baldwin et al. (1993) indicate that T_g depressions as high as 75 °C can occur during the microcellular processing of poly(ethylene terephthalate) using carbon dioxide.

3.2 Phase Separation and Nucleation of Microvoids

Once a single phase polymer/gas solution is formed during microcellular processing, the gas is then separated into a second phase in a controlled manner by subjecting the solution to a rapid thermodynamic instability. The phase separation is accomplished with what appears to be nucleation and growth phenomena. Nucleation is achieved by quickly lowering the soluble gas concentration through temperature and/or pressure changes. The system now seeks a state of lower free energy which results in the clustering of gas molecules in the form of cell nuclei. The formation of stable nuclei provides a relatively small mean free distance for the gas molecules in solution to diffuse through before reaching a cell nucleus (i.e., the gas phase). As the gas diffuses into and expands the cells, the free energy of the system is lowered. The cell nucleation process is very important in microcellular processing in that it governs the cell density, dominates the overall foam morphology, and determines the properties of the material.

3.2.1 Phase Separation Processes

However, phase separation in polymer solutions is a general phenomenon which encompasses nucleation and, in partially miscible solutions, spinodal decomposition (see Gutowski and Suh, 1982; Young and Lovell, 1991; and Zettlemoyer, 1969 for detailed reviews). In general, phase separation at high temperatures is a rare phenomenon for mixtures of similar size molecules. However, the unique structure of polymer/solvent and polymer/gas systems allows for phase separation at high temperatures due to the large free volume difference between the two species. During low temperature solution formation, a solvent vapor or gas experiences a large volume contraction as it diffuses into the polymer matrix. This restricts the vibrational motions of the solvent or gas molecules increasing the molecular order and decreasing the non-combinatorial entropy term. If the temperature of the system is increased, then the contribution of the non-combinatorial entropy term dominates the Gibbs free energy of mixing forcing the system to phase separate, where the solvent or gas "condenses" in the polymer matrix.

A typical equilibrium phase diagram is sketched in the upper portion of Figure 3.2 for a partially-miscible, binary polymer/solvent system at constant pressure. The figure shows a system characterized by a lower critical solution temperature, T_c (LCST) which occurs in systems having negative enthalpy of mixing and/or large volume contractions of the solvent or gas during mixing. Below the critical temperature, T_c, the polymer and solvent are miscible in all proportions forming a single phase solution. It should be noted that many polymer/solvent systems also experience an upper critical solution temperature (UCST) where the binodal and spinodal curves are concave down. For more detailed discussion of polymer/solvent phase separation and the related thermodynamics, readers are referred to Flory (1953), Gutowski and Suh (1982), and Young and Lovell (1991).

The equilibrium phase diagram of Figure 3.2 shows four regions bounded by the spinodal (dashed curve) and the binodal (solid curve). Outside of the binodal, the binary system is completely miscible consisting of stable single phase solutions. At T_1, the Gibbs free energy curve indicates stable single phase behavior for $0 < \phi_2 < \phi'_{2b}$ and $\phi''_{2b} < \phi_2 < 1$. In the second region, within the spinodal, the binary system is immiscible, consisting of two phases in equilibrium. The condition for equilibrium for two co-existing phases is that the chemical potentials for both phases are equal for each constituent. This follows since the chemical potential of constituent i is equal to $(\partial G/\partial n_i)_{n_j,T,p}$ where n_i is the number of moles of constituent i. In the Gibbs free energy graph of Figure 3.2, phase equilibrium corresponds to two phases sharing a common tangent, defined as the binodal compositions (i.e., given by ϕ'_{2b} and ϕ''_{2b} at T_1). Single phase solutions within the spinodal are unstable and will spontaneously phase-separate via spinodal decomposition into two phases having binodal compositions. At T_1, this unstable phase behavior holds for $\phi'_{2s} < \phi_2 < \phi''_{2s}$.

The regions between the binodal and spinodal are of the greatest interest to microcellular processing and correspond to metastable solutions which will tend to phase-separate (via nucleation and growth) if a finite energy barrier can be overcome. At T_1, the Gibbs free energy curve indicates metastable single phase behavior for $\phi'_{2b} < \phi_2 < \phi'_{2s}$ and $\phi''_{2s} < \phi_2 < \phi''_{2b}$. This follows since the points at ϕ'_{2s} and ϕ''_{2s} correspond to the inflection points on the Gibbs free energy curve where $(\partial^2 \Delta G_m/\partial \phi_2^2)' = (\partial^2 \Delta G_m/\partial \phi_2^2)'' = 0$. In the ranges of $\phi'_{2b} < \phi_2 < \phi'_{2s}$ and $\phi''_{2s} < \phi_2 < \phi''_{2b}$, the initial stages of phase separation give rise to an increase in the Gibbs free energy (i.e., the Gibbs free energy barrier). As phase separation proceeds further until the binodal compositions are achieved, the Gibbs free energy of the system decreases below that of the initial metastable solution. The metastable solutions tend to phase separate via nucleation and growth. In order for the nucleation of a phase to occur, a Gibbs free energy barrier must be overcome for the system to reach a final lower free energy state. Once nucleation has occurred, free energy differences drive the growth of the nucleated phase via mass transport of the nucleated phase which commonly occurs by a diffusion process.

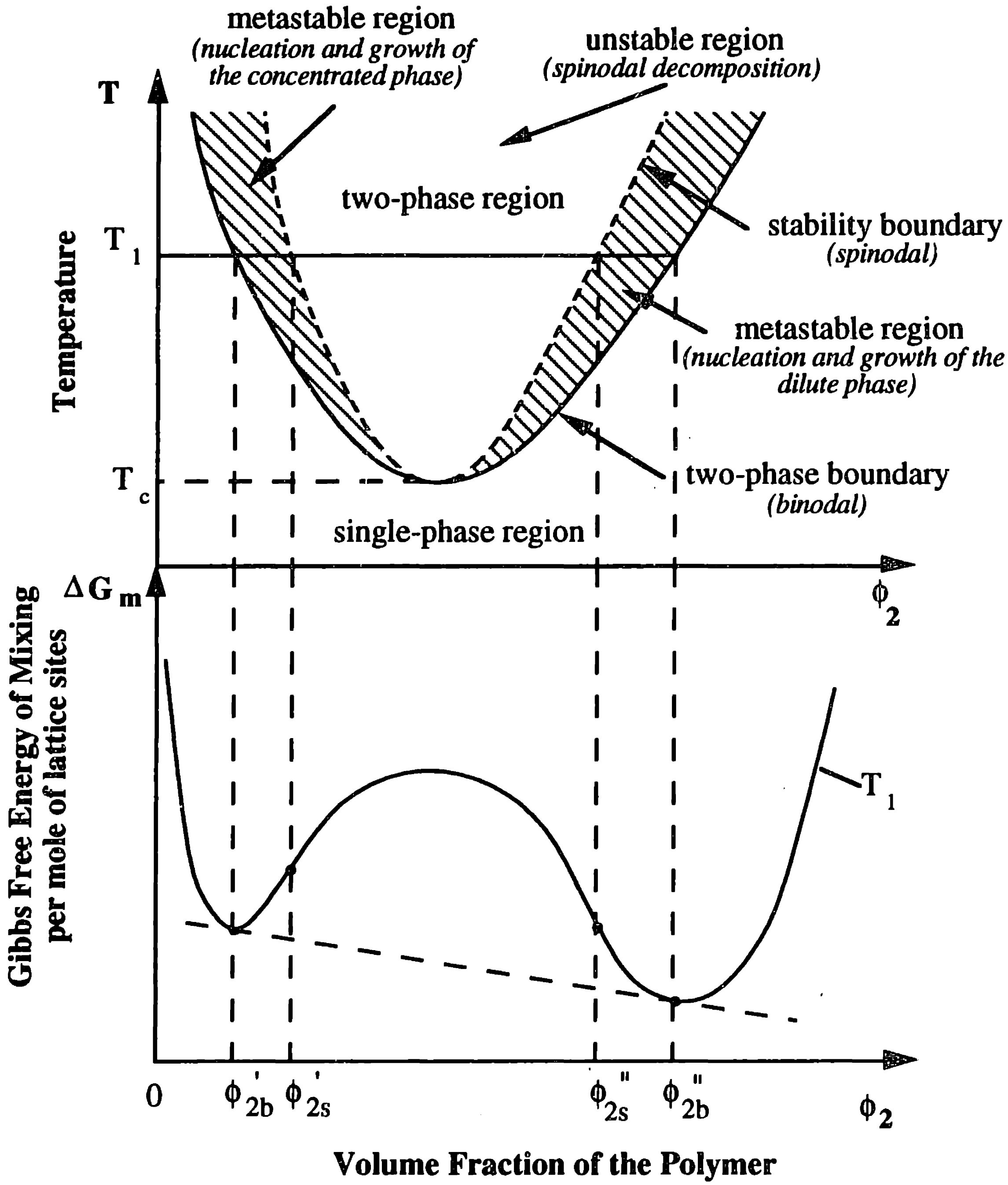

Figure 3.2: Typical phase diagram and its relation to the Gibbs free energy of mixing for a partially miscible binary system at constant pressure.

The relation between the polymer/solvent system phase separation and the phase separation which occurs during microcellular processing of polymer/gas systems is unclear at this point in time. It is widely accepted that the phase separation occurring in microcellular processing is of the nucleation and growth type. However, the specific shape of the phase diagram for typical polymer/gas systems is as yet undetermined. It appears that phase separation in microcellular processing is represented by something similar to the right hand side of Figure 3.2, in particular the metastable region. Nucleation and growth of microcells is commonly reported indicating the existence of a binodal phase boundary. No experimental evidence has yet been published indicating a spinodal boundary (with the accompanying spinodal decomposition phase separation) in polymer/gas systems typical of microcellular processing. Moreover, common polyethylene fractionation techniques using supercitical carbon dioxide indicate the existence of a binodal boundary at low polymer concentrations. †

To illustrate common nucleation techniques in microcellular processing using Figure 3.2, consider a closed system with a high polymer concentration, ϕ_2 at low temperatures. An increase in temperature will force the system to enter a metastable state where nucleation and growth are favored provided the energy barrier is overcome. Temperature driven nucleation has been observed in both batch and continuous microcellular processing (Kumar et al., 1992; Park and Suh, 1992b; Ramesh et al., 1993; Ramesh et al., 1992; Kweeder et al., 1991). If a spinodal boundary exists, one would expect that a sufficiently large temperature increase would place the system in a unstable state where spinodal decomposition is favored. Another way of forcing the polymer system into a metastable state is via a pressure change. In Figure 3.2, pressure changes are typified by translations of the critical point, spinodal curve, and binodal curve along the temperature and concentration axis. For a pressure decrease, one might expect the critical point to translate to a lower temperature and a lower polymer concentration. In the case of polymer/gas systems, the binodal boundary would seem to decrease with a pressure decrease. Thus, a pressure change can force the system into a metastable region where cell nucleation and growth can occur. Pressure driven nucleation is commonly observed in microcellular processing (Baldwin and Suh, 1992; Baldwin et al., 1992; Cha and Suh, 1992; Colton and Suh, 1987abc; Kumar and Weller, 1991a; Martini et al., 1982; Park et al., 1993; Youn and Suh, 1985). In addition, Figure 3.2 indicates that, provided a spinodal exists, a sufficiently large decompression will force a polymer/gas system into an unstable state where spinodal decomposition is favored. While the existence of a spinodal in polymer/gas systems is unknown at this time, microcellular foams generated in this manner may tend to have an open cell structure due to the unique interpenetrating phase network normally associated with spinodal decomposition. In this case, the systems would have to be stabilized quickly to maintain the open cell structure.

---

† In the fractionation process, the solubility of polyethylene in supercritical carbon dioxide is a function of molecular weight, pressure, and temperature. By controlling the solubility through the solution pressure or temperature, various molecular weight polyethylenes can be separated (i.e., precipitated) out from the solution. In this case, the highest molar mass species nucleate first followed by lower molar mass species.

3.2.2 Classical Nucleation Theory

The nucleation of microvoids is a process by which microscopic fluctuations resulting from thermodynamic state changes form clusters of gas molecules. The nucleated clusters will spontaneously grow if they exceed a critical size. Clusters smaller than the critical size will dissolve back into solution. This implies the existence of a finite energy barrier for stable cluster formation. The nucleation process can occur homogeneously throughout the material or heterogeneously at high energy regions such as phase boundaries. The formation of microvoids in the supersaturated solution can be quantified using elements of classical nucleation theory derived by Becker and Döring (1935) and by Zeldovich (1943) which are reviewed by Zettlemoyer and others (1969). The basic concept underlying classical nucleation kinetics theory is that supersaturated systems contain clusters of molecules that form discrete interfaces. A nucleated cluster grows by capturing additional molecules through an interface, and shrinks by the losing molecules through the interface. Agglomeration and other factors which can affect the detectable number of nuclei are neglected in the basic theoretical treatment. The cluster growth rate can be expressed as the difference between the rate molecules join a cluster containing i molecules and the rate they leave a cluster containing i+1 molecules.

$$J = n_i \beta_i A_i - n_{i+1} \alpha_{i+1} A_i \tag{3.2-1}$$

In equation (3.2-1), β_i is the frequency molecules impinge and join a cluster with i molecules per unit area, α_{i+1} is the frequency molecules evaporate and leave a cluster with i+1 molecules per unit area, A_i is the surface area of the cluster with i molecules, and n is the size distribution of clusters per unit volume such that n_i is the number of clusters containing i molecules. By definition, the cluster growth rate J is zero at equilibrium.

From the cluster growth rate, the rate of cluster formation (i.e., the nucleation rate) can be derived within a multiplicative constant (called the Zeldovich factor) by summing the growth rates over the nuclei distribution and substituting in the Gibbs-Thomson equation (Dunning, 1969). The classical form of the rate of nucleation takes the form of an Arrhenius relation:

$$J = Z \beta_k n_I \exp\left(\frac{-\Delta F_k}{kT}\right) \tag{3.2-2}$$

where Z is the Zeldovich factor, β_k is the frequency molecules are captured at the critical cluster size, n_I is the number of possible nucleated clusters, ΔF_k is the Helmholtz free energy of critical cluster formation, and k is Boltzmann's constant.

3.2.3 Nucleation in Microcellular Processing

The first theories to predict homogeneous and heterogeneous nucleation during microcellular processing were developed by Martini et al. (1982, also see Martini, 1981), Youn and Suh (1985, also see Youn, 1984), and Colton and Suh (1987abc, also see Colton, 1985). The theories developed by Martini et al. (1982) and Youn and Suh (1985) were based on classical nucleation theory while the theory of Colton and Suh (1987abc) extended classical nucleation theory to account for the free volume effects due to additives and gases in solution.

A more recent model predicting heterogeneous nucleation during microcellular processing is proposed and studied by Kweeder et al. (1991) with further refinements by Ramesh et al. (1993). For the polystyrene and nitrogen system studied, Kweeder et al. (1991) find that the thermal history of PS can affect the nucleation cell density by nearly two orders of magnitude and hypothesized that micro-damage caused by processing strongly influences the nucleation process. The authors state that the microcellular nucleation theories developed by Martini et al. (1982), Youn and Suh (1985), and Colton and Suh (1987abc) predict negligible nucleation rates over the processing conditions studied, and propose a model based on the hypothesis that there exists a population of microvoids within the polymer matrix promoting heterogeneous nucleation. The authors present model predictions and experimental results for microcellular polystyrene processed with nitrogen which show reasonable agreement over a limited range of data. However, the model does not predict the exponential variation in cell density over increasing saturation gas pressure as depicted by their experimental data. Ramesh et al. (1992) present a further study of heterogeneous nucleation in impact grade polystyrene processed with nitrogen and carbon dioxide. These preliminary results indicate that the heterogeneous domain size strongly influences nucleation mechanisms and that the number of heterogeneous microvoids may increase with saturation gas pressure due to the volumetric changes associated with large decompressions. Recently, Ramesh et al. (1993) has presented further extensions of the heterogeneous nucleation theory presented by Kweeder et al. (1991) specifically tailored to a polystyrene system containing low glass transition particles. The authors show good agreement between the model and experimental results for microcellular polystyrene containing polybutadiene particles processed with nitrogen. In addition, Kumar and Weller (1992) present nucleation results for microcellular polycarbonate processed with carbon dioxide which they assert deviate from classical nucleation theory. For example, the authors state that existing classical microcellular nucleation theories require twenty times larger pressure changes to predict nucleation densities comparable with experimental data although no details on the theoretical calculations are given.

Even though there is lack of consensus as to the predictive capability of classical nucleation models for microcellular processing, it is useful to present some of the basic elements underlying these classical nucleation theories as applied to microcellular processing. While the quantitative predictions of classical nucleation theory are conflicting for various polymer/gas systems, it appears that the qualitative trends exhibited by the classical models agree with most of the microcellular data available in literature. The most notable presentation of microcellular nucleation behavior with supporting theoretical developments are by Colton (1985), Colton and Suh (1987abc), and Colton (1989). In these studies, the authors present both homogeneous and heterogeneous microcellular nucleation data for polystyrene and zinc stearate systems as well as polyolefin systems processed with nitrogen which show good agreement with the predictions of their extended classical nucleation theory. Therefore, the theory of Colton and Suh will be summarized here for illustrative purposes.

Colton and Suh model three possible mechanisms for cell nucleation in thermoplastic polymers: homogeneous, heterogeneous, and mixed mode nucleation. In general, the formation of a gas cluster has an associated excess energy equal to the Gibbs free energy of bubble formation. Assuming a reversible, isothermal thermodynamic process, the change in Gibbs free energy during cluster formation is given by the energy associated with forming a new interface plus the volumetric work performed to generate the cluster volume. For homogeneous nucleation this is given by:

$$\Delta G_{hom} = -V_b \, \Delta p + A_{bp} \, \gamma_{bp} \tag{3.2-3}$$

where V_b is the volume of the cluster, Δp is the difference in the pressure of the gas in the cluster and the environmental nucleation pressure, and γ_{bp} is the surface energy of the polymer/cluster interface. For a spherical cluster of radius, r, equation (3.2-3) can be written as:

$$\Delta G_{hom} = -\frac{4}{3}\pi r^3 \Delta p + 4\pi r^2 \gamma_{bp} \tag{3.2-4}$$

To determine the critical cluster size, we impose the requirement that the Gibbs free energy of the system be a maximum where

$$\frac{d(\Delta G_{hom})}{dr} = 0 \quad \text{and} \quad \frac{d^2(\Delta G_{hom})}{dr^2} < 0$$

yielding

$$r^* = 2\,\frac{\gamma_{bp}}{\Delta p}\,. \tag{3.2-5}$$

Since the system will naturally seek a lower free energy state, gas clusters smaller than the critical radius will tend to dissolve back into the polymer matrix and gas clusters larger than the critical radius will tend to grow spontaneously. Both processes tend to lower the system free energy. The Gibbs free energy barrier necessary to form a critical cluster during homogeneous nucleation is given by substituting equation (3.2-5) into (3.2-4)

$$\Delta G^*_{hom} = \frac{16\,\pi\,\gamma_{bp}^{\,3}}{3\,\Delta p^2}\,. \tag{3.2-6}$$

Colton and Suh (1987abc) also discuss modifications to the Gibbs free energy of cluster formation associated with the free volume changes occurring when large amounts of gas and/or additives are mixed into the polymer matrix. In this discussion, these contributions are neglected. Following the same lines as classical nucleation theory by assuming a Boltzmann's distribution of gas clusters, the homogeneous nucleation rate, N_{hom}, is given by

$$N_{hom} = C_0 f_0 \exp\left(\frac{-\Delta G^*_{hom}}{kT}\right) \tag{3.2-7}$$

where C_0 is the concentration of available homogeneous nucleation sites, f_0 is the frequency factor of gas molecules joining the nucleus, and k is Boltzmann's constant. Equation (3.2-7) predicts increasing homogeneous nucleation rates with higher saturation gas pressures (i.e., higher gas concentrations), lower surface tensions, and higher temperatures. Colton and Suh (1987abc) also show that the homogeneous nucleation rate can increase with an increase in soluble additives through surface tension effects.

Heterogeneous nucleation occurs when a gas cluster forms at an interface between two phases such as a polymer and an additive. Consider the nucleation of a gas bubble at the interface of a polymer and a solid particle. One can show that at equilibrium the interfacial surface tensions must balance where

$$\gamma_{sp} = \gamma_{bp} + \gamma_{sb} \cos\theta \tag{3.2-8}$$

where γ_{sp} is the surface tension of the second phase particle and the polymer interface, γ_{sb} is the surface tension of the second phase particle and the gas interface, and θ is the wetting angle of the polymer-additive-gas interface on a flat surface. The Gibbs free energy associated with forming a cluster at an interface is given by

$$\Delta G_{het} = -V_b \, \Delta p + A_{bp} \, \gamma_{bp} + A_{sb} \, \gamma_{sb} - A_{sp} \, \gamma_{sp} \tag{3.2-9}$$

Substituting in equation (3.2-9) for a cluster taking the form of a spherical cap yields

$$\Delta G_{het} = \left[-\frac{4}{3} \pi r^3 \, \Delta p + 4\pi \, r^2 \, \gamma_{bp} \right] S(\theta) \tag{3.2-10}$$

where

$$S(\theta) = \frac{(2+\cos\theta)(1-\cos\theta)^2}{4} < 0. \tag{3.2-11}$$

Similar to the homogeneous nucleation case, the rate of heterogeneous nucleation, N_{het}, is given by

$$N_{het} = C_1 f_1 \exp\left(\frac{-\Delta G^*_{het}}{kT} \right) \tag{3.2-12}$$

where the Gibbs free energy associated with forming a critical cluster is

$$\Delta G^*_{het} = \frac{16 \, \pi \, \gamma_{bp}{}^3}{3 \, \Delta p^2} \, S(\theta) \tag{3.2-13}$$

C_1 is the concentration of heterogeneous nucleation sites, and f_1 is the frequency factor of gas molecules joining the nucleus. Relatively speaking, the Gibbs free energy of formation is lower for heterogeneous nucleation than for homogeneous nucleation due to the surface energy effects. This implies that in any given system, heterogeneous nucleation will tend to activate first, before homogeneous nucleation, resulting in the preferential growth of heterogeneously nucleated cells over the homogeneous nucleation of additional cells.

Moreover, systems experiencing heterogeneous nucleation will have lower cell densities since the number of heterogeneities is typically much lower than the number of available homogeneous sites (i.e., $C_1 << C_o$).

It is apparent from equations (3.2-7) and (3.2-12) that supersaturation (given by Δp) and surface tension play dominant roles in governing nucleation rates and cell density. Increasing the degree of supersaturation by lowering the system surface tension or increasing saturation pressure, decreases the Gibbs free energy barrier for nucleation, thus increasing the nucleation rate and cell density. Temperature increases can also increase the nucleation rate by increasing the frequency molecules join nuclei and increasing the distribution of potential stable nuclei (i.e., through the exponential term). It is important to note that the temperatures at the point of nucleation and during cell growth are not necessarily equal during microcellular processing, and this fact must be accounted for when evaluating processes characteristics.

In many cases nucleation occurs in a mixed mode fashion where both homogeneous and heterogeneous nucleation occur. As a first order approximation, the contributions of homogeneous and heterogeneous nucleation are additive as given by equation (3.2-14) (Colton and Suh, 1987abc). For mixed mode nucleation, it is assumed that heterogeneous nucleation initiates prior to homogeneous nucleation. Therefore, some of the available gas for nucleation is dissolved from the solution due to growth of existing nucleated clusters. This results in fewer gas molecules available for homogeneous nucleation. An expression for homogeneous nucleation in the presence of heterogeneous nucleation is given by equation (3.2-15) where the rate of homogeneous nucleation is decreased by the heterogeneously nucleated clusters.

$$N_T = N'_{hom} + N_{het} \tag{3.2-14}$$

$$N'_{hom} = (C_o - N_{het} n_b t) f_o \exp\left(-\frac{\Delta G^*_{hom}}{kT}\right) \tag{3.2-15}$$

In equation (3.2-15), n_b is the average number of gas molecules in a stable nuclei and t is the time elapsed from the first heterogeneous cluster nucleation.

Based on the experimental and model results presented by Colton and Suh (1987abc), they conclude that the greatest number of microcells can be produced through homogeneous nucleation. To accomplish this, one should dissolve an additive into a polymer at levels slightly less than the solubility limit and saturate at high gas pressures to form a solution. This will reduce the activation energy barrier to nucleation by reducing the surface tension and increasing supersaturation. The resulting system will have high nucleation rates and a large cell density.

3.2.4 Additional Observations in Microcellular Nucleation

In most foam processing techniques, one would expect some degree of heterogeneous nucleation due to inherent impurities in the polymer matrix. However, in the production of microcellular plastics, it is believed that both homogeneous and heterogeneous nucleation occur in relative amounts which depend on the specific processing conditions. This follows since free energy changes are instigated by equilibrium solubility changes (i.e., supersaturation). These free energy changes are typically very rapid (i.e., t is small in equation 3.2-15) when instigated via rapid pressure changes which can propagate near the speed of sound within the medium. Since decompressions are substantial in microcellular processing [i.e., as high as 41.3 MPa (6000 psi)], both homogeneous and heterogeneous nucleation may occur simultaneously. Numerous factors point to homogeneous nucleation contributions. Experimental evidence indicates increasing cell density with saturation gas pressures through 41.3 MPa (6000 psi) for both N_2 and CO_2, unlike the nucleation density plateau common in heterogeneous nucleation (Colton and Suh, 1987abc). In addition, current microcellular technology is capable of nucleating 10^{15} cells/cm^3 (Cha, et al., 1992). It would appear that nucleation at this scale must entail significant homogeneous contributions since it is unlikely that 10^{15} heterogeneities exist in a cubic centimeter of polymer.

Although not specifically detailed in current microcellular nucleation theories, it is believed physical limitations exist bounding the total number of microvoids that can be nucleated and thus the ultimate cell density of microcellular polymers. For a typical polymer with a molecular weight of 100,000 g/mole and a mass density of 1 g/cm^3, the polymer molecule density is on the order of 10^{18} molecules/cm^3. Current microcellular technology is capable of nucleating 10^{15} cells/cm^3 (see Cha et al., 1992) and is likely to be extended to produce cell densities on the order of 10^{18} cells/cm^3. A cell density of 10^{18} cells/cm^3 corresponds to cell sizes which are just one order-of-magnitude smaller than supermicrocellular foams currently produced (i.e., 0.01 μm compared to 0.1 μm). Nucleating 10^{18} cells/cm^3 implies that a single void or "cell" is nucleated for every polymer molecule. This is the target range for the ultra-microcellular polymers proposed by Suh et al. (1993). At this scale, differences between homogeneous and heterogeneous nucleation become increasingly subtle and perhaps indistinguishable.

Finally, it should be mentioned that some interesting techniques for enhancing cell nucleation have been proposed for conventional foam processing. One such method is the use of ultrasound to enhance cell nucleation. Byon and Youn (1990) discuss its use in the processing of thermoplastic foams, Park and Youn (1993) discuss its use in polyurethane processing, and Cho et al. (1992) discuss its use in polyurethane RIM applications. In addition, Ramesh et al. (1992) propose the use of microwave heating to induce higher nucleation densities in microcellular processing. Here the authors show preliminary results for impact grade polystyrene processed with carbon dioxide. An interesting nucleation technique is also presented by Hansen and Martin (1965), who discuss the use of finely-divided metals to enhance the nucleation of dissolved gas in various polymers. This method uses the differential heat capacities between the polymer and metal to promote local thermally activated bubble nucleation.

3.3 Growth of Cells and Density Reduction

Once stable microcells have nucleated, they continue to grow reducing the overall density of the polymer matrix. During cell growth, gas molecules diffuse into the nucleated cells from the polymer matrix (a distance on the order of 10 microns). The rate at which the cells grow is limited by the gas diffusion rate and the stiffness of the viscoelastic polymer/gas matrix. If the stiffness of the matrix is high, cell growth is extremely slow. In this case, the solution temperature can be increased to lower the matrix stiffness and the flow strength of the polymer. In general, the cell growth process is controlled by the time cells are allowed to grow, the temperature during growth, the state of supersaturation, the hydrostatic pressure or stress applied to the polymer matrix, the interfacial surface energy, and the viscoelastic properties of the polymer/gas solution.

To understand the driving force of cell growth, one can use the Gibbs free energy as given for a spherical bubble by equations (3.2-4) and (3.2-10) for homogeneous and heterogeneous nucleation, respectively. A plot of the Gibbs free energy is given in Figure 3.3 which shows the individual contributions of the interfacial energy term, the volumetric work term, and the total Gibbs free energy change as a function of cell radius. Below the critical radius size, r^*, nucleated clusters are unstable and will dissolve back into solution to lower the free energy of the system. This is evident from Figure 3.3 because below the critical radius, the interfacial energy term dominates. At the critical radius clusters are metastable since the Gibbs free energy is a maximum. Above the critical radius, clusters are stable. Since the system will naturally seek a state of lower free energy, stable cells will tend to grow, increasing the dominant volumetric work term and lowering the overall system free energy. While thermodynamics can explain the general trends associated with the growth of microvoids in a solution, cell growth in polymer foams is a kinetic process involving the dynamic growth of microvoids in a viscoelastic medium.

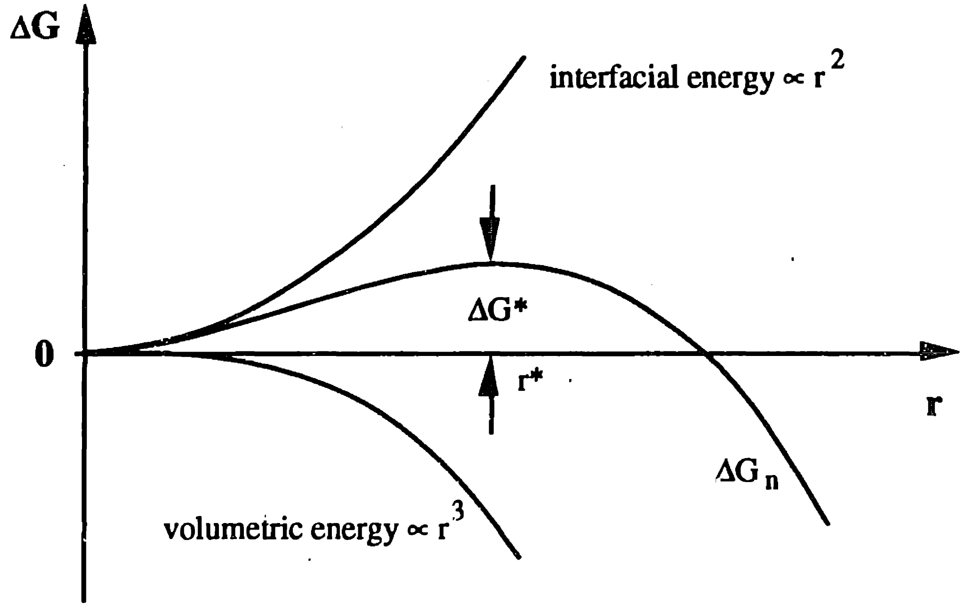

Figure 3.3: Typical Gibbs free energy and individual energy contributions associated with the nucleation of a spherical cluster of radius r.

The principles which govern the growth of microvoids in a viscoelastic medium are the diffusion of gas into the expanding cell and the dynamic growth of the cell due to pressure difference of the gas in the cell and the surrounding polymer/gas matrix.

At this point it is useful to present some of the basic underlying theory governing the growth of a microcell in a polymer matrix. In this treatment, relaxation phenomenon associated with cell growth such as coalescence of cells and bulk motion of the expanding matrix are neglected; however, these phenomenon are important in some systems, particularly in melt processing. First, the cells are approximated as spherical, the polymer matrix is modeled as a viscous fluid (both Newtonian and Non-Newtonian), the growth process is approximated as isothermal, and the polymer matrix is taken to be incompressible. The basic system under consideration is shown in Figure 3.4.

Consider a single cell having a fixed frame of reference at the center of the cell (i.e., in spherical coordinates) and negligible bulk motion of the fluid. For an incompressible fluid, continuity requires that the radial velocity of the fluid surrounding the cell, v_r, follow equation (3.3-1). Due to symmetry, the v_θ and v_ϕ velocity components are zero.

$$\frac{1}{r^2}\frac{\partial}{\partial r}\left(r^2 v_r\right)=0 \tag{3.3-1}$$

The boundary conditions of the system require that the radial velocity component, v_r, at the bubble interface and the bubble interface radial velocity, $\dot{R}$ be equal: $v_r(R) = \dot{R}$. Integrating equation (3.3-1) then yields

$$v_r=\frac{R^2\dot{R}}{r^2}\,. \tag{3.3-2}$$

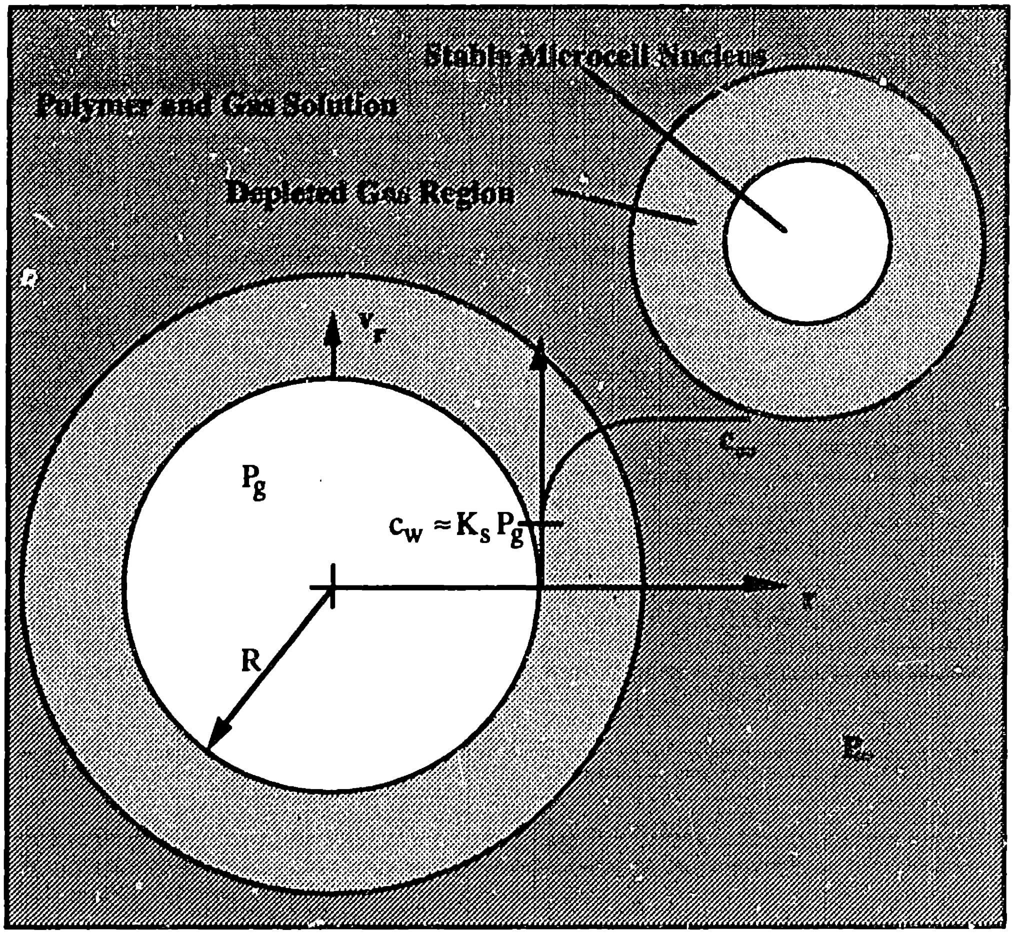

Figure 3.4: Schematic of growing microcells in a polymer/gas solution.

In order to model the dynamic nature of the growing cell, the radial component of the equation of motion is employed given by:

$$\rho\left(\frac{\partial v_r}{\partial t}+v_r\frac{\partial v_r}{\partial r}\right)=-\left[\frac{1}{r^2}\frac{\partial}{\partial r}\left(r^2\tau_{rr}\right)-\frac{\tau_{\theta\theta}+\tau_{\phi\phi}}{r}\right]-\frac{\partial p}{\partial r} \tag{3.3-3}$$

where τ_{ii} is the normal compressive stress component along the i-th coordinate, ρ is the density of the polymer, and p is the pressure of the system. Due to symmetry, the non-radial velocity components and the shear stress terms are zero.

Next, a constitutive equation must be employed to relate the flow stress to the shear rate. For Newtonian fluids, the constitutive relation is given by equation (3.3-4). For a non-Newtonian fluid which experiences shear thinning, the power-law constitutive equation is given by equation (3.3-5).

$$\tilde{\tau} = -\mu \tilde{\dot{\gamma}} \qquad (3.3\text{-}4)$$

$$\tilde{\tau} = -\eta \tilde{\dot{\gamma}} = -\left(m \dot{\gamma}^{n-1}\right) \tilde{\dot{\gamma}} \qquad (3.3\text{-}5)$$

where $\tilde{\tau}$ is the compressive stress tensor, $\tilde{\dot{\gamma}}$ is the rate-of-strain tensor, μ is the dynamic viscosity, η is the non-Newtonian viscosity, n is the power-law factor, m is the power-law constant, and $\dot{\gamma}$ is the magnitude of the rate-of-strain tensor. While polymer flows are typically non-Newtonian, the Newtonian fluid approximation serves as a useful comparison. Moreover, even though the power-law fluid model neglects the viscoelastic behavior of polymer flows, it does account for shear thinning behavior and is found to be a good approximation for predicting flow behavior in many polymer systems (Bird et al., 1987).

It is interesting to note that according to equation (3.3-3), the cell growth dynamics involves no shear flow. That is to say that the fluid surrounding a cell experiences pure biaxial elongational flow. This would seem to imply that the elongational fluid viscosity should be employed when formulating the constitutive equation. However, it can be shown that the elongational viscosity contributions reduce to zero for incompressible fluids (Potter and Foss, 1982).

Substituting in the constitutive equations (3.3-4) and (3.3-5) as well as the geometric relations relating the rate-of-strain to the velocity gradients yields equations (3.3-6) and (3.3-7), respectively.

$$\rho\left(\frac{\partial v_r}{\partial t} + v_r \frac{\partial v_r}{\partial r}\right) = \frac{2\mu}{r^2}\frac{\partial}{\partial r}\left(r^2 \frac{\partial v_r}{\partial r}\right) - \frac{4\mu v_r}{r^2} - \frac{\partial p}{\partial r} \qquad (3.3\text{-}6)$$

$$\rho\left(\frac{\partial v_r}{\partial t} + v_r \frac{\partial v_r}{\partial r}\right) = \frac{2m}{r^2}\frac{\partial}{\partial r}\left(r^2 \dot{\gamma}^{n-1} \frac{\partial v_r}{\partial r}\right) - \frac{4m\dot{\gamma}^{n-1} v_r}{r^2} - \frac{\partial p}{\partial r} \qquad (3.3\text{-}7)$$

Next, the radial velocity expression (3.3-2) is substituted into equations (3.3-6) and (3.3-7) and the pressure is integrated from $r = R^+$ to $r \rightarrow \infty$ where R^+ is the radius just outside the cell interface. Here, an infinite media approximation has been used which neglects pressure and flow interactions between adjacent cells. In order to relate the pressure in the cell $p(R^-) = p_g$ to that just outside the cell interface $p(R^+)$, a force equilibrium is applied to the interface of the cell hemisphere. This mandates that $p(R^+) = p_g - 2\gamma_{bp}/R - \tau_{rr}(R^+)$ where γ_{bp} is the surface tension of the polymer/gas interface and $\tau_{rr}(R^+) = -\eta\,\dot{\gamma}_{rr}(R^+)$. Simplifying the resulting relations yields equations (3.3-8) and (3.3-9) for Newtonian and non-Newtonian fluids, respectively.

$$\rho\left(\frac{3}{2}\dot{R}^2 + R\ddot{R}\right) = -\frac{4\mu\dot{R}}{R} + \left(p_g - p_\infty - \frac{2\gamma_{bp}}{R}\right) \qquad (3.3\text{-}8)$$

$$\rho\left(\frac{3}{2}\dot{R}^2 + R\ddot{R}\right) = -\frac{4m}{n}\left(2\sqrt{3}\right)^{n-1}\left(\frac{\dot{R}}{R}\right)^n + \left(p_g - p_\infty - \frac{2\gamma_{bp}}{R}\right) \qquad (3.3\text{-}9)$$

In equations (3.3-8) and (3.3-9), p_∞ is the hydrostatic pressure of the polymer at large distances from the cell. The initial conditions of cell growth are $p_g(0) = p_{go}$ = the gas pressure of a stable cluster and $R(0) = r^*$ = radius of a stable cluster. It is interesting to note that while the viscous force terms in equations (3.3-6) and (3.3-7) cancel out, as expected for the pure extensional flow, there are viscous force terms present in equations (3.3-8) and (3.3-9). These viscous force terms result from the dynamics of the expanding interface and appear in equations (3.3-8) and (3.3-9) due to the $\tau_{rr}(R^+)$ term in the interface force balance.

The differential equations of (3.3-8) and (3.3-9) relate the radius of the growing cell to the gas pressure within the cell. In order to solve for the radius of the cell and the cell gas pressure, a second relation is needed. This can be derived by applying conservation of mass for the diffusing species (i.e., the gas) at the cell interface. The gas within the cell is assumed to be ideal, and it is assumed that no pressure gradients exist within a cell. In addition, diffusion of polymer molecules into the cell is neglected and the polymer/gas solution is assumed to have the same density as the polymer (i.e., negligible swelling). Applying continuity for the gas to the cell interface yields:

$$\frac{1}{R\,T}\frac{\partial}{\partial t}\left(p_g R^3\right) = 3\,\rho_p D R^2 \left.\frac{\partial c}{\partial r}\right|_R \qquad (3.3\text{-}10)$$

where R is the gas constant, T is the temperature, D is the diffusivity, ρ_p is the polymer density, and c is the local concentration of gas in the polymer. Since the local gas concentration surrounding a cell depends on the rate gas diffuses towards the cell and the rate at which the cell expands, the local gas concentration is governed by:

$$\frac{\partial c}{\partial t} + v_r \frac{\partial c}{\partial r} = \frac{1}{r^2} \frac{\partial}{\partial r}\left(r^2 D \frac{\partial c}{\partial r} \right) . \qquad (3.3\text{-}11)$$

The boundary conditions for equation (3.3-11) are $c(R,t) = K_s\, p_g$ and $(\partial c/\partial r)_{t,r\to\infty} = 0$. The initial condition is $c(r,0) = K_s\, p_{sat}$.

By simultaneously solving equations (3.3-2), (3.3-8), (3.3-10), and (3.3-11) for a Newtonian fluid, the cell radius, the radial velocity distribution, the cell gas pressure, and the gas concentration distribution can be determined as functions of time relative to the instant a stable cluster is formed. Likewise, by simultaneously solving equations (3.3-2), (3.3-9), (3.3-10), and (3.3-11), these variables can be determined as functions of time for a non-Newtonian fluid.

Numerical simulations of both of these cases are presented by Ramesh et at. (1991) and compared with experimental results for microcellular polystyrene processed with nitrogen and carbon dioxide. Literature is rich with other theoretical, and to a lesser extent, experimental treatments of cell growth in viscous, viscoelastic, and elastic media. For example, Epstein and Plesset (1950) present one of the first theoretical treatments of cell growth in a supersaturated liquid-gas solution. Gent and Tompkins (1969) and Hobbs (1976) present theoretical and experimental treatments of cell growth in elastomeric materials. Martini (1981) discusses an initial cell growth model for microcellular processing that accounts for the competition between stable nuclei for the limited amount of available gas in solution. Amon and Denson (1984) also present a cell growth model to predict cell growth where neighboring cells compete for available gas. Youn and Suh (1985) present a basic model for estimating the cell growth during processing of microcellular composites. Arefmanesh et al. (1990) have extended Amon and Denson's analysis by relaxing the assumption that a single cell is representative of all cells.

CHAPTER 4

INTRODUCTION TO THE AXIOMATIC DESIGN PRINCIPLES

4.0 Introduction

Design is the central tie inter-linking all engineering disciplines and is the process by which "loosely defined" societal needs are translated into physical systems, structured information, or organizational frameworks. There are numerous strategies and methods which are commonly used for engineering systems design. Commonly used strategies include concurrent engineering, quality function deployment, design for X (manufacture, assembly, maintenance, quality, etc.), Taguchi methods, "total" design methods, and the axiomatic design principles. Most of the former strategies stress one or two critical issues in the design process. For example, quality function deployment stresses the voice of the customer and quality (Hauser and Clausing, 1988; Clausing, 1988); Taguchi methods stress robust designs and optimization (Taguchi, 1987; Taguchi and Phadke, 1984); "total" design stresses the conceptual design stage (Pugh, 1991); and concurrent engineering stresses the simultaneous execution of principle design tasks (Nevins and Whitney, 1989). In contrast, the axiomatic design principles (Suh, 1990) abstract the design process to a level higher. The axiomatic design principles, in general, provide a structured framework from which to approach and evaluate designs on a fundamental basis, stressing both the independence of design functions and the hierarchical nature of design. Moreover, the framework is amenable to the major elements of most other design strategies and methods.

In this thesis, the axiomatic design principles are effectively utilized as a structured framework from which to formulate an innovative microcellular polymer sheet extrusion system. The design axioms serve as essential guidelines in approaching the problem, synthesizing a solution, determining critical process parameters, and evaluating system performance. This chapter is intended to present a brief introduction to the axiomatic design principles focusing on their application to manufacturing systems designs which span multiple hierarchy levels. Such physical systems have received relatively little detailed treatment to date.

4.1 Design and the Design Axioms

By definition, design is the process of mapping requirements of the functional design space into specifications of the physical design space. In other words, design encompasses the mapping between "what we want to achieve" and "how we want to achieve it." This mapping process can be seen as spanning four domains, the first two residing in the functional design space and the second two residing in the physical design space. First, the "customer" needs must be formalized in a set of requirements (CRs). These needs must then be mapped into the functional domain by specifying a non-unique but complete set of independent functional requirements (FRs) of the design. The functions are next mapped into the physical domain through design parameters (DPs) which specify the physical embodiments for satisfying the functional requirements. Finally, the design parameters must be mapped into the process domain by specifying a non-unique set of process variables (PVs). This mapping process is shown diagrammatically in Figure 4.1.

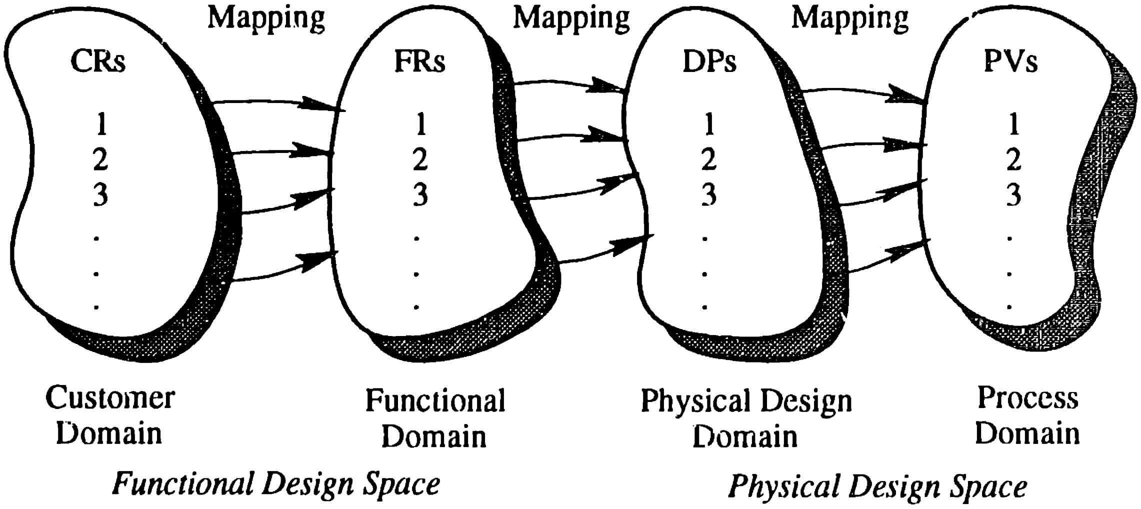

Figure 4.1: Mapping from the functional space to the physical space during the design process.

The design principles are based on two axioms (Suh, 1990). The first axiom deals with the fundamental relationship between the design functions and the physical implementations. The second axiom addresses the acceptable complexities of designs. These axioms are stated as follows:

Axiom 1: The Independence Axiom:
Maintain independence of the functional requirements (FRs) of the design.

Axiom 2: The Information Axiom:
Minimize the information content of the design.

Axiom One states that the independence of the design's functional requirements must be maintained by the design parameters and process variables selected to satisfy the FRs. Axiom Two states that the best design of those satisfying Axiom One is that which contains the least "information" content. Simply interpreted, this means the simpler the design, the better. By synthesizing a design that satisfies the Independence Axiom, the designer is insured feasibility and manufacturability of the design. In addition, satisfying Axiom One guarantees a robust design. By satisfying the Information Axiom, the designer is insured that the resulting design is the best among those satisfying the Independence Axiom particularly with regard to the robustness issue. It should be noted that in this thesis, the design of a continuous microcellular sheet processing system is analyzed using only the Independence Axiom.

The natural mapping process of design from the functional space into the physical space can be represented mathematically using design equations (Suh, 1990). First, the design is characterized using a set of customer requirements specified as a vector **CR**, a set of functional requirements specified as a vector **FR**, a set of design parameters specified as a vector **DP**, and a set of process variables specified as a vector **PV**. The mapping between the functional space and the design space is then given in the form of design matrices, **A**, **B**, and **C**. The design can then be represented by matrix equations as follows:

$$\{\mathbf{CR}\}_m = [\mathbf{A}]_{mxn}\{\mathbf{FR}\}_n \tag{4-1}$$

$$\{\mathbf{FR}\}_n = [\mathbf{B}]_{nxr}\{\mathbf{DP}\}_r \tag{4-2}$$

$$\{\mathbf{DP}\}_r = [\mathbf{C}]_{rxs}\{\mathbf{PV}\}_s \tag{4-3}$$

where the design matrix elements are given by

$$A_{ij} = \frac{\partial CR_i}{\partial FR_j} \qquad B_{ij} = \frac{\partial FR_i}{\partial DP_j} \qquad C_{ij} = \frac{\partial DP_i}{\partial PV_j} \tag{4-4}$$

Using this mathematical representation of the design, a convenient form of the Independence Axiom can be formulated. By definition, the Independence Axiom requires that the design matrices be square to maintain independence of the FRs. Moreover, the Independence Axiom mandates that the design parameters and process variables be selected such that independence of the FRs is maintained. This requires that the design equations have diagonal or triangular matrices. In the case of a decoupled design, the design matrices are triangular as shown in equations (4-6) and (4-7). For decoupled designs, the DPs and PVs must be selected in successive rows beginning with row one so that the independence between the FRs is maintained. In equations (4-6) and (4-7), the 'X's represent a strong dependence of the FR on perturbations in the respective DPs, and the '0's represent a relatively weak dependence. The functional dependence is weak provided that

$$\frac{\partial FR_i}{\partial DP_j} << \frac{\partial FR_i}{\partial DP_i} \tag{4-5}$$

implying that $\partial FR_i/\partial DP_j$ is on the order of zero compared with $\partial FR_i/\partial DP_i$. If the design matrix were diagonal (i.e., with X's only on the diagonal), then the design would be uncoupled. By definition, uncoupled and decoupled designs satisfy Axiom One and are feasible.

$$\begin{Bmatrix} FR_1 \\ FR_2 \\ FR_2 \end{Bmatrix} = \begin{bmatrix} X & 0 & 0 \\ X & X & 0 \\ X & X & X \end{bmatrix} \begin{Bmatrix} DP_1 \\ DP_2 \\ DP_3 \end{Bmatrix} \tag{4-6}$$

$$\begin{Bmatrix} DP_1 \\ DP_2 \\ DP_3 \end{Bmatrix} = \begin{bmatrix} X & 0 & 0 \\ X & X & 0 \\ X & X & X \end{bmatrix} \begin{Bmatrix} PV_1 \\ PV_2 \\ PV_3 \end{Bmatrix} \tag{4-7}$$

4.2 Hierarchical Design of Systems

Unlike piece-part design, the design of large-scale engineering systems requires the specification of hundreds if not thousands of functional requirements. Attempting to satisfy all of these requirements simultaneously is certainly an insurmountable task. As a result, large scale systems are commonly decomposed into smaller subsystems. In the context of the axiomatic design framework, the design of large scale systems transcends numerous levels of specification forming a functional hierarchy. However, the main difference between decomposing a system into subsystems and designing a system using a functional/physical hierarchy is that the hierarchical design structure forces the designer to synthesize the system from top-down rather than the typical approach of bottom-up design. The common bottom-up approach follows since designers naturally formulate concepts which solve low-level design problems first. Only later are the system design concepts and interactions integrated around the specific subsystems designed.

A hierarchical design strategy is an integral component of the design principles and is a very powerful tool. It provides a structured means of synthesizing the design problem in smaller, more manageable elements. In addition, it provides a formal guide to redesigns and troubleshooting. The true power of using the hierarchical design strategy follows from the Independence Axiom. When at a given hierarchy level, the independence of the FRs is maintained, in accordance with Axiom One, the designer is assured that subsequent levels of the design hierarchy are independent. Therefore, sub-systems can be designed without consideration of the effects of these design decisions on other sub-systems at the same hierarchy level.

When using the axiomatic design principles in the context of a hierarchical design, the mapping process must be performed by alternating between the functional space and the physical space as shown in Figure 4.2. The functional requirements at a given hierarchy level must first be independently satisfied by a physical embodiment specified by a set of design parameters. At this point, the next level of functional requirements can be formulated. These functional requirements must be based on the physical embodiment specified by the previous hierarchy level (i.e., the parent design parameters). In other words, the design process requires zigzagging from the functional space to the physical space and back again at each hierarchy level.

4.3 Constraints in Design

Another important element of the design principles are constraints which represent bounds on feasible design solutions. In the context of axiomatic design, constraints are classified as *input constraints* which are constraints in design specifications and *system constraints* which are constraints imposed by systems which interact with the design. The input constraints represent bounds on the design specifications such as cost, materials, weight, size. The system constraints represent bounds on the interactions between the specific design and the systems in which the design operates. System constraints are typically limits on geometric shape, machine capacity, control signals, etc.

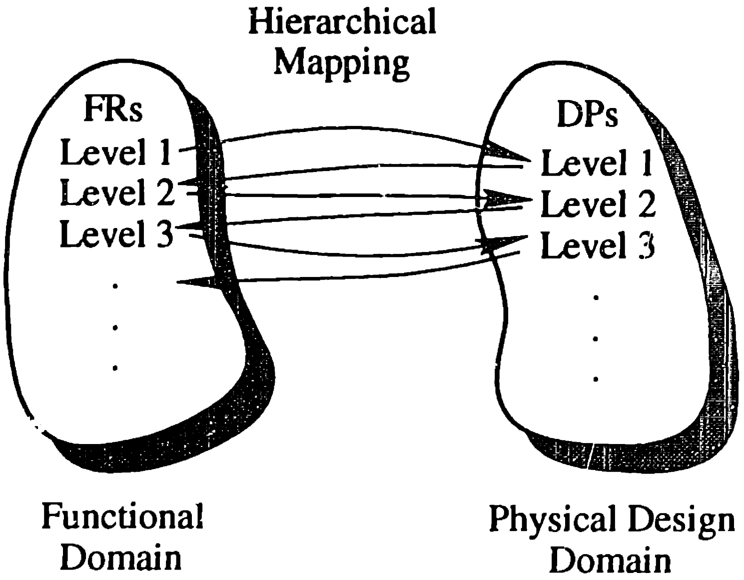

Figure 4.2: Mapping from the functional domain into the physical domain in a hierarchical design which involves propagating design decisions and physical embodiments through sub-hierarchy levels.

It is often difficult to distinguish and identify whether design specifications should be classified as functional requirements or constraints. The major difference between the two kinds of specifications are that constraints can be satisfied by one or all of the DPs/PVs. FRs must be satisfied independently. Constraints also are specified as limits or inequalities. Therefore, constraints are satisfied provided the DPs and PVs are chosen such that the system operates within the constraint limits. In contrast, FRs are specified as finite values having tolerances. To satisfy the FRs, the DPs/PVs must be selected such that the FRs fall within their tolerance band.

In addition, it is worth noting that the hierarchical nature of systems design also imposes system constraints during the design process. As the design hierarchy is built by zigzagging between the functional space and the physical space, design parameters (i.e., the physical embodiment) of parent levels impose system constraints on all subsequent levels. This follows since a physical embodiment has been specified for the sub-system by the parent levels. This embodiment must be propagated into the lower levels, constraining the system in shape, form, dimension, etc. For example, the highest functional requirement for the system design of this thesis is to develop a process for continuously producing microcellular polymer sheets. It so happens that the physical processing systems selected to satisfy this requirement is an extrusion process. Therefore, all of the subsequent FRs are formulated under the constraint that an extrusion process is to be used.

CHAPTER 5

MICROCELLULAR PROCESSING CHARACTERIZATION OF AMORPHOUS AND SEMI-CRYSTALLINE POLYMERS

5.0 Introduction

Semi-crystalline microcellular polymers have the potential to impact a large market sector for microcellular plastics where lightweight materials are needed in load-bearing applications. Such applications could range from high-strength, light-weight conduit for the aerospace industry to sandwich panel cores in automobile body panels. However, very little work has been reported on the microcellular processing of semi-crystalline polymers. Therefore, in this chapter, a characterization of the microcellular processing of amorphous and semi-crystalline polymers is presented.

The goals of this work are (1) to characterize the microcellular processing of an engineering thermoplastic in an amorphous and semi-crystalline form so as to identify critical process parameters that may be relevant in the continuous sheet processing system and (2) to discern the effects of crystallization and crystallinity in microcellular processing. The microcellular processing technique adopted in this analysis is that of the low-temperature batch processing technique detailed in section 2.2.1.

While numerous aspects of microcellular processing have been studied over the last decade (as discussed in chapter 2), very little work has been done on semi-crystalline polymers, and no studies have been presented specifically comparing the microcellular processing of amorphous and semi-crystalline polymer. Colton (1989) and Colton and Suh (1992) were the first to apply the microcellular processing technique to semi-crystalline polymers where Colton's (1989) analysis concerned namely the nucleation aspects of semi-crystalline polymers. However, the process employed in these works involved the use of high temperature gas saturation and foaming where the temperatures were in excess of the melting point of the neat polymer. The main reason for using such high temperatures was to promote gas saturation since in semi-crystalline polymers the solubility decreases with the degree of crystallinity. Therefore, these previous works would tend to parallel the microcellular processing of amorphous polymers. In contrast, the microcellular processing technique employed in this chapter uses temperatures below the melting point thus processing the polymers in a semi-crystalline state. The resulting microcellular semi-crystalline polymers process in a manner notably different from that of the amorphous polymer. In this particular study, carbon dioxide was selected as the gas. The polymer selected was poly(ethylene terephthalate) (PET) because (1) it cab be processed in either an amorphous or semi-crystalline polymer, and (2) it exhibits some interesting gas dissolution and crystallization behavior.

In the first part of this study (section 5.2), the formation of a gas and semi-crystalline thermoplastic solution is studied in the presence of a crystallizing matrix with particular emphasis on the ultimate effects of crystallinity on microcellular processing. [‡] Polymer/gas solution formation is the precursor to nucleation and growth. In batch processing, solution formation is typically accomplished by placing a polymer sample in a high pressure gas environment resulting in the diffusion of gas into the polymer matrix. For semi-crystalline thermoplastic systems, the solution formation process is notably more complex. In particular, PET crystallizes in the presence of high CO_2 solution concentrations (Baldwin and Suh, 1991 and 1992; Chiou et al., 1985; Kumar and Gebizlioglu, 1991 and 1992; Mizoguchi et al., 1987). The crystallization results in a solution that is relatively difficult to microcellular process requiring relatively high temperatures as compared to amorphous polymer/gas solutions. However, the resulting crystalline foam has a superior microcellular morphology.

In the second part of this study (section 5.3), the microcellular processing characteristics of amorphous and semi-crystalline polymers are compared with respect to each of the three basic processing steps (i.e., polymer/gas solution formation, microcell nucleation, and cell growth), and are analyzed with respect to the relevant process variables and material characteristics. The process variables studied include saturation time, saturation pressure, foaming time, and foaming temperature.

[‡] This work was initially presented at the 1992 American Society of Mechanical Engineers Winter Annual Meeting (Baldwin et al., 1992) and subsequently published by ASME (Baldwin et al., 1994).

5.1 Experimentation

The experimental characterization of amorphous and semi-crystalline PET includes four elements. First, polymer/gas solution formation was studied by dissolution of CO_2 into PET over varying times and gas concentrations. Second, the samples crystallized during gas dissolution were studied to determine the degree of crystallinity using thermal analysis techniques and to determine the crystalline morphology using x-ray scattering techniques. Third, the viscoelastic behavior of polymer/gas solutions was studied using dynamic mechanical analysis to determine the influence of gas concentration and crystallinity. Fourth, microcellular foam processing experiments were performed on both amorphous and semi-crystalline polyesters to determine the effects of the major process variables on the cell morphology.

Materials

Three different PET resins were studied during the course of this investigation. A PET homopolymer (subsequently referred to as PET †) and a polyolefin modified PET (subsequently referred to as CPET) were supplied by Unitika Co. Ltd. in the form of 0.4 mm thick extruded sheets. The Unitika PET samples were experimentally processed in an as-received condition. The third PET resin was supplied by the Eastman Chemical Co. in pellet form. The Eastman PET was extruded, according to manufacturers specifications, into 0.6 mm thick sheets having a melt stretch ratio of approximately 1.5 to 1. All Eastman PET samples were experimentally processed in an as-processed condition and are subsequently referred to as K-PET. While the polyester samples were not annealed prior to experimental processing, it is believed that some degree of molecular relaxation occurred during the gas dissolution process due to the plasticizing effect of the gas as discussed in the following sections. Table 5.1 presents the as-received and as-processed material characteristics of the PET materials.

Gas Dissolution Procedure

The CO_2-induced crystallization of PET was investigated using the following high pressure gas saturation technique. The samples were cleaned, cut into two centimeter squares, and weighed using a Mettler balance model H51AR. Next, the samples were placed in a pressure vessel. The pressure vessel was then charged with the saturation gas, 98% pure carbon dioxide, to a constant saturation pressure (reported in the experimental

---

† The abbreviation PET will also be used to refer generally to all thermoplastic polyesters studied. The usage should be clear from the context.

plots) using a Matheson model 3-320 pressure regulator. The pressure regulator maintained isobaric conditions throughout sample saturation, and the samples were maintained at room-temperature during saturation (i.e., approximately constant at 20 °C). Once the required saturation time (reported in the experimental plots) was reached, the pressure vessel was discharged, the samples removed, cleaned, and weighed within a time reported as the release time.

Table 5.1: The as-received and as-processed material characteristics for the thermoplastic polyester materials used for experimental samples.

	Material		
Characteristic	Unitika PET	Unitika CPET	Eastman 9921 PET
data symbol	PET	CPET	K-PET
density (g/cm^3)	1.34	1.34	1.34
intrinsic viscosity	0.83	0.79	0.70
molecular weight, M_n	38,000	36,000	23,000
crystallinity (% mass)*	< 2	< 5	< 5
T_g (°C)**	71	73	70
T_m (°C)**	235	238	230
transparency	Clear	Semi-Opaque	Clear
nucleating agent weight percent (polyolefin)	N/A	≈ 0.5 %	N/A
sheet thickness (mm)	0.4	0.4	0.6

* Determined using a DSC analysis with a heat of fusion enthalpy value of 125.6 J/g.

** Determined using an onset value from a DSC analysis with a scan rate of 20 °C/min.

To further study the gas dissolution process, desorption experiments were conducted at room-temperature on amorphous and crystalline (having mass fraction crystallinities of 8 and 28%, respectfully) PET/CO_2 solutions with 7.7% and 6.6% CO_2 by mass, respectfully. The solutions were generated using the high pressure gas saturation technique outlined above. The samples were weighed before and after saturation using the Mettler balance. After saturation, the samples were weighed at various time intervals over a thirty day period. After the thirty day degassing period, the samples had no measurable gas concentration (within a tolerance of 0.05% mass fraction).

Crystallinity Measurement Procedure

To measure the degree of crystallinity due to CO_2 dissolution, the polyester samples were thermally analyzed using a Perkin-Elmer DSC-7 differential scanning calorimeter (with a PC series thermal analyzer) at a 20 °C/minute scan rate. Prior to analysis, the PET samples were allowed to desorb gas for at least 30 days. The desorption experiments run on the PET/CO_2 systems verified that sufficient time was allowed for the samples to completely degas prior to analysis. The desorption experiments indicated that a thirty day desorption period is sufficiently long to allow all of the measurable gas concentration (within a tolerance of 0.05% mass fraction) to desorb from the sheets. The effects of any trace gas concentration on the DSC scans was not considered in this study; however, it is expected any trace amount would have little influence on the analysis data due to the small amount in question. The degree of crystallinity reported is a mass fraction relative to a maximum PET heat of fusion of 125.6 J/g.

To further verify the CO_2 induced crystallization, wide angle x-ray scattering (WAXS) analysis was performed on Unitika PET samples crystallized using the gas saturation technique outlined above. The WAXS analysis was performed using a Rigaku model RU300 x-ray diffraction analyzer. The PET samples were allowed to desorb gas for 30 days prior to analysis to insure that appreciably all of the initial gas had diffused out of the sample before analysis.

Viscoelastic Behavior Measurements

The viscoelastic behavior characterization of PET/CO_2 solutions was performed using a Seiko Instruments, model DMS-200, dynamic material analyzer (DMA). The DMA was used to measure the dynamic tensile storage modulus, E', and dynamic tensile loss tangent, E'/E", of Unitika PET and PET/CO_2 solutions. The solutions were formed using the technique described above. After determining the CO_2 concentrations, the solutions were analyzed using a dynamic tensile loading over a temperature range from -50 °C to 50 °C. The tests were conducted on 10 mm by 30 mm rectangular test specimens at atmospheric pressure conditions, a frequency of 1 Hz, a temperature ramp rate of 2 °C/minute, a extension amplitude of 30 µm, and a gage length of 20 mm. The 50 °C temperature limit was selected as an upper bound since the samples began to foam at analysis temperatures greater than 50 °C [see Baldwin et al. (1993) for further discussion]. The time between saturation gas pressure release and DMA analysis was held constant at 20 minutes. Based on the desorption experiments conducted at 20 °C for these high concentration PET/CO_2 solutions, an estimated 7.7% of the gas diffuses out of a sample in the twenty minute period prior to analysis. This estimate was formulated using the gas concentration immediately after saturation and the gas concentration after degassing twenty minutes. The amorphous and semi-crystalline PET samples were analyzed using the same DMA technique.

Microcellular Foam Processing Procedure

The microcellular processing experiments used the following procedure. First, a PET/CO_2 solution was formed using the gas saturation procedure outlined above. The time between the pressure vessel discharge and sample foaming was held constant and is reported as the time to foaming. The majority of specimens were foamed, unconstrained, in a glycerin bath controlled at the foaming temperature using a Corning hot plate model PC-300. In a few instances, a temperature controlled hot press (Carver Laboratory Press Model H with Carver Model 49 proportioning platen temperature controllers) was used as a foaming medium. After the foaming time had elapsed, the samples were quenched in a water bath.

The characterization of the foamed samples was accomplished using scanning electron microscope (SEM) micrographs. The SEM samples were prepared by freezing the foam samples in liquid nitrogen and fracturing them. The fractured cross-section was then gold-coated and analyzed in an SEM. The SEM micrographs were then used to measure an average cell diameter or size, D_c, and an average two-dimensional density of cells. This two-dimensional cell density (relative to the foamed material) was then extrapolated into three dimensions. The extrapolated cell density, N_f, represents the average number of cells per unit volume of foamed polymer. Equations (5-1) and (5-2) were then used to calculate the cell density normalized relative to the unfoamed material, ρ_c. In equation (5-1), V_f is the void fraction of the foamed material.

$$V_f = \pi D_c^3 N_f / 6 \qquad (5\text{-}1)$$

$$\rho_c = N_f / (1 - V_f) \qquad (5\text{-}2)$$

5.2 Gas Dissolution and Induced Crystallization in Microcellular Polymer Processing

In this section, a systematic study of the gas dissolution process in semi-crystalline polymers is presented in an attempt to provide further insight and engineering analysis into the roles of gas dissolution with induced crystallization, viscoelastic behavior, and crystallinity in microcellular processing. We have chosen a PET/CO_2 system for study due to the diverse applications of PET as an engineering plastic and the solution's unique gas dissolution and crystallization characteristics. Our analysis includes (1) an experimental characterization of the carbon dioxide-induced crystallization occurring during microcellular polymer processing, (2) an experimental estimation of the viscoelastic behavior of amorphous and semi-crystalline PET/CO_2 solutions, and (3) an experimental investigation of the effects of crystallinity on microcellular processing and the resulting cell morphology.

5.2.1 Background

The phenomenon of solvent-induced crystallization is well known, and is commonly observed during sorption of low molecular weight, interactive penetrants (Desai and Wilkes, 1974; Durning and Russel 1985; Durning et al., 1986; Jameel et al., 1981; Lin and Koenig, 1983; and Moore and Sheldon, 1961). Solvent-induced crystallization involves the sorption and diffusion of an interactive penetrant into the polymer, resulting in plasticization. Concurrent with plasticization is an increase in the rates of polymer chain-segment motions such that crystallization is kinetically feasible through the realignment of the chains. The author and others (Baldwin and Suh, 1991 and 1992; Chiou et al., 1985; Kumar and Gebizlioglu, 1991 and 1992; and Mizoguchi et al., 1987) have observed a similar phenomenon with sorption of gases in various polymer/gas systems, such as carbon dioxide (CO_2) and poly(ethylene terephthalate) (PET). This implies a coupling between gas diffusion, solubility, and polymer crystallization.

Chiou et al. (1985) have reported on the plasticizing effect of CO_2 dissolved in PET and the resulting crystallization. Their results indicate that the presence of CO_2 decreases the glass transition temperature, T_g, and that higher degrees of crystallinity result from longer CO_2 exposure times along with limited data showing the effect of saturation gas pressure. Mizoguchi et al. (1987) have reported on the plasticizing effect of CO_2, on the effect of crystallization resulting from longer CO_2 exposure times, and on increased crystallization rates for PET/CO_2 solutions above T_g compared with thermally crystallized

PET. Baldwin and Suh (1991 and 1992) and Kumar and Gebizlioglu (1991 and 1992) have both reported on the crystallization of PET due to sorption of CO_2 during microcellular processing. Their results show a distinctive knee in the CO_2 mass uptake curve indicating that PET matrix rejects CO_2 during crystallization.

In addition, it is relatively well known that the sorption of vapors and liquids by polymers can result in significant plasticization and the depression of the glass transition temperature (Chiou et al., 1985; Chow, 1980; Condo et al., 1992; Koros and Paul, 1980; Mizoguchi et al., 1987; Wang et al., 1982; Wissinger and Paulaitis, 1987, 1991). However, it is not as widely known that the sorption of gases can also result in the plasticization of polymers since equilibrium gas concentrations are relatively low at moderate gas pressures (Chiou et al., 1985; Condo et al., 1992; Koros and Paul, 1980; Mizoguchi et al., 1987; Wang et al., 1982; Wissinger and Paulaitis, 1987, 1991). In microcellular plastics production, gas concentrations are relatively high, typically seven to ten percent by weight. The result is a gas and polymer solution having a much lower glass transition temperature than the pure homopolymer.

A number of studies have been performed showing the plasticization and glass transition temperature depression resulting from sorption of high pressure gases (Chiou et al., 1985; Koros and Paul, 1980; Mizoguchi et al., 1987; Wang et al., 1982; Wissinger and Paulaitis, 1987, 1991). In these studies, CO_2 was used as the plasticizer in polystyrene (PS), polycarbonate, poly(vinyl chloride), and poly(methyl methacrylate) and its blends with poly(vinylidene fluoride). However, relatively little work has been done on PET/CO_2 systems (Chiou et al., 1985; Mizoguchi et al., 1987).

5.2.2 Results

This investigation of gas dissolution and induced crystallization of microcellular thermoplastics involved three steps. First, the CO_2-induced crystallization of thermoplastic polyesters was quantified through experimentation. Here, the degree of crystallinity as a function of gas saturation time and gas concentration was investigated using differential scanning calorimetry (DSC). In addition, the crystalline microstructure of the PET was verified using wide angle x-ray scattering (WAXS). Second, the viscoelastic behavior of PET/CO_2 solutions was investigated to determine the effects of dissolved CO_2 on the mechanical characteristics of PET, with particular emphasis on comparing amorphous and semi-crystalline polymer/gas systems. Finally, the role crystallinity plays in the microcellular foaming process was studied by producing amorphous and crystalline foams under the same processing conditions and by varying the foaming temperature of the crystalline systems. For consistency, polymers with crystallinities less than or equal to 10% by weight will be considered amorphous, and polymers with crystallinities higher than 10% by weight will be considered crystalline. This classification was selected arbitrarily; however crystallinities are typically greater than 20% for the crystalline polymers and less than 6% for the amorphous polymers.

Figure 5.1 (a) shows the CO_2 uptake for PET and CPET sheets as a function of saturation time, and Figure 5.1 (b) shows the CO_2 uptake for all three PET resins as a function of dimensionless saturation time, Dt/l^2. The mean diffusion coefficient at 20 °C, $D = 8\times10^{-9}$ cm^2/s, was estimated from the time required for half of the CO_2 to be absorbed by the PET. Using a technique outlined by Crank (1975), the mean diffusivity can be estimated from the relation $D = 0.196\ (l^2 / t_{1/2})$ where $t_{1/2}$ is the time required for half of the CO_2 to diffuse into a sheet of thickness $2l$ [i.e., from Figure 5.1 (a), $t_{1/2} = 2.7$ hours]. Note that this diffusion coefficient is eight times larger than that typically reported for PET/CO_2 systems at low gas concentrations. For example, Van Krevelen (1976) reports $D = 1.5\times10^{-9}$ cm^2/s for PET/CO_2 systems at 20 °C, and Koros and Paul (1980) report $D = 1.0\times10^{-9}$ cm^2/s for PET/CO_2 systems at 35 °C. Based on Fick's second law, equation (5-3), the approximate time required for gas diffusion and saturation can be derived and is given by equation (5-4). If the diffusion coefficient is on the order of 10^{-9} cm^2/s, then an approximate lower bound on saturation time for a 0.4 mm sheet is 111 hours.

$$\frac{\partial c}{\partial t} = \nabla\cdot(D\nabla c) \tag{5-3}$$

$$t \approx l^2/D \tag{5-4}$$

Based on the diffusivity estimated from the data of Figure 5.1 (a), $D = 8 \times 10^{-9}$ cm^2/s, an approximate lower bound on the saturation time is 13.9 hours. From the mass uptake data of Figure 5.1 (a) showing a maximum uptake at approximately 12 hours, the stated mean diffusion coefficient seems to be an appropriate estimate for use in this analysis. One possible reason for the higher diffusivity value is the concentration dependence of the diffusivity at temperatures below T_g. Concentration dependent diffusion coefficients have been reported by Koros and Paul (1980) for PET/CO_2 systems. For a CO_2 concentration of 0.0089 kg(CO_2)/kg(PET) (which are an order of magnitude smaller than the maximum concentration in Figure 5.1), Koros and Paul report a diffusivity of 2.0×10^{-9} cm^2/s at 35 °C.

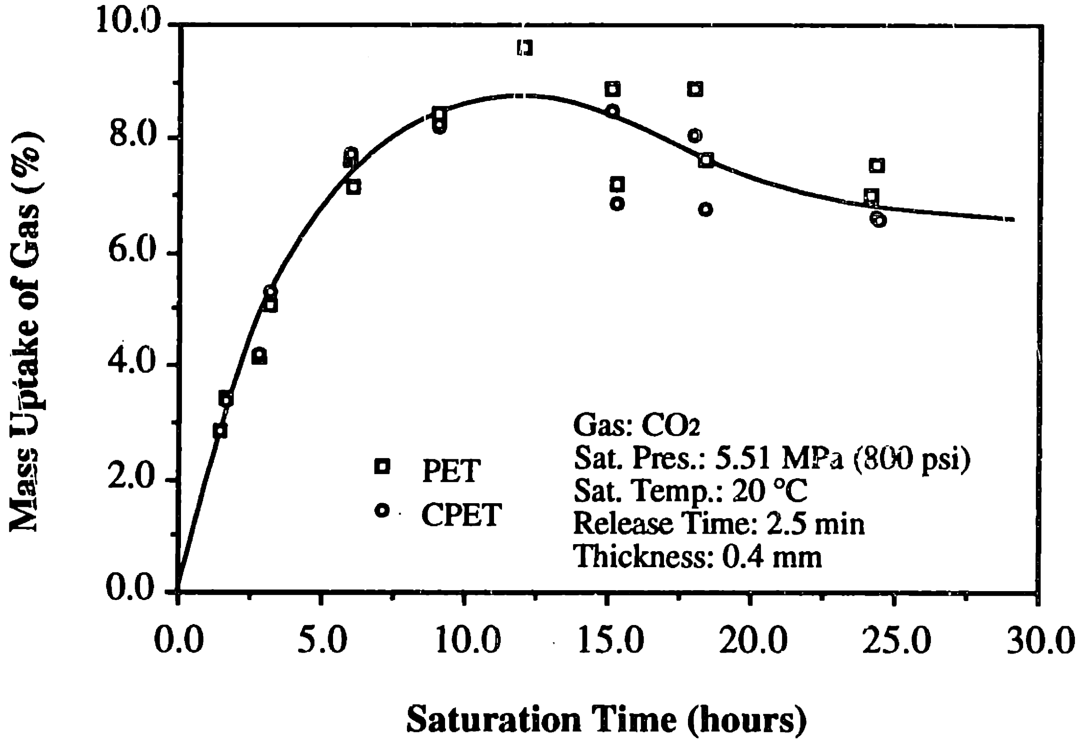

Figure 5.1(a): Mass uptake of CO_2 in 0.4 mm thick Unitika PET and CPET samples versus gas saturation time.

The distinctive knee in the mass uptake curves of Figure 5.1 is a preliminary indication of crystallization and has been observed by Kumar and Gebizlioglu (1991 and 1992). The knee indicates that during CO_2 dissolution the PET sheet rejects CO_2. The rejection of CO_2 is indicative of the fact that the solubility of gas in a polymer is approximately a linear function of crystallinity, and to a first order approximation is given by the relation, $K_{sc} = K_{sa}\ (1-\chi)$, where K_{sc} and K_{sa} are the equilibrium solubility coefficients of crystalline and amorphous polymers, and χ is the mass fraction crystallinity (Van Krevelen, 1976). Thus, as the PET crystallizes in the presence of high CO_2 concentrations, the system solubility decreases, resulting in the rejection of CO_2 from the PET matrix via diffusion. As a result, the difference in mass uptake between the peak and post-peak values in Figure 5.1 (b) can be used to estimate the change in solubility and therefore the change in crystallinity. From Figure 5.1 (b), the maximum gas concentration is 8.5% and occurs at $Dt/l^2 \approx 1$. An average post peak gas concentration falling between $Dt/l^2 = 2$ and 4 is 6.5%. This post-peak range was selected based on Figure 5.2 which indicates that crystallization has completed within this time period. Using the above equation, the PET crystallinity has increased an estimated 23%. The actual change in crystallinity can be calculated from the DSC data of Table 5.1 and Figures 5.2 and 5.3 where the change in crystallinity during gas dissolution with CO_2 at 5.51 MPa (800 psi) is on average 25% for the PET, CPET, and K-PET. Notice that the estimated change in crystallinity errs by only 8 percent. Thus, the relative magnitude of the knee in the mass uptake curve gives a reasonable estimate of the change in crystallinity due to gas dissolution.

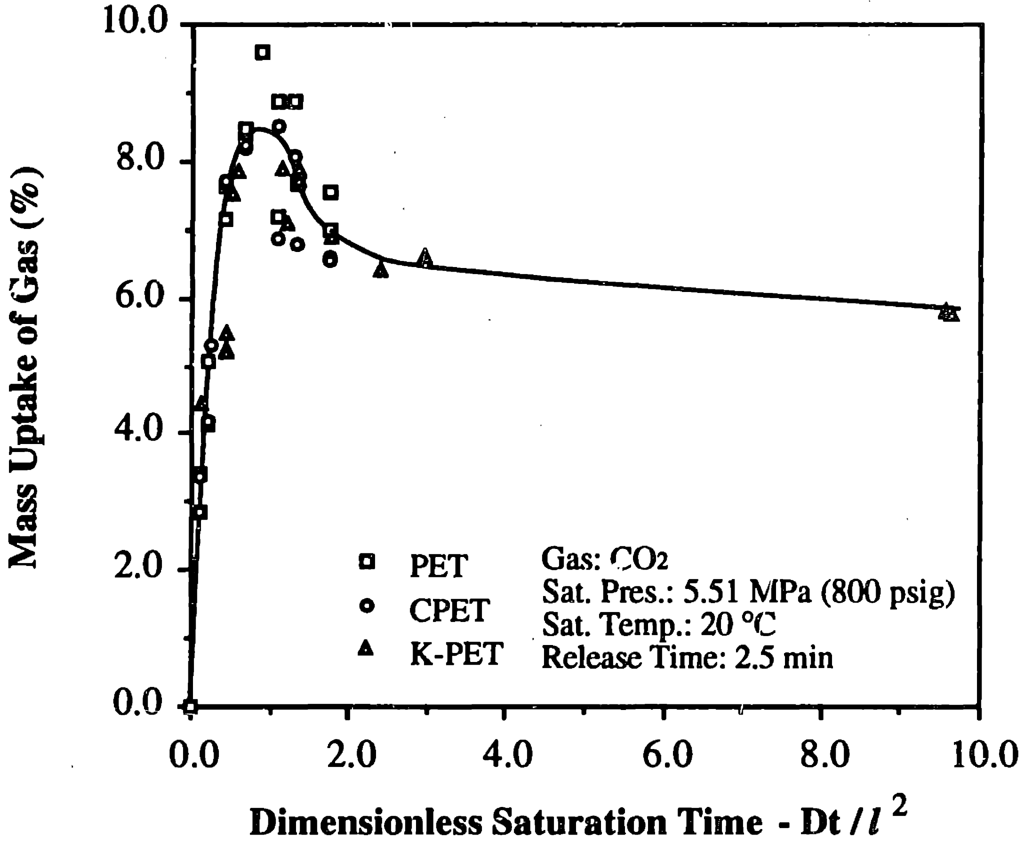

Figure 5.1(b): Mass uptake of CO_2 *in the 0.4 mm thick Unitika PET and CPET samples and in the 0.6 mm thick Eastman PET (K-PET) samples plotted versus dimensionless saturation time. Here an average diffusivity value of* 8×10^{-9} cm^2/s *was used to compute* Dt/l^2*. Note that crystallization begins at approximately* $Dt/l^2 = 0.6$ *as shown in Figure 5.2.*

Figure 5.2 shows the change in crystallinity of the Eastman PET samples as a function of dimensionless CO_2 saturation time. These results are similar to those reported by Kumar and Gebizlioglu (1991 and 1992). The general shape of the crystallization curve has the same form as that for thermally crystallized PET. Figure 5.2 shows that the crystallization begins during the primary gas saturation process, and proceeds after a maximum concentration is reached. This indicates that sufficiently high gas concentrations are required before crystallization can occur within the experimental time scale. It is interesting to note in Figure 5.2 that the CO_2 mass uptake tends to decrease well after the crystallization process has completed. This non-steady state behavior could be a result of the crystalline regions which may tend to slow the diffusion rate of the displaced or rejected gas or a result of molecular relaxation in the amorphous domains which may tend to decrease gas solubility through reductions in free volume between amorphous chains. The specific causes for this behavior have not been ascertained at this point.

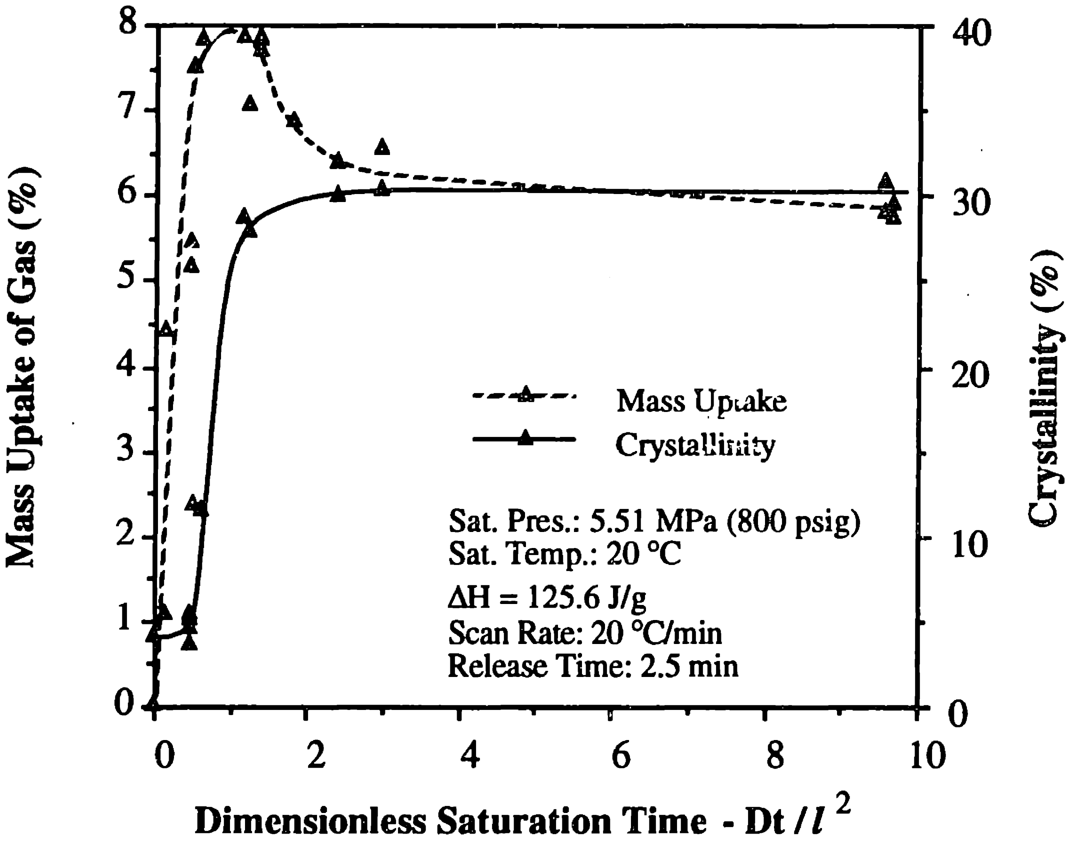

Figure 5.2: Comparison of the CO_2 mass uptake and gas-induced crystallization for the 0.6 mm thick Eastman PET (K-PET) plotted as a function of dimensionless saturation time. Here an average diffusivity value of 8×10^{-9} cm^2/s was used to compute Dt/l^2. Note that crystallization begins at approximately $Dt/l^2 = 0.6$ and approaches a maximum at $Dt/l^2 = 3$.

Figure 5.3 shows the change in crystallinity of the Unitika PET and CPET as a function of gas concentration. The purpose of the analysis was to determine the degree of CO_2-induced crystallization which occurs during the time scale associated with microcellular processing. The gas concentration data reported in Figure 5.3 was obtained by allowing the samples to saturate with gas at a given saturation pressure until they reached a constant mass uptake value (i.e., within an gas concentration measurement variation of ± 2%) suggesting that an approximately uniform gas concentration was reached. The saturation time did not exceed five days in any case. Once the constant mass uptake was reached, the samples were removed and allowed to degas prior to DSC analysis. The crystallinities reported are not necessarily equilibrium values since the kinetics of the crystallization process, particularly at low gas concentrations, are far longer than the experimental time scale (Chiou et al., 1985; Mizoguchi et al., 1987).

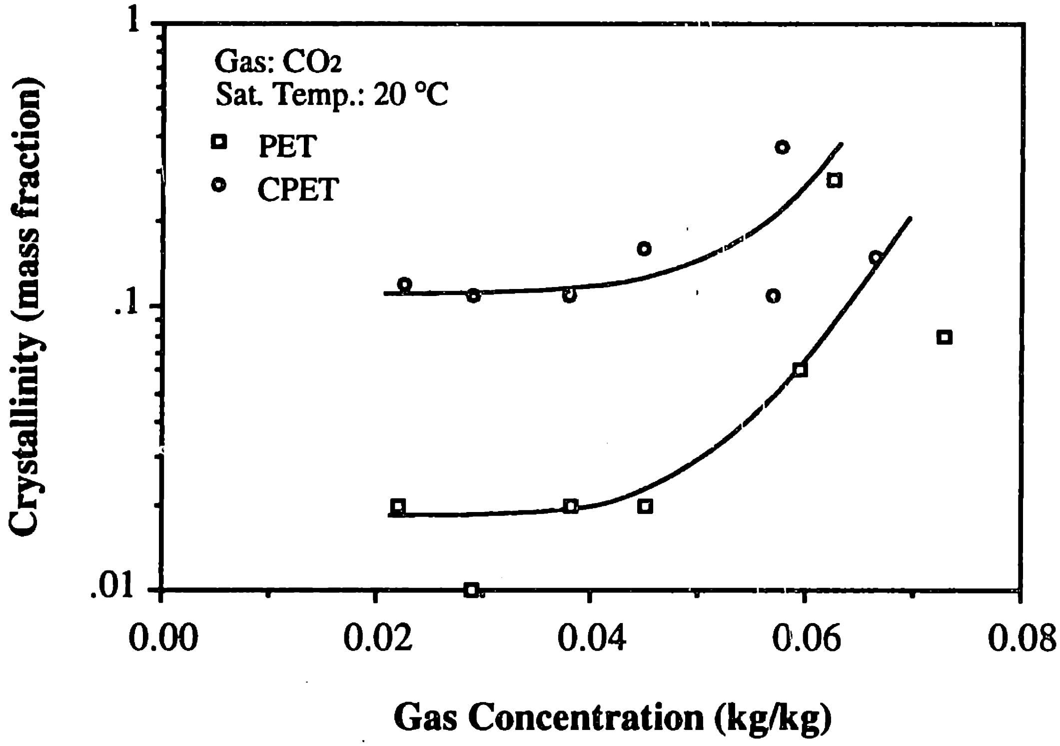

Figure 5.3: Effect of uniform CO_2 concentration on the gas-induced crystallization occurring during microcellular processing of 0.4 mm thick Unitika PET and CPET samples.

Figure 5.3 indicates that a critical gas concentration is necessary for the crystallization kinetics to proceed during the microcellular processing window. Above the critical gas concentration, crystallization kinetics are favorable allowing the polymer chains to realign into crystalline phases. As will be discussed later, the gas-induced crystallization process occurring during microcellular processing can have a great impact on the resulting foam morphologies and change the mechanisms governing cell nucleation and growth.

The CO_2-induced crystallization of PET was further examined by wide angle x-ray scattering (WAXS) analysis yielding results that support the findings of Mizoguchi et al. (1987). Intensity peaks were observed at 2Θ angles of 17, 22.5, and 25.5 degrees corresponding to the reflections from the (100), (010), and $(1\bar{1}0)$ crystallographic planes, respectively, indicating crystalline phases comparable to thermally crystallized PET (Johnson, 1959). The WAXS analysis did not verify any additional intensity peaks corresponding to a second crystalline phase in the CO_2 induced crystallized PET. Note no second crystalline phase was reported by Mizoguchi et al. (1987) for CO_2-induced crystallization of PET or by Durning and Russel (1985) and Durning et al. (1986) for the interactive penetrate-induced crystallization of PET.

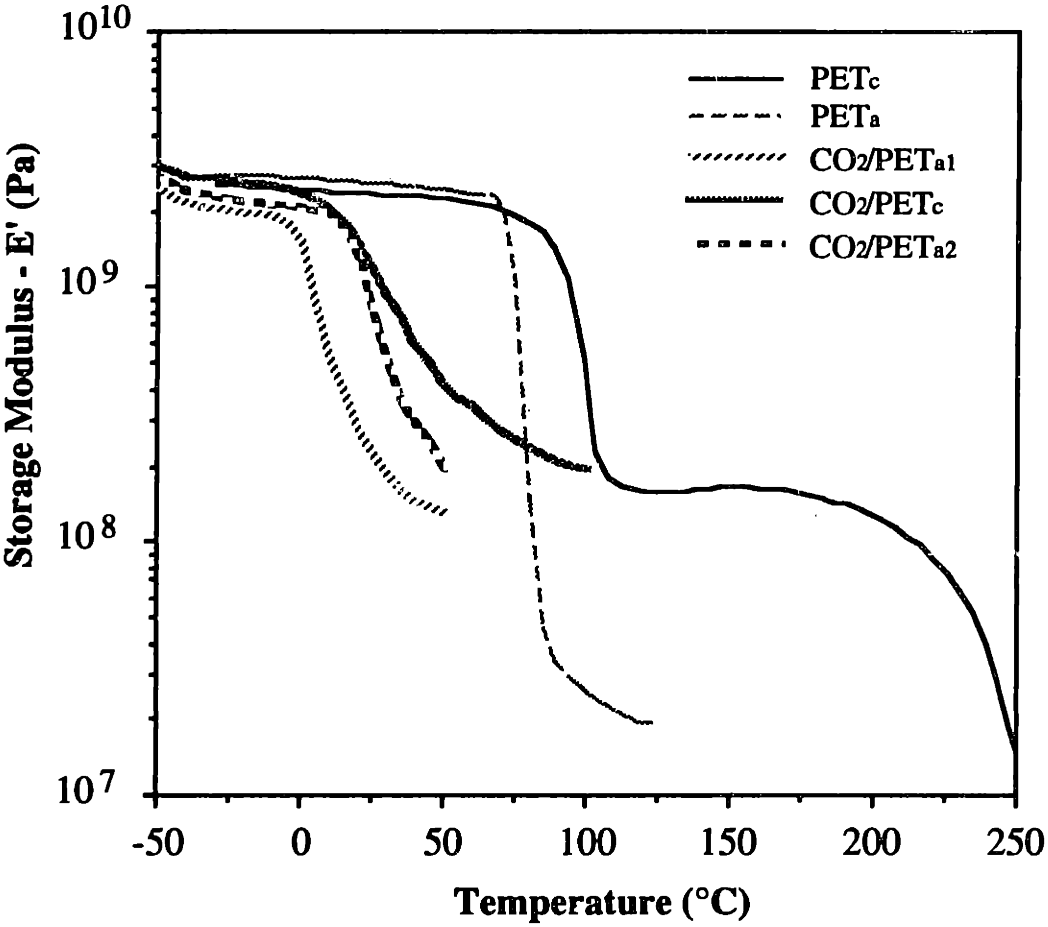

Figure 5.4: Temperature dependence of dynamic tensile storage modulus (E') for the Unitika PET and PET/CO_2 solutions, measured at 1 Hz. See Table 5.2 for sample nomenclature, specifications, and measured characteristics.

Figure 5.4 shows the storage modulus, E', for both amorphous and crystalline PET and PET/CO_2 solutions over varying temperatures measured at 1 Hz. Figure 5.5 shows the loss tangent, tan δ = E"/E', for amorphous and crystalline PET and PET/CO_2 solutions measured at 1 Hz. For a relative comparison, we can define the peak temperature of the loss tangent curve as the glass transition temperature, T_g where the correlation with thermal analysis measurements is reasonably good. A summary of the sample nomenclature used in Figures 5.4 and 5.5 is given in Table 5.2 along with a summary of the respective T_gs. In Figure 5.4, the storage modulus of the amorphous PET, PET_a, is not reported above 125 °C since crystallization of the PET sample occur during dynamic mechanical analysis above this temperature. Based on the trends shown in the PET_a curve, it is believed that the storage modulus for the amorphous PET in the rubbery region is on the order of 20 MPa. From desorption experiments for the PET/CO_2 solutions, it is estimated that up to 20% of the initial gas concentration is lost during the total 70 minute DMA analysis time (including post-saturation sample preparation and DMA testing).

Additional viscoelastic data for various amorphous PET/CO_2 solutions is shown in Figures 5.6 and 5.7 measured at 1 Hz (also see Baldwin et al., 1993). Figure 5.6 shows a plot of the relative storage moduli versus temperature for the Unitika PET solutions of Table 5.3, and Figure 5.7 shows a plot of the loss tangent versus temperature. In Figure 5.6, the relative storage modulus is defined as the ratio of the storage modulus to the glassy storage modulus (the storage modulus at -50 °C given in Table 5.3). It is evident from Figures 5.4 through 5.7 that as the gas concentration increases the temperature marking the onset of the transition zone decreases or shifts to the left. This shifting effect indicates a decrease in the glass transition temperature and a plasticization of the polymer due to the dissolved gas.

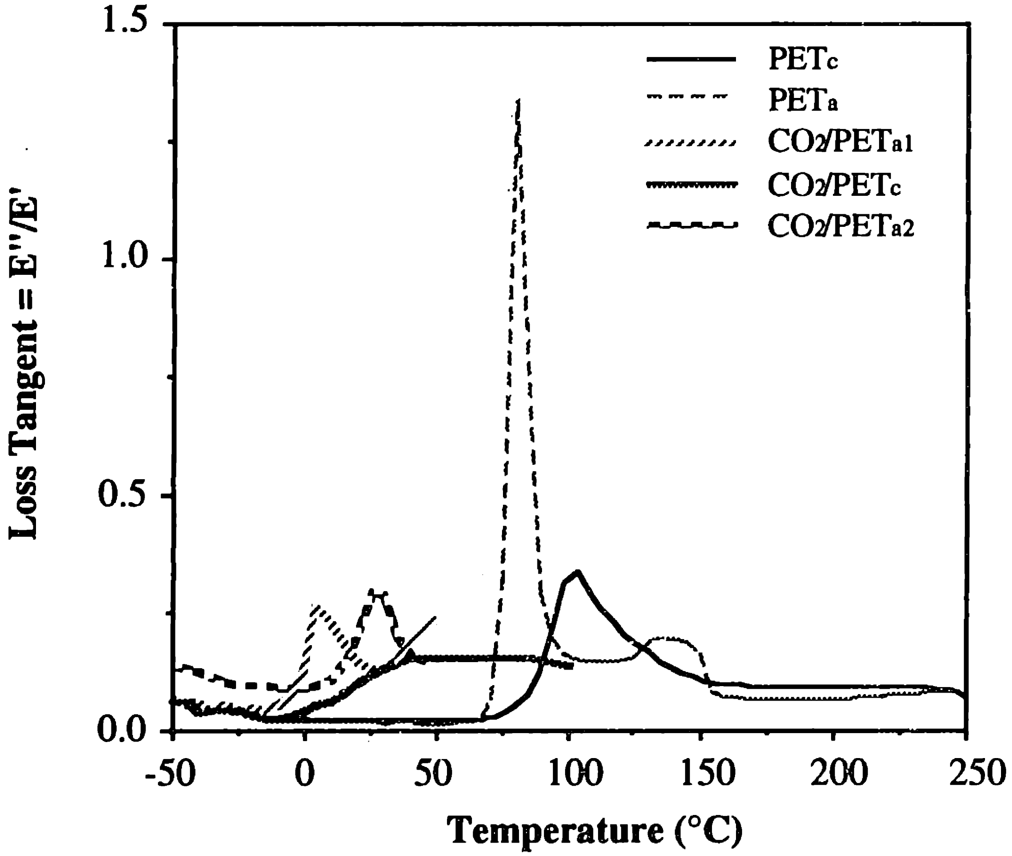

Figure 5.5: Temperature dependence of the dynamic tensile loss tangent (E''/E') for the Unitika PET and PET/CO_2 solutions, measured at 1 Hz. See Table 5.2 for sample nomenclature, specifications, and measured characteristics.

Table 5.2: Nomenclature and glass transition temperatures of viscoelastic test specimens used in Figure 5.4 and 5.5.

Sample	CO_2 Concentration by Weight (%)	Crystallinity (% mass fraction)	T_g (°C)
PET_a	0	< 2	80
PET_c	0	28	105
CO_2/PET_{a1}	9.2	< 6	5
CO_2/PET_{a2}	6.3	< 6	27
CO_2/PET_c	6.6	28	45

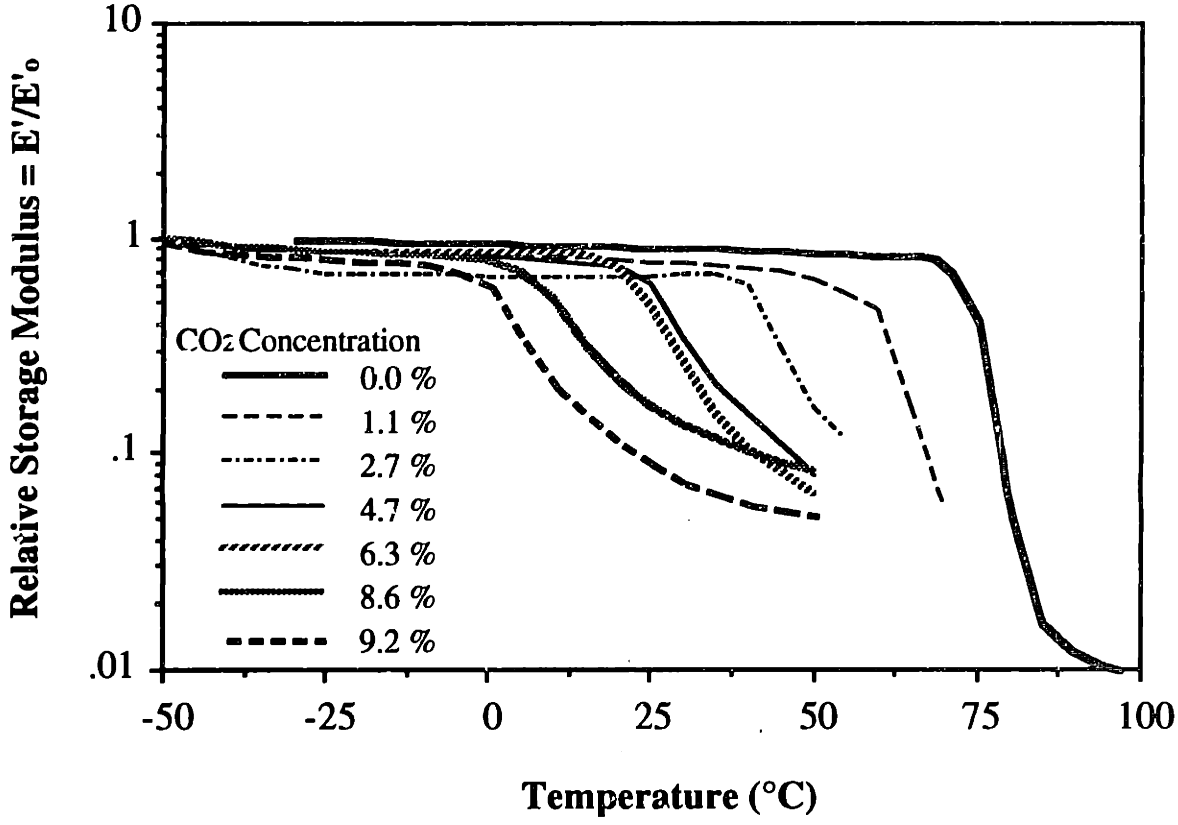

Figure 5.6: Relative storage moduli of PET/CO_2 solutions as a function of temperature (at 1 Hz). See Table 5.3 for the sample characteristics.

In Figure 5.8, the glass transition temperatures of the amorphous PET/CO_2 solutions are plotted as a function of CO_2 concentration. The T_gs represent the temperatures of the loss tangent peaks shown in Figure 5.7. Figure 5.8 clearly exhibits the plasticizing effect of CO_2 dissolved in PET. This figure shows a nearly linear relationship between the glass transition temperature and CO_2 concentration. The plasticizing nature of the gas results primarily from a decrease in the intermolecular forces in the polymer matrix.

The intermolecular forces decrease because the spacing between adjacent polymer chains increases during gas sorption as evidenced by the polymer swelling (Wissinger and Paulaitis, 1987). As the spacing between adjacent chain increases, the intermolecular forces decrease resulting in an increase in molecular mobility and a plasticizing effect. In general, the higher the CO_2 concentration the higher the molecular mobility and the lower the solution T_g.

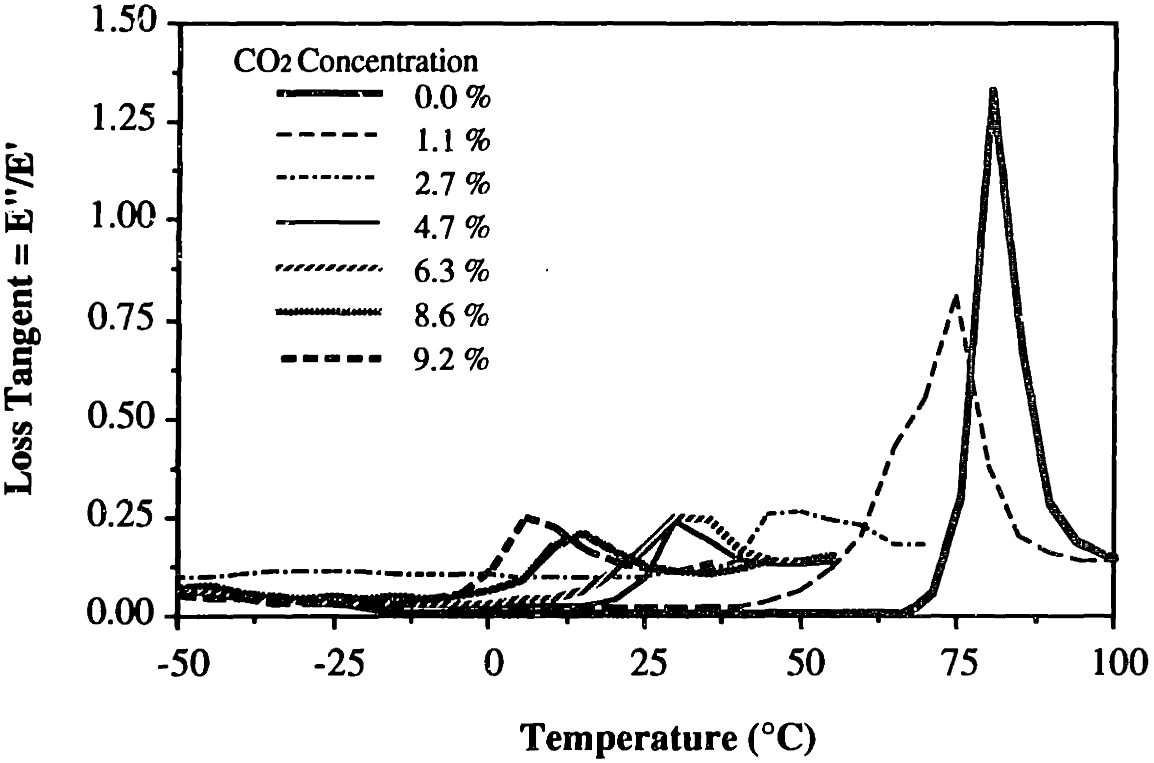

Figure 5.7: Loss tangent of amorphous PET/CO_2 solutions as a function of temperature (at 1 Hz). See Table 5.3 for sample characteristics.

Table 5.3: Gas concentrations and glassy modulus of the amorphous Unitika PET used in Figures 5.6 through 5.8.

Sample	Sat. Pressure (MPa / psi)	Saturation Time (hrs)	Gas Concentration (Weight %)	Storage Modulus @ -50 °C (GPa)
A	5.51 / 800	10	6.3	3.38
B	4.83 / 700	20	9.2	2.45
C	3.45 / 500	48	4.7	2.32
D	2.07 / 300	48	2.7	2.57
E	0.69/ 100	48	1.1	2.40

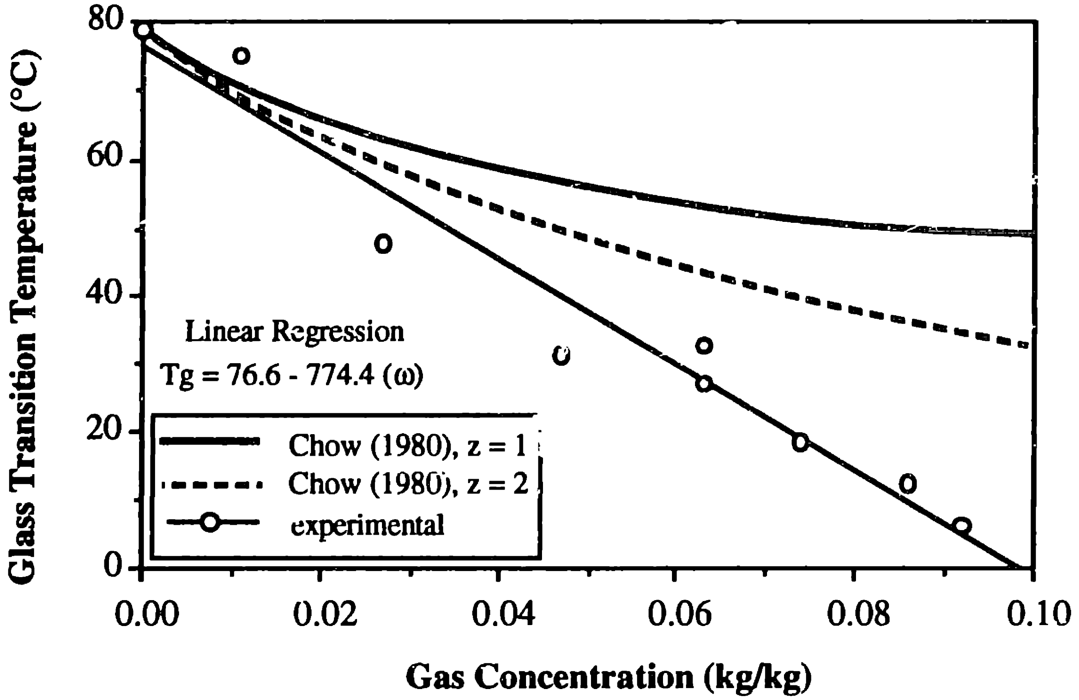

Figure 5.8: Effect of CO_2 concentration on the glass transition temperature of amorphous Unitika PET.

The final set of experimental results presented is intended to demonstrate the role gas-induced crystallization plays in microcellular processing. In order to illustrate the difference between amorphous and semi-crystalline microcellular plastics, Unitika PET and CPET samples with various degrees of crystallinity were processed under identical foaming conditions. Each sample was saturated with a mean CO_2 concentration of 6% by weight and foamed in a glycerin bath at 150 °C for 10 seconds. The PET micrographs are shown in Figure 5.9 (a) and (b) and have mass fraction crystallinities of 6% and 28%, respectively (as measured by DSC analysis). The CPET micrographs are shown in Figure 5.9 (c) and (d) and have mass fraction crystallinities of 10% and 35%, respectively.

In Figures 5.10 and 5.11, the microcellular morphology of semi-crystalline Unitika PET and CPET samples are shown processed at various foaming temperatures. Figure 5.10 shows micrographs of PET samples with crystallinities of 28%, foamed under the conditions of a mean CO_2 concentration of 6.5%, a time to foaming of 5 minutes, a foaming time of 10 seconds, and foaming temperatures from 80 to 230 °C. The fracture surfaces shown in Figure 5.10 are of the center sections of the PET samples. Figure 5.11 shows the cell morphology of 35% crystalline CPET microcellular foams. The processing conditions were a mean gas concentration of 6%, a time to foaming of 5 minutes, a foaming time of 10 seconds, and foaming temperatures from 100 to 200 °C.

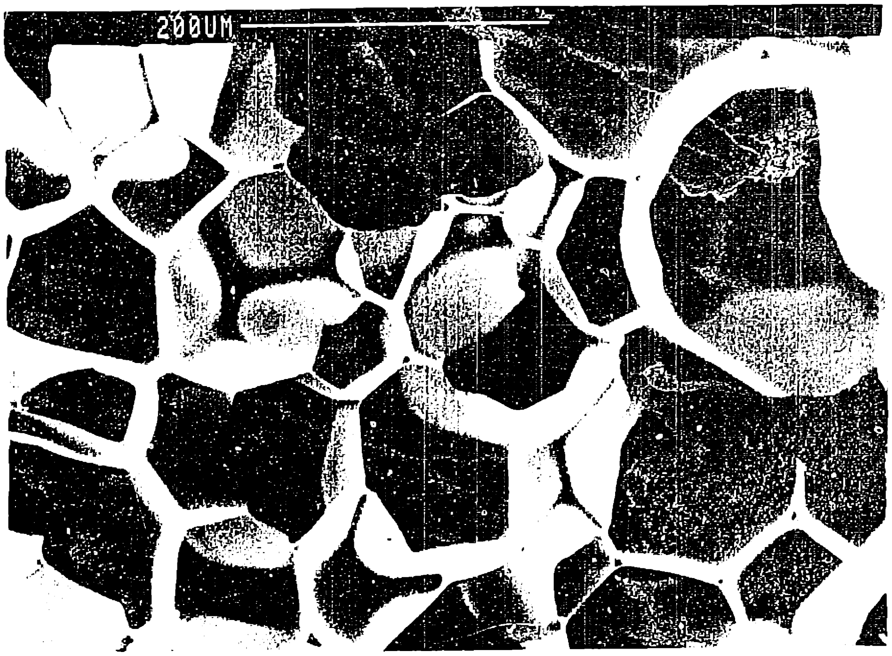

(a) Amorphous PET

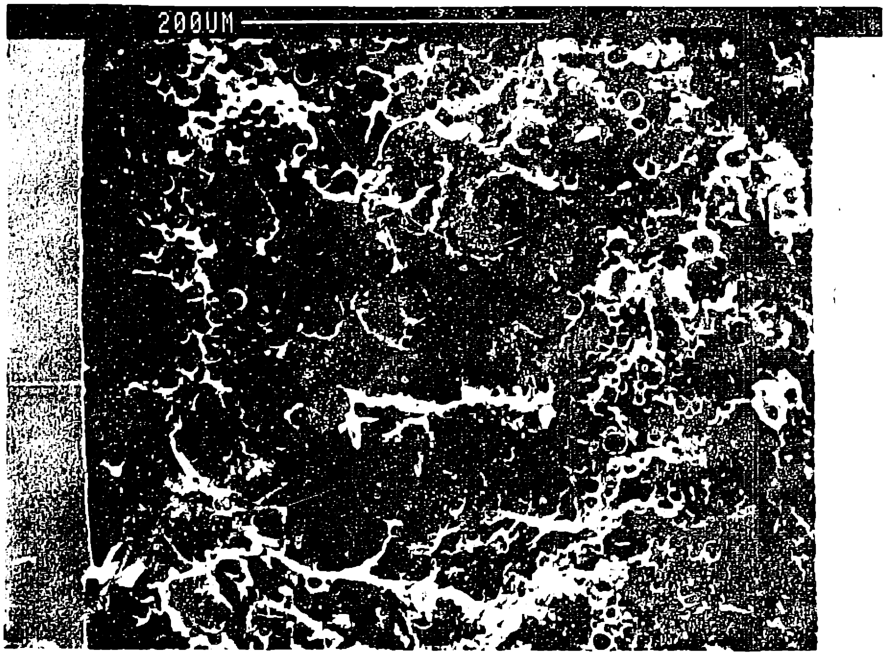

(b) Semi-crystalline PET

Figure 5.9: Micrographs of amorphous and semi-crystalline Unitika PET and CPET microcellular processed under equivalent conditions each saturated with approximately 6% CO_2 by weight.

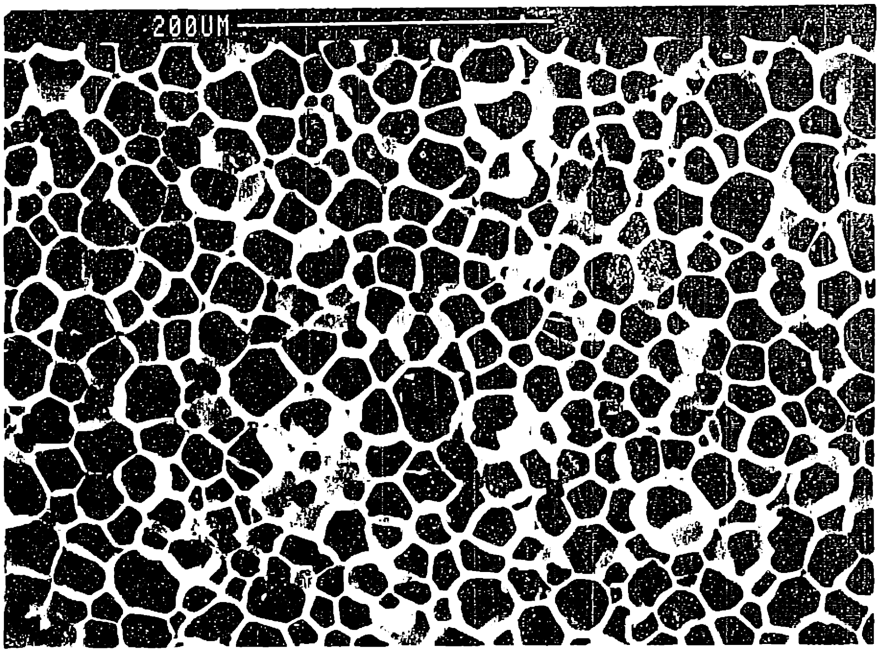

(c) Amorphous CPET

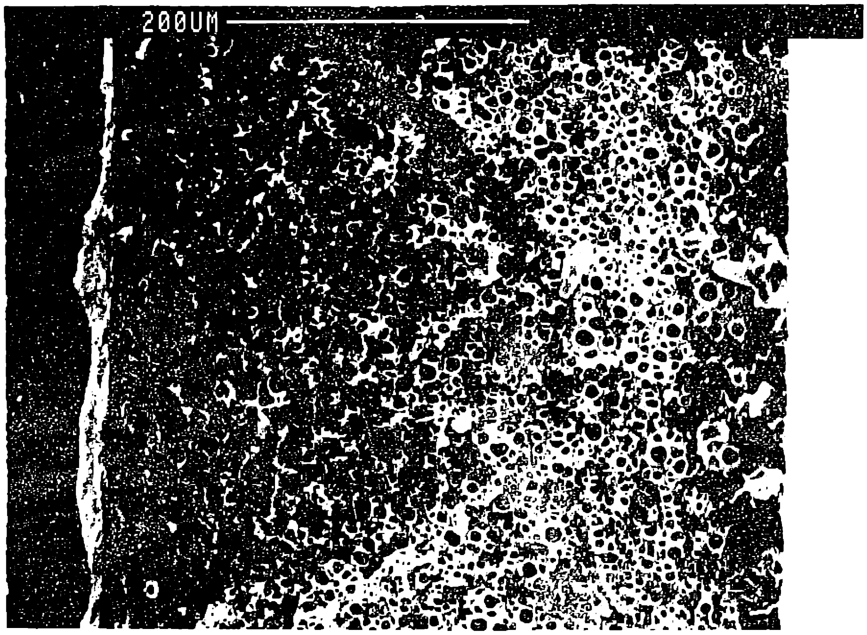

(d) Semi-crystalline CPET

Figure 5.9: Micrographs of amorphous and semi-crystalline Unitika PET and CPET microcellular processed under equivalent conditions each saturated with approximately 6% CO_2 by weight.

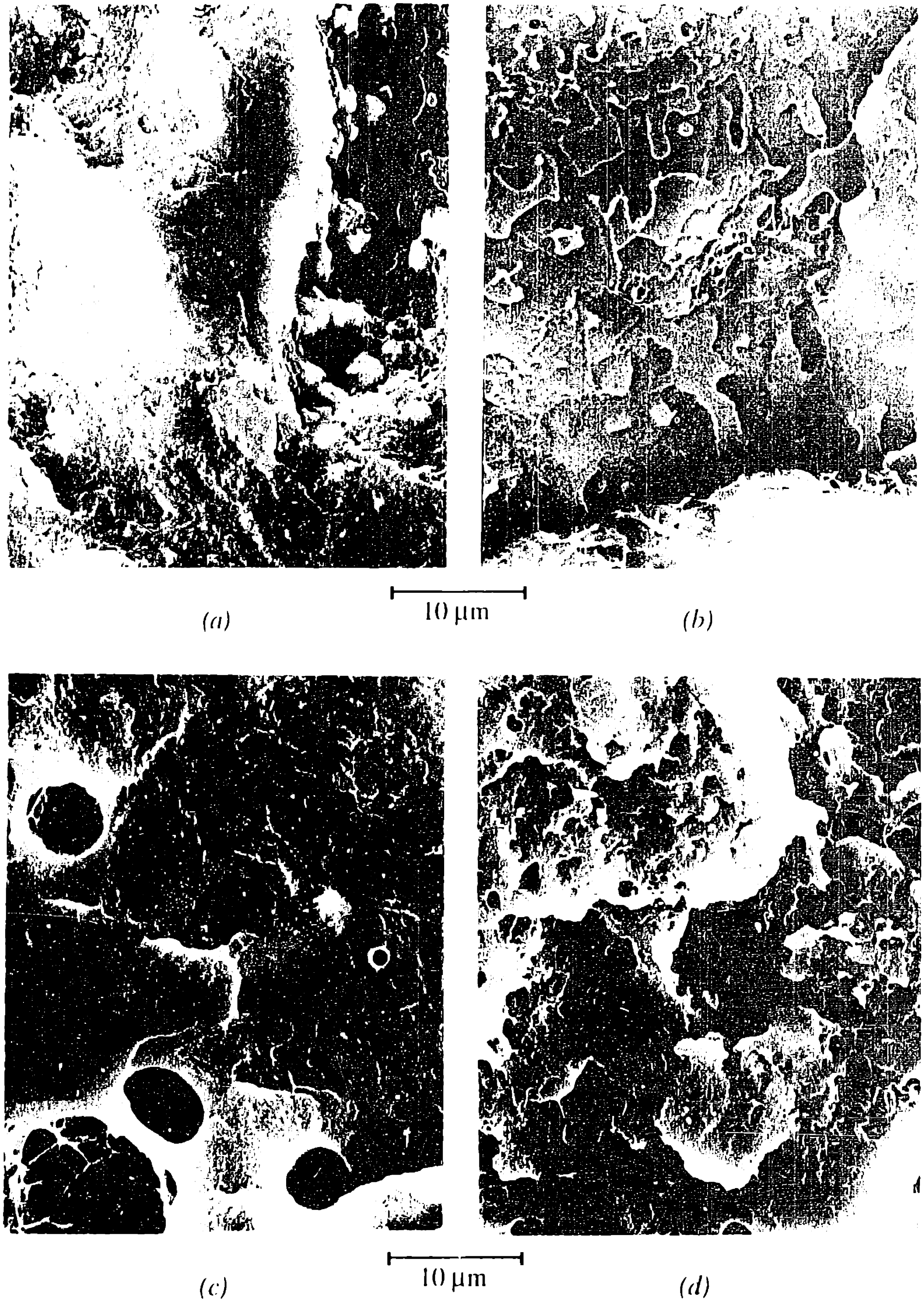

Figure 5.10: Micrographs of semi-crystalline Unitika PET with mass fraction crystallinities of 28% processed at various foaming temperatures. Foaming temperatures were (a) 80°C, (b) 100°C, (c) 125°C, (d) 150°C, (e) 175°C, (f) 200°C, (g) 230°C. See Table 5.4 for cell morphology characteristics.

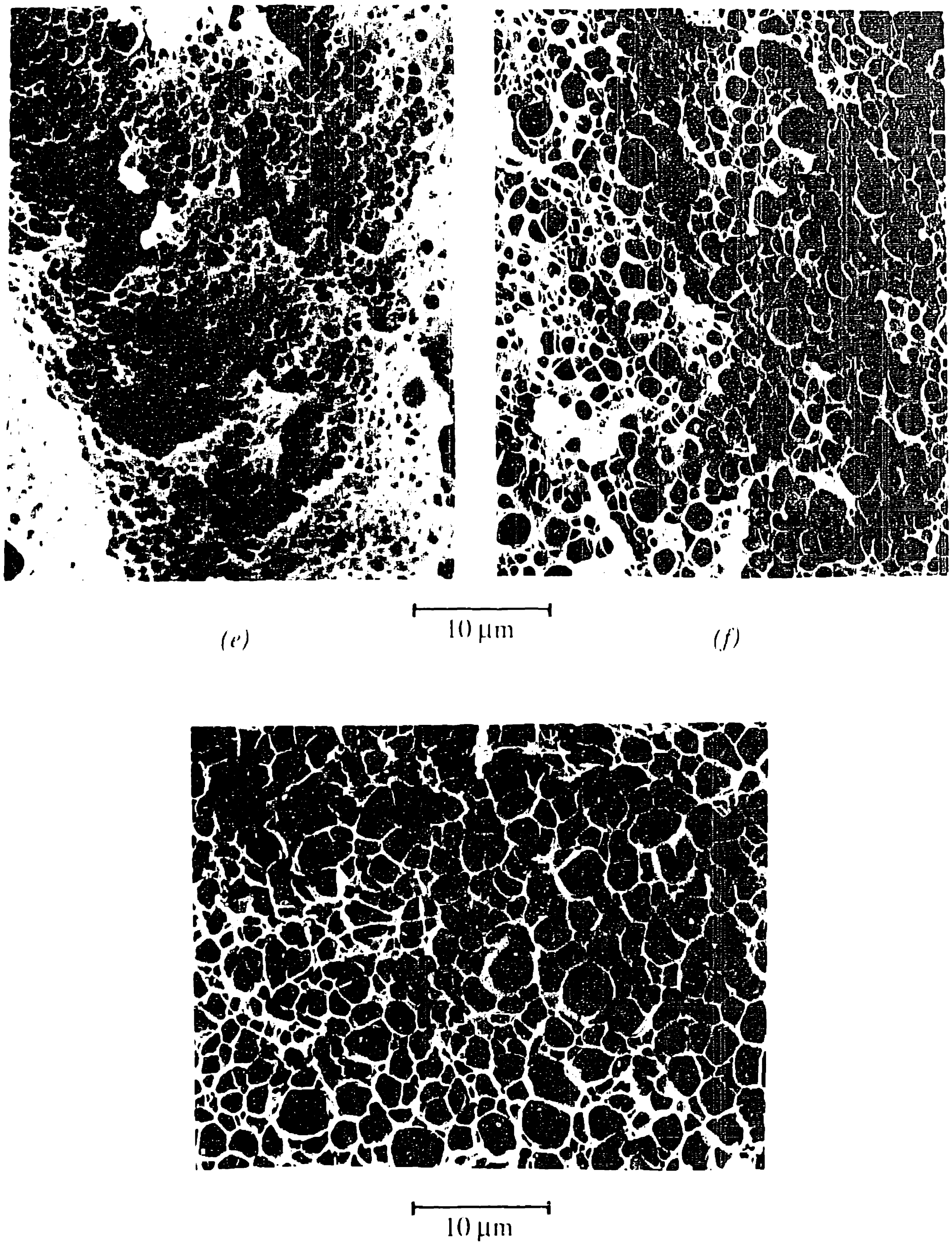

Figure 5.10: Micrographs of semi-crystalline Unitika PET with mass fraction crystallinities of 28% processed at various foaming temperatures. Foaming temperatures were (a) 80°C, (b) 100°C, (c) 125°C, (d) 150°C, (e) 175°C, (f) 200°C, (g) 230°C. See Table 5.4 for cell morphology characteristics.

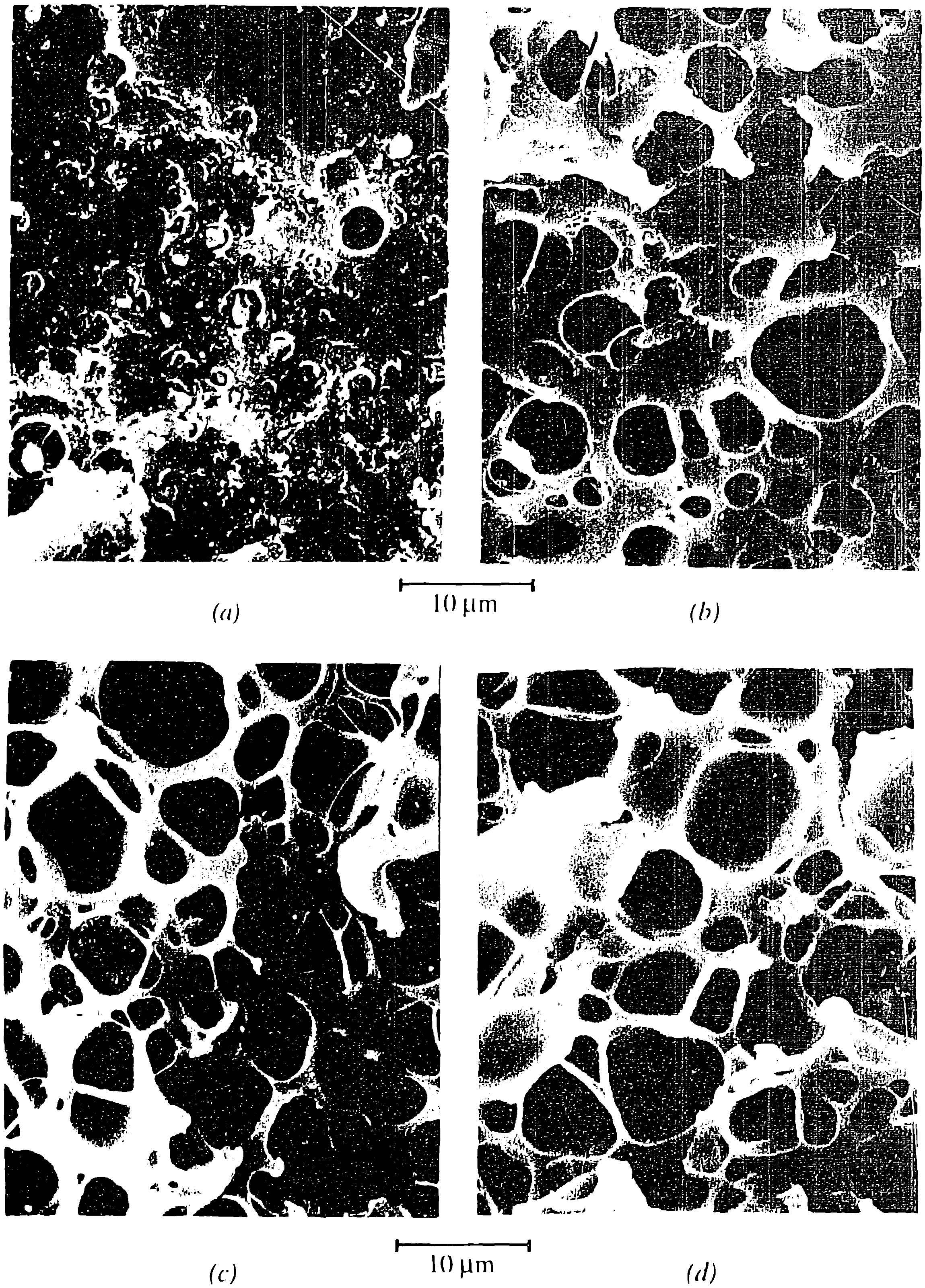

Figure 5.11: Micrographs of semi-crystalline Unitika CPET with mass fraction crystallinities of 35% processed at various foaming temperatures. Foaming temperatures were (a) 100°C, (b) 150°C, (c) 175°C, (d) 200°C. See Table 5.4 for cell morphology characteristics.

Table 5.4: Cell morphology characteristics of the semi-crystalline PET and CPET samples shown in Figures 5.10 and 5.11. Standard deviations are indicated for the cell size values and standard measurement errors are indicated for the cell density values.

	PET (for center sections)		CPET (for cross sections)	
Foaming Temperature (°C)	Cell Size (μm)	Cell Density (cells/cm^3)	Cell Size (μm)	Cell Density (cells/cm^3)
80	0	N/A	-	-
100	0	N/A	1.5 ± 0.7	$9.8 \pm 2 \times 10^9$
125	0	N/A	-	-
150	0.63 ± 0.4	$2.2 \pm 1 \times 10^{11}$	3.0 ± 1	$8.4 \pm 3 \times 10^9$
175	1.0 ± 0.4	$7.4 \pm 3 \times 10^{11}$	4.3 ± 2	$10.0 \pm 5 \times 10^9$
200	1.5 ± 0.5	$3.3 \pm 2 \times 10^{11}$	5.7 ± 2	$11.0 \pm 9 \times 10^9$
230	2.3 ± 0.5	$4.4 \pm 4 \times 10^{11}$	-	-

5.2.3 Discussion

CO_2 Induced PET Crystallization

The data presented in Figure 5.2 indicates that the gas dissolution process and the crystallization process are uncoupled at low temperatures which agrees with the findings of Kumar and Gebizlioglu (1991 and 1992). Figure 5.2 shows that the gas-induced crystallization process does not complete until after the majority of the mass uptake has occurred indicating that the crystallization kinetics lag behind the gas diffusion kinetics. However, at higher temperatures typical of polymer melt processing (i.e., 100 to 200 °C), this may not be the case. When processing at high temperatures, the gas diffusion kinetics and the crystallization kinetics may be on the same time scale. In fact, Mizoguchi et al. (1987) reported higher crystallization rates of PET/CO_2 solutions at temperatures above T_g compared with neat PET. In general, the polymer/gas-solution crystallization kinetics are composed of two parts: thermally-activated crystallization and solvent-activated crystallization.

During the course of microcellular plastics production (e.g., by extrusion or injection molding), the situation may arise where high pressure gas is introduced into a molten crystallizable polymer to form a single phase polymer/gas solution (Park and Suh, 1992; Park et al., 1993). In general, the polymer is plasticized resulting in a lower glass transition temperature (i.e., for Unitika PET with 6.3% dissolved CO_2, T_g decreases 53

°C, see Figures 5.4 and 5.5) and a higher degree of molecular mobility. As the polymer temperature is lowered below the melting point, T_m, crystallization occurs to achieve an energetically favorable state. For polymers with stiff backbone chains (such as PET), thermal crystallization kinetics are typically slow such that amorphous samples can easily be cast from a melt. However, in the presence of high gas concentrations as used in microcellular processing, the crystallization kinetics can be enhanced. Preliminary evidence of this is presented by Mizoguchi et al. (1987), who show increased crystallization rates of PET/CO_2 solutions above T_g. Therefore, during microcellular plastics production of semi-crystalline polymers, crystallization enhanced by gas dissolution may occur during microcellular processing resulting in cellular morphologies vastly different from those expected of the amorphous material.

The CO_2-induced crystallization data presented in Figures 5.1 through 5.3 leads to the conclusion that during the microcellular processing window, detectable crystallization occurs once a critical gas concentration level is reached. Using the data of Figure 5.3, the critical gas concentration found for the PET/CO_2 systems studied was approximately 0.045 kg(CO_2)/kg(PET) at 20 °C. During gas dissolution, the gas molecules occupy the free volume of the polymer, and in some cases, secondary bonding between the gas and polymer molecules may occur. As the gas concentration is increased, the polymer begins to swell corresponding to an increase in the mean spacing between polymer chain segments. Once a critical gas concentration is reached, the mean distance between polymer chain segments reaches a critical value. Above this critical spacing, chain segments have sufficient energy and mobility such that molecular relaxation and/or realignment forming crystalline structures is feasible during the time scale associated with microcellular processing. If secondary bonding is prevalent in the system, an additional energy contribution would be required to sever the secondary bonds and displace the gas molecules prior to molecular alignment and crystallization. Gas molecules remaining in the crystalline domains may tend to act as crystal defects or may play a role in [illegible] new crystalline microstructures.

Viscoelastic Behavior of PET/CO_2 Solutions

The plasticizing effect of gas dissolved in a polymer during microcellular processing is clearly exhibited by Figures 5.4 through 5.8 and has been observed in other studies (Baldwin et al., 1993; Baldwin et al., 1992; Chiou et al., 1985; Mizoguchi et al., 1987). The effect of the gas, as seen in Figure 5.4, is to shift the storage modulus curve along the temperature axis representing a depression in the glass transition temperature. In general, the higher the CO_2 concentration, the lower the solution T_g, and the increased molecular mobility of the PET molecules. An important result of this study, exhibited in Figure 5.4, is that the crystalline PET/CO_2 solution has a higher stiffness in the transition region and a broader transition region relative to a comparable amorphous PET/CO_2 solution. This fact is evidenced by the smaller negative slope of the storage modulus curve in the transition region for the crystalline solutions compared with the amorphous solutions. In contrast, the unmodified crystalline and amorphous curves show similar slopes in the transition region. In the case of the amorphous and crystalline solutions with comparable gas concentrations (i.e., the CO_2/PET_{a2} and CO_2/PET_c curves), the crystalline solution storage modulus (at 50 °C) is over twice that of the amorphous solution. In the next section, it will be shown that this increase in matrix stiffness plays a major role in microcellular processing through its effects on cell growth.

While it is true that CO_2 continuously diffused out of the PET during the DMA analysis, the data of Figures 5.4 through 5.7 gives a good estimation of the effect of the CO_2 and induced crystallization on the polymer/gas solution matrix stiffness. This follows since three quarters of the total testing time of each sample was carried out at temperatures between -50 °C and 20 °C where diffusivities are relatively low. Based on the desorption experiments conducted at 20 °C for high concentration PET/CO_2 solutions, only 19.2% of the gas diffuses out of the polymer over the total 70 minute testing time. A very conservative upper bound on the amount of gas that had diffused out of the sample up to a 20 °C DMA testing temperature is 15.4%. Therefore, when interpreting the results of Figures 5.4 through 5.8, it is important to account for the fact that up to 15% of the gas diffuses out of the samples prior to reaching a testing temperature of 20 °C and on the order of 20% of the gas diffuses out by the time the testing temperature reaches 50 °C. This can be done using a conservative gas concentration estimate over the testing time. For example, the viscoelastic behavior of sample CO_2/PET_c (Figure 5.4) should be interpreted as having a minimum gas concentration during analysis of 5.3%. [§]

Next, it is interesting to compare the glass transition temperature change shown in Figure 5.8 with available theoretical models predicting T_g as a function of a diluent concentration. Chow (1980) has developed a lattice model predicting T_g depressions resulting from the sorption of a diluent. Chow's model estimates the glass transition temperature as follows

---

[§] It should be further noted that a concentration profile exists over the sample thickness due to the surface gas diffusion during testing. Although numerous surface coatings where tied to prevent the degassing, no effective coatings were found.

$$\ln\left(\frac{T_g}{T_{g0}}\right) = \beta\,[(1-\theta)\ln(1-\theta) + \partial\ln\theta] \qquad (5\text{-}5)$$

where $$\theta = \frac{M_p}{z\,M_d}\,\frac{\omega}{1-\omega} \quad \text{and} \quad \beta = \frac{zR}{M_p\,\Delta c_p}\ . \qquad (5\text{-}6)$$

In equations (5-5) and (5-6), T_{g0} is the glass transition temperature of the pure polymer, T_g is the glass transition temperature when the weight fraction of the gas is ω, M_d is the molecular weight of the gas, M_p is the molecular weight of the polymer repeat unit, and Δc_p is the change in specific heat of the polymer at its glass transition temperature. The coordination number z is usually given as one or two, and *R* is the gas constant. For comparison, Figure 5.8 shows the theoretical predictions of equations (5-5) and (5-6) for PET/CO_2 systems with coordination numbers of one and two. It is clear from Figure 5.8 that Chow's model under predicts the T_g depression for CO_2 concentrations above 1%. This contrasts the results of Chiou et al. (1985), who found good experimental agreement with Chow's model for various poly(vinylidene fluoride)/poly(methyl methacrylate) blends containing dissolved CO_2.

Additionally, semi-empirical T_g depression models have been develop by Condo et al. (1992) and Wissinger and Paulaitis (1987, 1991). Both models predict nearly linear T_g depressions with gas concentration, and have been shown to agree well with a polystyrene/CO_2 system and a poly(methyl methacrylate)/CO_2 system, respectively. While the semi-empirical nature of these models makes direct comparisons difficult, the nearly linear variation in T_g with gas concentration is encouraging in that the PET/CO_2 data in Figure 5.8 shows a linear trend.

Effect of Crystallinity on Microcellular PET Foaming

One of the major findings of this work was to determine, the effect crystallinity has on the microcellular foaming process which is clearly illustrated in Figure 5.9. For both the PET homopolymer (PET) and polyolefin modified PET (CPET), the average cell size is smaller and the cell density is larger for the crystalline foams compared to the amorphous foams. In the case of PET, the cell size decreased from 115 μm to 7 μm. In the case of CPET, the cell size decreased from 24 μm to 4.5 μm. Moreover, the polymer crystallization has increased the cell density of the polyester foams. The amorphous PET had a cell density of $\rho_c = 1.1 \times 10^6$ cells/cm^3, and the crystalline PET had a cell density of $\rho_c = 1.0 \times 10^8$ cells/cm^3. For the CPET, the effect is less pronounced where the amorphous foam had $\rho_c = 1.2 \times 10^8$ cells/cm^3 and the crystalline foam had $\rho_c = 3.7 \times 10^9$ cells/cm^3. Since the amorphous and crystalline materials were processed under equivalent foaming conditions, one could conclude that crystallization results in higher cell nucleation densities and smaller cell sizes.

First, consider the effects of additive particles on cell density and the mechanisms governing microcellular nucleation. In general, the amorphous CPET material has a higher cell density over the thickness of the specimen than that of the PET. This results from the polyolefin nucleating particles in the CPET, primarily used for rapid crystallization, which act as heterogeneous nucleation sites for microvoid nucleation. Figure 5.11 (a) shows cells nucleated and grown around small particles that are believed to be polyolefin particles and/or PET crystalline domains. In general, the interface between a polyolefin particle and the PET is a high energy region resulting from interfacial surface effects. In these regions, the Gibbs free energy necessary to nucleate a stable microvoid is less than that for homogeneous nucleation, resulting in the preferential nucleation of microvoids at the interface. If sufficiently large numbers of particles are added, then heterogeneous nucleation can dominate as would seem to be the case for the CPET systems shown in Figure 5.11 (a).

Next, consider the effects of crystallinity on cell density and the mechanisms governing microcellular nucleation. It is believed that the increased cell density of the crystalline foams results from increased heterogeneous nucleation contributions. This follows since the interface between the crystalline and amorphous regions is a higher energy region resulting in a lower free energy barrier for microvoid nucleation and the preferential nucleation of microvoids at these interfaces. The "web" structure within the large cells shown in Figure 5.10 (c) might be characteristic of nucleation occurring at crystalline/amorphous interfaces. Qualitatively, the nucleation results agree with the microcellular nucleation model developed by Colton and Suh (1987) where for heterogeneous systems, the nucleation rate is given by equations (5-7) and (5-8) (see section 3.2.3). Only a qualitative comparison is given here since quantitative predictions have large variances due partly to the uncertainty associated with surface tension values for gas and polymer solutions and for crystalline interfaces. Quantitative comparison with heterogeneous systems having additive particles have been reported by Colton and Suh (1987) and Colton (1989) with some success.

$$N_1 = C_1 f_1 \exp\left(-\Delta G^{*}_{het} / kT\right) \tag{5-7}$$

where $$\Delta G^{*}_{het} = \left(16\,\pi\,\gamma^{3}_{bp} / 3\,\Delta p^{2}\right) f(\theta) \qquad f(\theta) = (2 + \cos\theta)(1 - \cos\theta)^{2} / 4 \tag{5-8}$$

In general, microvoid nucleation may occur both homogeneously and heterogeneously; the relative contributions depending on the processing conditions. For the amorphous PET homopolymer, it is expected that nucleation occurs both homogeneously due to rapid free energy changes and heterogeneously due to inherent impurities. The amorphous CPET is believed to experience primarily heterogeneous nucleation as is exhibited in Figure 5.11 (a) where the majority of cells have nucleated around isolated particles. The crystalline PET homopolymer appears to experience simultaneous homogeneous and heterogeneous nucleation in its amorphous regions similar to its amorphous counterpart and a substantial heterogeneous nucleation component at the amorphous/crystal interfaces. The effects of homogeneous and heterogeneous nucleation are largely additive resulting in the higher cell density of the crystalline PET foams. For the crystalline CPET, heterogeneous nucleation occurs at both the interface of the nucleation particles and the amorphous/crystal interface. From equations (5-7) and (5-8) as the number of heterogeneous nucleation sites, C_1, is increased, the nucleation rate, N_1 is increased. Assuming instantaneous nucleation to a first order approximation, it follows that the total number of nucleated microvoids should increase with crystallization.

Finally, it should be noted that the heterogeneous nucleation phenomenon observed for the semi-crystalline systems may be further influenced by the possible formation of microcavities [as discussed by Mizoguchi et al. (1987)] at the crystalline interfaces in PET systems crystallized using CO_2. Mizoguchi et al. (1987) argue that such microcavities form as the CO_2 diffuses out of the system due to the hindering of volumetric relaxation by the crystalline regions. However, during microcellular processing, the nucleation of voids occurs while the majority of gas remains in solution. Therefore, these potential microcavities may not have a chance to form prior to cell nucleation and may not influence the nucleation process.

At this point, consider the effects of crystallinity on cell size and the mechanisms governing cell growth. It is important to first account for the influence of cell nucleation density on cell size. In general, cell density and cell size follow a cubic relation derivable from equations (5-1) and (5-2) where, for a fixed void fraction, an order of magnitude decrease in cell size increases the cell density by a factor of 10^3. With an increase in cell nucleation density due to crystallization, a respective decrease in cell size is expected. However, the cell morphologies in Figures 5.9, 5.10, and 5.11 exhibit even smaller cell sizes than one would expect or predict from the cell density effects. Notice that the amorphous foams in Figure 5.9 have honeycomb cell structures while the crystalline foams have spherical type cells with relatively large distances, compared with the average cell size, between cells. If crystallinity did not affect cell growth mechanisms, one would expect a honeycomb structure in the crystalline foams. This can be shown using a first order approximation, given by the ratio of the total gas amount available for cell growth and the gas amount required to expand the cells. This ratio predicts that a sufficient solution gas supply is available to expand a given nucleation cell density to a fixed void fraction. Since the semi-crystalline foams have much lower void fractions compared to the amorphous foams, it follows that the cell growth mechanisms are different in these systems. In the following, it will be shown that the decreased cell size of the crystalline foam is due primarily to the increased matrix stiffness associated with crystallization.

In order to study the effect of crystallinity on microcellular processing particularly with respect to cell growth, a series of experiments were conducted where all processing variables were held constant except the foaming temperature resulting in the microcellular PETs shown in Figures 5.10 and 5.11. For a microcellular foaming process having varying temperature, two major mechanisms controlling cell growth and cell size are the rate of gas diffusion into the cells (i.e., diffusion controlled growth) and the physical constraint imposed by the polymer matrix stiffness surrounding the cells (i.e., viscoelastic controlled growth). For the systems studied, a consideration of the relative importance of these factors is presented in the following.

First, consider the possibility of diffusion controlled cell growth being the dominant mechanism experienced during the microcellular processing yielding Figures 5.10 and 5.11. For diffusion controlled cell growth, the growing cells would tend to expand against minimal external constraints since the surrounding polymer matrix has a low stiffness. Therefore, the limiting kinetic process for growth is gas diffusion into the matrix such that the size of the cells is governed by the time allowed for gas diffusion. In this case, an increase in foaming time would result in larger cell sizes since more gas is allowed to diffuse into the cells driving the expansion. To determine if the gas diffusion rate is dominant for the semi-crystalline microcellular foams in Figures 5.10 and 5.11, an upper bound for the gas diffusion time during cell growth must be determined.

An upper bound on the gas diffusion time can be determined using equation (5-4) where the characteristic diffusion length of the gas during microcellular foaming is on the order of half of the average cell size. For the crystalline PET systems studied, the maximum average cell size, taken from Table 5.4, is $D_c \approx 6$ µm, therefore $l \sim D_c/2 = 3$ µm. An estimate of the diffusivity for use in equation (5-4) is given by the values reported by Koros and Paul (1980) for thermally softened PET/CO_2 systems. Since cell growth was not evident at temperatures below 100 °C, a conservative estimate of the diffusivity is given by the value reported by Koros and Paul (1980) at 95 °C, $D = 3.1 \times 10^{-8}$ cm^2/s. An upper bound on the total diffusion time for diffusion cell growth is then on the order of $l^2/D \approx 2.9$ seconds. Moreover, at still higher temperatures, Koros and Paul (1980) report a diffusivity of $D = 8.5 \times 10^{-8}$ cm^2/s (at 115 °C) from which the estimated total diffusion time is one second. From these estimates, it is apparent that the foams in Figures 5.10 and 5.11 were allowed sufficient foaming time for appreciably all of the available solution gas to diffuse into the cells. Therefore, if diffusion controlled cell growth were the dominant mechanism governing the microcellular foams shown in Figures 5.10 and 5.11, one would expect to see a relatively constant cell size with increasing temperature which is not the case in Figures 5.10 and 5.11. It is interesting to note that for comparable amorphous PET foams processed over varying foaming temperatures, a constant cell size has been reported indicating that the amorphous systems experience diffusion controlled cell growth (see section 5.3.1).

It appears that the foaming temperature effect on cell size demonstrated in Figures 5.10 and 5.11 can not be attributed to diffusion controlled cell growth since in each case all of the available solution gas has sufficient time to diffuse into the cells during the allotted foaming time of 10 seconds. To further confirm that foaming times were sufficient to observe any diffusional controlled cell growth, CPET samples were foamed for 20 to 90 seconds. These microcellular CPET samples were found to have no appreciable change in cell morphology compared with the samples foamed for 10 seconds.

Therefore, it would seem that the physical constraint imposed by the polymer matrix stiffness surrounding the cells dominates over the gas diffusion rate on controlling the growth of the cells and the cell size. In systems experiencing constrained cell growth, gas diffusion is the driving force for growth by increasing the gas pressure within the cells. While gas diffusion may occur throughout the cell growth process, it is not the limiting factor dominating the cell growth rate or cell size. In this case, the viscoelastic constraint resulting from the stiff polymer matrix is the dominant mechanism. Here, the large matrix stiffness imposes a stringent boundary condition on the diffusion process by requiring larger gas pressures in the cells for a given amount of expansion. Viscoelastic controlled cell growth would be typified by larger cell sizes as the foaming temperature is increased. This follows since the matrix stiffness typically decreases with temperature. Note that

Figures 5.10 and 5.11 clearly show an increase in cell size with foaming temperature. Therefore, the constraint or viscoelastic behavior of the semi-crystalline systems would seem to govern the cell growth process occurring in these foams due to the boundary condition imposed on the diffusion process. This is a noteworthy result of this study and warrants further discussion.

The cell morphology of Figures 5.10 and 5.11 are summarized in Table 5.4. The foaming behavior exhibited in Figures 5.10 and 5.11 for the semi-crystalline thermoplastic polyesters can be explained primarily by the role in which solution matrix stiffness plays in the cell growth process. Figure 5.10 shows that PET foaming begins at 150 °C, and the cell density is nearly constant at 6×10^{11} cells/cm^3 through foaming temperatures of 230 °C so that cell density effects on cell size are negligible. Moreover, Figure 5.10 shows that the cell size increases with increasing foaming temperature. From Figure 5.4, it is evident that the crystalline solutions have higher storage moduli in the transition region than the amorphous solutions (i.e., approximately twice as large as the amorphous solutions). Furthermore, from the unsaturated PET samples, PET$_a$ and PET$_c$, we can reasonably conclude that the crystalline solutions have an order of magnitude larger storage modulus in the rubbery region compared with the amorphous solutions (i.e., approximately 2×10^7 Pa for the amorphous solutions and 2×10^8 Pa for the crystalline solutions [‡]). The role matrix stiffness plays in cell growth becomes clear when we consider the energy required to expand the cells over a fixed foaming time. During the first instance of foaming while the cell gas pressures increase to overcome the matrix stiffness, cell growth is a diffusion controlled process. In the later stages, cell growth is governed by the viscoelastic nature of the polymer/gas solution. The work required to expand the cell by a fixed amount increases as the matrix stiffness increases. This follows since the expansional work performed by the cell, must overcome the additional stress resulting from a high matrix stiffness.

To qualitatively understand the effects of increased matrix stiffness, we can use equation (5-9), relating stress and strain to the time and temperature dependent relaxation modulus, E_r (an analogous property to the storage modulus E'). For the case of cell growth, σ can be thought of as a hoop stress and ε as a hoop strain. The initial diffusional growth of a cell results in an approximately equal tensile hoop stress, σ around the cell induced from the increased pressure of gas in the cell. The hoop stress is roughly constant

---

[‡] During foaming, the PET samples do not crystallize (i.e., mass fraction crystallinity varied less than 2% before and after microcellular foaming). Therefore, it is expected that the storage modulus for the amorphous CO$_2$/PET solution in the rubbery region is about 2×10^7 Pa.

throughout the later foaming stages since appreciably all of the available solution gas has diffused into the cells. For an increasing foaming temperature, T, and a constant foaming time, t, Figure 5.4 indicates a decrease in the solution matrix stiffness corresponding to a decreasing value of E_T. As E_T decreases under a constant hoop stress, the hoop strain ε must increase corresponding to an increase in cell size with foaming temperature. An increasing cell size with temperature is exhibited in Figure 5.10.

$$\varepsilon = \frac{\sigma}{E_T(t,T)} \tag{5-9}$$

Thus, one could conclude that crystalline PET experiences cell growth governed by the viscoelastic behavior of the polymer/gas solution. These results are contrasted by those for amorphous PET foams presented in section 5.3 which indicate cell growth is diffusion controlled. For amorphous PET foams processed under comparable conditions, fully grown honeycomb cells are achieved within a two second foaming time at foaming temperatures of 150 °C and a change in foaming time does not appreciably change the cell morphology. This is expected for the amorphous PET foams since their cell growth is weakly constrained by the amorphous matrix and governed by the gas diffusion rate. The diffusion controlled growth of the amorphous foams follows since they have an order of magnitude lower storage modulus in the rubbery region compared with the crystalline foams (see Figure 5.4).

The effect of foaming temperature on the crystalline CPET is shown in Figure 5.11, and its cell morphology is summarized in Table 5.4. The crystalline CPET exhibits the same general trends as the crystalline PET homopolymer where the cell density is roughly constant and the cell size increases with foaming temperature. While the specific viscoelastic data for this material was not presented, it is believed that the cell growth process is governed by the matrix stiffness in a similar fashion to the crystalline PET homopolymer.

5.2.4 Summary

One of the critical steps in the production of microcellular polymers is the dissolution of gas into a polymer matrix. In this section, the formation of a gas and semi-crystalline thermoplastic solution was studied in the presence of a crystallizing matrix with particular emphasis on the ultimate effects of crystallinity on microcellular polymer processing. Based on the experimental characterization of gas dissolution with induced crystallization, it appears that the degree of crystallinity can be controlled by the gas saturation time and the gas concentration further supporting the findings of Chiou et al. (1985) and Mizoguchi et al. (1987). Furthermore, this study has revealed that the gas-induced crystallization process tends to occur within the microcellular processing window once a critical gas concentration is reached. For the microcellular processing of PET/CO_2 systems, the critical gas concentration was approximately 0.045 kg(CO_2)/kg(PET) at 20 °C. Therefore, during microcellular processing, it is important to consider the effects of gas-induced crystallization if the gas concentrations achieved during saturation are in excess of the critical concentration. The crystallization resulting from gas dissolution can have a major impact on microcellular processing as summarized below.

Based on the viscoelastic behavior characterization of polymer/gas solutions, this study has found that solutions of crystalline polymer and gas tend to have higher storage moduli compared with their amorphous counterparts. In the transition region at 50 °C, solutions of crystalline PET and CO_2 have a storage modulus twice that of comparable solutions of amorphous PET and CO_2.

For the polymer/gas systems studied, the crystallization and the resulting change in viscoelastic behavior tends to play a major role in microcellular processing. Knowledge of the mechanisms controlling both cell nucleation and cell growth are important for the proper functional design of microcellular processing equipment. In this study, it is found that crystallization influences microcellular processing through its effects on (1) cell nucleation mechanisms resulting in larger cell densities and (2) cell growth mechanisms resulting in smaller cell sizes. The results indicate that polymer crystallization increases the number of microvoids nucleated which is attributed to the additional contributions of heterogeneous nucleation at the amorphous/crystal interfaces. The semi-crystalline PET/CO_2 systems studied showed an increase in cell density of two orders-of-magnitude compared with the amorphous systems while the semi-crystalline CPET/CO_2 systems showed an order-of-magnitude larger cell density. Additionally, this study presents results indicating that the cell growth process of the semi-crystalline PET systems tends to be dominated by the viscoelastic behavior of the PET/CO_2 solution due to the relatively large matrix stiffness associated with the semi-crystalline systems. Moreover, the large matrix stiffness appears to be a major contributor to the smaller cell sizes observed in the semi-crystalline PET resins. In contrast, the amorphous PET foams appear to have cell growth processes that are dominated by the gas diffusion rate due to the lower matrix stiffness associated with these systems.

5.3 Microcellular Processing Comparison of Semi-Crystalline and Amorphous Polymers

From the gas dissolution study presented in the pervious section, it is clear that crystallization can influence microcellular processing through its effects on solution formation, cell nucleation, and cell growth. In this section, the processing of amorphous and semi-crystalline PET is investigated further so as to discern the process phenomena which dominate each step of microcellular processing. The goal of this section is to present a systematic study comparing the microcellular processing of amorphous and semi-crystalline polymers. Specifically, cell nucleation and growth are studied with respect to four major process variables: saturation time, saturation pressure, foaming time, and foaming temperature.

5.3.1 Results

This microcellular processing investigation of amorphous and semi-crystalline polyesters centered around the nucleation and growth stages of batch processing. First, microcell nucleation was studied with respect to the process variables of gas saturation time, gas saturation pressure, foaming time, and foaming temperature. Second, the cell growth process was investigated with respect to the same process variables. Similar to section 5.2, the foams are considered to be amorphous if they have less than 10% crystallinity by mass, and semi-crystalline if they have crystallinities greater than 10%.

Figures 5.12 and 5.16 show the effect of CO_2 saturation time on the cell density and cell size, respectively, of Unitika PET and CPET. These samples correspond to those of Figure 5.1 (a) which were saturated at 20 °C and a pressure of 5.51 MPa (800 psi) over varying saturation times. The plot uses the same dimensionless saturation time, Dt/l^2 as Figure 5.1 (a) where the diffusivity is $D = 8 \times 10^{-9}$ cm^2/s (measured at 20 °C). These samples were foamed five minutes after saturation in a glycerin bath at a foaming temperature of 130 °C for 20 seconds. In the later stages of primary gas saturation, the Unitika PET samples crystallized. As indicated in Figure 5.2, it is expected that crystallization begins at $Dt/l^2 \approx 0.6$ and approaches a maximum at $Dt/l^2 = 1.2$. The resulting microcellular morphology of the semi-crystalline Unitika PET showed a bimodal cell structure having large cells along the surfaces and small cells in the center core while the semi-crystalline Unitika CPET showed a uniform cell structure (Baldwin et al., 1992). The PET's bimodal structure initiated at $Dt/l^2 \approx 0.8$. In Figures 5.12 and 5.16, the cell morphology given for $Dt/l^2 > 0.8$ is of the center sections. Note further that the cell morphologies of the amorphous foams (i.e., for $Dt/l^2 < 0.8$) were uniform over the cross section.

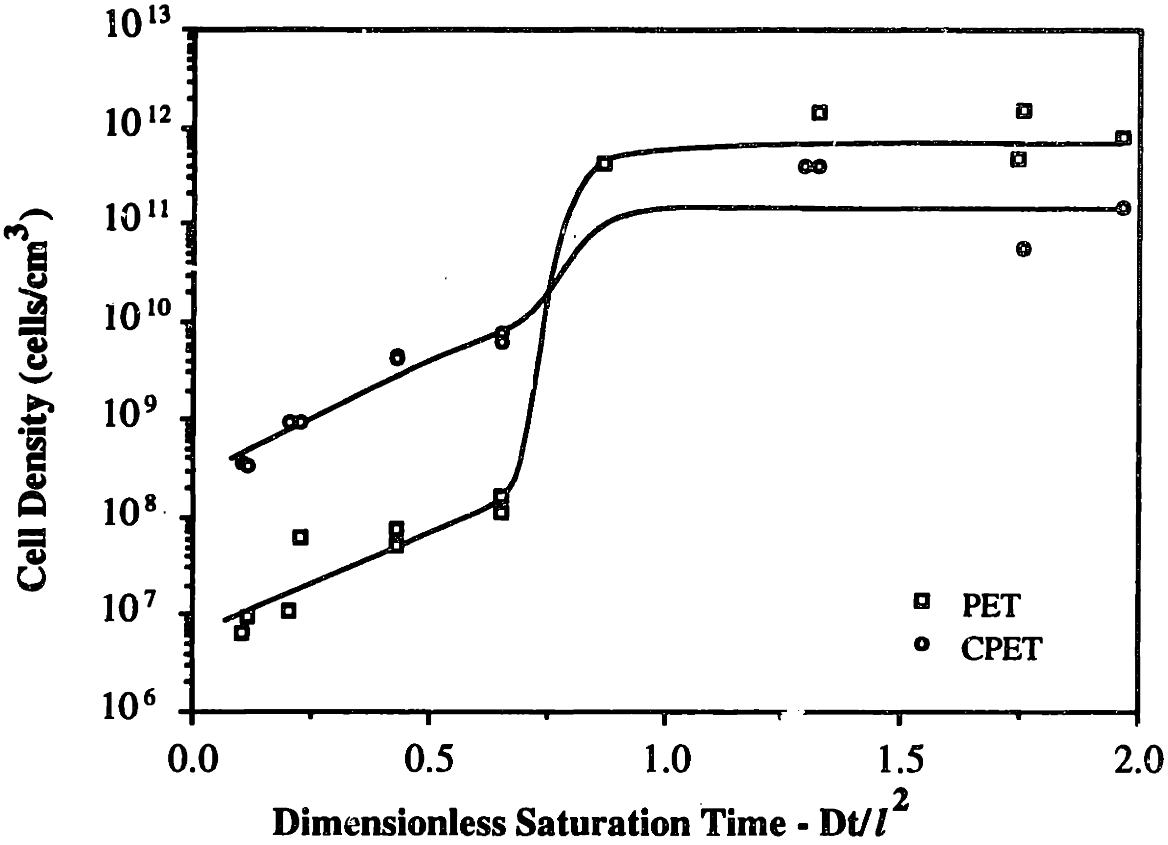

Figure 5.12: Effect of CO_2 saturation time on the cell density of Unitika PET and CPET.

Figures 5.13 and 5.17 show the effect of CO_2 saturation pressure on the cell density and cell size, respectively, of amorphous and semi-crystalline Unitika PET and CPET. The data symbols 'PET' and 'CPET' correspond to the samples of Figure 5.3 which were saturated at 20 °C over various saturation pressures. The samples were largely amorphous except at the highest saturation pressures where crystallization was prevalent. These samples were saturated with CO_2 over sufficient times to reach a constant mass uptake then foamed ten minutes after saturation in a glycerin bath at 150 °C for 10 seconds. As indicated in Figure 5.3, the amorphous samples had begun to crystallize at the higher saturation pressures where at 5.51 MPa the PET and CPET were 28% and 35% crystalline by mass, respectively. For comparison, semi-crystalline PET and CPET samples were prepared by saturating amorphous specimens at 6.20 MPa (900 psi) for 46.5 hours. The samples were then allowed to degas for at least 11 days. This gas dissolution technique resulted in 32% crystalline PET samples and 33% crystalline CPET samples. The crystalline samples were again saturated with CO_2 at various pressures until a constant mass uptake was reached. The samples were then foamed five minutes after saturation in the Carver hot press at 200 °C for 30 seconds. To verify no further crystallization occurred during the second saturation process and the foaming process, DSC scans were taken on various samples and indicated a maximum variation of one percent crystallinity after the second saturation and/or foaming process. Here again, the semi-crystalline Unitika PET samples showed a bimodal cell structure having large cells along the surfaces and small cells in the center core while the CPET samples showed uniform cell structures (Baldwin et al., 1992). Both surface and center cells show the same trends, and the curves in Figures 5.13 and 5.17 show the cell morphology of the center core.

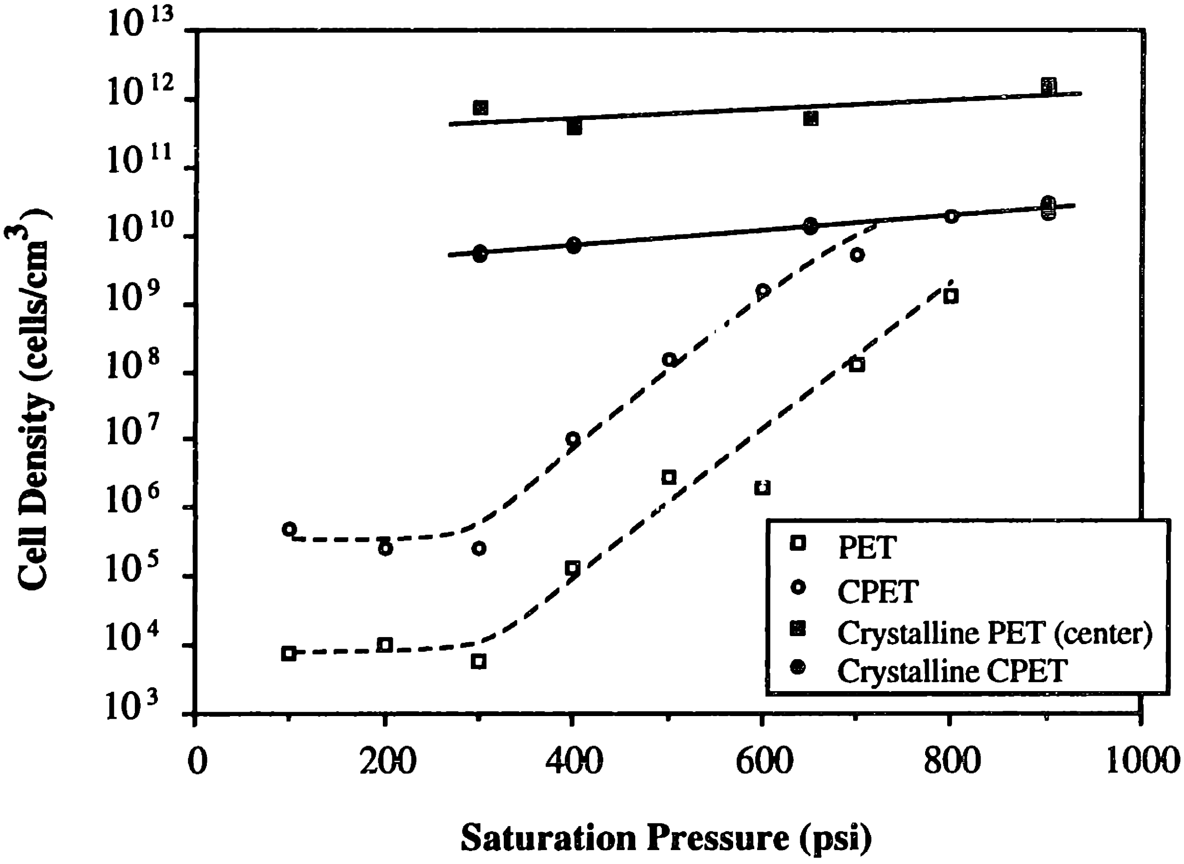

Figure 5.13: Effect of CO_2 saturation pressure on the cell density of amorphous and semi-crystalline Unitika PET and CPET.

Figures 5.14 and 5.18 show the effect of foaming time on the cell density and cell size, respectively, of amorphous Unitika PET and CPET and semi-crystalline CPET. The amorphous PET and CPET resins were saturated with CO_2 for 10 hours at 5.51 MPa (800 psi) and 20 °C such that the crystallinity was less than 10%. The samples were foamed 10 minutes after saturation in a glycerin bath at 150 °C over various foaming times. To form the semi-crystalline CPET samples, amorphous CPET was saturated with CO_2 for 24 hours at 6.20 MPa (900 psi) and 20 °C resulting in CPET samples having 33% crystallinity by mass. These gas saturated semi-crystalline samples were foamed within 5 minutes of the saturation pressure release in the Carver hot press at 200 °C over various foaming times.

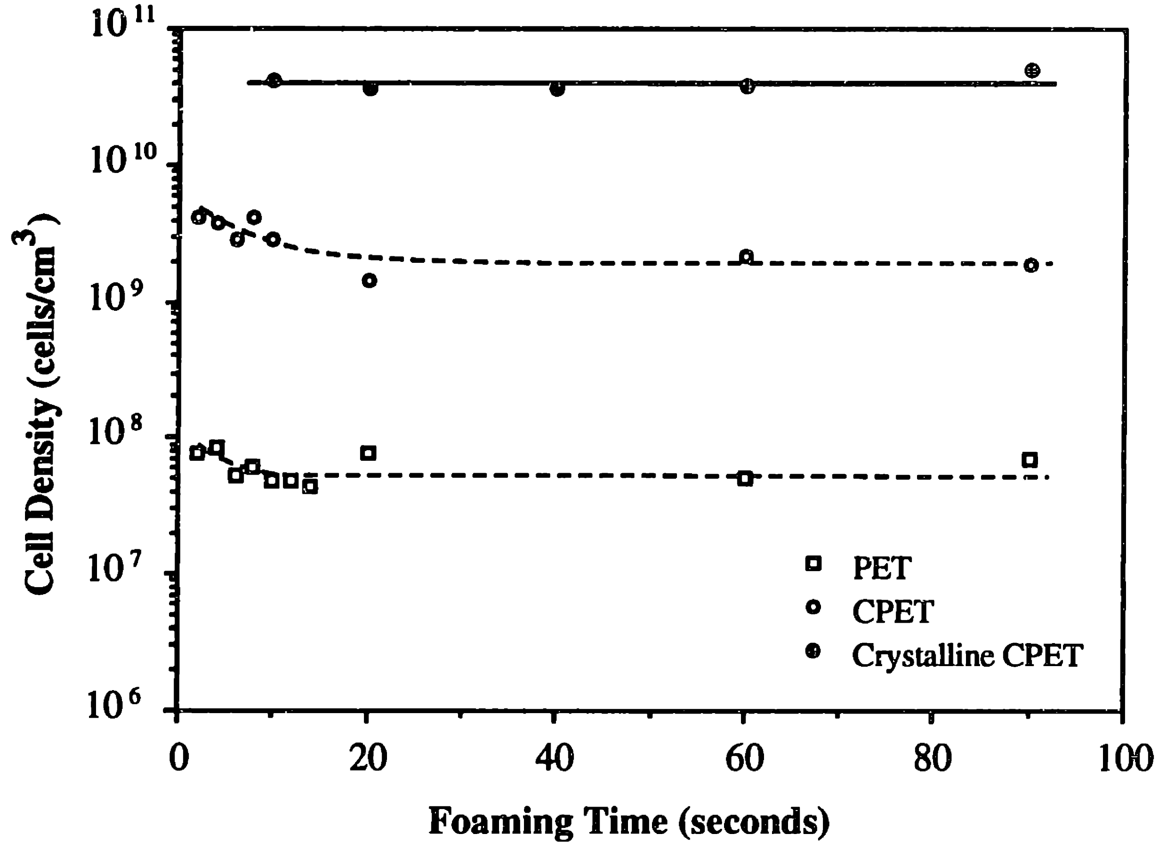

Figure 5.14: Effect of foaming time on the cell density of amorphous and semi-crystalline Unitika PET and CPET processed with CO_2.

Figures 5.15 and 5.19 show the effect of foaming temperature on the cell density and cell size, respectively, of amorphous and semi-crystalline Unitika PET and CPET. The amorphous PET and CPET samples were saturated with CO_2 for 10 hours at 5.51 MPa (800 psi) and 20 °C. The samples were foamed five minutes after saturation in a glycerin bath for 10 seconds over varying foaming temperatures. The semi-crystalline PET and one set of semi-crystalline CPET samples (data symbol CPET-800/10) were formed by saturating amorphous PET and CPET with CO_2 for at least 24 hours at 5.51 MPa (800 psi) and 20 °C resulting in average crystallinities of 28% and 35% for the PET and CPET, respectively. The samples were foamed five minutes after saturation in a glycerin bath for

10 seconds over varying foaming temperatures. Here again, the crystalline Unitika PET was found to have a bimodal cell structure with larger cells on the surface and smaller cells in the center core (Baldwin et al., 1992). In Figures 5.15 and 5.19, this bimodal cell structure is shown using curves corresponding the surface cells and center cells. A second set of crystalline CPET samples (data symbol CPET-900/30) was generated by saturating amorphous CPET with CO_2 for 24 hours at 6.20 MPa (900 psi) and 20 °C resulting in an average crystallinity of 34% by mass. These samples were foamed five minutes after saturation in the Carver hot press for 30 seconds over varying foaming temperatures.

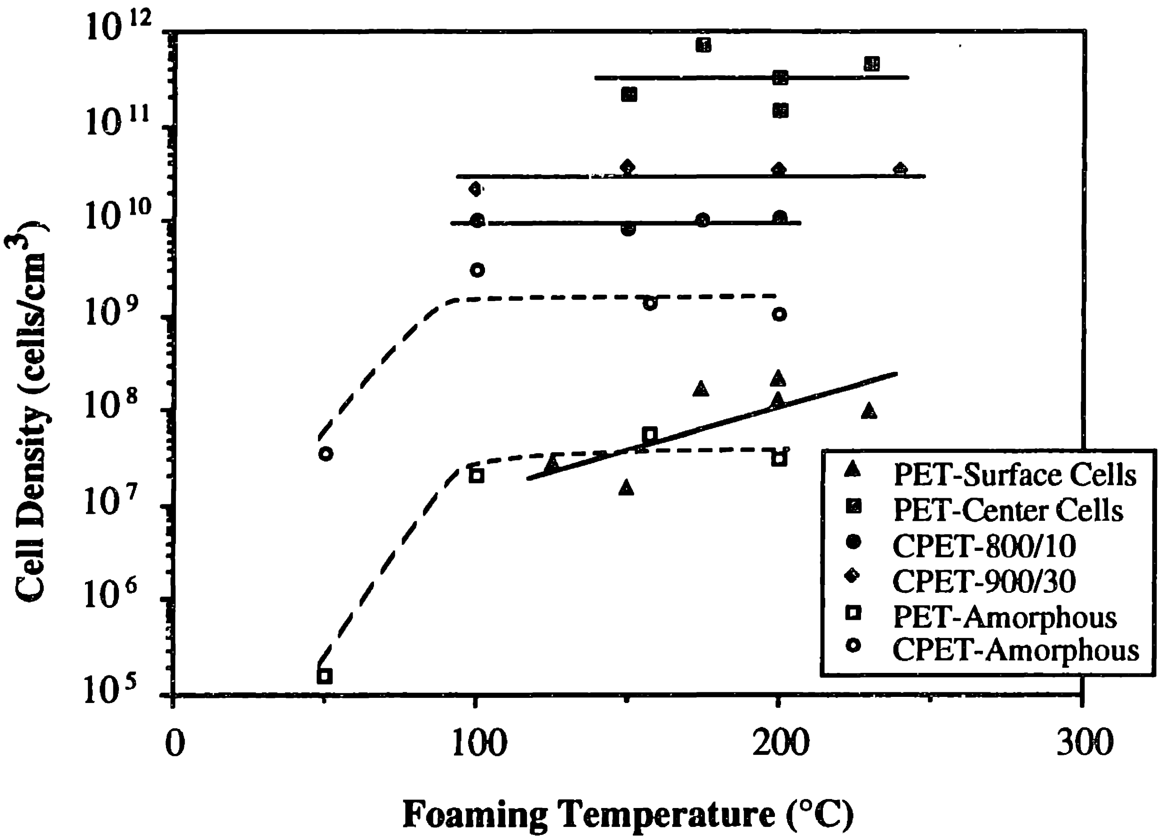

Figure 5.15: Effect of foaming temperature on the cell density of amorphous and semi-crystalline Unitika PET and CPET processed with CO_2.

At this point, some general observations of the PET and CPET foams presented in Figures 5.15 and 5.19 are in order. The amorphous PET and CPET samples foamed at 50 °C which is approximately 20 °C below the neat polymer's glass transition temperature. In some cases, the amorphous PET and CPET samples were observed to foam at room-temperature, some 45 °C below the glass transition temperature. Such low temperature foaming is feasible because of the plasticizing effect of the dissolved CO_2 on the PET matrix which can lower the glass transition temperature by as much as 75 °C (see Figure 5.8, Baldwin et al., 1993). On the other hand, the semi-crystalline PET samples showed no detectable cell structures (i.e., within a resolution of 0.3 μm) when foamed at or below 100 °C. The bimodal cell structure in the semi-crystalline PET was observed only at forming temperatures of 150 °C and higher. Finally, the semi-crystalline CPET samples showed no detectable cell structures when foamed at or below 80 °C.

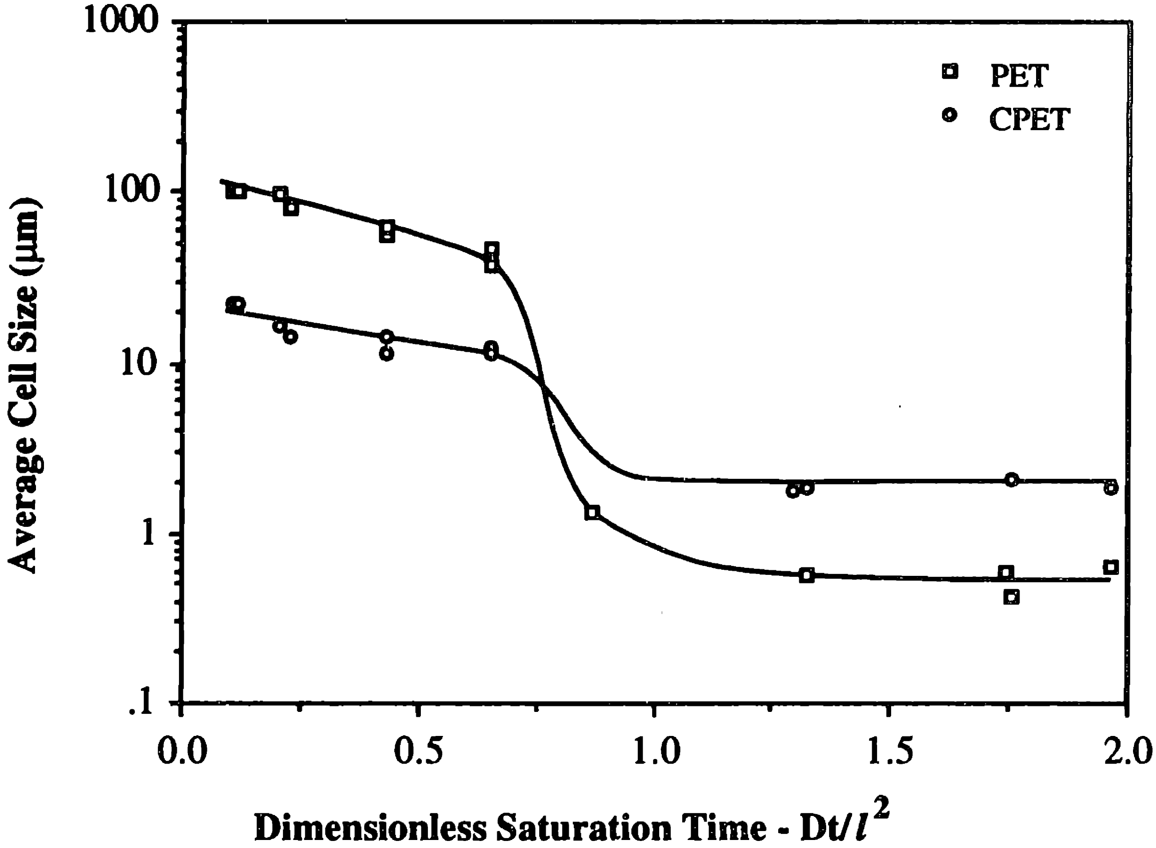

Figure 5.16: Effect of CO_2 saturation time on the cell size of Unitika PET and CPET.

5.3.2 Discussion

The microcellular processing characterization presented in Figures 5.12 through 5.19 shows some very interesting processing differences between the amorphous and semi-crystalline polyesters. Moreover, the results suggest considerably different process design strategies for the amorphous and semi-crystalline systems. In this discussion, the focus will be on the nucleation and cell growth functions of microcellular processing. Each of these process functions will be analyzed with respect to the four major processing variables studied: saturation time, saturation pressure, foaming time, and foaming temperature. In addition, a basic engineering analysis will be used to help identify the dominant physical mechanisms underlying the cell nucleation and growth effects exhibited by the amorphous and semi-crystalline polymers. Finally, the process design implications of the results will be discussed.

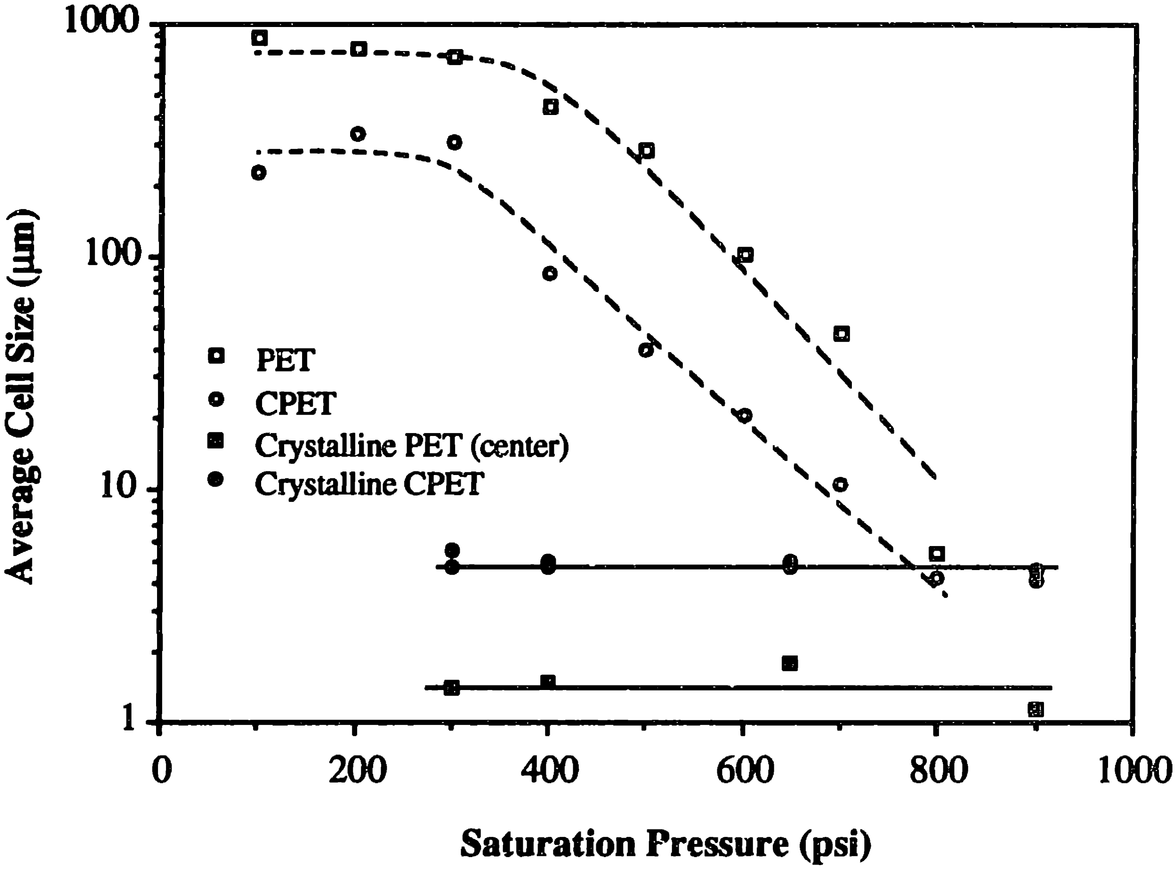

Figure 5.17: Effect of CO_2 saturation pressure on the cell size of amorphous and semi-crystalline Unitika PET and CPET.

Microcell Nucleation

In general, saturation time is a process variable with limited scope namely because uniform cell nucleation is achieved provided that uniform gas concentrations are present. Uniform gas concentrations are achieved only if sufficient gas diffusion time is allowed. Therefore, unless non-uniform cell structures are desired, saturation times selected should be the minimum necessary to achieve an approximately uniform gas concentration. For crystallizable polymers, the solution formation function has the added complexity of a polymer matrix that can crystallize during gas dissolution as discussed in section 5.2. The crystallization process and resulting change in microstructure alter the mechanisms by which cell nucleation and cell growth occur leading to a coupled process design unless the appropriate processing window is selected. Thus, it is important to realize the crystallization potential of the polymer matrix during processing, and to design the process accordingly.

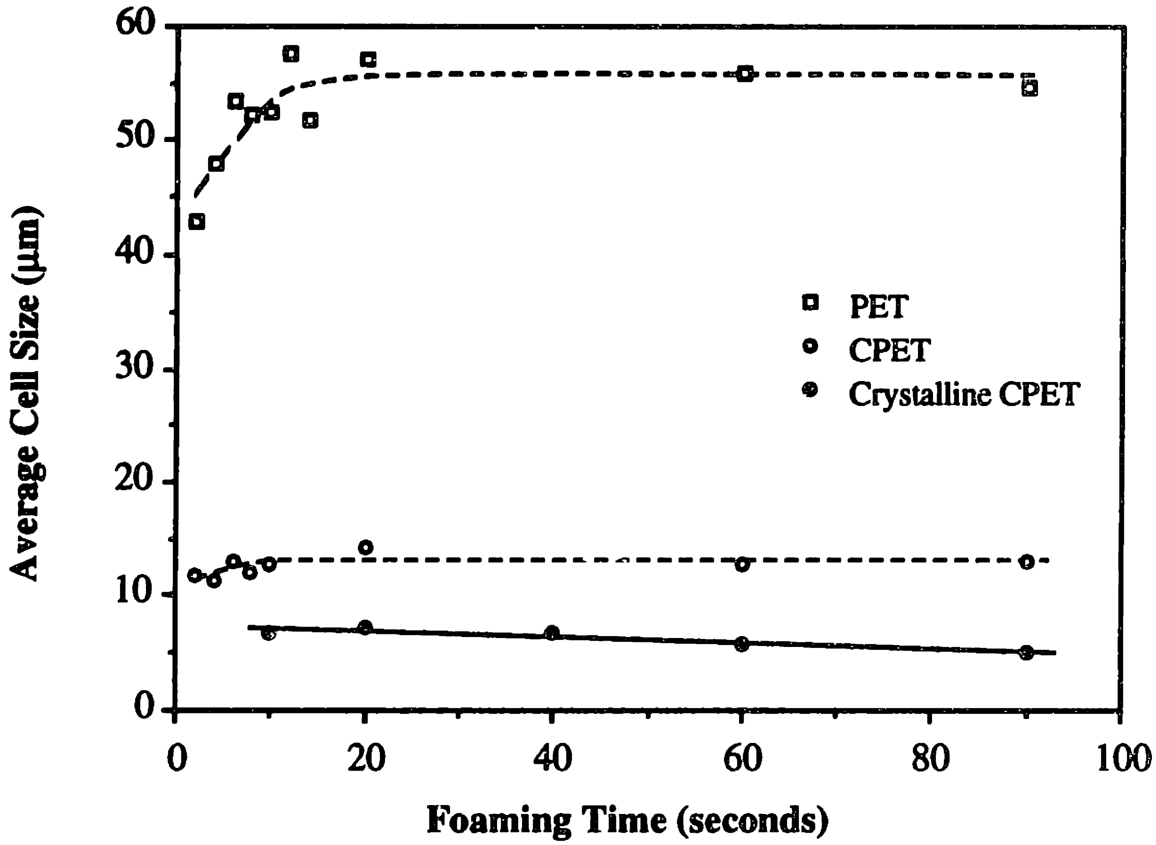

Figure 5.18: Effect of foaming time on the cell size of amorphous and semi-crystalline Unitika PET and CPET processed with CO_2.

Although saturation time is not an effective process variable for controlling cell nucleation or cell growth, the results of Figure 5.12 illustrate some important differences in the nucleation of amorphous and semi-crystalline microcellular foams. Looking first at the amorphous PET and CPET data (i.e., for $Dt/l^2 < 0.8$), it is apparent that both resins have a strong concentration dependence on cell nucleation. This result is expected and follows since the maximum mass uptake of gas is achieved at $Dt/l^2 \approx 1$. The strong concentration dependence seems to indicate considerable homogeneous nucleation contributions and/or the activation of additional nucleation sites at higher gas concentrations. † In addition, the CPET samples show cell densities nearly two orders of magnitude larger than the PET samples. Since the gas concentrations in these PET and CPET samples was comparable [see Figure 5.1(a)], the larger cell density of the amorphous CPET is attributed to a lower surface tension and/or heterogeneous nucleation contributions resulting from the polyolefin modifier. Next, consider the results in Figure 5.12 for the crystallized polymers (i.e., for $Dt/l^2 > 0.8$).

---

† The possible activation of additional nucleation sites could result from matrix swelling and free volume changes accompanying the gas dissolution process.

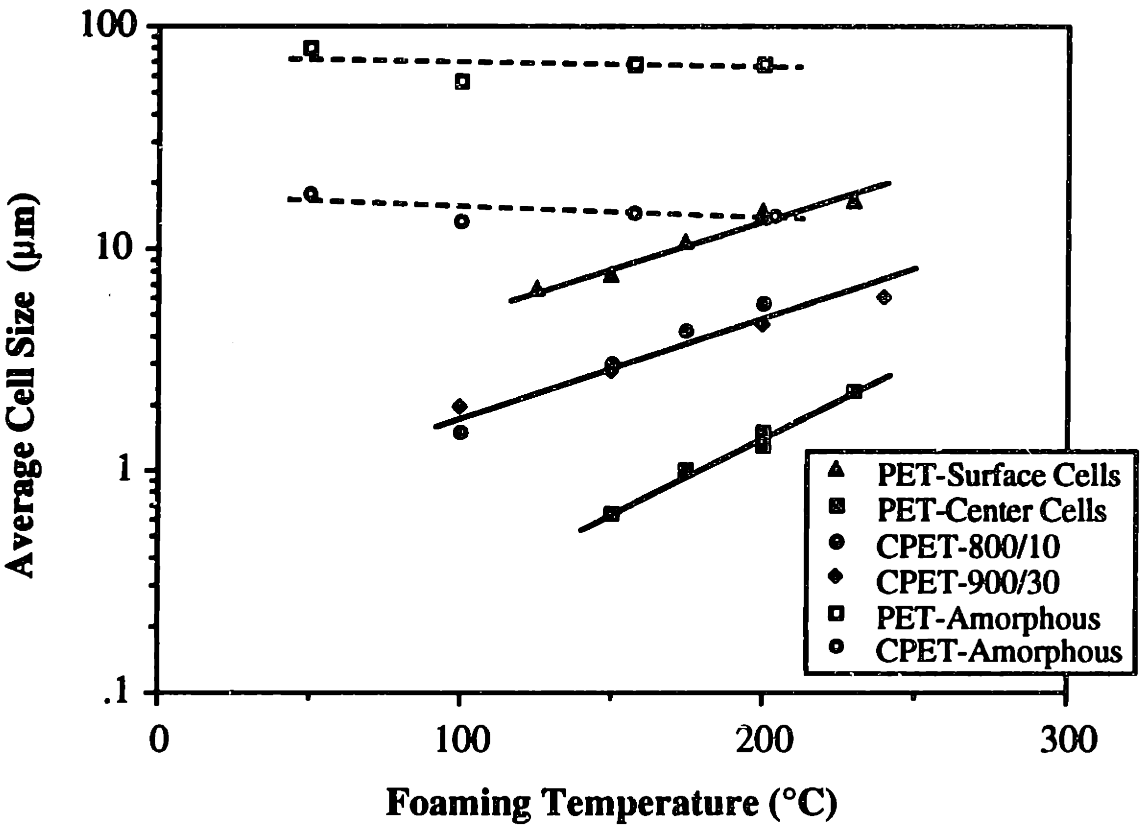

Figure 5.19: Effect of foaming temperature on the cell size of amorphous and semi-crystalline Unitika PET and CPET processed with CO_2.

When the PET and CPET samples crystallize due to gas dissolution, the nucleation behavior changes dramatically, resulting in 1000-fold cell density increases. Moreover, the increase in cell nucleation density occurs despite the fact that the gas solubility decreases with crystallinity. This suggests that the nucleation mechanisms differ between the amorphous and semi-crystalline polymers further supporting the hypothesis of section 5.2. In general, the increase in cell density is attributed to the predominant heterogeneous nucleation at the newly formed amorphous/crystalline interfaces. These interfacial regions are not necessarily distinct surfaces, as is the case with additive particles, but may encompass transition regions of finite thickness. Nonetheless, the interfacial regions have a finite free energy differential across the thickness due to changes in the magnitude of secondary bonding. The higher energy crystalline interfaces reduce the free energy barrier for nucleation increasing the probability of forming a stable nuclei and more importantly increase the number of potential nucleation sites.

Next, consider the influence of a changing saturation gas pressure on the cell nucleation mechanisms. Saturation pressure is the most commonly cited process variable for controlling nucleation and cell density, and is typically the most appropriate for this function. Changes in saturation pressure can influence microcell nucleation and cell density through two primary effects: (1) a decrease in the free energy barrier for the formation of stable nuclei and/or (2) the activation of additional nucleation sites due to matrix swelling, free volume changes, and/or the formation of crystalline interfaces all accompanying the gas dissolution process. Figure 5.13 shows that the cell density of amorphous PET and CPET can be varied over a wide domain (i.e., by a factor of 10^5 and 10^4 for PET and CPET, respectively) using the saturation pressure. Likewise, the cell density of the semi-crystalline PET and CPET can be controlled using the saturation pressure. However, the influence of saturation pressure on the semi-crystalline polymers is far weaker producing only an order of magnitude change in cell density.

The results of Figure 5.13 also indicate some very interesting nucleation characteristics for the amorphous and semi-crystalline materials. Looking first at the amorphous PET and CPET curves, the cell density is relatively independent of saturation pressures between 0.69 MPa (100 psi) and 2.06 MPa (300 psi). This indicates that nucleation is independent of saturation pressure and suggests predominant heterogeneous nucleation of a fixed number of potential sites. In the case of the PET, these heterogeneities are likely the inherent flaws and contaminants which result from conventional extrusion processing. The CPET has heterogeneities resulting from the polyolefin modifier as well as inherent flaws and contaminants which account for the nearly 100 fold higher cell densities of the amorphous CPET samples.

Above 2.06 MPa (300 psi), the mechanisms governing nucleation in the amorphous polyesters appear to change such that heterogeneous nucleation of the inherent inclusions no longer dominates. The exponential increase in cell density with saturation pressure suggests that the amorphous polyesters experience large homogeneous nucleation contributions and/or the activation of additional heterogeneous nucleation sites. Moreover, the comparable slopes of the PET and CPET above 2.06 MPa (300 psi) indicate that the saturation pressure contributions to the nucleation activation energy are nearly the same for both resins. The equal activation energy contributions imply: (1) that the underlying nucleation mechanisms are the same for the PET and CPET resins even though the CPET resin contains polyolefin partials and (2) the presence of the polyolefin modifier in the CPET consistently maintains a 100 fold larger cell density. The latter finding suggests the amorphous CPET contains approximately 100 times as many (potential) nucleation sites as the amorphous PET. The polyolefin additive certainly contributes to this larger number of nucleation sites. Furthermore, SEM micrographs of various CPET samples processed at

5.51 MPa (800 psi) showed clear signs of cell nucleation around small particles suggesting primarily heterogeneous nucleation. Since the CPET and PET samples in Figure 5.13 show similar activation energies and nucleation mechanisms, the implication is that the PET samples of Figure 5.13 also experience significant heterogeneous nucleation. While the PET samples are largely amorphous, they do have a finite degree of crystallinity ranging from one to ten percent by mass which could account for heterogeneous nucleation.

In contrast to the amorphous material, the crystalline PET and CPET resins in Figure 5.13 show considerably different nucleation behavior. The semi-crystalline PET and CPET resins show a much weaker relationship between saturation pressure and cell density. The relatively weak dependence of cell density on saturation pressure indicates predominant heterogeneous nucleation and the activation of these sites at far lower saturation pressures than for the amorphous polymers. Moreover, the comparable slopes for the semi-crystalline PET and CPET indicate similar saturation pressure contributions to the nucleation activation energy. Therefore, the same nucleation mechanism are active in the semi-crystalline PET and CPET resins. Notice further that the semi-crystalline polymers have far weaker saturation pressure contributions to the nucleation activation energy as indicated by the smaller slopes relative to the amorphous resins. It is also interesting to note that the semi-crystalline PET showed cell densities 100 times larger than the CPET which is the opposite effect shown for the amorphous materials. Therefore, the crystallization of the PET matrix can increase the number of potential heterogeneous nucleation sites by 10^4 fold. The higher cell densities of the semi-crystalline PET may indicate finer crystalline microstructures in the PET compared with the CPET.

At this point, it is illustrative to compare the nucleation results of Figure 5.13 with the trends predicted by classical nucleation theory (equations 5-5 and 5-6). Classical nucleation theory predicts an inverse square relationship for the saturation pressure with the log of the nucleation rate. Since the cell nucleation density is a weak function of the foaming time, as shown in Figure 5.14, the cell density should follow the same trends as the nucleation rate. Figure 5.20 shows the cell density plotted versus the square of the reciprocal saturation pressure [for pressures above 200 psi (1.38 MPa)]. The linear regression curves shown in Figure 5.20 have correlation coefficients of 0.10 for the crystalline PET, 0.84 for the crystalline CPET, 0.83 for the amorphous PET, and 0.96 for the amorphous CPET. For comparison, the regression curves of Figure 5.13 [for pressures above 200 psi (1.38 MPa)] have correlation coefficients of 0.44, 0.97, 0.96, and 0.96, respectively. Therefore, it is not clear from the data of Figure 5.13 that classical nucleation theory can provide more than a qualitative explanation of the polyester nucleation data. The activation energy appears to show more of a linear dependence on saturation pressure rather then an inverse square dependence. It is interesting to note that Kumar and Weller (1991) and Kweeder et al. (1991) also present data for polycarbonate and polystyrene, respectively, showing a nearly linear dependence of cell density on saturation pressure. Neither classical nucleation theory nor recent heterogeneous nucleation theories (Kweeder et al., 1991; Ramesh et al., 1993) are capable of predicting this linear trend.

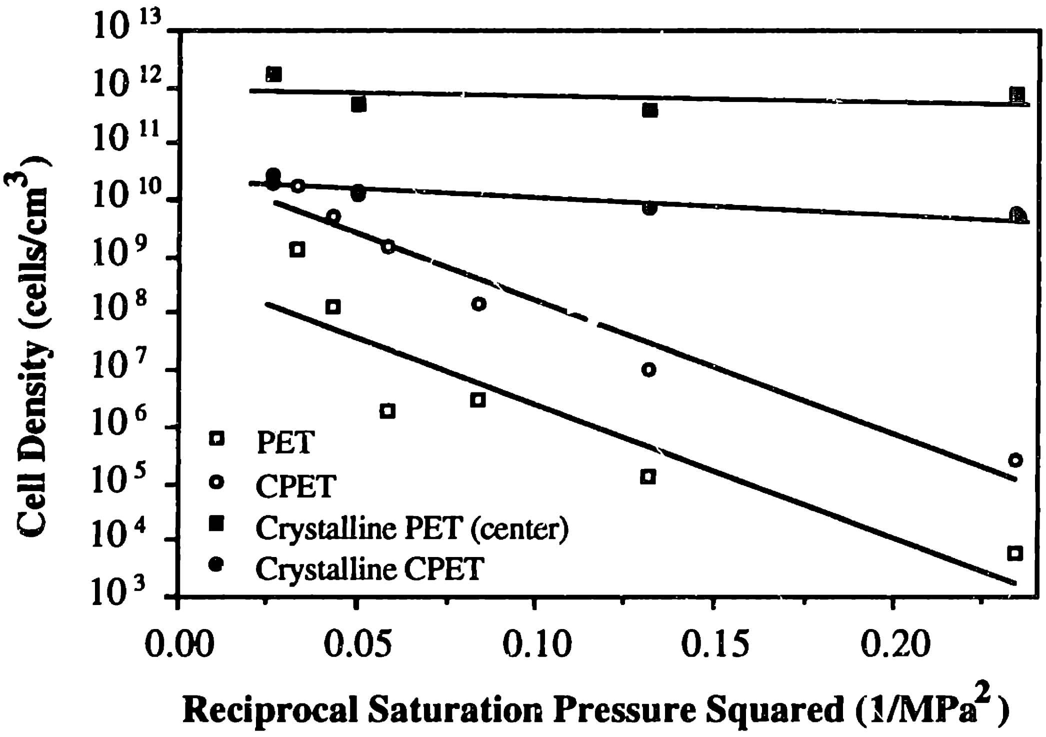

Figure 5.20: Comparison of saturation pressure results with trends expected from classical nucleation theory.

The important conclusion to draw from this cell density data is that the nucleation mechanism of the amorphous and semi-crystalline polymers differ considerably and necessitate the use of different process design strategies. Specific process design strategies will be discussed below. Next, consider the effect of foaming time on cell nucleation.

Foaming time can influence cell nucleation if the nucleation kinetics and growth kinetics are on the same time scale or if the cell morphology relaxes through cell coalescence and related effects during the growth process. In the former case, the cell density tends to increase with foaming time, and in the latter case, the cell density tends to decrease with foaming time. However, it is desirable to have a nearly constant cell density over the foaming time because foaming time is a potential process variable for controlling cell growth and cell size. The amorphous PET and CPET foams in Figure 5.14 show signs of cell morphology relaxation during the early stages of growth. Between 10 and 20 seconds, the relaxation process subsides and a relatively constant cell density is achieved. In order to produce the highest possible cell densities, it is desirable to minimize cell morphology relaxation. Therefore, the foaming times for the amorphous polymers should be kept as short as possible. In this study, the shortest foaming times achieved were two seconds.

The semi-crystalline CPET shows an essentially constant cell density over the foaming times studied. No relaxation phenomenon was observed for the semi-crystalline polymers. However, foaming times less than ten seconds were not achieved since a hot press was used as the foaming medium.

From the results of Figures 5.14 and 5.18, it can be concluded that the cell nucleation kinetics occur over a relatively short time scale compared with the cell growth kinetics. Although not surprising, this is a noteworthy finding for batch processing which indicates that the cell nucleation process and cell growth process are uncoupled over the processing window studied. The independence of the cell nucleation and cell growth suggests that nucleation occurs during the saturation pressure release and/or during the first seconds the foaming temperature is applied. To understand the effect of foaming temperature on cell nucleation consider the results presented in Figure 5.15.

Based on classical nucleation theory (equations 5-7 and 5-8), one would expect an Arrhenius-type relationship between cell density and the nucleation temperature. Therefore, the nucleation temperature could potentially be an effective process variable for controlling the cell density. For the amorphous PET and CPET in Figure 5.15, the potential of controlling the cell density is evident at processing temperatures below 100 °C, suggesting that some detectable nucleation occurs during the application of the foaming temperature. In general, Figure 5.15 indicates that the cell density of the amorphous materials is a strong function of temperature below 100 °C and is relatively independent of temperature above 100 °C. However, the cell density range is considerably lower than is required for microcellular foams. In contrast, the cell densities of the semi-crystalline PET and CPET are relatively constant over the temperatures studied. This indicates that the cell density is relatively independent of foaming temperature. The only exception is the surface cells of the semi-crystalline PET which show some temperature dependence.

The results for the amorphous PET and CPET shown in Figure 5.15 suggest these materials experience some degree of thermally activated nucleation. In general, microcell nucleation is induced by generating a rapid thermodynamic instability in a polymer/gas solution. Therefore, thermally induced nucleation can be understood by considering the effects of temperature on the solubility of gas in the polymer matrix. When a gas is dissolved in a polymer at lower temperatures, the gas molecules experience large free volume contractions which restrict the vibrational motions of the molecules whereby decreasing the entropy and free energy of the system. As the temperature is increased, the gas molecules attempt to activate additional vibrational modes but are restricted by the confines of the polymer matrix. This results in a negative entropy change and an increase in the system free energy, eventually forcing gas molecules to form stable nuclei whereby lowering the system free energy.

It is interesting to compare the results of the amorphous polyesters in Figure 5.15 with the trends predicted by classical nucleation theory for thermally activated nucleation. This is accomplished by plotting the cell density data for the amorphous PET and CPET on a semi-log graph against the ratio of the surface tension cubed to the absolute foaming temperature (shown in Figure 5.21). [§] In constructing this plot, the surface tension is taken as a linear function of temperature and estimated from the PET-melt surface tension data of presented by Wu (1982). Notice in Figure 5.21 that neither the PET nor CPET data showed a clear linear trend as predicted from classical nucleation theory. This suggests that classical nucleation theory does not adequately model the physical mechanisms promoting thermally activated nucleation in the amorphous polyesters.

Next, consider the foaming temperature effects on nucleation for the semi-crystalline PET and CPET shown in Figure 5.15. The center cells of the PET and both CPET samples show a nearly constant cell density over the higher foaming temperatures. Notice further that the CPET samples saturated at 5.51 MPa (800 psi) and 6.20 MPa (900 psi) (i.e., samples CPET-800/10 and CPET-900/30, respectively) showed an increase in cell density from 10^{10} to 3×10^{10} cells/cm^3 as expected with the increase in saturation pressure. At the lower foaming temperatures, none of the semi-crystalline materials showed detectable cell structures. This effect may or may not be a result of thermally activated nucleation as may be the case for the amorphous polymers. The lack of detectable cell structures at the lower foaming temperatures could be attributed to the cell growth behavior of the semi-crystalline polymers.

[§] Strictly speaking, this comparison is not far in that classical nucleation theory assumes an isothermal nucleation process which is not the case when solubility changes are generated by thermal effects.

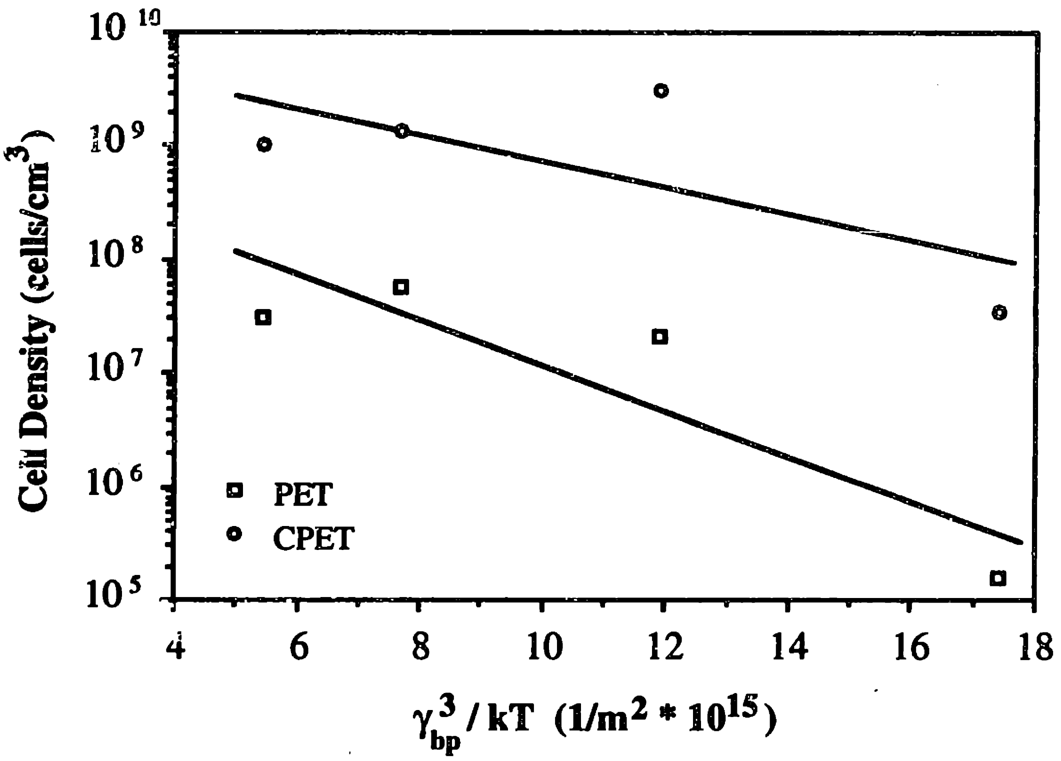

Figure 5.21: Comparison of the cell density results for amorphous PET and CPET with trends expected from classical nucleation theory.

A strong cell size dependence on foaming temperature is shown in Figure 5.19 for the semi-crystalline polyesters where at 150 °C the PET (center) had 0.6 μm cells and at 100 °C the CPET had 1.5 μm cells. At lower foaming temperatures, the matrix stiffness may be sufficiently large to prevent nucleated cells from growing to detectable sizes even though the allotted foaming time was sufficient to allow all of the available gas to diffuse into the cells. This would account for the negligible cell densities observed at the lower foaming temperatures. In this study, the resolution of detectable cells was 0.3 μm which is half the size of the smallest PET cells and one fifth that of the smallest CPET cells. Further evidence supporting this hypothesis is given by estimates of the critical stable nuclei size. The critical stable nuclei size can be estimated using equation (5-10) [also see equation (3.2-5)] and the PET surface tension data of Wu (1982). At $\Delta p = 5.51$ MPa (800 psi), the estimated critical sizes range from 0.02 μm to 0.03 μm (i.e., an order of magnitude smaller then the detectable resolution) for a melt temperature of 270 °C and a glassy temperature of 20 °C, respectively. Therefore, nucleation may have occurred in the low temperature samples, but the growth of the stable nuclei is not sufficient for them to be detected.

$$D_c = \frac{4\,\gamma_{bp}(T)}{\Delta p} \tag{5-10}$$

If this is the case, then the constant cell density effects for the semi-crystalline materials shown in Figure 5.15 would seem to indicate that the foaming stage of microcellular processing is independent of the nucleation process. In other words the nucleation and foaming of these materials are uncoupled. This implies that the nucleation process occurs primarily during the initial thermodynamic instability generated by the saturation gas pressure release (occurring at a constant temperature of 20 °C). If nucleation occurred at a constant temperature, then the constant cell density results shown in Figure 5.15 follow because the foaming temperature is applied subsequently to the nucleation process and therefore would not influence the detectable cell density.

Cell Growth

Next, consider the effects of the major processing variables on cell size and the mechanisms governing cell growth. In general, cell growth is controlled by the degree of supersaturation, rate of gas diffusion into the cells, the hydrostatic pressure or stress applied to the polymer matrix, the interfacial surface energy, and the viscoelastic properties of the polymer/gas solution. It is also important to acknowledge the influence of cell nucleation density on cell size. Cell density and cell size follow an inverse cubic relation for constant void fraction foams which is derivable from equations (5-1) and (5-2). In general, a factor of 1000 increase in the cell density decreases the cell size by a factor of ten. In the following paragraphs, the cell size results and cell growth characteristics are discussed with respect to the process variables of saturation time, saturation pressure, foaming time, and foaming temperature.

Similar to the case of cell nucleation, the gas saturation time is an inappropriate process variable for controlling cell size. In general, saturation times should be selected as the minimum necessary to achieve an approximately uniform gas concentration whereby controlling the solution formation step. However, the results shown in Figure 5.16 illustrate some important characteristics that must be integrated into the process design strategies.

Looking first at the amorphous materials (i.e., for $Dt/l^2 < 0.8$), the data indicates a decreasing cell size with saturation pressure. Since, these materials had fully grown cells (i.e., a dodecahedron geometry) and similar void fractions, the decrease in cell size is attributed namely to the increase in cell density resulting from the increasing gas concentration during saturation.

At saturation times greater than $Dt/l^2 \approx 0.8$, the PET and CPET experience significant crystallization. The crystallization results in a 100-fold decrease in cell size for the PET and 10-fold decrease in cell size for the CPET. In this case, the majority of the cell size decrease can be attributed to the increase in cell density associated with crystallization. However, the semi-crystalline PET and CPET did not exhibit fully grown cells (i.e., having a dodecahedron geometry), and these microcellular foams have considerably higher specific densities than the amorphous foams. Therefore, the cell growth mechanisms dominating in the semi-crystalline polymers differ from that of the amorphous materials, further supporting the hypothesis of section 5.2. In general, the amorphous foams experience diffusional controlled cell growth while the semi-crystalline foams experience viscoelastic controlled cell growth. To better understand the differences between the cell growth mechanisms of the amorphous and semi-crystalline polymers next consider the influence of the saturation pressure.

The cell size results of Figure 5.17 show some stark contrasts between the amorphous and the semi-crystalline PET and CPET resins. Based on Figure 5.12, the saturation pressure was determined to be an effective process variable for controlling cell density. Therefore, to insure an uncoupled process, it is desirable to have a relatively independent cell size with varying saturation pressure. In Figure 5.17, the semi-crystalline PET and CPET show an independent cell size with saturation pressure illustrating the potential for a decoupled process. In contrast, the amorphous materials show a strong cell size dependence on saturation pressure.

To understand the growth mechanisms which govern the cell size results of Figure 5.17, first consider the amorphous PET and CPET samples. These foams had fully grown cell structures with a characteristic dodecahedron geometry and similar void fractions. Therefore, the decreasing cell size is attributed primarily to the exponential increase in cell density of these amorphous foams.

In contrast, the semi-crystalline PET and CPET microcellular foams showed no appreciable change in cell size with saturation pressure even though the cell density varies by a factor of ten over this range. In addition, these microcellular foams did not exhibited fully grown cell structures. The lack of such cell structures could indicate cell growth which is governed by the gas diffusion rate. Using equation (5-4) and a diffusivity of $D = 8.5 \times 10^{-8}\ \mathrm{cm^2/s}$ (reported by Koros and Paul, 1980, at 115 °C), the gas diffusion time necessary for diffusion limited cell growth can be estimated where the characteristic diffusion length is taken as $l \approx D_c/2$. The semi-crystalline PET and CPET foams have cell sizes of 1.5 μm and 5 μm yielding estimated diffusion times of $t \approx 0.3$ and 1.4 seconds, respectively. Since these materials were allowed to foam at 200 °C for 10 seconds, the cell growth characteristics shown in Figure 6 are not the result of diffusion limited growth.

The relatively constant cell size and lack of a fully grown cell structure is attributed to the viscoelastic behavior of the semi-crystalline polymer matrix. While it is expected that the tensile modulus of the neat semi-crystalline polymer is larger than that of the neat amorphous polymer, this does not necessarily follow for polymer/gas solutions which exhibit significant plasticization. However, Figure 5.5 clearly shows higher moduli in the transition region for the semi-crystalline polymer/gas solutions compared to similar amorphous polymer/gas solutions. Since the semi-crystalline polymer/gas system has a high modulus and the modulus is a strong function of temperature, it is expected that the constant cell size results shown in Figure 5.17 are governed by the influence of temperature on cell growth. The semi-crystalline polymers where all foamed at a constant 200 °C resulting in similar moduli and viscoelastic behavior during cell growth. In that the semi-crystalline polymers seem to experience viscoelastic controlled cell growth, the constant foaming temperature results in a nearly constant cell size despite saturation pressure changes.

The next process variable studied was the foaming time. In general, foaming time is a potential process variable for controlling the cell size because under some circumstances cell growth is governed by the rate of gas diffusion into the cells. The longer the gas is allowed to diffuse into the cells (i.e., the foaming time) the larger the cell size.

To understand the results of Figure 5.18, it is useful to consider the possible kinetic mechanisms that contribute to the cell growth process for a varying foaming time which are (1) the rate of gas diffusion into the cells, (2) the flow/relaxation of the viscoelastic matrix, and (3) the coalescence of cells. To estimate the contribution of the gas diffusion rate, equation (5-4) is used with $D = 8.5 \times 10^{-8}$ cm^2/s (reported by Koros and Paul, 1980 at 115 °C). For the amorphous PET, the estimated cell growth time is $t \approx l^2/D = 89$ seconds where $l \approx 55/2$ μm. For the amorphous CPET, $l \approx 13/2$ μm, and the estimated growth time is 5 seconds. The semi-crystalline CPET foams have a typical cell size of 7 μm yielding an estimated diffusion time of $t \approx 1.4$ seconds. Thus, it is not surprising that the amorphous polyesters show an increasing cell size during the shorter foaming times due in part to limiting gas diffusion rates. In contrast, the estimated diffusion time of the semi-crystalline

CPET, would suggest that the foaming time has very little influence on cell growth which is supported by the data of Figure 5.18.

The initial increase in cell size with foaming time for the amorphous polyesters may also be influenced by the decrease in cell density over this range of foaming time (see Figure 5.14). The initial decrease in cell density was attributed to relaxation of the cell structures through cell coalescence. Since the amorphous foams of Figure 5.18 exhibited fully grown cell structures and similar void fractions, some degree of the cell size increase over the shorter foaming times is likely due to the relaxation of the cell structure and the system's natural tendency to seek a lower free energy state through cell coalescence. One can conclude then that the foaming time is a relatively poor process variable for controlling cell growth and the cell size for both amorphous and semi-crystalline polyesters.

The foaming temperature is also a potential process variable for controlling cell growth and cell size during microcellular processing. The results of Figure 5.19 show some very interesting contrasts between the cell growth characteristics of the amorphous and semi-crystalline polyester resins. The first is the relatively independent cell size with changing foaming temperature for the amorphous PET and CPET. In contrast, the semi-crystalline PET and CPET show a strong positive relationship between the foaming temperature and the cell size. These results suggest a process strategy for the semi-crystalline polymers where the foaming temperature is used to control cell growth and the cell size. However, the foaming temperature cannot be used to control the cell size of the amorphous polymers.

At this point, it is worth exploring the mechanisms which govern cell growth and cell size in more detail. In general, the foaming temperature can affect cell growth through the gas diffusion rate, the interfacial surface energy (i.e., surface tension), and the viscoelastic behavior of the polymer/gas matrix.

The amorphous PET and CPET foams processed above 50 °C showed a fully grown cell morphology (i.e., a dodecahedron geometry) and a nearly constant cell size. However, the amorphous foams processed at 50 °C did not show a fully grown cell structure, and the cell density of these materials is considerably lower than those processed above 50 °C. At the lower temperature, it is possible that both the gas diffusion rate and the viscoelastic behavior of the polymer/gas matrix are responsible for the cell growth characteristics. To estimate the extent of the gas diffusion rate contribution at the lower temperatures, an approximate gas diffusion time can be obtained from equation (5-4) using a diffusivity of $D = 8 \times 10^{-9}$ cm^2/s [at 20 °C from the data of Figure 5.1(a)]. Using characteristic diffusion distances of $l \approx 70/2$ µm and $l \approx 20/2$ µm, the estimated gas diffusion times for the amorphous PET and CPET are 25 minutes and 2 minutes, respectively. Therefore, it is likely that amorphous foams experience primarily diffusion limited growth at lower temperatures.

In contrast, the semi-crystalline PET and CPET show a strong cell size dependence on foaming temperature over the range studied. The contributions of diffusion controlled cell growth can be estimated using equation (5-4) with $D = 8.5 \times 10^{-8}$ cm^2/s [reported by Koros and Paul for PET/CO$_2$ systems at 115 °C]. For the PET surface cells, the estimated cell growth time is 10 seconds, while for the center cells, the estimated diffusion time is 0.1 seconds. For the CPET microcellular foams, the estimated cell growth time is 2.9 seconds. These diffusion limited growth times are compared with the 10 second foaming time for these samples. Therefore, it seems that the gas diffusion kinetics are sufficiently rapid such that the growth phenomenon observed for the semi-crystalline materials in Figure 5.19 are not the result of diffusion limited growth rates.

Another factor that can contribute to the cell size effect as the foaming temperature changes is the surface tension. To a first order approximation, the surface tension contributions to the equilibrium (spherical) cell size are proportional to the factor of equation (5-11), and the relative contributions are given by equation (5-10).

$$(D_c)_{\text{surface}} \propto \frac{4\,\gamma_{bp}(T)}{\Delta p} \qquad (5\text{-}11)$$

$$\left(\frac{D_{c2}}{D_{c1}}\right)_{\text{surface}} = \frac{\gamma_{bp}(T_2)}{\gamma_{bp}(T_1)} \qquad (5\text{-}12)$$

Next, since $-(\partial\gamma_{bp}/\partial T)_p$ is proportional to the entropy, it follows from the second law of thermodynamics that the surface tension must decrease with an increasing temperature. From equation (5-12), this implies the surface tension effects tend to decrease the equilibrium cell size when the foaming temperature is increased. Using the PET surface tension data presented by Wu (1982), the estimated surface tension contribution is a 22% decrease in equilibrium cell size when the foaming temperature increases from 100 to 230 °C. It is clear then that the surface tension effects do not account for the cell growth mechanisms exhibited by the semi-crystalline polymers in Figure 5.19 (i.e., an increasing cell size with foaming temperature).

Therefore, the cell growth effects demonstrated by the semi-crystalline polymers in Figure 5.19 seem to result primarily from the viscoelastic behavior of the polymer/gas matrix, further supporting the hypothesis of section 5.2. ‡ In general, the viscoelastic behavior of the semi-crystalline polymer matrix is a strong function of temperature and time. Moreover, the modulus of semi-crystalline PET has been shown to be an order of magnitude larger than that of the amorphous PET, at temperatures above the glass transition (see Figure 5.4 and Shimbo et al., 1993). It is not surprising that the amorphous PET and CPET show little cell size dependence at the higher foaming temperatures. Whereas the higher modulus of the semi-crystalline material helps to explain the cell size dependence. As the foaming temperature increases, the stiffness of the semi-crystalline matrix relaxes, promoting larger strains and cell sizes for a given stress level [see equation (5-9)].

To conclude this discussion, some final observations are in order. From the data of Figures 5.12 through 5.19, it is clear that: (1) the amorphous CPET foams show a much finer cell structure than the amorphous PET, (2) the semi-crystalline PET foams show a finer cell structure (in the center regions) than the semi-crystalline CPET (i.e., the inverse behavior of the amorphous resins), and (3) the semi-crystalline PET and CPET foams show finer cell morphologies than the amorphous materials.

5.3.3 Process Design Implications

From the microcellular processing characterization shown in Figures 5.12 through 5.19, it is concluded that (1) for the crystallizable polymers studied, multiple processing windows exist which cover unique process variables ranges and (2) different process design strategies must be derived within these processing windows to insure independent control of the process functions (i.e., solution formation, cell nucleation, and cell growth). In general, the feasible processing windows for the amorphous and semi-crystalline polyesters differ considerably. These differences must be integrated into the process design strategies for the respective materials so as to take advantage of their unique processing characteristics. Strictly speaking, the process strategies presented below hold only for the amorphous and semi-crystalline polyesters studied. However, it is expected that comparable process strategies apply for other crystallizable polymers that exhibit similar gas dissolution and crystallization behavior [e.g., poly(vinylidene fluoride) / poly(methyl methacrylate) blends, Chiou et al. (1985)].

---

‡ SEM micrographs of these microcellular polymers are shown in Figures 5.10 and 5.11. These foams exhibited spherical cell geometries indicating only partially grown cell structures. The exception is at the highest processing temperatures where the cells were fully grown having a dodecahedron geometry.

The process design strategies derived from this study are presented in the form of matrix equations where the matrix elements indicate the relative dependence of the major process functions (i.e., solution formation, microcell nucleation, and cell growth) on the process variables (i.e., saturation time, saturation pressure, foaming time, and foaming temperature). The matrix elements consist of an 'X' indicating a relatively strong dependence, an '⊗' indicating a relatively weak dependence, and an '0' indicating a nearly independent behavior between the process function and the process variable.

The data of Figures 5.12 through 5.19 suggest a number of processing domains or windows for the polyester materials. For each separate processing window, an independent process design strategy was derived under the assumption that homogeneous foams are to be produced. In the case of the amorphous polymers, three processing windows are suggested by the data. The first applies for foaming temperatures near the glass transition (of the neat PET) and for higher saturation pressures (i.e., ≥ 2.07 MPa or 300 psi). In this processing domain, the design strategy for the amorphous materials is given by equation (5-13). Since equation (5-13) can be rearranged into a triangular form, it is clear that at least one independent process variable exists for satisfying or controlling each of the process functions provided that the processing variables are set in a specific order. In the case of equation (5-13), the foaming temperature should be selected first at a value near the glass transition temperature. Next, the saturation pressure should be selected to achieve the required cell nucleation density. Finally, the saturation time and foaming time can be selected to achieve the required solution formation and cell growth (i.e., cell size) requirements, respectively. It is important to realize that the saturation time must be long enough to achieve a uniform gas concentration but short enough to minimize crystallization.

$$\begin{Bmatrix} \text{Solution Formation} \\ \text{Cell Nucleation} \\ \text{Cell Growth} \end{Bmatrix} = \begin{bmatrix} X & X & 0 & 0 \\ 0 & X & 0 & X \\ 0 & X & \otimes & 0 \end{bmatrix} \begin{Bmatrix} \text{Saturation Time} \\ \text{Saturation Pressure} \\ \text{Foaming Time} \\ \text{Foaming Temperature} \end{Bmatrix} \tag{5-13}$$

Strictly speaking, equation (5-13) is a redundant process design since it has more process variables than functional requirements. Rearranging equation (5-13) and eliminating one of the redundant process variables yields a decoupled process design strategy given by equation (5-14). Notice in equation (5-14) that the matrix is diagonal suggesting the specification of saturation pressure first to satisfy the cell growth requirement followed by specification of the saturation time and foaming time, to satisfy the solution formation and cell nucleation requirements, respectively. This is an alternate process control strategy than that stated for equation (5-13). However, non-redundant process design equations are sometimes misleading in that the effects of the redundant process variables are not explicitly stated. This sometimes leads to the common mistake of assuming these redundant process variables can be set arbitrarily. In fact, the redundant process variables must be specified prior to the process variables used to satisfy the functions. For the remaining process design strategies, the redundant form of the equations are presented rather than the non-redundant forms so as to explicitly show the effect of the major process variables.

$$\begin{Bmatrix} \text{Cell Growth} \\ \text{Cell Nucleation} \\ \text{Solution Formation} \end{Bmatrix} = \begin{bmatrix} X & 0 & 0 \\ X & X & 0 \\ X & 0 & X \end{bmatrix} \begin{Bmatrix} \text{Saturation Pressure} \\ \text{Foaming Temperature} \\ \text{Saturation Time} \end{Bmatrix} \tag{5-14}$$

For the amorphous polyesters at foaming temperatures above the glass transition and at higher saturation pressures, the results suggests the following process design strategy:

$$\begin{Bmatrix} \text{Solution Formation} \\ \text{Cell Nucleation} \\ \text{Cell Growth} \end{Bmatrix} = \begin{bmatrix} X & X & 0 & 0 \\ 0 & X & 0 & 0 \\ 0 & X & \otimes & 0 \end{bmatrix} \begin{Bmatrix} \text{Saturation Time} \\ \text{Saturation Pressure} \\ \text{Foaming Time} \\ \text{Foaming Temperature} \end{Bmatrix} \tag{5-15}$$

Notice at the higher foaming temperatures, cell nucleation is independent of the foaming temperature, and therefore, the process strategies given for equations (5-13) and (5-14) hold except the foaming temperature can be selected arbitrarily above the glass transition without influencing any of the process functions.

A third process design strategy applies for the amorphous PET and CPET at relatively low saturation pressures and is given by equation (5-16). In this case, the process variables studied were not sufficient to satisfy each of the process functions indicating an uncontrollable process. Notice that none of the process variables influence cell nucleation. At low saturation pressures, the amorphous PET and CPET experience predominant heterogeneous nucleation governed by the inherent flaws, inclusions, and/or process additives. In order to satisfy the cell nucleation function within this processing window, an additional process variable is needed. One potential process variable for controlling cell nucleation in this domain would be a specified concentration of second phase particles to act as heterogeneous nucleation sites.

$$\begin{Bmatrix}\text{Solution Formation}\\ \text{Cell Nucleation}\\ \text{Cell Growth}\end{Bmatrix}=\begin{bmatrix}X & X & 0 & 0\\ 0 & 0 & 0 & 0\\ 0 & 0 & \otimes & 0\end{bmatrix}\begin{Bmatrix}\text{Saturation Time}\\ \text{Saturation Pressure}\\ \text{Foaming Time}\\ \text{Foaming Temperature}\end{Bmatrix} \tag{5-16}$$

A significant implication of equations (5-13) through (5-16) for the amorphous materials is that only limited control over cell growth can be achieved once the saturation pressure has been selected. In general, the saturation pressure limits the ultimate size of the cells. Within this limit, the cell size can be varied using the foaming time. However, in order to span the full size range, foaming times less than two seconds are needed which are difficult to achieved due to limits in the heat transfer kinetics. Moreover, the relaxation of the cell structure through cell coalescence limits the repeatability of cell growth control. Therefore, cell growth is a relatively difficult process function to satisfy for the amorphous polyesters within the scope of process variables studied.

At sufficiently high saturation pressures and over sufficiently long saturation times, the PET and CPET resins crystallize. The crystallization process changes both the cell nucleation and cell growth mechanisms through its effects on interfacial energy and viscoelastic behavior, respectively. This results in a coupled foaming process as given by equation (5-17) which holds during any processing window encompassing the crystallization process. During the crystallization process, solution formation and cell nucleation cannot be satisfied independently. Therefore, the process design strategies for the amorphous and semi-crystalline must be specified independently.

$$\begin{Bmatrix}\text{Solution Formation}\\ \text{Cell Nucleation}\\ \text{Cell Growth}\end{Bmatrix}=\begin{bmatrix}X & X & 0 & 0\\ X & X & 0 & 0\\ X & X & \otimes & X\end{bmatrix}\begin{Bmatrix}\text{Saturation Time}\\ \text{Saturation Pressure}\\ \text{Foaming Time}\\ \text{Foaming Temperature}\end{Bmatrix} \tag{5-17}$$

In contrast to the amorphous materials, the results for the semi-crystalline PET and CPET suggest a single process design strategy given by equation (5-18). The gas saturation pressure should be selected first to satisfy the cell nucleation function followed by the selection of the saturation time to satisfy the solution formation function. Finally, the foaming temperature should be selected to satisfy the cell growth function, and the foaming time can be selected arbitrarily without influencing the resulting cell morphologies.

$$\begin{Bmatrix} \text{Solution Formation} \\ \text{Cell Nucleation} \\ \text{Cell Growth} \end{Bmatrix} = \begin{bmatrix} X & X & 0 & 0 \\ 0 & X & 0 & 0 \\ 0 & 0 & 0 & X \end{bmatrix} \begin{Bmatrix} \text{Saturation Time} \\ \text{Saturation Pressure} \\ \text{Foaming Time} \\ \text{Foaming Temperature} \end{Bmatrix} \tag{5-18}$$

Controlling cell growth using the foaming temperature rather than the foaming time is an important difference between the processing of the semi-crystalline polymers and amorphous polymers. Moreover, it is important to realize that although cell nucleation can be controlled for the semi-crystalline polymers using the saturation pressure, the range of this control is significantly less than that of the amorphous foams. The somewhat limited cell nucleation control for the semi-crystalline polymers results from the additional heterogeneous nucleation contributions at the amorphous/crystalline interfaces. Finally, notice that the process design strategy for the semi-crystalline polymers is decoupled allowing for independent control over each of the process functions.

5.3.4 Summary

The findings of this study clearly illustrate significant differences in the microcellular processing characteristics of amorphous and semi-crystalline polymers. Moreover, these differences in processing characteristics require the specification of independent process design strategies for the amorphous and semi-crystalline polymers since the crystallization process was found to couple the solution formation and cell nucleation requirements. The amorphous polyesters studied revealed three separate processing windows and process design strategies. Within these processing domains, the amorphous CPET exhibited primarily microcellular morphologies whereas the amorphous PET showed larger cell structures. In contrast, all of the semi-crystalline polymers exhibited microcellular morphologies and showed a very broad processing window over the spectrum of the process variables studied suggesting a single process design strategy.

Furthermore, the results presented give considerable insight into the mechanisms which govern cell nucleation and cell growth during the microcellular processing of amorphous and semi-crystalline polymers. While the amorphous CPET showed additional heterogeneous nucleation contributions resulting from the polyolefin additive, both the amorphous PET and CPET exhibited similar nucleation characteristics and therefore nucleation mechanisms. At low saturation pressures, these materials appear to experience heterogeneous nucleation due to inherent flaws. At higher pressures, both the amorphous PET and CPET showed a strong cell density dependence indicating the activation of additional nucleation sites and/or homogeneous nucleation contributions. The semi-crystalline polymers also showed similar nucleation mechanisms and a cell density dependence on the saturation pressure that was considerably less than the amorphous materials. In general, the semi-crystalline polymers exhibited considerably higher cell densities than the amorphous polymers which is attributed to the significant contributions of heterogeneous nucleation in the amorphous/crystalline interfacial regions. Moreover, it was found that classical nucleation theory was not adequate to quantitatively predict the effects of saturation pressure on cell nucleation for either the amorphous or semi-crystalline polymers.

In addition, the foaming time was found to have a relatively weak influence on cell nucleation and cell growth for both the amorphous and semi-crystalline polyesters. This contrasts the strong cell size dependence on foaming time reported for styrenic resins (Martini, 1981; Kumar, 1988; Ramesh et al., 1991).

For the amorphous polymers, foaming temperatures near the glass transition were found to influence the cell density, indicating thermally activated nucleation. Moreover, the cell density dependence on foaming temperature was found not to follow the quantitative trends predicted by classical nucleation theory. In contrast, the semi-crystalline polymers exhibited a strong cell size dependence on foaming temperature and a relatively independent cell density. The foaming temperature dependence on the cell size is attributed to the viscoelastic behavior of the semi-crystalline polymers.

CHAPTER 6

MICROCELLULAR SHEET PROCESSING SYSTEM DESIGN CONCEPTS

6.0 Introduction

The results of the microcellular processing characterization described in chapter 5 provide some invaluable insights into the design of a continuous sheet processing system, particularly with respect to the selection of feasible process variables. For instance, the foaming time was shown to be an ineffective process variable for controlling cell growth at temperatures appreciably above the glass transition temperature. An effective process variable for controlling cell nucleation was shown to be the saturation pressure. Moreover, the foaming temperature was shown to be an effective process variable for controlling cell growth. Using the basic knowledge derived from the microcellular processing characterization of chapter 5, three conceptual system designs were synthesized for the continuous production of microcellular sheets.

In the design of any processing system, it is important to first identify the customers and their requirements. The customers for the continuous microcellular sheet processing system were the member companies of the MIT-Industry Microcellular Plastics Consortium. These companies expressed a need for processing technology capable of large-scale production of microcellular thin films and sheets. Since these companies had a number of undisclosed applications for which microcellular plastics were being considered, it was decided that the sheet processing system be designed and developed as a generic technology platform which could be later tailored to meet the requirements of specific applications. This customer requirement was translated into a top-level functional requirement: FR = the development of a prototype processing system for the continuous production of microcellular polymer sheets. To map this functional requirement into the physical domain, a means for continuous polymer processing must be selected. For this research, an extrusion based system was selected.

Based on an extrusion system, the top-level functional requirement was expanded into three level-two functional requirements.

FR_1 = Processing a polymer melt
FR_2 = Processing a microcellular structure
FR_3 = Processing a thin film or sheet †

These functional requirements were selected so as to isolate the major processing stages required in continuous microcellular polymer sheet processing. The mapping of these FRs into the physical domain was relatively simple at this hierarchy level, resembling something like a "black box". The design parameters selected to satisfy the level-two functional requirements are given below.

DP_1 = Single screw plasticating extrusion system
DP_2 = Microcellular processing system
DP_3 = Sheet processing system

Notice here that the top-level requirement of an extrusion based process has been propagated as a system constraint into the level-two DPs. The effects of this constraint appear explicitly in DP_1 which specifies the use of a single screw plasticating extrusion system.

The top-level design equation for the continuous microcellular sheet processing system is given in equation (6-1).

$$\begin{Bmatrix} FR_1 \\ FR_2 \\ FR_3 \end{Bmatrix} = \begin{bmatrix} X & X & X \\ 0 & X & X \\ 0 & 0 & X \end{bmatrix} \begin{Bmatrix} DP_1 \\ DP_2 \\ DP_3 \end{Bmatrix} \tag{6-1}$$

Equation (6-1) can also be represented graphically as shown in Figure 6.1. In this convenient graphical form, the functional and physical hierarchy are represented as trees, and the influence of the selected DPs on the FRs is shown as directed lines. Notice that the microcellular sheet extrusion system design is decoupled. The decoupled nature of equation (6-1) mandates that sheet processing system be specified first, followed by specification of the microcellular processing system, and finally specification of the polymer processing system. In the following chapters, it will be shown that the decoupled nature of the design results from the physical interlink created by the continuous flow (e.g., from pressure effects).

---

† Note here that the subscripts indicate the hierarchy path where FR_{ijk} has a grandparent requirement i, a parent requirement j, and the current requirement k.

The design equation (6-1) is formulated based on a simple thought experiment. Assuming the functional requirement is satisfactorily achieved, will a perturbation in the design parameter force the functional requirement outside its tolerance band? Admittedly, at such a high level in the hierarchy, without more detailed embodiments in the physical design, the form of the design equation is not guaranteed. Therefore, it is treated as a guideline for the next hierarchy levels. Design equation (6-1) must be constantly revisited at subsequent hierarchy levels to insure the system design remains decoupled.

In the next sections, three conceptual designs for the microcellular sheet extrusion system will be discussed. These concepts are based on design equation (6-1). [§] It is important to realize that the following sections present conceptual designs which incorporate fundamental processing strategies for microcellular sheet extrusion. The specific hardware shown is intended to illustrate the major processing functions in a conceptually simple manner and does not necessarily correspond to the actual hardware used. This hardware is discussed in chapters 7, 8, and 9.

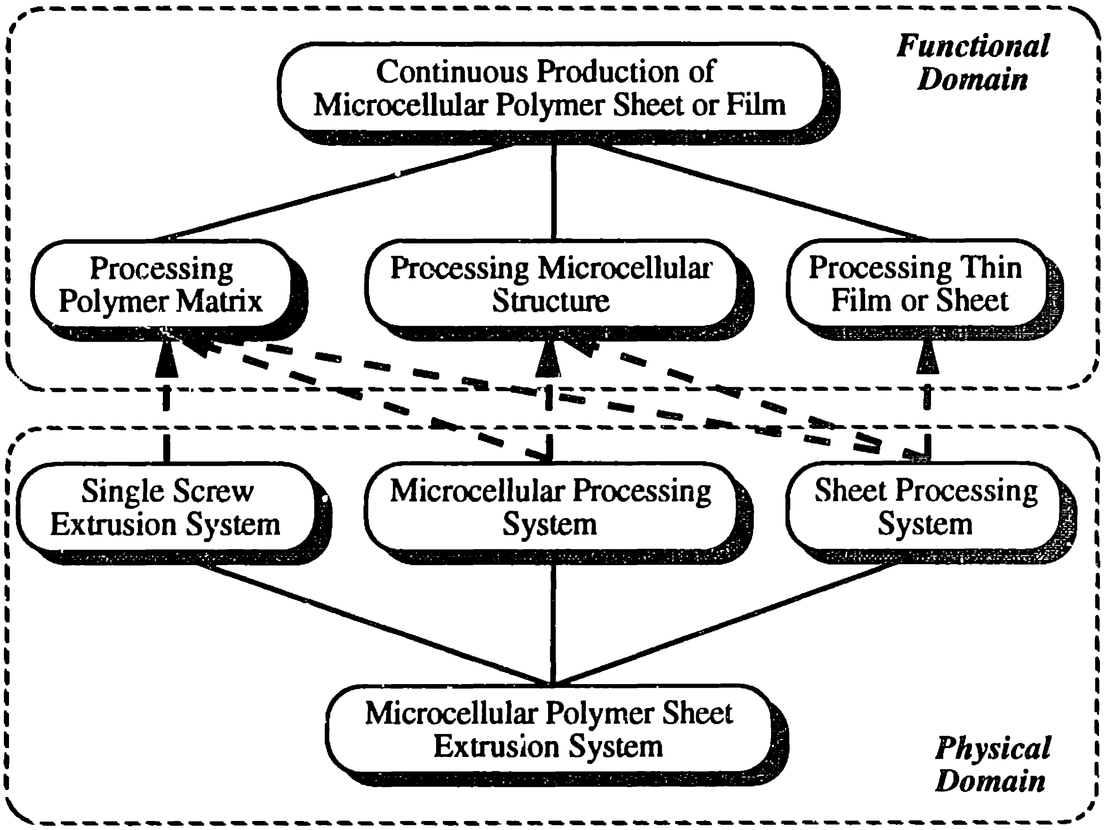

Figure 6.1: Graphical view of the top level microcellular sheet processing system design equation.

[§] Note that the processing system concepts discussed here were initially disclosed by the author as part of recent MIT patents (Cha et al., 1992; Suh et al., 1994).

6.1 Post Saturation and Expansion Concept

The basic idea underlying this concept is to extrude a thin film or sheet which is then saturated with gas and foamed using a thermodynamic instability generated by a rapid decompression and, if necessary, a temperature increase to soften the polymer and allow the cells to grow. A schematic view of this conceptual processing system is shown in Figure 6.2.

In this process, neat polymer pellets are fed by gravity into a plasticating single screw extruder via a hopper. The pellets are transported forward and compacted in the feed zone of the screw by the high frictional force between the pellets and the barrel. In the tapered section of the screw, also called the melting zone, the solid bed of polymer within the screw flights is slowly melted at the barrel/solid bed interface due to mechanical shear work and heat transfer from the temperature controlled barrel. About two-thirds of the way down the screw length, the solid bed is completely molten, and the polymer is further homogenized and pumped in the metering zone of the screw. The polymer then exits the extruder under sufficient pressure to overcome the flow resistance imposed by the downstream components. In the case of Figure 6.2, the flow resistance consists mainly of a standard sheet die.

The sheet emerges from the die into a saturation chamber where, under isothermal conditions, a pressurized gas is diffused into the polymer. At the conceptual level, isothermal conditions are maintained using a series of rollers as shown in Figure 6.2. For a preselected polymer flow rate, the residence time of the sheet in the saturation chamber (i.e., the saturation time) is controlled by the sheet length within the chamber. This length can be preselected at an appropriate value for the sheet thickness or varied using a positionable roller. The pressurized saturation gas (preferably in a supercritical state) is supplied by a compressor. The saturated sheet passes from the saturation chamber into the foaming chamber through a dynamic seal which maintains isobaric saturation conditions.

The decompression occurring as the sheet exits the dynamic seal induces a sufficiently rapid thermodynamic instability to nucleate the cells. The nucleated sheet is then quenched to maintain the proper cell density. Conceptually, Figure 6.2 shows chilled rolls as a means of quenching the sheet. The cell growth and expansion stage of microcellular processing is achieved by passing the nucleated sheet through a heating process where the temperature of the sheet is raised to near the glass transition temperature. This softens the polymer matrix and allows the cells to grow to a selected size.

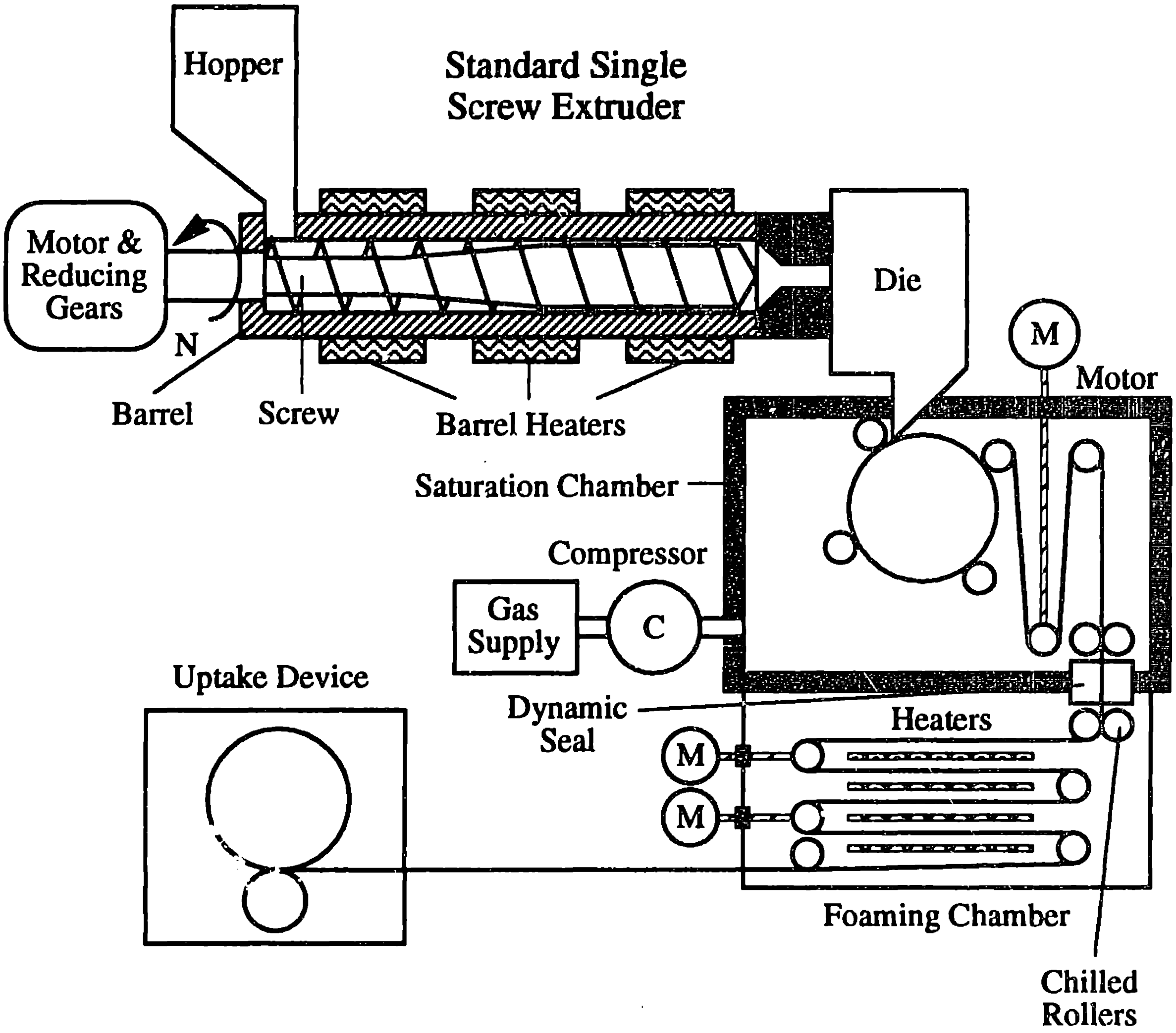

Figure 6.2: Schematic of microcellular sheet extrusion system concept implementing post-saturation and expansion.

Finally, post-processing operations can be performed using standard sheet line equipment not shown in Figure 6.2. Such operations could include annealing to impart crystallinity for improved mechanical properties, surface treatments to impart a surface finish for aesthetic appearance, and/or stretching operations to impart molecular orientation for improved mechanical properties.

6.2 Melt Saturation and Thermal Expansion Concept

As an alternative design concept, consider the microcellular sheet processing system shown in Figure 6.3. The basic idea of this microcellular extrusion system is the formation of a polymer/gas solution in the polymer melt. Microcell nucleation is achieved using a thermodynamic instability generated by a rapid decompression, and independent cell growth is achieved using a thermally activated process to control the viscoelasticity of the polymer matrix.

In the conceptual design of Figure 6.3, the polymer pellets are fed into the extruder via a hopper. As discussed above, the relative motion of the screw and barrel plasticates and pumps the polymer matrix. Within a select region of the metering zone, a metered amount of gas or supercritical fluid is injected into the molten polymer stream forming a two-phase mixture. Mixing of the polymer/gas system and the formation of a single-phase solution is achieved by the shearing action of the screw and a secondary mixing system which promotes gas diffusion into the polymer matrix. Next, the single phase polymer/gas solution is shaped in a near-net form via a die. As the solution flows through the die, it experiences a rapid decompression resulting in microcell nucleation due to the thermodynamic instability associated with the pressure change. The nucleated sheet is now quenched and stabilized. In Figure 6.3, this is shown conceptually using a series of chilled rollers. The sheet is next heated to a temperature near the glass transition allowing the nucleated cells expand to a selected size. In addition, by controlling the residence time of the sheet between the quenching step and the cell growth step, an integral unfoamed skin can be generated on the microcellular sheet. This follows since the gas will continuously diffuse out of the sheet as it moves from the nucleation step to the cell growth step. As in the previous design, various post-processing operations can be performed on the foamed sheet so as to improve the surface finish, molecular orientation, etc.

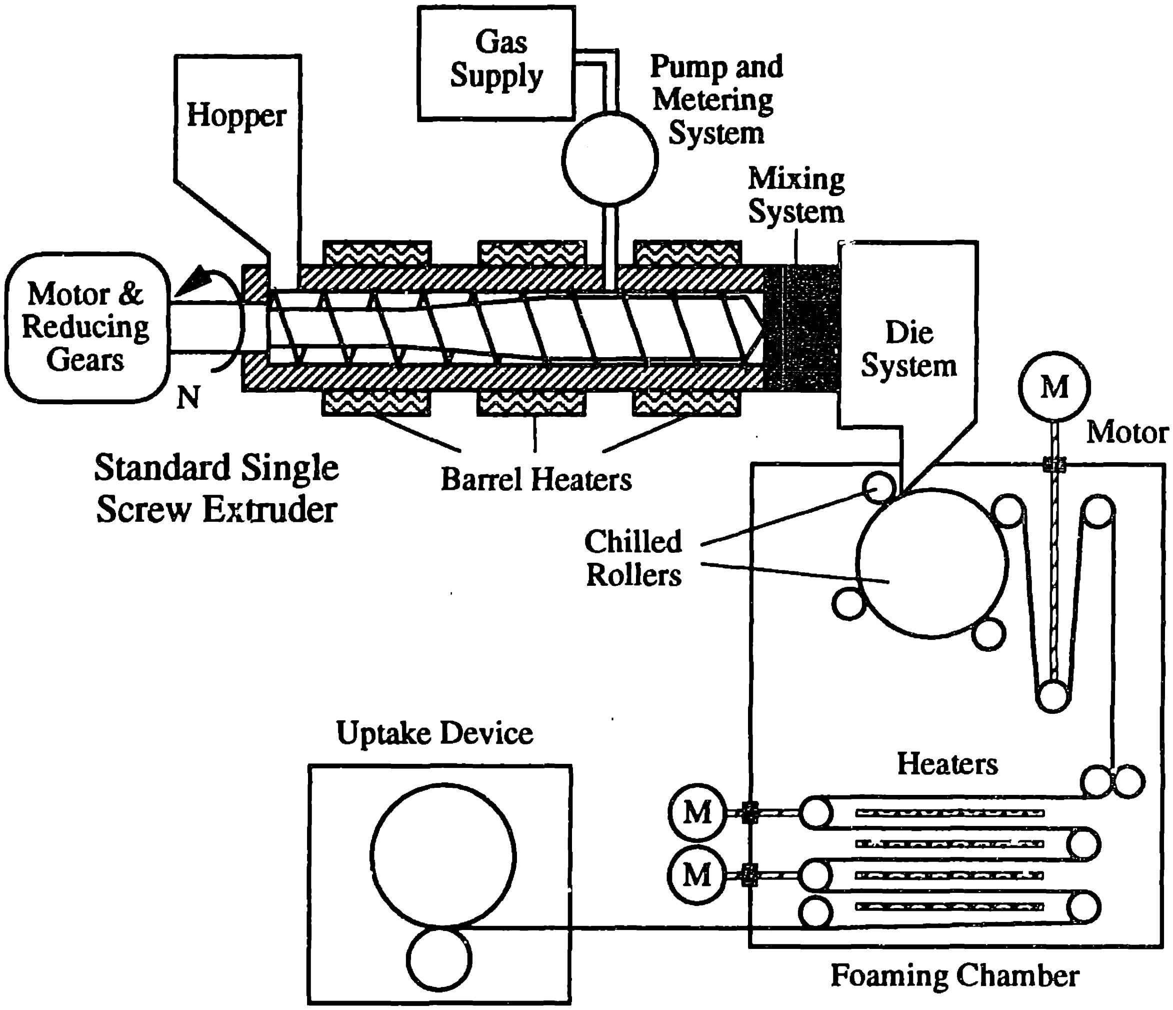

Figure 6.3: Schematic of microcellular sheet extrusion system concept implementing melt saturation and thermal expansion.

6.3 Melt Saturation and Pressurized Expansion Concept

A third conceptual design for the microcellular sheet extrusion system is shown in Figure 6.4. The basic idea of this system is to form a polymer/gas solution in the polymer melt. Microcell nucleation is achieved using a thermodynamic instability generated by a rapid decompression. A pressurized environment is used to maintain the nucleated cells followed by a secondary decompression which controls and stabilizes cell growth.

As in the previous concepts, an extruder is used to melt and pump the polymer matrix. The polymer/gas solution is formed by injecting gas into the molten polymer matrix along the metering zone of the screw. This two-phase polymer/gas system is then mixed and the gas is allowed to diffuse into the polymer matrix to form a single-phase solution. Next, the polymer/gas solution is formed into a near-net shape using a die. This preform is then nucleated as it flows through the die system and the solution pressure rapidly decreases. The nucleated sheet emerges into a secondary chamber which is pressurized. If this chamber is maintained at a pressure substantially the same as the saturation pressure, then the surface gas will diffuse out of the sheet forming an integral skin. In this case, nucleation and growth occur as the sheet passes through the dynamic seal.

Alternately, the secondary chamber can be maintained at ambient pressures so that the formation of an integral skin is minimized. In this case nucleation occurs as the solution pressure drops during flow through the die system. Cell growth occurs as the sheet exits from the die.

Yet another configuration for the secondary chamber is to maintain a sufficient pressure to prevent appreciable cell growth while allowing nucleation to occur as the near-net shape passes through the die and into the secondary chamber. In this case, cell growth occurs as the sheet passes though the dynamic seal and is stabilized by quickly cooling the sheet.

As in the previous processing concepts, post-processing of the microcellular sheet can be performed after the expanding cells are stabilized.

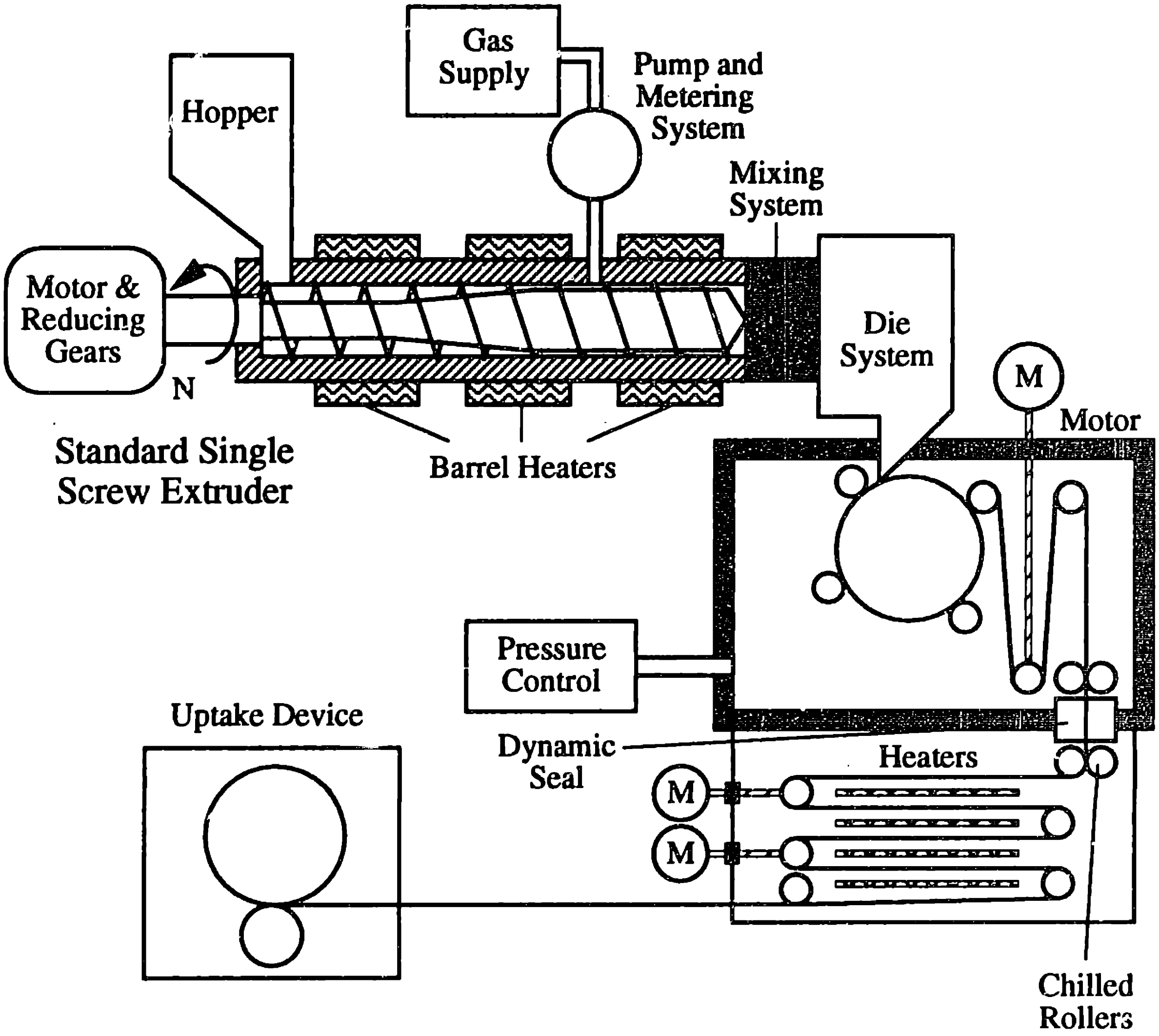

Figure 6.4: Schematic of microcellular sheet extrusion system concept implementing melt saturation and pressurized expansion.

6.4 Discussion of Design Concepts

The conceptual microcellular processing systems presented here have a number of advantages over conventional foam extrusion techniques. The first is the use of dissolved gases rather than chemical blowing agents. As discussed in chapter one, conventional foam extrusion is typically accomplished using either chemical blowing agents or physical blowing agents. The use of chemical blowing agents has a distinct disadvantage in that they are generally low molecular weight organic compounds which decompose when heated to a critical temperature (i.e., usually above the polymer melt or flow temperature). Decomposition of the blowing agent generates both gaseous and solid by-products. While it is possible to dissolve sufficient gas concentrations for microcellular processing using a chemical blowing agent, it is virtually impossible to generate microcellular structures spanning the cell density range of 10^9 to 10^{15} cells/cm^3. This follows since the typical solid by-products range in size form 0.5 to 1 μm. This results in heterogeneous nucleation of the polymer/gas solution at the phase interfaces thereby limiting the number and distribution of the nucleated cells to the number and distribution of the by-product phase. The result is large cell foams having non-uniform cell distributions.

The conceptual designs presented here also have advantages over the conventional foam extrusion processes which use physical blowing agents. In general, the conventional processes cannot dissolve sufficient gas concentrations for microcellular processing nor can they nucleate polymer/gas solution flows at the rates necessary for microcellular processing.

A final advantage of these conceptual designs over conventional processes is the decoupling of the primary functional requirements: solution formation, cell nucleation, cell growth, and shaping. In conventional foam extrusion, the nucleation and growth requirements are treated as a single operation (i.e., foaming) and are therefore coupled. The conceptual designs presented here provide for independent control of cell nucleation and cell growth as well as independent control of solution formation and shaping.

CHAPTER 7

DETAILED SYSTEM DESIGN

7.0 Introduction and Concept Selection

In order to proceed with the detailed system design, a selection between the conceptual designs of chapter 6 must be made. After a feasible design concept is selected, the detailed design of the microcellular sheet extrusion system will be presented. The selection of a feasible design concept is based on two criteria:

C_1 = The process should be capable of medium volume industrial production rates (e.g., a linear sheet velocity of 2 cm/s).
C_2 = The process should maintain safety requirements when scaled-up.

Of particular interest is the production rate constraint since it makes some major distinctions between the process concepts.

First, let's look at the post-saturation and expansion design concept of Figure 6.2. In this process, a thin sheet or film is extruded though a die and post-saturated with gas under high pressure. Here the processing rate is limited by the gas saturation step since diffusion processes are inherently slow. To determine the gas saturation rate or time, the diffusion rate can be estimated using a generalized form of Fick's law given by equation (7-1). From this equation, an approximate relation can be derived for the gas diffusion time (equation 7-2) base on a characteristic diffusion length, l. To estimate an upper bound on the gas diffusion time in the post-saturation process, equations (7-2) and (7-3) can be used where the characteristic diffusion distance l is taken as the half sheet thickness. As a typical case, consider the extrusion of polystyrene (PS) which has a recommended extrusion temperature of 200 °C. The constants in equation (7-3) for PS are adopted from Stannett (1968), $D_o = 0.128\ \mathrm{cm^2/s}$ and $\Delta E_D/R = 4381$ K (resulting in diffusivities for thermally softened PS which agree favorably with the data of Newitt and Weale, 1948). The estimated sheet saturation times at various temperatures are shown in Figure 7.1 as a function of the half sheet thickness.

$$\frac{Dc}{Dt} = \nabla \bullet (D\, \nabla c) \qquad (7\text{-}1)$$

$$\tau \approx \frac{l^2}{D} \tag{7-2}$$

$$D = D_0 \exp\left(-\frac{\Delta E_D}{RT}\right) \tag{7-3}$$

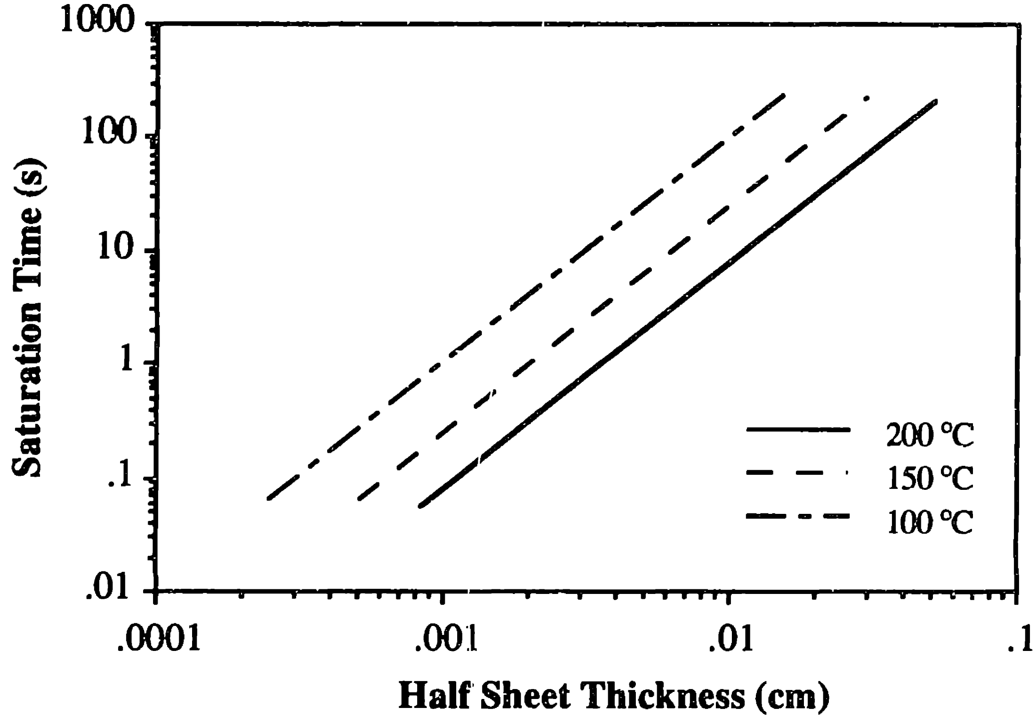

Figure 7.1: Estimated saturation times for saturating a continuous sheet PS having thickness 2·l.

In order to keep the production rates within an acceptable range, the saturation process should take less than one minute. ‡ Based on Figure 7.1, it is evident that the post-saturation technique is feasible only if films under 0.3 mm are used (at temperatures above 150 °C). Although thicker sheets can be saturated within one minute at temperatures near 200 °C, the polymer matrix is exceedingly weak at these elevated temperatures, resulting in large scale relaxation and the loss of dimensional stability. The inability to microcellular process cross-sections thicker than 0.5 mm is a decisive drawback of the post-saturation and expansion concept.

---

‡ For the case where the sheet saturation takes approximately one minute and the sheet has a linear velocity of 2 cm/s, the required sheet length within the saturation chamber is 1.2 m. This is an excessive sheet length requiring a large, high-pressure saturation chamber. Such chambers are relatively unsafe compared with a melt saturation technique. Therefore, the saturation time should be kept under one minute to reduce the saturation chamber size.

Another potential limiting factor of both the post-saturation/expansion concept (Figure 6.2) and the melt saturation/thermal expansion concept (Figure 6.3) is the use of a thermal cycle to activate the cell growth process. In general, polymers have low thermal conductivities and are classified as insulators. Therefore, the heat conduction times necessary to uniformly soften the polymer sheet and allow for cell growth can be relatively long, resulting in large temperature gradients across the sheet thickness. If large thermal gradients exist, then cell growth occurs unevenly over the sheet cross-section where the cells closest to the surface expand first. The expansion of the surface cells depletes the gas available for expanding the cells of the center core, resulting in larger cells towards the surface and smaller cells in the center. Such cell morphologies are undesirable since wide cell size distributions degrade mechanical performance (Martini et al., 1982, Waldman, 1982).

In order to bound the production rate of the thermally activated expansion process, an estimate of the heating time necessary to achieve uniform temperatures is needed. As a first order approximation, the heat conduction time will be taken as the limiting heat transfer process. Starting with the heat conduction equation (7-4), an estimate of the heating time can be derived and is given by equation (7-5) where l is the half sheet thickness, ρ_p is the polymer density, c_p is the polymer specific heat, and k is the polymer thermal conductivity. Figure 7.2 shows the heating time of a PS sheet as a function of the half sheet thickness and various temperatures where: $\rho_p = 1.05$ g/cm^3; $c_p = 1850$, 1950, and 2040 J/kg·K; and k = 0.100, 0.138, and 0.160 J/m·s·K at temperatures of 100, 150, and 200 °C, respectively (Hall, 1989; Kline and Hansen, 1970; Tadmor and Gogos, 1979). Figure 7.2 clearly shows a limiting sheet thickness exists for a maximum foaming time of one minute. At 200 °C, the sheet must be less than 1.5 mm, and at 100 °C, the sheet must be less then 1.1 mm.

$$\rho\, c_p \frac{DT}{Dt} = \nabla \bullet (k\, \nabla T) \tag{7-4}$$

$$\tau \approx \frac{\rho\, c_p}{k}\, l^2 \tag{7-5}$$

Since polymers absorb electromagnetic radiation in a limited band of the infrared spectrum, another possible heating method for thermally activated expansion is infrared radiation. For incident radiation along a single axis, the radiation absorption rate is normally characterized by a monochromatic extinction coefficient, β. Using a variation of Beer's law, the rate at which energy is absorbed can be shown to follow equation (7-6)

(Holman, 1981). For thermoplastics, the extinction coefficient is on the order of 250 cm^{-1}. Due to the exponential nature of the heat absorption, it is clear that at characteristic distances, x, greater than $l \approx 0.12$ mm, the magnitude of absorbed energy is negligible and the heat transfer problem simplifies to a conduction problem as discussed above. One can conclude then that thermally activated expansion processes cannot meet the production rate constraint except for relatively thin sheets.

$$q_{rad} = I_o e^{-\beta x} \tag{7-6}$$

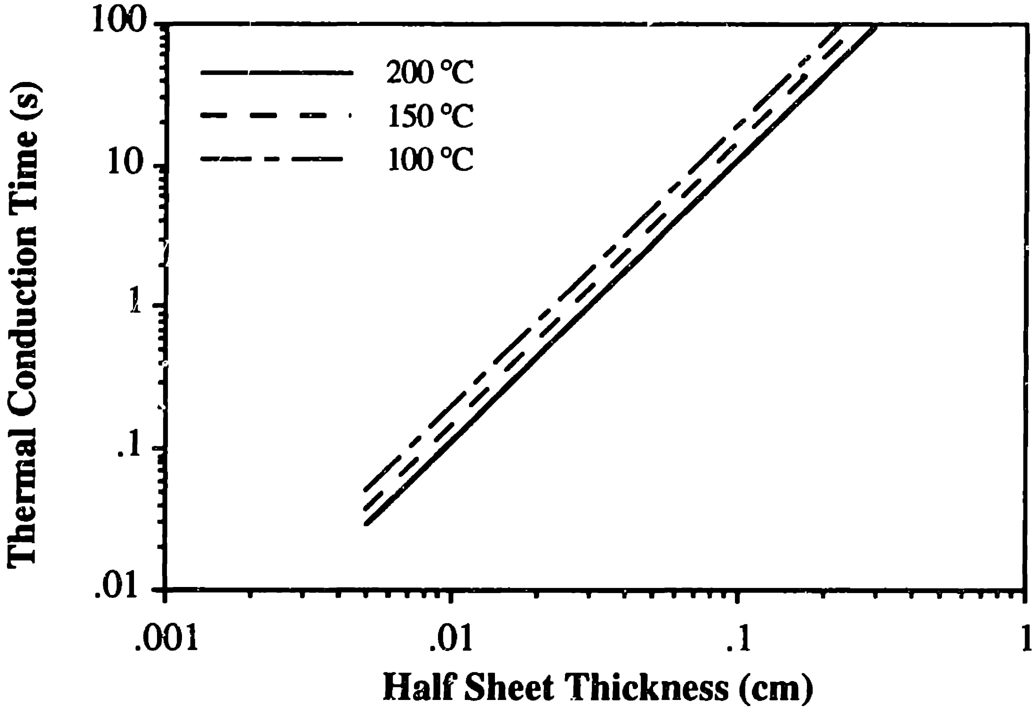

Figure 7.2: Estimated heat conduction times for foaming a continuous PS sheet having thickness 2·l.

Safety is another important criteria/constraint to consider when selecting a feasible design concept, particularly since the microcellular extrusion process involves the use of high pressure gas (i.e., on the order of 20.7 to 41.4 MPa). The safety issues involved with high pressure gas stem from the fact that gas is highly compressive and has the ability to store a great deal of energy. In order to relieve a high pressure, large volumetric expansions are needed. In contrast, liquids such as polymer melts require relatively small expansions to relieve large pressures since they have low compressibilities. Taking a closer look at the post-saturation and expansion process (Figure 6.2), a particular concern is the high pressure saturation chamber which is sized based on the dimensions of the final sheet. While the use of a suitable roller system can reduce the height and to some extent the length of the saturation chamber, the width of the chamber is mandated by the width of the sheet. If the specific application requires narrow sheets on the order of 10 cm wide, then the construction of a suitable pressure chamber for high-temperature, corrosive environments is feasible. However, if the application requires wider sheets, then the required pressure chambers become unreasonably heavy and bulky in order to meet safety requirements. For wide sheets and high production rates, the liability involved in using the post-saturation technique is too large to justify its use over the other microcellular sheet extrusion concepts.

Based on this first order analysis of the design concepts, it is clear that both the post-saturation/expansion (Figure 6.2) and the melt saturation/thermal expansion (Figure 6.3) concepts satisfy constraints C_1 and C_2 within only a limited range of cross-sectional sheet dimensions. Such dimensional constraints put undo limitation on the prototype microcellular processing system particularly with respect to potential industrial applications. Therefore, it was decided not to pursue these concepts further in the detailed design stage.

The following detail design is based on the melt saturation and pressurized expansion concept shown in Figure 6.4. The key advantage of this concept is that it provides a relatively convenient technique for controlling and stabilizing the microcellular foaming process by using a staged pressure drop.

7.1 Hierarchical System Design

In the detailed system design, the melt saturation and pressurized expansion concept presented in section 6.3 is expanded into a functional and physical hierarchy consisting of five levels. The scope of the system design is shown in the functional requirement, design parameter, and process variable design trees of Figures 7.3, 7.4, and 7.5. These design trees represent the expanded functional and physical hierarchy of equation (6-1). The decoupled nature of equation (6-1) implies that each of the level-two functional requirements can be expanded independently. In the next three sections, detailed sub-system designs for processing the polymer matrix, processing the microcellular structure, and processing the sheet will be presented with the use of a basic engineering analysis.

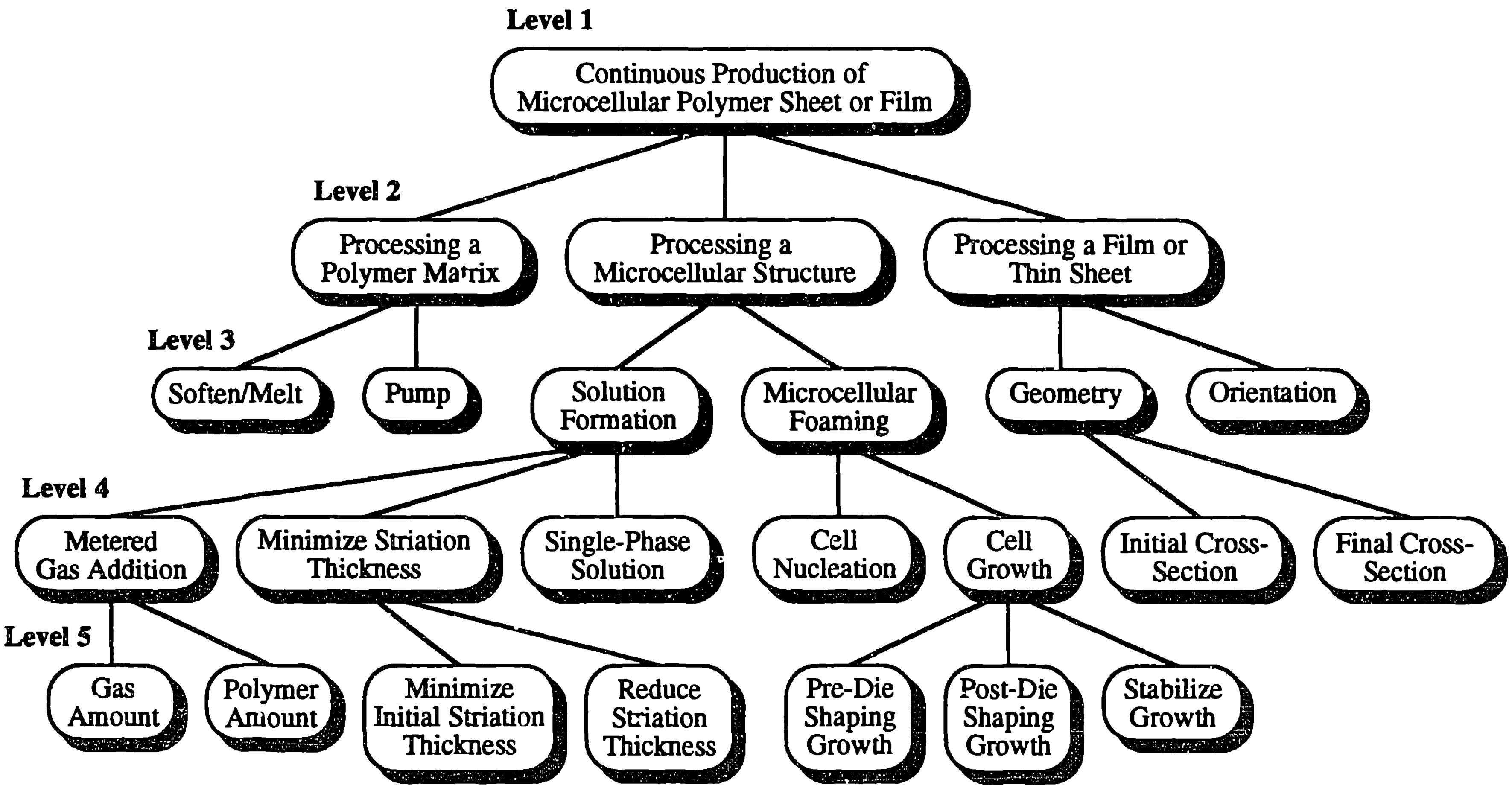

Figure 7.3: Functional requirement hierarchy for the microcellular sheet processing system.

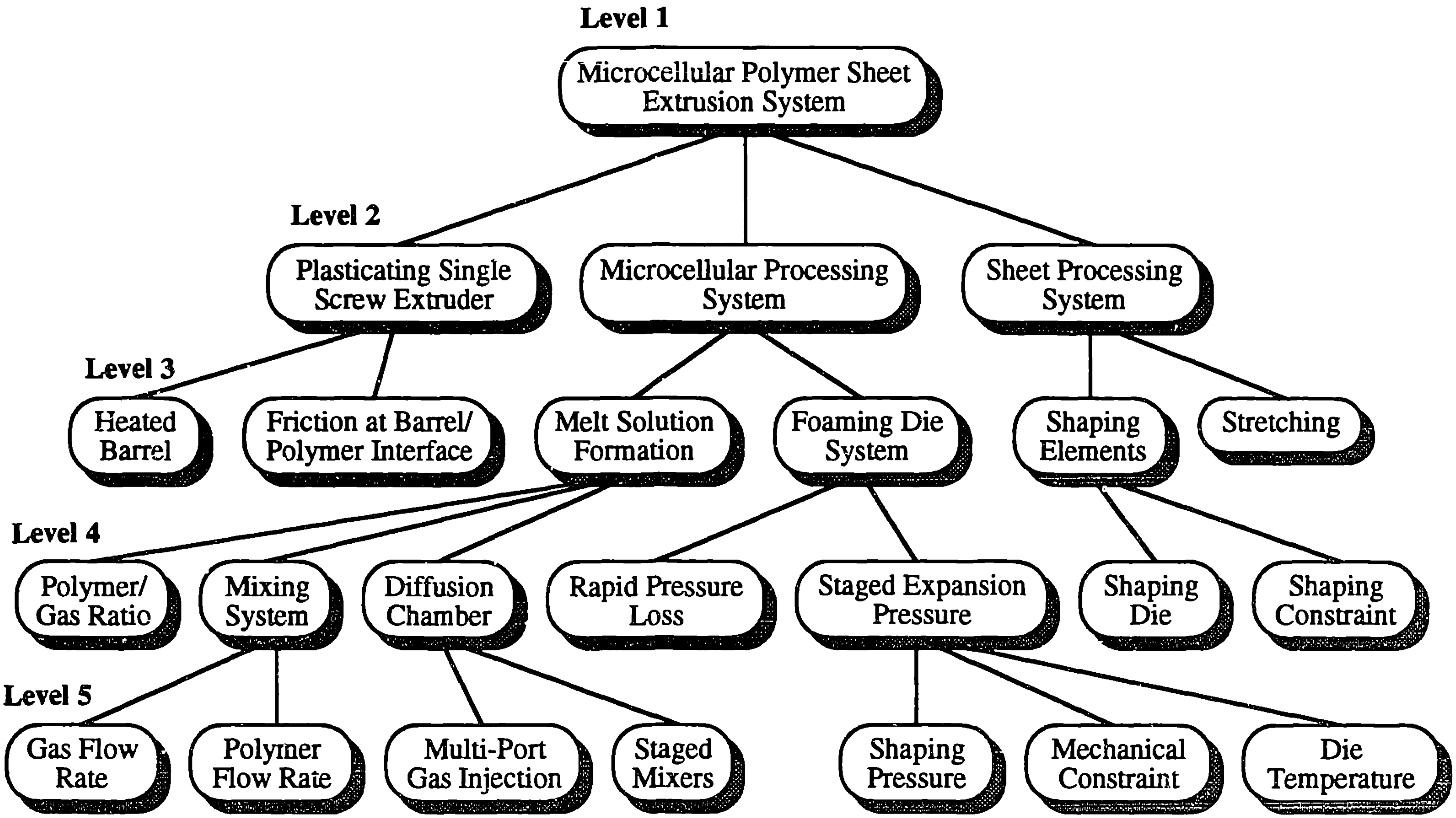

Figure 7.4: Design parameter hierarchy for the microcellular sheet processing system.

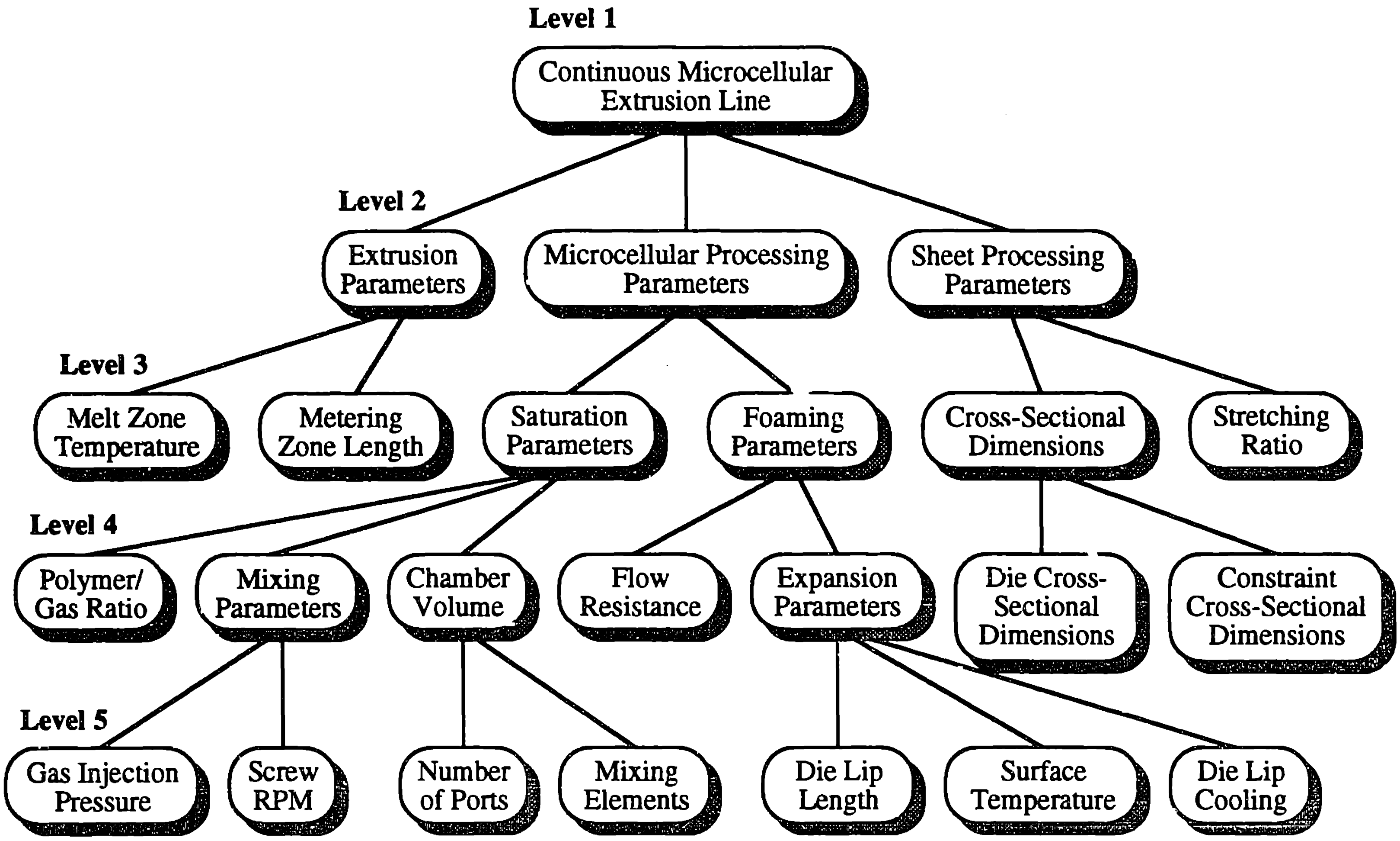

Figure 7.5: Process variable hierarchy for the microcellular sheet processing system.

7.2 Polymer Processing System Design

First, consider FR_1 which is the functional requirement to process the polymer matrix. This requirement is satisfied by a plasticating single screw extruder (Figure 7.6). There are two functional requirements for the extrusion system in continuous microcellular processing: (1) to soften or melt the polymer and (2) to transport or pump the polymer so that a continuous supply exists for shaping and microcellular processing operations. Based on these functional requirements, the physical design parameters and process variables specified for the extrusion system are given in equations (7-5) and (7-6).

$$\begin{Bmatrix} FR_{11} = \text{Melting} \\ FR_{12} = \text{Pumping} \end{Bmatrix} = \begin{bmatrix} X & 0 \\ X & X \end{bmatrix} \begin{Bmatrix} DP_{11} = \text{Heated Barrel} \\ DP_{12} = \text{Friction at Barrel/Polymer Interface} \end{Bmatrix} \tag{7-5}$$

$$\begin{Bmatrix} DP_{11} = \text{Heated Barrel} \\ DP_{12} = \text{Friction at Interface} \end{Bmatrix} = \begin{bmatrix} X & 0 \\ X & X \end{bmatrix} \begin{Bmatrix} PV_{11} = \text{Melt Zone Temp.} \\ PV_{12} = \text{Metering Zone Length} \end{Bmatrix} \tag{7-6}$$

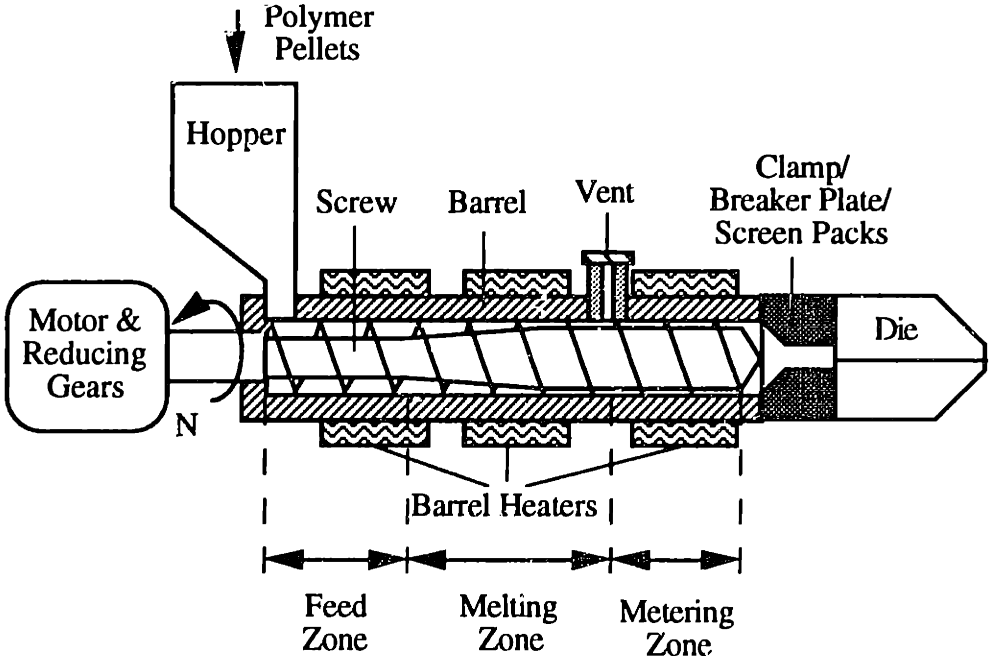

Figure 7.6: Schematic of a plasticating single screw extruder.

The decoupled nature of equations (7-5) and (7-6) follows from a basic analysis of the plasticating extrusion process. Such an analysis was performed by Tadmor (1966) and Tadmor and Klein (1970) to reveal the physical mechanisms that underlie the plasticating extrusion process. Consider first the melting process. A cross-sectional view of the melting zone in Figure 7.6 is shown in Figure 7.7 illustrating a single channel of the barrel, screw, and polymer system. In general, the compacting process of the feed zone transports a solid polymer bed into the melting zone. A combination of the shear work done at the barrel/solid interface and the heat transferred from the barrel melt the polymer near the barrel surface. The wiping motion of the trailing screw flight transports the film of molten polymer at the barrel interface towards the front side of the channel forming a pool of molten polymer in front of the solid bed. The thickness of the molten polymer film remains constant throughout the melting zone while the width of the solid bed decreases as the polymer melts. Within the molten pool, the polymer experiences a vortex motion. The vortex flow enhances the homogeneity of the polymer melt through laminar mixing. Upon exiting the melting zone, a uniform polymer melt is produced.

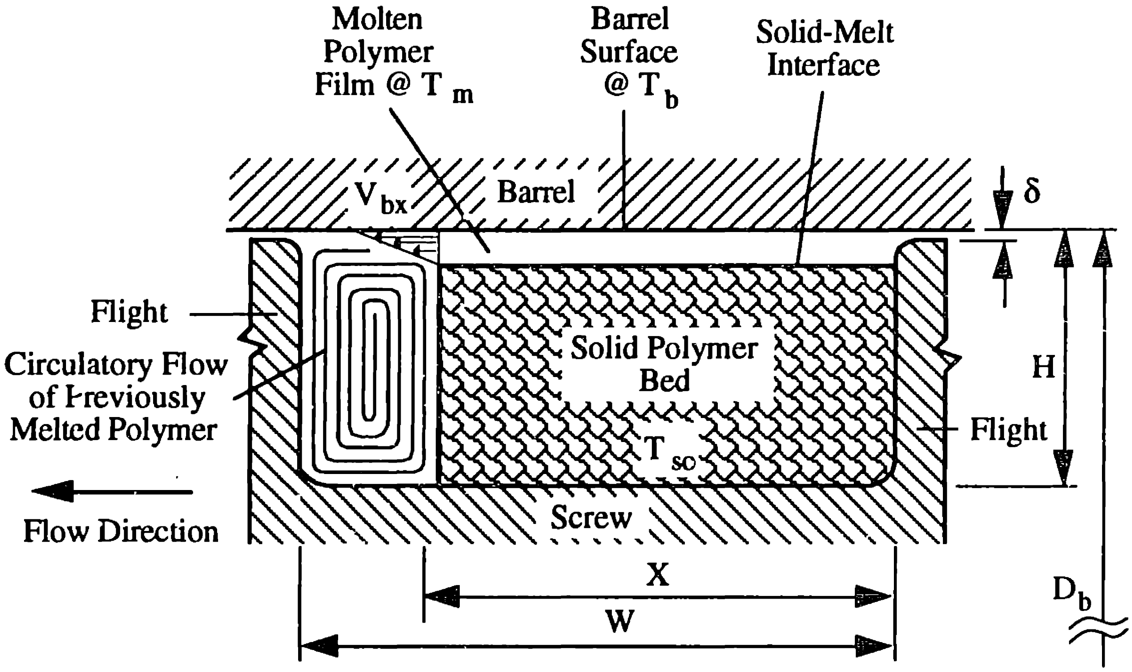

Figure 7.7: Idealized cross-section of the melting process in a single screw extruder.

A number of basic assumptions are made for the analysis of the melting process. First, it is assumed that the entire process is at steady state conditions. The solid polymer bed is assumed to be deformable and continuous, and the width of the solid bed is assumed to decrease gradually. The deformable nature of the polymer bed is evident by the fact that the molten polymer film maintains a constant thickness even though melting occurs at the barrel interface. In order to raise the temperature of the solid polymer interface to the melting or softening point and to supply the heat of fusion, ΔH, there are two contributing heating sources: (1) the viscous shear work of the molten polymer film and (2) the heat transferred from the barrel. Using an energy balance, the melting rate per length along the melting zone of the screw, q_Z, for an incompressible Newtonian flow is given by (Tadmor and Klein, 1970):

$$q_Z = \left(\frac{V_{bx}\,\rho_m \left[k_m (T_b - T_m) + \mu(T)\, V_j^2 / 2 \right] X}{2 \left[\Delta H + c_p (T_m - T_{so}) \right]} \right)^{1/2} \tag{7-7}$$

where $V_{bx} = \pi\, N\, D_b \sin\theta_b$ and is the velocity along the barrel axis of the molten polymer film across the screw channel, ρ_m is the melt density, k_m is the polymer thermal conductivity, μ is the viscosity at the average temperature of the polymer film, V_j is the scalar velocity of the polymer-film in shear flow, X is the width of the solid bed, c_p is the heat capacity of the polymer, T_m is the polymer melt temperature, T_b is the barrel temperature, T_{so} is the solid-bed core temperature, N is the screw speed, D_b is the barrel diameter, and θ_b is the screw helix angle at the barrel.

Equation (7-7) illustrates that the barrel temperature in the melting zone, T_b, can be used to control the heat flux into the solid bed, q_Z, whereby satisfying the melting requirement, FR_{11}. It should be noted that equation (7-7) also indicates that the shear work is a very effective means of melting the polymer. In general, the shear work provides the majority of the heat for melting. However, the shear work (governed by the magnitude of the relative shear velocity, V_j) was not chosen as the design parameter to satisfy the melting requirements since it is a strong function of the screw speed, N. As will be shown momentarily, the screw speed is a design parameter utilized to satisfy the polymer/gas solution formation requirements of the system. The dependence of both melting and solution formation requirements on the screw speed is one of the primary reasons that DP_2 is shown to influence FR_1 in design equation (6-1) (i.e., a decoupled process).

The pumping requirement of the polymer processing system mandates that a continuous, stable supply of molten polymer be delivered by the extruder within a pressure range suitable for downstream processing equipment. To understand the pumping stage of the extrusion process, consider the flow of the molten polymer in the metering zone. Here the polymer flow is controlled by (1) the drag effect of the barrel on polymer melt which acts as a positive displacement mechanism and (2) the backward flow down the channel and the leakage flow over the screw flights resulting from the pressure increase along the screw. Approximating the flow along a screw of constant channel depth as isothermal, incompressible, and Newtonian yields an extrusion flow rate, Q, given by equation (7-8) (see Tadmor and Gogos, 1979 for a derivation).

$$Q = \frac{1}{2}\pi N D_b \cos\theta_b W H F_d - \frac{W H^3}{12\,\mu(T)} \frac{\Delta P}{L}(1 + f_L) F_p \tag{7-8}$$

In equation (7-8), the leakage flow factor is

$$f_L = \left(\frac{\delta}{H}\right)^3 \frac{e}{W}\frac{\mu}{\mu_f} + \frac{\left(1 + \frac{e}{W}\right)\left[\frac{1 + e/W}{\tan^2\theta} - \frac{6\pi\,\mu(T)\,N D_b \cos\theta_b (H - \delta)}{H^3(\Delta P/L)}\right]}{1 + \frac{e}{W}\frac{\mu}{\mu_f}\left(\frac{H}{\delta}\right)^3} ,$$[†]

the drag flow shape factor is

$$F_d = \frac{16 W}{\pi^3 H} \sum_{i\,\mathrm{odd}}^{\infty} \frac{1}{i^3} \tanh\left(\frac{i\pi H}{2W}\right) ,$$

the pressure flow shape factor is

$$F_p = 1 - \frac{192 H}{\pi^2 W} \sum_{i\,\mathrm{odd}}^{\infty} \frac{1}{i^5} \tanh\left(\frac{i\pi W}{2H}\right) .$$

W is the channel width, H is the channel depth, ΔP is the pressure differential across the metering zone, L is the metering zone length, δ is the clearance of the screw flight and barrel, e is the width of the screw flight, θ is the screw helix angle, and μ_f is the viscosity across the flight (i.e., at a higher shear rate than in the channel).

While equation (7-8) is somewhat cumbersome, it illustrates that the length of the metering zone L can be used to control the pumping requirement, such that the polymer melt is maintained as a stable high pressure flow. In other words, by using a longer metering zone in the extruder, it is possible to reduce the sensitivity of the polymer flow rate to perturbations in the pumping pressure. An alternate design would be to use a gear pump at the head of the extruder to satisfy the pumping requirement. In general, gear pumps provide a better means of maintaining independence between the pressure and the flow rate. However, resource constraints precluded the use of a gear pump in this work.

Since the length of the metering zone is constant for a given screw design, it is also convenient to specify a secondary process variable which can be controlled during the process to satisfy the pumping requirement. From equation (7-8), it is apparent that the

---

[†] While it is very difficult to evaluate the leakage flow in a screw pump, Tadmor and Gogos (1979) present this modified leakage flow factor f_L for isothermal Newtonian flow in rectangular channels (i.e., non-helical) as an approximation for the leakage flow in a screw pump.

viscosity of the polymer melt, μ, has a similar effect to the metering zone length. In the context of the extruder, the viscosity can be controlled using the barrel temperature, T_b. Therefore, the metering-zone barrel temperature can be specified as an alternate design parameter for satisfying the pumping requirement during processing.

In addition to the melting and pumping functional requirements, there are three constraints associated with the polymer processing requirement:

C_{11} = Minimize the decomposition of the polymer.
C_{12} = Minimize the molecular weight breakdown of the polymer.
C_{13} = Homogenize the temperature of the polymer melt.

The necessity of these constraints follows from the macromolecule structure of the polymer matrix. The two former constraints relate to the microstructure of the final polymer matrix and its influence on mechanical performance. The latter constraint relates to the macrostructure of the final sheet influencing dimensional stability and aesthetic appearance. In either case, if these constraints are not satisfied, then the resulting polymer sheet will have poor, non-uniform mechanical properties.

In order to minimize the decomposition or degradation of the polymer during processing, the flow channels must be streamlined to minimize the formation of stagnation points and vortex flows. Such flow phenomena can occur as a result of abrupt changes in the flow cross-section. Stagnation points and vortex flows result in long residence times of polymer flow particles at elevated temperatures, leading to the thermal degradation of the polymer matrix and poor mechanical properties.

Many hygroscopic polymers, which are typically polymerized by a polycondensation technique, can suffer from severe breakdown of the polymer chains at high temperatures in the presence of water. The breakdown of molecular chains results from a reverse polymerization process where the water molecules react with the polymer chains forming some precursor monomers and diminishing the molecular weight of the polymer matrix. In order to minimize this problem and satisfy C_{12}, the pellets of hygroscopic polymers are dried in a forced-air dehumidifying dryer utilizing a desiccant material. The drying requirements for commercial thermoplastics are typically supplied by the material manufacturers.

Finally in order to insure the molten polymer supplied by the extruder is homogeneous having a uniform temperature, it is important to promote the vortex motion of the polymer melt in the melting zone (i.e., the melt pools) so that the melt experiences laminar mixing to homogenize the flow. In order to promote the vortex motion in the melting zone, a minimum head pressure at the extruder discharge is necessary. Typical microcellular extrusion pressures are on the order of thousands of pounds per square inch and fall well within the pressure range necessary for satisfying constraint C_{13}. In addition, the polymer/gas solution formation system includes an intense mixing phase. These mixing operations also promote homogeneity of the polymer melt. Therefore, constraint C_{13} is met by the inherent nature of the microcellular extrusion process.

7.3 Microcellular Processing System Design

The next level-two functional requirements that must be satisfied relate to continuously producing a microcellular structure. As discussed in detail in chapter 3, microcellular processing must incorporate three elements: (1) the formation of a polymer/gas solution, (2) the nucleation of billions of microcells, and (3) the growth of stable nuclei to reduce the bulk density. Figure 7.3 presents these processing functional requirements over the span of two hierarchy levels. The first two functional requirements that must be satisfied by the microcellular processing system are:

FR_{21} = Formation of a polymer/gas solution.
FR_{22} = Processing of a microcellular foam structure.

To satisfy these FRs, the following DPs and PVs were selected and are given in design equations (7-9) and (7-10).

$$\begin{Bmatrix} FR_{21} = \text{Solution Fomation} \\ FR_{22} = \text{Microcellular Foaming} \end{Bmatrix} = \begin{bmatrix} X & X \\ 0 & X \end{bmatrix} \begin{Bmatrix} DP_{21} = \begin{matrix}\text{Polymer Melt} \\ \text{Solution Formation}\end{matrix} \\ DP_{22} = \text{Foaming Die System} \end{Bmatrix} \tag{7-9}$$

$$\begin{Bmatrix} DP_{21} = \text{Melt Solution Formation} \\ DP_{22} = \text{Foaming Die System} \end{Bmatrix} = \begin{bmatrix} X & X \\ 0 & X \end{bmatrix} \begin{Bmatrix} PV_{21} = \text{Saturation Parameters} \\ PV_{22} = \text{Foaming Parameters} \end{Bmatrix} \tag{7-10}$$

The solution formation requirement is satisfied using a continuous solution formation technique where the gas is injected directly into the polymer melt during the extrusion process. The particular solution formation system used was developed by Park (1993), and the basic principles are presented in section 3.1.2. The design aspects of this system are presented here so as to demonstrate an integrated system design. In general, the configuration of the solution formation system is such that within a finite processing window, variations in the saturation parameters will have relatively little influence on the microcellular foaming requirements. This fact will become clearer as the design hierarchy is expanded further.

The microcellular foaming requirement is satisfied by a foaming die system which performs the cell nucleation and growth functions. In order to better understand the decoupled nature of the design equations (7-9) and (7-10), it is useful to expand these requirements into the next hierarchy level.

Once a polymer/gas solution is formed, microcellular processing proceeds by first nucleating stable microcells followed by the growth of the stable nuclei. Nucleation is initiated using a rapid thermodynamic state change which creates a supersaturated polymer/gas matrix (see chapter 3). In this design, a rapid pressure loss was chosen as a means for generating the thermodynamic instability. The rationale for this selection can be seen by looking back at equations (3.2-6) and (3.2-7). From these equations, it is apparent that a pressure change, Δp, is a dominant factor in controlling the nucleation rate and therefore cell nucleation density. The second stage of the foaming process is the growth of stable nuclei. Based on the cell growth analysis of section 3.3 and equations (3.3-8) and (3.3-9), it is apparent that the pressure of the polymer matrix surrounding the expanding cells, p_∞, can be used to suppress the growth rate and control the expansion process.

Based on this first order analysis, design equations (7-11) and (7-12) were formulated to satisfy the functional requirements of cell nucleation and cell growth. The nucleation requirement is satisfied by subjecting the polymer/gas solution to a large flow resistance creating a rapid pressure loss. Cell growth control is achieved using a set of expansion parameters to implement a pressurized, two-stage expansion process. The decoupled nature of equations (7-11) and (7-12) follows from the fact that in a continuous processing system (i.e., a continuous flow stream), downstream pressure changes will always influence upstream pressures. [§] On the other hand, the decompression used to satisfy the nucleation requirement does not influence the growth of the cells. The specific embodiments designed to satisfy the cell nucleation and cell growth requirements will be presented in chapters 8 and 9.

[§] Strictly speaking, this is not always true, since in compressible fluid flows approaching Mach one, changes in downstream pressure are isolated form the upstream conditions. This follows since the pressure waves which "feedback" the downstream conditions propagate at the same speed as the fluid flow and therefore can not reach the upstream.

$$\begin{Bmatrix} FR_{221} = \text{Cell Nucleation} \\ FR_{222} = \text{Cell Growth} \end{Bmatrix} = \begin{bmatrix} X & X \\ 0 & X \end{bmatrix} \begin{Bmatrix} DP_{221} = \text{Rapid Pressure Loss} \\ DP_{222} = \text{Staged Expansion Pressure} \end{Bmatrix} \tag{7-11}$$

$$\begin{Bmatrix} DP_{221} = \text{Rapid Pressure Loss} \\ DP_{222} = \text{Staged Expansion Pressure} \end{Bmatrix} = \begin{bmatrix} X & X \\ 0 & X \end{bmatrix} \begin{Bmatrix} PV_{221} = \text{Flow Resistance} \\ PV_{222} = \text{Expansion Parameters} \end{Bmatrix} \tag{7-12}$$

Next, let's look at the solution formation requirements for the extrusion system. The analysis of this system is presented by Park (1993) and summarized in section 3.1.2. Three functional requirements must be independently satisfied when using a saturation technique where gas is injected directly into the melt.

FR_{211} = Inject a metered amount of gas into the polymer melt.
FR_{212} = Minimize the striation thickness.
FR_{213} = Form a single-phase polymer/gas solution.

Metering of the gas is necessary, since only a soluble amount of gas should be injected into the polymer melt. If gas is injected beyond the soluble limit, as estimated from equation (3.1-21), then a single-phase solution cannot be formed thereby preventing microcellular nucleation. The second requirement for solution formation is to minimize the striation thickness. The striation thickness is a measurement of mixing effectiveness and represents the characteristic distance between discrete phases. For the polymer/gas solution formation process, the striation thickness is twice the characteristic diffusion distance of the gas molecules. Therefore, minimizing the striation thickness minimizes the gas diffusion time for saturation. Finally, to form a single-phase solution, the gas must completely diffuse into the polymer matrix. Based on these FRs, the DPs and PVs selected for the solution formation system are given in equations (7-13) and (7-14) with the corresponding hardware shown in Figure 7.8.

$$\begin{Bmatrix} FR_{211} = \text{Metered Gas} \\ FR_{212} = \text{Striation Thickness} \\ FR_{213} = \text{Single Phase Solution} \end{Bmatrix} = \begin{bmatrix} X & 0 & 0 \\ X & X & 0 \\ X & X & X \end{bmatrix} \begin{Bmatrix} DP_{211} = \text{Polymer/Gas Ratio} \\ DP_{212} = \text{Mixing System} \\ DP_{213} = \text{Diffusion Chamber} \end{Bmatrix} \tag{7-13}$$

$$\begin{Bmatrix} DP_{211} = \text{Polymer/Gas Ratio} \\ DP_{212} = \text{Mixing System} \\ DP_{213} = \text{Diffusion Chamber} \end{Bmatrix} = \begin{bmatrix} X & 0 & 0 \\ X & X & 0 \\ X & X & X \end{bmatrix} \begin{Bmatrix} PV_{211} = \text{Polymer/Gas Flow Rates} \\ PV_{212} = \text{Mixing Parameters} \\ PV_{213} = \text{Flow Length} \end{Bmatrix} \tag{7-14}$$

As shown in Figures 7.3 through 7.5, the metered gas requirement is expanded into functional requirements governing the mass of the gas injected and the mass of the polymer supplied to the solution formation system. These requirements are satisfied by the physical design parameters of gas flow rate and polymer flow rate, respectively (equation 7-15). The process variables used to control these DPs are the pressure of the gas supplied to the metering system, P_i, and the rotation speed of the screw, N, as shown in Figure 7.8 (equation 7-16). Equation (7-8) illustrates the functional dependence of the screw speed, N, to the polymer flow rate, Q. The metering system for supplying the required gas flow rate is discussed by Park (1993). The metering is accomplished using a porous flow resistance and a high pressure gas supply. By controlling the gas pressure supplied to the porous material, P_i, the flow rate of the gas, Q_g, can be controlled (i.e., $P_i - P_b \approx R_p Q_g$ where R_p is the flow resistance of the porous material). The decoupled nature of equations (7-15) and (7-16) follow from the fact that the polymer flow rate can influence the barrel pressure P_b at the point of gas injection [see equation (7-8)] and therefore affects the gas flow rate. In contrast, the gas flow rate does not appreciably influence the polymer flow rate provided it is maintained within a narrow range. If the gas flow rate is outside this acceptable range, then design equations (7-15) and (7-16) are coupled due to (1) backflow instabilities generated if the gas flow rate is too large and (2) clogging instabilities which occur if the gas flow rate is too small. These issues will be discussed further in chapter 8.

$$\left\{\begin{matrix} FR_{2111} = \text{Gas Amount} \\ FR_{2112} = \text{Polymer Amount} \end{matrix}\right\} = \begin{bmatrix} X & X \\ 0 & X \end{bmatrix} \left\{\begin{matrix} DP_{2111} = \text{Gas Flow Rate} \\ DP_{2112} = \text{Polymer Flow Rate} \end{matrix}\right\} \tag{7-15}$$

$$\left\{\begin{matrix} DP_{2111} = \text{Gas Flow Rate} \\ DP_{2112} = \text{Polymer Flow Rate} \end{matrix}\right\} = \begin{bmatrix} X & X \\ 0 & X \end{bmatrix} \left\{\begin{matrix} PV_{2111} = \text{Gas Injection Pressure} \\ PV_{2112} = \text{Screw RPM} \end{matrix}\right\} \tag{7-16}$$

The final functional requirements governing the solution formation system relate to minimizing the striation thickness (i.e., reducing the gas diffusion time for saturation). The striation thickness is minimized in two stages. First, a gas injection port is used which consists of a large number of small holes. This multi-port injection device reduces the initial bubble size injected into the polymer melt and minimizes the initial striation thickness (see Figure 3.1). Second, staged mixing operations are used to disperse the injected bubbles and shear the bubbles. The dispersive mixing operation creates a fine bubble morphology within the polymer matrix. The laminar mixing operation creates a shear flow which increases the surface area to volume ratio of the bubbles (see Figure 3.1). These mixing operations reduce the striation thickness and minimize the gas diffusion time. As shown in Figure 7.8, the staged mixing operations are performed by the shear flow in the metering zone, the mixing pins located at the end of the screw (i.e., a continuous mixer), and a static mixer. This mixing technique results in a decoupled solution formation system as given by equations (7-17) and (7-18).

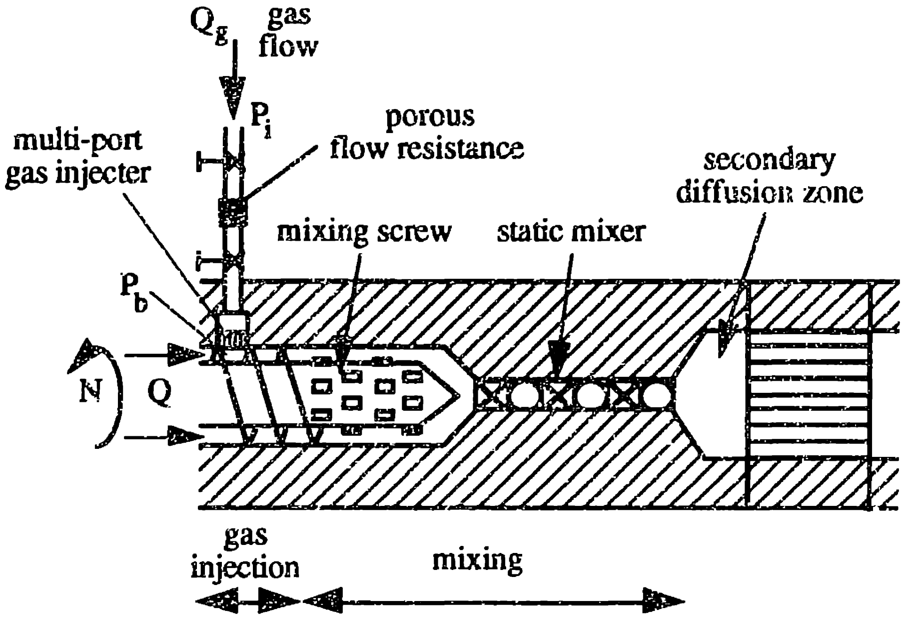

Figure 7.8: Polymer/gas solution formation in the extrusion barrel.

$$\begin{Bmatrix} FR_{2121} = \text{Minimize Initial Striation Thickness} \\ FR_{2122} = \text{Reduce Striation Thickness/ Diffusion Distance} \end{Bmatrix} = \begin{bmatrix} X & 0 \\ X & X \end{bmatrix} \begin{Bmatrix} DP_{2121} = \text{Multi-Port Gas Injection} \\ FR_{2122} = \text{Staged Mixers} \end{Bmatrix} \tag{7-17}$$

$$\begin{Bmatrix} DP_{2121} = \text{Multi-Port Gas Injection} \\ DP_{2122} = \text{Staged Mixers} \end{Bmatrix} = \begin{bmatrix} X & 0 \\ X & X \end{bmatrix} \begin{Bmatrix} PV_{2121} = \text{Number of Ports} \\ PV_{2122} = \text{Mixing Parameters} \end{Bmatrix} \tag{7-18}$$

7.4 Sheet Processing System Design

The final set of functional requirements that must be satisfied for the continuous production of microcellular sheets relate to the processing specifications for the sheet shown in Figures 7.3 through 7.5. During processing, it is necessary to produce a sheet having controllable dimensions which are specified through geometric requirements and an oriented molecular structure in order to meet the mechanical performance specifications. The functional requirements, design parameters, process variables, and design matrices are presented in equations (7-19) and (7-20).

$$\begin{Bmatrix} FR_{31} = \text{Sheet Geometry} \\ FR_{32} = \text{Molecular Orientation} \end{Bmatrix} = \begin{bmatrix} X & X \\ 0 & X \end{bmatrix} \begin{Bmatrix} DP_{31} = \text{Shaping Elements} \\ DP_{32} = \text{Stretching} \end{Bmatrix} \tag{7-19}$$

$$\begin{Bmatrix} DP_{31} = \text{Shaping Elements} \\ DP_{32} = \text{Stretching Equipment} \end{Bmatrix} = \begin{bmatrix} X & X \\ 0 & X \end{bmatrix} \begin{Bmatrix} PV_{31} = \text{Cross Sectional Dimensions} \\ PV_{32} = \text{Stretching Ratio} \end{Bmatrix} \tag{7-20}$$

The geometric requirements are satisfied by the appropriate specification of the cross-sectional dimensions of various shaping elements. The detailed design of the shaping elements will be presented in chapter 9. The molecular orientation requirements are satisfied using a stretching process. Depending on the die configuration, the stretching process can occur as an integral part of shaping, or it must occur as a secondary processing step post-shaping. In the case of plane sheet extrusion, the stretching process must be performed after the extrudate has been shaped into a sheet. Extrusion of tubes, on the other hand, allow for the integration of the geometric and orientation requirements due to the symmetry of the tube configuration. The decoupled nature of equations (7-19) and (7-20) follows from the intimate interdependence of stretching operations and the sheet geometry which follows from the continuity relation.

This completes the detailed microcellular sheet extrusion system design. The components of this system were manufactured and assembled for experimental verification which is presented in chapters 8 and 9. The microcellular sheet extrusion system is shown schematically in Figure 7.9, and a detailed description is presented in appendix A. The design equations presented above, along with the basic analysis, illustrate that the overall system is decoupled. The decoupled nature of the design mandates that the functional requirements be satisfied in a fixed order. From the level-two design equation (6-1), it is clear that the sheet processing parameters must be satisfied first, followed by the microcellular processing parameters, and finally the polymer processing parameters.

To conclude this chapter, the following section addresses some of the complexities associated with the design of large scale systems.

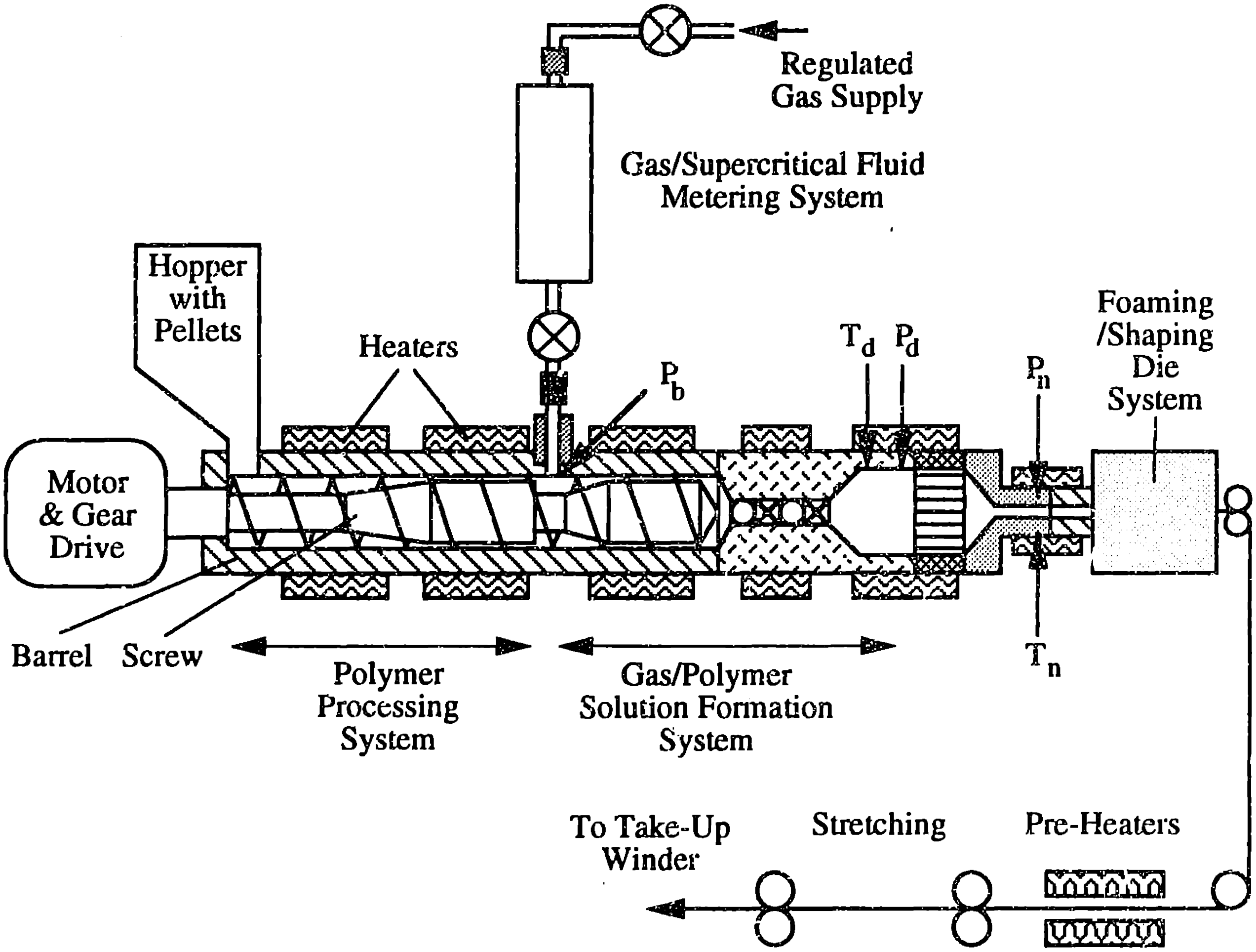

Figure 7.9: Overall microcellular sheet extrusion system design.

7.5 Complexities of Large Scale System Design

In this section, two complexities associated with the design of large-scale systems are discussed. The first deals with the inadvertent coupling which can occur as lower level DPs and PVs are selected to satisfy the FRs of the hierarchy. The second concerns start-up transients which are common in continuous systems and in some circumstances mandate the specification of additional functional requirements.

7.5.1 Inadvertent Coupling

The design of systems involves the identification of a few critical functional requirements and the expansion of these requirements into lower-level requirements as physical embodiments are identified in greater detail. Since the high-level FRs are typically broad in scope, it is sometimes difficult to insure the uncoupled or decoupled nature of the design equations. Therefore, these top-level design equations should be treated as system design guidelines. As the functional hierarchy is expanded into lower levels, specific design parameters and process variables are selected. Within the context of a local detail design, DPs and PVs are selected to locally satisfy the Independence Axiom. However, the selection of these physical parameters can lead to the inadvertent coupling of the higher level design equations.

To determine if inadvertent coupling has occurred and to illustrate the potential for inadvertent coupling, it is useful to compose a system design equation with includes the leaf nodes of the functional and physical hierarchy trees shown in Figures 7.3 and 7.4. Equation (7-21) presents one such system design equation for the microcellular sheet extrusion process. The major diagonal of the design matrix contains the design matrices of the lowest level requirements shown in Figures 7.3 and 7.4 and is partitioned accordingly. The system design matrix has been organized into an upper triangular configuration representing a decoupled design. Based on the design equation (6-1), all of the lower triangular elements are presumed to be '0's. However, if any one of the DPs is chosen inappropriately, then a lower triangular element could be an 'X' representing a strong interaction and coupling the system design. For example, if the shear work was chosen as the melting control variable instead of using a heated barrel to control polymer melting, then the design would be coupled since both the shear work and the polymer flow rate are functions of the screw speed. This poor design parameter choice would yield a non-triangular design matrix in (7-21), do to inadvertent coupling.

$$\left\{\begin{array}{c}\text{Pumping}\\ \text{Melting}\\ \text{Single-Phase Solution}\\ \text{Reduce Striation Thickness}\\ \text{Initial Striation Thickness}\\ \text{Gas Amount}\\ \text{Polymer Amount}\\ \text{Cell Nucleation}\\ \text{Cell Growth}\\ \text{Geometry}\\ \text{Orientation}\end{array}\right\} = \left[\begin{array}{cc|ccc|cc|cc|cc} X & X & \otimes & \otimes & & & X & X & X & X & \\ 0 & X & & & & & X & X & & & \\ \hline & & X & X & X & X & X & X & & & \\ & & 0 & X & X & & X & & & & \\ & & 0 & 0 & X & X & X & X & & & \\ \hline & & & & & X & X & X & \otimes & \otimes & \\ & & & & & 0 & X & X & \otimes & \otimes & \\ \hline & & & & & & & X & X & X & \\ & & & & & & & 0 & X & X & \\ \hline & & & & & & & & & X & X \\ & & & & & & & & & 0 & X \end{array}\right] \left\{\begin{array}{c}\text{Friction}\\ \text{Heated Barrel}\\ \text{Diffusion Chamber}\\ \text{Staged Mixers}\\ \text{Injection Ports}\\ \text{Gas Flow Rate}\\ \text{Polymer Flow Rate}\\ \text{Decompression}\\ \text{Pressure}\\ \text{Die}\\ \text{Stretching}\end{array}\right\} \qquad (7\text{-}21)$$

To minimize the potential of inadvertent coupling and to allow for quick identification of coupling problems, it is useful to identify some common situations where inadvertent coupling can occur in continuous systems. A short list is given below.

(1) Physically integrated components which satisfy multiple functions on the process flow.
(2) A single component which satisfies multiple functions.
(3) Pressure "feedback" to upstream flow.
(4) Feedforward of absolute pressure.
(5) Feedforward and feedback of local temperature settings to the downstream and upstream flow.
(6) Instabilities in non-robust designs.
(7) Separate processing steps which influence microstructure or macrostructure.

Whenever mechanical components are physically integrated, performing multiple functions on a single process flow, there is always the potential for coupling. This follows since the integration components themselves provide a "communication" path through which local stresses, strains, heat transfer, mass transfer, etc. can be transferred to mating components. A second possible coupling mechanism is the use of a single component to satisfy multiple functions. While the Information Axiom encourages the integration of components into a single component, this can lead to inadvertent coupling of the system particularly if the functions satisfied by the single component fall within different functional hierarchy branches. An example of this type of coupling occurred in the microcellular extrusion system design since a single die was used to satisfy both the cell growth and shaping requirements. Fortunately, this coupling resulted in just a decoupled design since the die cross-sectional dimensions affects the total pressure loss of the flow and therefore microcellular nucleation. A final mechanism which can couple the system design is the microstructure and macrostructure of the material. For example, the molecular orientation functional requirement and sheet geometry requirement can potentially be coupled via the interdependence of microstructure and macrostructure.

7.5.2 Transient Functional Requirements

An additional issue arising in continuous systems is the complexities associated with system start-up. This design complexity arises when systems experience large transients. Such transients can force the FRs outside their tolerance band to an extent that cannot be compensated for by adjustments in the DPs and PVs. This situation may occur despite the fact that the design satisfies the Independence Axiom for steady-state operation and for minor operating perturbations. In order to solve this problem, many continuous system designs require the specification of transient functional requirements which must be satisfied only over a brief period during the process start-up. As the process approaches steady-state operation, the transient FRs no longer need to be satisfied independently and become system constraints.

CHAPTER 8
CONTINUOUS NUCLEATION SYSTEM

8.0 Introduction

Now that the basic design of the microcellular sheet extrusion system has been presented, it is appropriate to look at a key aspect of the overall system design: a continuous nucleation system. This chapter will first review the thermodynamic and kinetic aspects of nucleation and develop primary design criteria for comparing and evaluating the nucleation device designs. The second part of this chapter will present three continuous nucleation device designs including supporting analyses and critical experiments verifying the designs. Finally, this chapter presents a series of secondary design criteria which must be satisfied by the nucleation devices. These design criteria are particularly relevant to the scale-up of the various nucleation device designs.

Nucleation is a complex phenomenon where a single-phase solution is separated into two discrete phases. The process proceeds when a saturated polymer/gas system is subject to a rapid thermodynamic state change. To understand the process, consider the Gibbs free energy of mixing given by equation (3.1-6). This equation relates the change in free energy of a system from an initial state having two discrete phases (i.e., two separate constituents) to a final state consisting of a single-phase solution. Spontaneous solution formation occurs for a two-phase system if the Gibbs free energy of mixing is negative. Spontaneous phase separation occurs for a single-phase solution if the Gibbs free energy of mixing is positive (i.e., the free energy of formation barrier is overcome).

Nucleation can be understood based on a solubility argument by relating the change in thermodynamic state to a typical phase diagram as shown in Figure 8.1 for a partially miscible, binary polymer/solvent system. ‡ Figure 8.1 shows three thermodynamic states: state 1 at $(P_1, T_1, \phi_{2,1})$, state 2 at $(P_2, T_1, \phi_{2,1})$, and state 3 at $(P_1, T_3, \phi_{2,1})$ where

---

‡ In polymer/gas systems, the gas experiences a large specific volume contraction upon diffusion into the polymer matrix which leads to a phase diagram characterized by a lower critical solution temperature (LCST) as shown in Figures 3.2 and 8.1.

$P_2 > P_1$, $T_1 > T_3$, and $\phi_{2,1}$ is the constant volume fraction of polymer. Phase separation through nucleation can be illustrated in Figure 8.1 via two different thermodynamic process paths. Beginning at state 3, an isobaric process on a closed system which increases the temperature from T_3 to T_1 (i.e., to state 1) creates a positive Gibbs free energy change. The positive free energy change follows from the enthalpy contributions associated with the free volume differences of the polymer and gas constituents. In the initial state, 3, the system is in a single-phase equilibrium. The temperature increase forces the system into a two-phase equilibrium at state 1. In state 1, the polymer/gas system is supersaturated promoting the nucleation and growth of the gas phase. A second process by which nucleation and growth can be induced is through a pressure cycle. Beginning at state 2 under high pressure P_2, the system is in a single-phase equilibrium. Subjecting the closed system to an isothermal process where the pressure is lowered to P_1 (i.e., to state 1) results in the nucleation and growth of the gas phase.

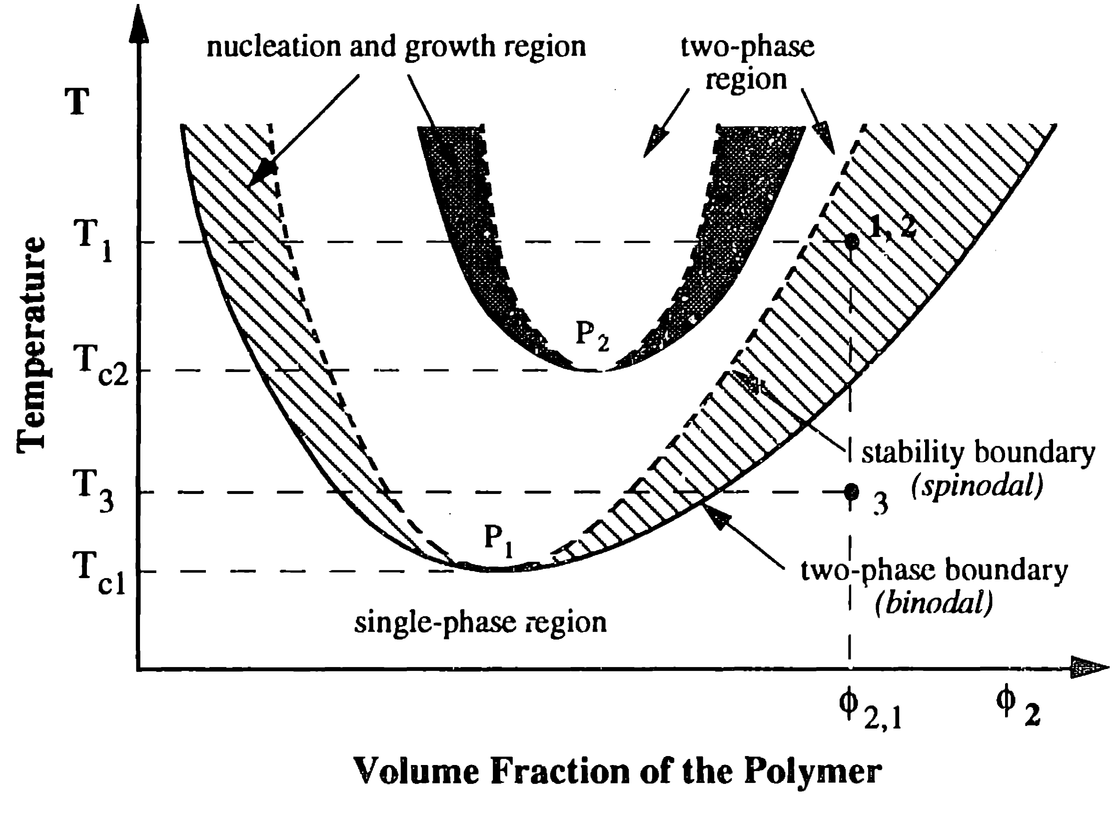

Figure 8.1: Typical phase diagrams for a partially miscible binary system at pressures of P_1 and P_2 where $P_2 > P_1$.

Based on this thermodynamic argument, it is clear that microcell nucleation can be induced in continuous processes by thermodynamic state changes through either temperature, pressure, or a combination thereof. In continuous melt processing, there are distinct drawbacks to using temperature increases to induce nucleation. First, polymers have limited thermal stability and can degrade at typical processing rates when subject to elevated temperatures. For example, PVC and PMMA are highly heat sensitive polymers and degrade within minutes of reaching their melt processing temperatures. A second problem associated with using thermally activated nucleation is the difficulty associated with isolating heat transfer in continuous flow processes making close control of the melt temperature difficult. The preheating of the flow and the inability to accurately control the heat transfer limit the practical implementation of thermally activated nucleation in melt processing.

In contrast, pressure is a very effective mechanism for inducing phase separation via nucleation, and it was the method of choice for the microcellular sheet extrusion process. Pressure changes in fluid flows can be initiated by frictional effects, as is the case in viscous flows, or by Bernoulli effects, as is the case in inviscid flows. Through proper design of the flow field it is relatively easy to instigate a large pressure decrease over a relatively short distance. This increases production rates. Another advantage of pressure induced nucleation is that pressure changes within a material propagate by compression and rarefaction waves at approximately the speed of sound. Therefore, pressure changes are transmit very quickly compared to the diffusion process associated with temperature changes by heat conduction. The ability to induce rapid thermodynamic state changes promotes uniform cell nucleation and cell morphologies.

8.1 Competition Between Cell Nucleation and Growth

In addition to the thermodynamic equilibrium effects discussed above, it is also important to consider the kinetic aspects of nucleation when designing continuous nucleation devices. Nucleation is a kinetic process whereby gas molecules cluster together to form stable discrete interfaces. As discussed in chapter 3, this process has been modeled using classical nucleation theory (Becker and Döring, 1935; Colton, 1985; Martini, 1981; Youn, 1984; Zeldovich, 1943). In general, the Gibbs free energy of stable nuclei formation is given by equation (3.2-6), and the homogeneous nucleation rate is given by equation (3.2-7). Typical nucleation rates are presented by Colton (1989) and Colton and Suh (1987) and are on the order of 10^9 to 10^{13} cells/cm^{3}s. From equations (3.2-6) and (3.2-7), it is clear that increased nucleation rates can be achieved by higher nucleation temperatures and larger saturation pressure changes.

$$\Delta G^{*}_{hom} = \frac{16\,\pi\,\gamma_{bp}^{\;3}}{3\,\Delta p^{2}} \qquad (3.2\text{-}6)$$

$$N_{hom} = C_o f_o \exp\left(\frac{-\Delta G^{*}_{hom}}{kT}\right) \qquad (3.2\text{-}7)$$

It is also important to study the kinetic aspects of nucleation in the context of cell growth and gas diffusion. The competition between cell nucleation and cell growth is inherent to all microcellular processing and is of particular importance in melt processing. The basic concept is as follows. During a solubility drop, which instigates the thermodynamic instability, some stable cells nucleate during the initial solubility decrease. The gas in solution will preferentially diffuse to the nucleated cells. The diffusion process is driven by concentration gradients and the system free energy. As the gas diffuses to these cells, low gas concentration regions having insufficient gas to nucleate additional cells are generated adjacent to the stable nuclei as shown in Figure 8.2. As the solubility drops further, the system will nucleate additional microcells and/or expand the existing cells by gas diffusion. To determine whether further microcells are nucleated, one must look closely at the depleted gas regions around the previously nucleated cells. If the spacing between adjacent stable nuclei is on the same order as the characteristic thickness of the depleted gas region, then no further nucleation will occur. This follows since the gas has preferentially diffused to existing cells, depleting the gas between cells which is needed for further nucleation. However, if the size of the depleted gas regions is less than the characteristic spacing between cells, then additional cells will tend to nucleate between existing cells increasing the cell density.

In order to better understand the competition between cell nucleation and growth, consider the following analysis. In this analysis, expressions for determining the relative contributions of cell nucleation and cell growth are derived based on dimensional analysis. These expressions provide a means of comparing, evaluating, and synthesizing new nucleation device designs. Moreover, such expressions provide considerable insight into the phenomena governing continuous nucleation systems. The analysis presented contrasts previous treatments of the subject which concentrated on detailed analyses (Martini, 1981; Shafi and Flumerfelt, 1992). The focus here is to develop simple expressions for estimating the relative contributions of cell nucleation and cell growth kinetics.

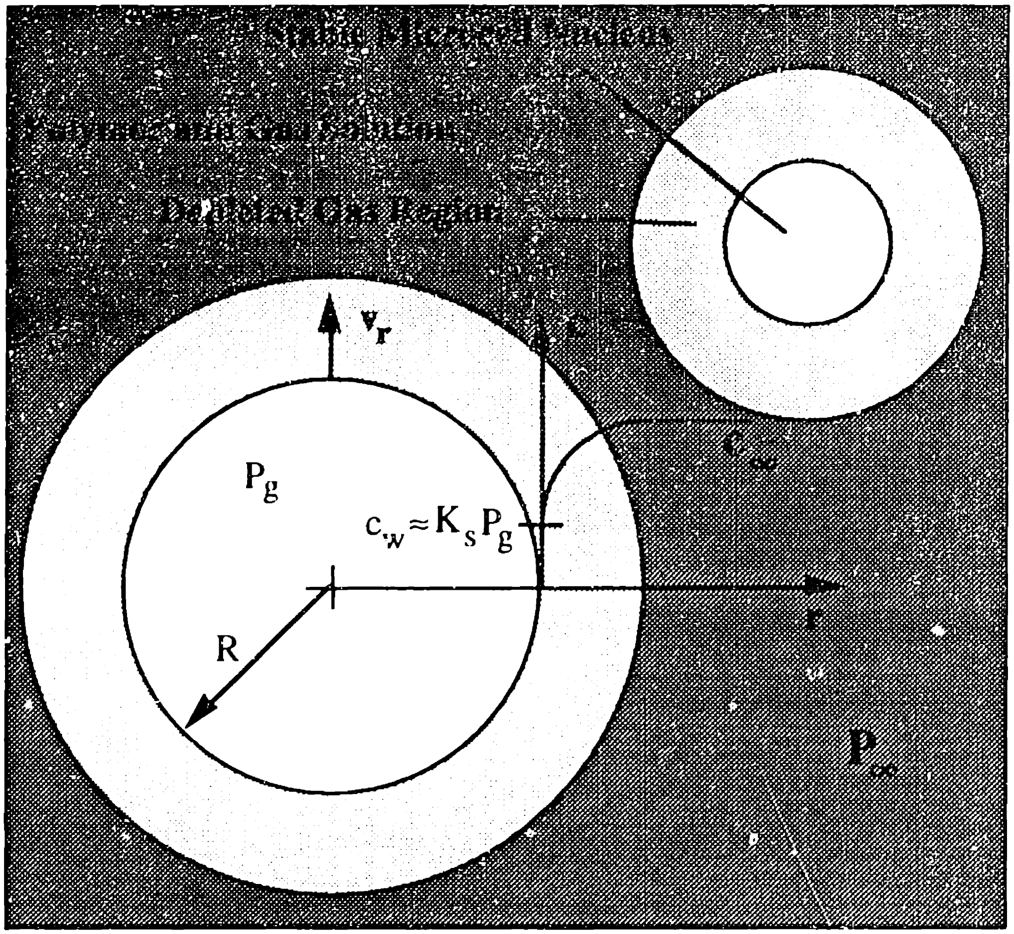

Figure 8.2: Schematic of growing microcells in a polymer/gas solution.

The competition between cell nucleation and growth can be understood using two expressions which represent limits of the nucleation kinetics at (1) the instant of cell nucleation and (2) over time when existing cells begin to grow. The first expression relates the characteristic time of microcell nucleation and gas diffusion during initial cell nucleation. The second expression compares the length over which the kinetics occur within a characteristic nucleation time. To develop the former expression, it is useful to perform a dimensional analysis on the characteristic time associated with microcell nucleation, Δt_n, where adjacent cells compete for finite gas. This characteristic nucleation time is a function of the characteristic length in microcellular nucleation, $l \approx D_c$ or alternately $l \approx \rho_c^{-1/3}$ the nucleation rate, $N \approx N_{hom}$, and the gas diffusivity, D [i.e., $\Delta t_n = f(l, N, D)$] (Also see appendix B for the details of the dimensional analysis.). Using the fundamental units of length and time, a dimensionless form of this functional dependence can be formulated where $\Delta t_n^* = \Delta t_n N l^3 = f(D/N l^5)$. Therefore, the characteristic nucleation time is on the order of $\Delta t_n \sim 1/N l^3$, and the characteristic diffusion time is on the order of $\Delta t_d \sim l^2/D$. The competition between nucleation and growth is minimized provided that the nucleation time is much shorter than the diffusion time. The mathematical form of this criteria is given in equations (8-1) through (8-3). [§] The dimensionless ratios of these equations are of particular interest when designing nucleation devices. In general, equations (8-2) and (8-3) state that under conditions where the gas diffusivity is high, such as melt processing, the nucleation rate must be equally large so as to minimize the competition between cell nucleation and growth (i.e., to maintain the nucleated cell density or microcell size). From equations (3.2-6) and (3.2-7), this implies that the nucleation pressure drop must be sufficiently large to overcome the effects of the higher diffusivity. As a general rule, equations (8-2) and (8-3) indicate that nucleation device designs should provide for high nucleation rates and low diffusivities.

$$\frac{\text{Characteristic Nucleation Time}}{\text{Characteristic Diffusion Time}} << 1 \tag{8-1}$$

$$\frac{D}{N l^5} << 1 \tag{8-2}$$

$$\frac{D}{N D_c^5} << 1 \qquad \text{or} \qquad \frac{D \rho_c^{5/3}}{N} << 1 \tag{8-3}$$

A second bound on the competition between microcell nucleation and cell growth can be formulated from an estimate of the length associated with the nucleation and growth of cells over finite processing times. The mean diffusion distance of gas molecules can be estimated using equation (8-4) where l is the mean molecular diffusion distance, D is the diffusivity, and t is the characteristic diffusion time during nucleation.

$$l \approx \sqrt{Dt} \tag{8-4}$$

The mean diffusion distance is approximately the characteristic thickness of the gas depleted regions in Figure 8.1. Therefore, competition between microcell nucleation and cell growth is negligible provided that:

$$l << \delta / 2 \tag{8-5}$$

or

$$\sqrt{D t} << \frac{1}{2} \rho_c^{-1/3} \tag{8-6}$$

[§] Notice here that a constant of one has been used to compare the time of nucleation and growth. This represents the theoretical limit. However, the practical magnitude for this constant is not known and requires considerably more analysis and experimentation to determine than will be presented in this work.

where δ is the average spacing between stable nuclei, and ρ_c is the instantaneous cell density. In equation (8-6), the average spacing between cells is based on a cubic packing of characteristic volumes surrounding each nucleus. In dimensionless form equation (8-6) becomes:

$$\frac{\text{Characteristic Gas Diffusion Distance}}{\text{Characteristic Spacing Between Stable Nuclei}} << 1 \qquad (8\text{-}7)$$

$$2\,\rho_c^{1/3}\sqrt{D\,t} << 1 \ . \qquad (8\text{-}8)$$

In continuous melt processing of microcellular polymers, the competition between cell nucleation and growth is prominent due to the high diffusivities of polymer melts. Preliminary evidence of this was illustrated by the pressure drop rate effects discussed by Park et al. (1993). Therefore in melt processing, it is important to consider the competition between cell nucleation and cell growth when designing nucleation devices. The design implications of equation (8-8) are that the time over which solubility changes (i.e., pressure changes) are instigated should be increased in proportion with the increase in diffusivity associated with melt processing. As a general rule, equation (8-8) indicates that nucleation device designs should provide for low diffusivities and short characteristic nucleation times.

Furthermore, equations (8-3) and (8-8) give considerable insight into the major differences in the melt processing requirements of microcellular polymers compared with conventional foams. Looking first at equation (8-3), the diffusivities of microcellular and conventional melt processing are typically on the same order of magnitude. The diffusivities of polymer melts range in magnitude from 10^{-6} to 10^{-5} cm^2/s (Durril and Griskey, 1966, 1969; Newitt and Weale, 1948; Stannett, 1968; Van Krevelen, 1976). The characteristic fully grown cell size, D_c of microcellular polymers range from 1 to 10 μm whereas conventional polymer foams have cell sizes ranging from 100 to 1000 μm. From equation (8-3), it is apparent that the nucleation rates in microcellular processing must be six to ten orders of magnitude larger than those of conventional processes in order to maintain comparable competition between cell nucleation and growth. Similar trends are also indicated by equation (8-8). In microcellular processing, cell densities range from 10^9 to 10^{12} cells/cm^3 whereas in conventional processing, cell densities range from 10^3 to 10^6 cells/cm^3. From equation (8-8), the characteristic nucleation times for microcellular processing must be a factor of 10^{-4} smaller than for conventional processes. This is further evidence of the substantial technological differences between microcellular and conventional foam processing.

In the remainder of this chapter, the design of three nucleation devices will be presented. The basic concept of each design will be presented along with a supporting analysis. In addition, critical experiments will be presented for each design which verify the nucleation technique.

8.2 Microcell Nucleation Via Decompression

To illustrate the use of a rapid pressure loss for continuous microcell nucleation, it is useful to look at the simplest configuration for accomplishing the task in a viscous flow field: a nozzle. A nozzle configuration was utilized by Park (1993) to perform preliminary studies on the effects of the gas concentration, the saturation pressure, and the pressure drop rate on impact grade polystyrene (HIPS) and carbon dioxide systems. It should be noted that the results of Park (1993) apply to a heterogeneous polymer system in that the HIPS contains polybutadiene rubber particles on the order of 2 to 4 μm. Therefore, the nucleation phenomenon observed by Park (1993) was predominantly heterogeneous in nature due to the phase boundaries present in the polybutadiene modified polystyrene matrix. In contrast, the system of interest here is a pure homopolymer, namely atactic polystyrene. Moreover, studying microcellular nucleation in nozzles will provide baseline cases from which two new nucleation techniques are compared in section 8.3.

In order to provide sufficient pressure losses, the nozzle must be sized based on the frictional flow losses in the nozzle. For the purposes of design, the flow of a polymer through a nozzle can be adequately modeled as steady, incompressible, and fully-developed. As a first order approximation, the flow will be assumed isothermal and entrance effects will be neglected. § Based on these assumptions, the momentum equation reduces to:

$$0 = -\frac{dp}{dz} - \frac{1}{r}\frac{d}{dr}(r\,\tau_{rz}) \tag{8-9}$$

---

§ The former assumption neglects any viscous shear work which can raise the flow temperature. For the nozzle flows presented here, the viscous dissipation localized near the nozzle walls can increase the melt temperature by 10 to 15 K. The later assumption can lead to large pressure errors in some flow fields (Tadmor and Gogos, 1979; White et al., 1987). Since the validity of these assumptions is not assured, the nozzle designs will be experimentally calibrated to insure the necessary pressure losses are generated.

where p is the pressure of the flow and τ_{rz} is the shear stress along the flow direction in the radial plane (see Figure 8.3). Integrating equation (8-9) and imposing a finite shear stress boundary condition (along the center flow) yields equation (8-10).

$$\tau_{rz} = -\frac{r}{2}\frac{dp}{dz} \qquad (8\text{-}10)$$

Next, the shear stress can be related to the velocity gradient, dv_z/dr, using the non-Newtonian viscosity, η, through equation (8-11). The non-Newtonian flow of a polymer (i.e., the shear thinning) can be modeled using Ostwald (1925) and de Waele's (1923) power law constitutive equation which relates the viscosity, η, to the shear rate, $\dot{\gamma}$. For a power law fluid, the viscosity is given by equation (8-12) where m and n are the temperature dependent power law parameters. Substituting equation (8-12) into (8-11) yields the differential equation of (8-13).

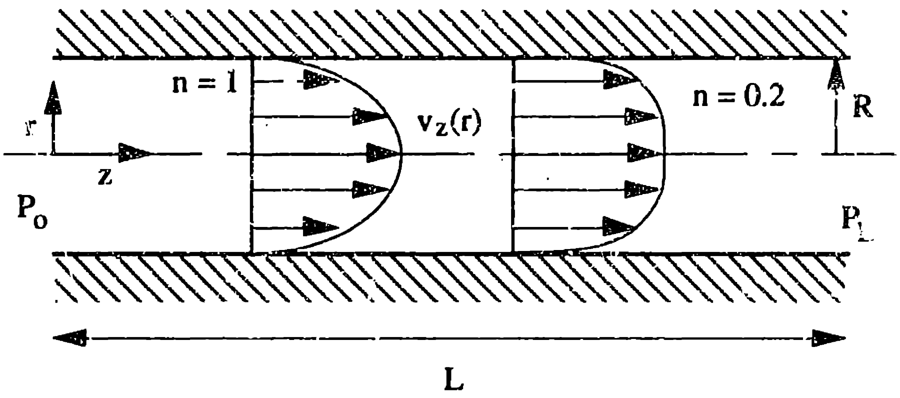

Figure 8.3: Flow of a non-Newtonian fluid through a nozzle for a power law coefficient of n = 1 (Newtonian fluid) and n = 0.2.

$$\tau_{rz} = -\eta\frac{dv_z}{dr} \qquad (8\text{-}11)$$

$$\eta = m\,\dot{\gamma}^{n-1} \qquad (8\text{-}12)$$

$$-\frac{r}{2}\frac{dp}{dz} = m\left(-\frac{dv_z}{dr}\right)^n \qquad (8\text{-}13)$$

The velocity distribution is obtained by integrating equation (8-13) over the nozzle radius (from 0 to R) and applying the no slip boundary condition at the wall, $v_z(R) = 0$.

$$v_z = \left(\frac{R\,\Delta P}{2\,m\,L}\right)^{1/n}\frac{R}{1+1/n}\left[1-\left(\frac{r}{R}\right)^{1+1/n}\right] \qquad (8\text{-}14)$$

Finally, the relationship between the volume flow rate, Q, and pressure gradient can be determine by integrating the velocity profile over the nozzle cross-sectional area (equation 8-15) resulting in equation (8-16) where L is the nozzle length and ΔP is the pressure loss over the nozzle ($\Delta P = P_0 - P_L$).

$$Q = 2\pi \left(\frac{R\,\Delta P}{2\,m\,L}\right)^{1/n} \frac{R}{1 + 1/n} \int_0^R \left[1 - \left(\frac{r}{R}\right)^{1+1/n}\right] r\,dr \tag{8-15}$$

$$\Delta P = \frac{2\,m\,L}{R} \left[\frac{3 + 1/n}{\pi R^3}\right]^n Q^n \tag{8-16}$$

Equation (8-16) represents a design equation for the nozzle which can be used to size the appropriate flow channel.

In equation (8-16), it is apparent that the design variable most sensitive to the pressure loss is the nozzle radius, R. Therefore, the nozzle radius is selected as the process variable for satisfying the pressure loss requirement in the design hierarchy of Figure 7.3. In addition, the nozzle length can be used to reduce the characteristic nucleation time in order to minimize the competition between cell nucleation and growth. A typical example is plotted in Figure 8.4 showing the pressure loss of polystyrene in a nozzle of length 6.35 mm for a flow rate of $Q = 31$ cm^3/min. The power law parameters used were determine from rheology data of Novacor Chemicals Inc. for Novacor 103 polystyrene. [†]

The minimum pressure drop necessary for continuous nucleation is determined by the solubility of gas in the polymer. Based on the available batch processing data, it is known that the gas solubility levels necessary for producing microcellular nucleation vary for different polymer/gas systems and are in the range of 2 to 10 percent by mass. Using equation (3.1-21), estimates of gas solubility in molten polymers were compiled by Park (1993). These estimates indicate, at typical polymer melt temperatures of 200 °C, the required gas saturation pressures range between 13.79 and 34.46 MPa (2000 and 5000 psi).

Using Figure 8.4 and equation (8-16) as design guides, nucleation nozzles having diameters of 0.508 mm and 0.533 mm and length to diameter ratios (L/D's) of 25 and 11.9 were machined. A typical nozzle configuration is shown in Figure 8.5. The pressure losses of these nozzles were calibrated using the extrusion system shown in Figure 8.6

[†] The power law constants for Novacor 103 PS are: $n = .286$ and $m = 40{,}747$ Pa s^n at 190 °C; $n = .255$ and $m = 33{,}543$ Pa s^n at 210 °C; and $n = .290$ and $m = 18{,}518$ Pa s^n at 230 °C.

with the gas injection system turned off. For example, unmodified polystyrene flow in the 0.533 mm nozzle had a total pressure drop ($\Delta P \approx P_n$) of 24.81 MPa (3600 psi) at 230 °C at a flow rate of 32 g/min which compares favorably with the predicted pressure loss of 21.03 MPa (3100 psi). The slightly higher pressure loss in the actual flow is attributed to entrance effects in the nozzle flow and the finite pressure loss between the nozzle pressure tap, P_n, and the nozzle entrance.

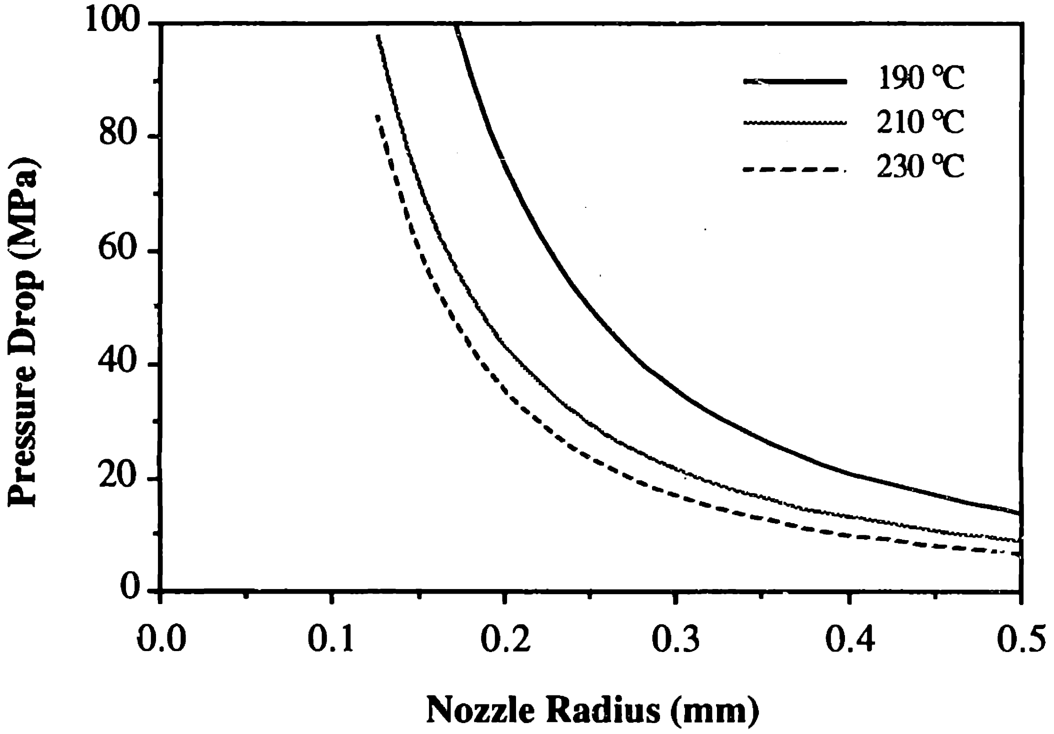

Figure 8.4: Analysis of pressure loss in a nozzle of length 6.35 mm for an incompressible polystyrene flow.

In order to verify the solution formation system and the use of a rapid pressure loss to nucleate a homopolymer such as polystyrene, a series of experiments was performed using the microcellular extrusion system configuration of Figure 8.6. The results of these experiments provide a baseline from which new microcellular nucleation, shaping, and cell growth control concepts can be compared. The solution formation/nucleation experiments were conducted using Novacor 101 atactic polystyrene (commonly called "crystal" PS in industry) and Novacor 3350 impact grade polystyrene (HIPS). A typical scanning electron microscope micrograph of an extruded microcellular PS filament (run C) is shown in Figure 8.7, and a summary of the experiments is presented in Table 8.1.

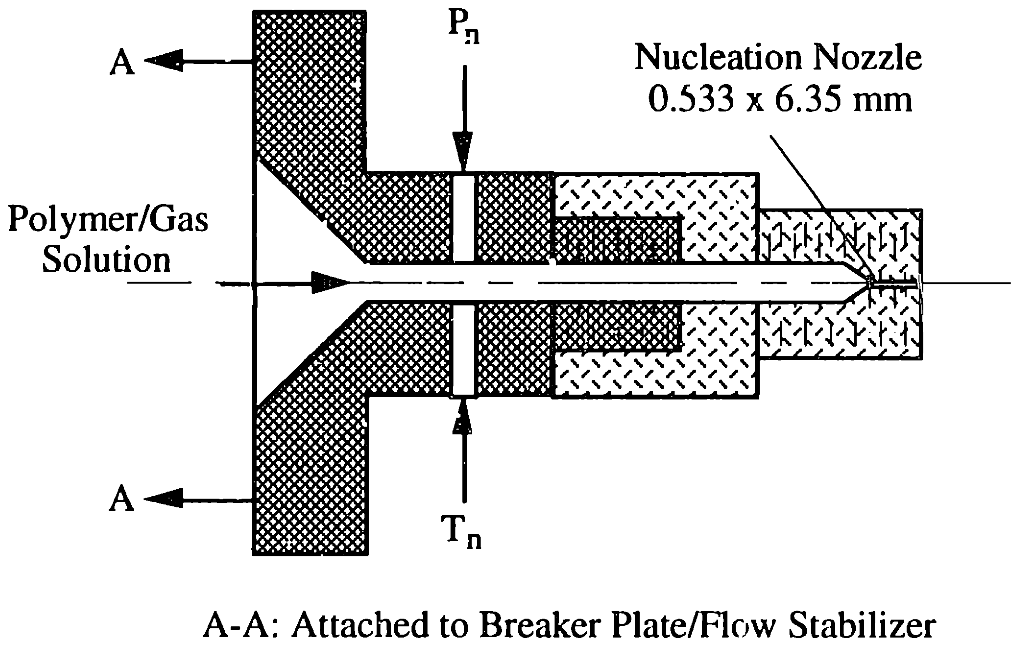

Figure 8.5: Configuration of a nozzle design used for continuous nucleation.

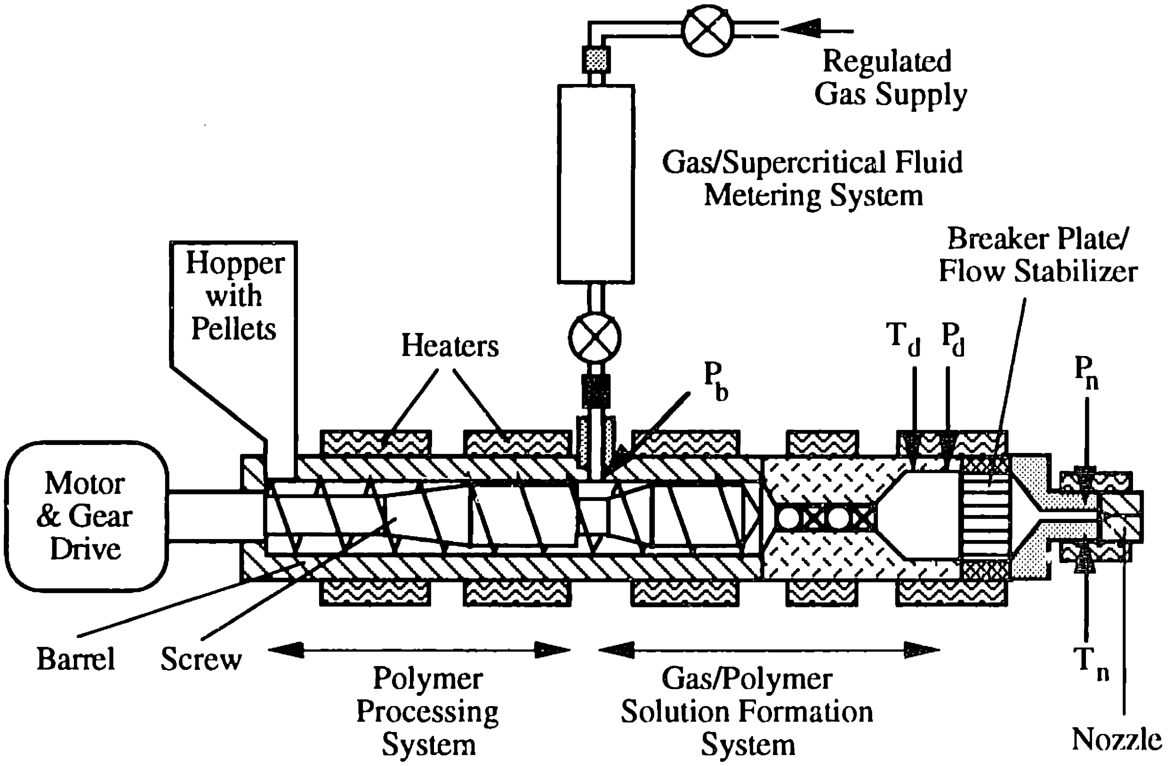

Figure 8.6: Schematic of the microcellular extrusion system configuration used for the nucleation experiments. (See appendix A for system details.)

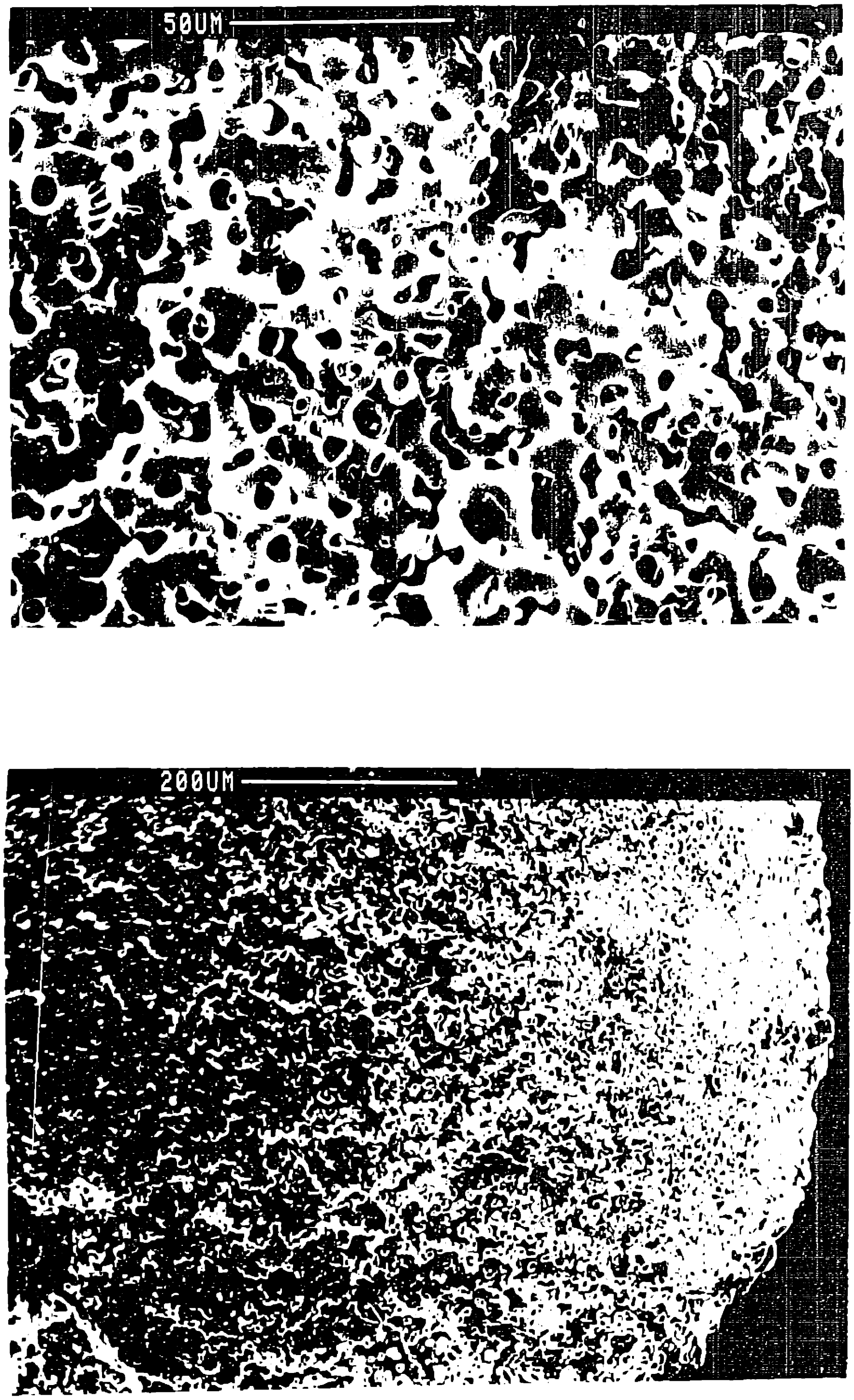

Figure 8.7: Typical scanning electron microscope micrographs of extruded microcellular polystyrene filament.

Table 8.1: Results from microcellular filament extrusion experiments.

Run	Polymer	Nozzle Diameter (mm)	L/D	Flow Rate (g/min)	Nozzle Temp. (°C)	Est. Gas Amount (%)	Nozzle Pressure (MPa)	Cell Size (μm)	Cell Density (cells 10^9 /cm^3)
A	PS	0.508	25	27	277	4	24.12	10.5	1.8
B	PS	0.533	11.9	32	213	3	20.68	12.0	2.1
C	PS	0.533	11.9	32	193	3	20.68	5.0	12.0
D	HIPS	0.508	25	12	232	8	37.91	10.7	3.1
E	HIPS	0.533	11.9	19	210	6	31.71	7.2	5.7

The results of Table 8.1 verify the operation of the solution formation system. Moreover, they demonstrate the feasibility of using rapid pressure loss nozzles for continuous microcellular nucleation in homopolymers such as polystyrene. Notice each of the extruded filaments had cell densities well within the microcellular range (greater than 10^9 cells/cm^3). The nucleation results of Table 8.1 also illustrate the importance of the nucleation nozzle temperature. Notice for the PS runs A, B, and C having nozzle temperatures of 277, 213, and 193 °C, respectively, the extruded filaments have increasing cell densities spanning nearly an order of magnitude. This increase in cell density is observed despite the fact that the total pressure drop and gas concentration is highest for run A which exhibits the lowest cell density. Equation (8-8) can be used to better understand the influence of the nucleation temperature. As the nucleation temperature increases, the diffusivity, D, increases exponentially as given by equation (7-3). The time factor in equation (8-8) can be interpreted as the characteristic nucleation time which for the nozzle flow is approximately the mean residence time of a polymer element in the nozzle given by:

$$t \approx \frac{L}{\bar{v}} = \frac{\pi D^2 L}{4Q} \qquad (8\text{-}17)$$

For runs A, B, and C, the average nozzle flow velocities, $\bar{v}$, are approximately equal (240 cm/s). Therefore, the characteristic nucleation time in run A is approximately twice that of runs B and C. The net effect of the increased diffusivity and nucleation time is a longer characteristic diffusion distance, *l*, during the course of nucleation. This depletes the available gas surrounding existing cells resulting in lower cell nucleation densities despite the fact that the polymer/gas solution favors higher cell densities. One can conclude then that the nucleation die temperature is a critical process parameter.

8.3 Nucleating in a Near-Net Shape

While nucleation using a nozzle provides a proven way of generating rapid pressure losses for continuous microcellular nucleation, the use of nozzles has a number of drawbacks. The small nozzles necessary for microcellular nucleation tend to clog easily requiring frequent system shutdown. Moreover, the final geometry of the nucleated solution is in the form of a filament which has very limited use as a final product. Finally, the nucleated nozzle flow is not necessarily formable into a sheet using standard extrusion dies without serious degradation of the cell morphology. † Therefore, it is important to explore new concepts for continuous nucleation.

The concept explored here is the nucleation of a near-net shape. This process involves the simultaneous shaping and nucleation of the polymer/gas solution flow into a form having dimensions as close as possible to the desired product. In the next sections, two such nucleation devices will be designed and verified: a planar sheet configuration and a tubular film configuration. The main advantages of near-net shape nucleation devices are that they reduce the complexity of secondary shaping devices and that they overcome some of the flow instabilities which can occur in nozzle flows (which are discussed in section 8.4). Moreover, near-net shape nucleation is capable of producing final products with considerable utility compared with nozzle nucleation, particularly in the case where the final product is a microcellular film or thin sheet.

8.3.1 Plane Sheet Case

The first near-net shape nucleation concept investigated was the use of a thin planar slit flow to continuously nucleate a polymer/gas solution resulting in a thin microcellular sheet. To design an appropriate flow channel for microcellular nucleation, it is critical to

---

† The shaping of nucleated flows will be discussed in chapter 9.

produce a large, rapid pressure loss in the flowing polymer. Typical pressure instabilities range from 20.68 to 34.46 MPa (3000 to 5000 psi) corresponding to soluble gas concentrations of 8% to 14% by weight at 200 °C (Park, 1993). Similar to the nozzle nucleation design, it is necessary to size the flow channel to produce the required pressure losses. The flow of a non-Newtonian fluid through a thin slit can be adequately modeled as steady, incompressible, and fully developed with negligible edge effects. Based on these approximations and the slit flow configuration of Figure 8.8, the momentum equation reduces to equation (8-18). Following a derivation similar to the nozzle flow equations, the pressure loss for a power law fluid in a slit of length L and width 2·B is given by equation (8-19) (Bird et al., 1987).

$$0 = \frac{dp}{dz} - \frac{d\tau_{xz}}{dx} \tag{8-18}$$

$$\Delta P = \frac{m\,L}{B}\left[\frac{(1/n)+2}{2\,W\,B^2}\right]^n Q^n \tag{8-19}$$

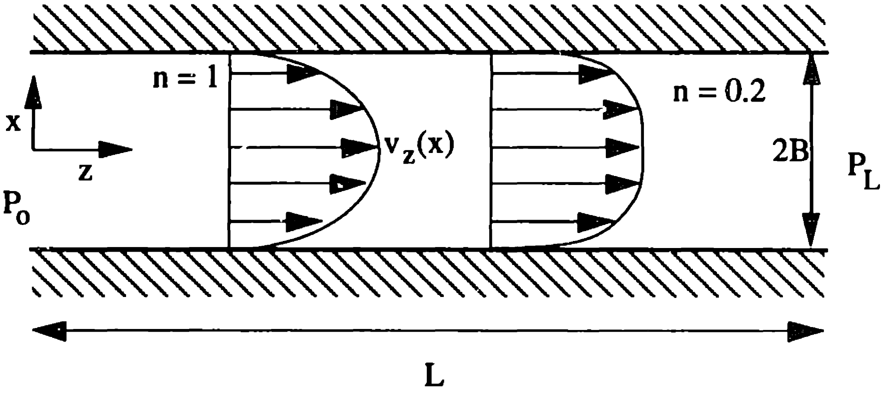

Figure 8.8: Flow of a non-Newtonian fluid through a thin slit for a power law coefficient of n = 1 (Newtonian fluid) and n = 0.2.

To design the planar near-net shape nucleation device, the flow of PS at 230 °C through a slit of width 25.4 mm and length 20.32 mm was used in conjunction with equation (8-19). For example, the estimated pressure losses for a flow rate of 21 cm^3/min in slits of height 0.254 and 0.508 mm are 28.06 and 9.39 MPa (4100 and 1400 psi), respectively. Notice the extreme sensitivity of the pressure loss to the slit height. Using this type of first order analysis, the planar sheet nucleation die sketched in Figure 8.9 was designed and manufactured. The sheet die was then calibrated without gas injection. The calibration experiments indicated a pressure drop of 26.88 MPa (3900 psi) at a flow rate of

21 cm^3/min which is in reasonable agreement with the estimated pressure loss of 28.06 MPa (4100 psi).

Next a critical experiment was run to verify the near-net shape nucleation concept using the extrusion system configuration shown in Figure 8.6. In the experimental configuration, the planar sheet die of Figure 8.9 was substituted for the nozzle. The process parameters for the experiment were: material = Novacor 103 PS, slit height = 0.254 mm, slit width = 25.4 mm, slit length = 20.3 mm, flow rate = 47 g/min, die temperature = 166 °C, estimated gas concentration = 3%, nucleation pressure = 22.75 MPa (3300 psi). The critical experiment was successful in demonstrating the feasibility of continuous near-net shape nucleation. A typical scanning electron microscope micrograph of the microcellular polystyrene sheet is shown in Figure 8.10 exhibiting an average cell size of 14 μm and an average cell density of 0.5 x 10^9 cells/cm^3.

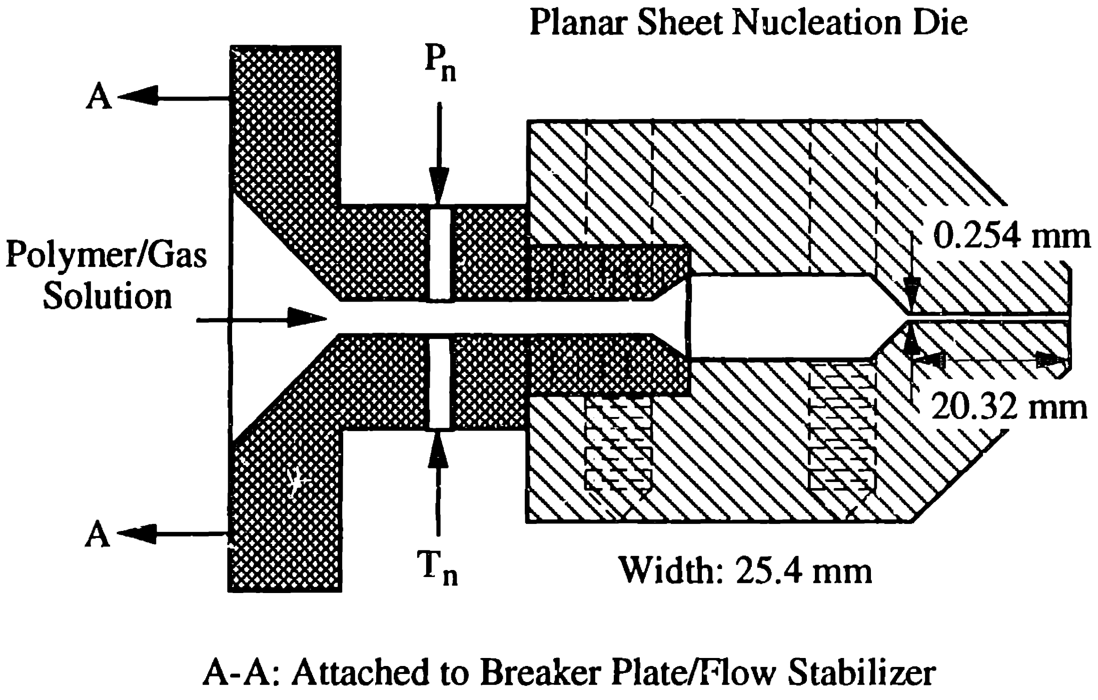

Figure 8.9: Planer sheet nucleation die design used to verify near-net shape nucleation concept.

It is interesting to note that like the nozzle case, the nucleation die temperature was found to be a critical process variable. During the state-up of the extrusion system, the die temperature was maintained at about 230 °C to prevent over-pressurization of the system. After the solution formation system began to stabilize, the emerging foamed sheet was observed to have a large average cell size (on the order of 100 μm) and a poor cell density

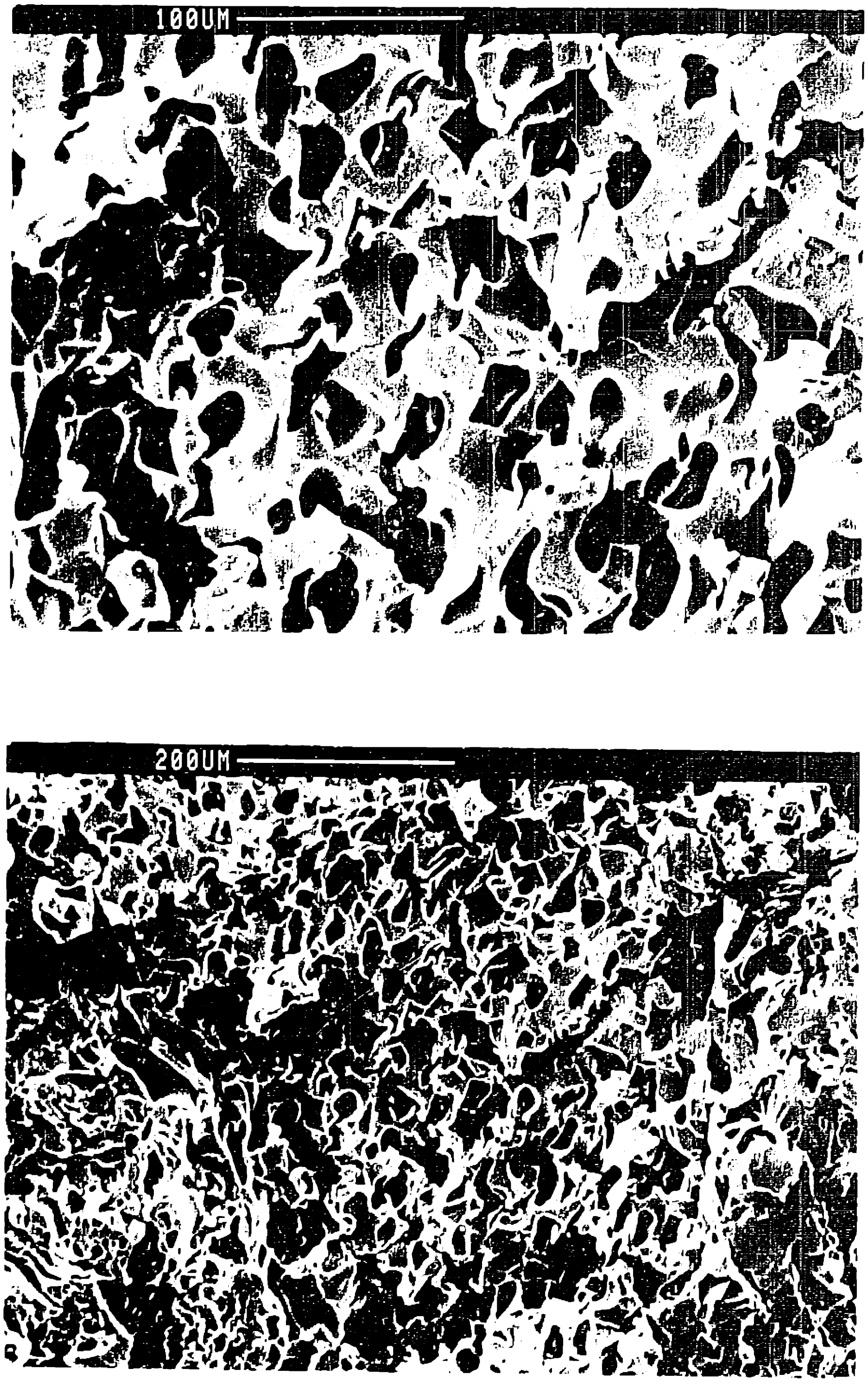

Figure 8.10: Scanning electron microscope micrograph of extruded near-net shape microcellular polystyrene sheet.

(on the order of 10^6 cells/cm^3). Moreover, the emerging sheet illustrated that at the high nucleation die temperatures, cell nucleation and growth were not stable. In order to improve the foam morphology and produce a microcellular structure, the die temperature was steadily lowered. As the die temperature decreased, the cell morphology steadily improved. The best microcellular morphology resulted at the lowest die temperature for which the solution formation system remained stable (see Figure 8.10). This was at a die temperature of approximately 166 °C. Notice that this die temperature is 30 to 60 °C lower than recommended processing temprratures of the Novacor polystyrene. This is an interesting fact which is believed to result from the decrease in apparent viscosity of the polymer/gas solution.

At this point, it is appropriate to discuss some of the interesting elements of these critical experiments and their relation to the system design of chapter 7. During the start-up of the process when the gas is initially injected into the melt flow, the extrusion system pressures are comparable with those of the nucleation die calibration experiments (i.e., without gas injection). Once the system pressurizes, the gas is injected into the polymer melt and flows through the mixing system forming a single-phase mixture. As the polymer/gas solution reaches the nucleation device, the extrusion pressures decrease. For example, the initial start-up pressures of the extrusion system with the planar nucleation die (Figure 8.9) were approximately 31.02 MPa (4500 psi). The extrusion pressures during stable microcellular foam processing were approximately 22.75 MPa (3300 psi). This 8.27 MPa (1200 psi) reduction in extruder head pressure is attributed to two effects. First, the stable injection of gas tends to decrease the pumping effectiveness of the second extrusion screw stage due to the heterogeneous nature of the polymer/gas mixture which sustains lower shear stresses than the neat polymer. Second, the polymer/gas system may tend to have a lower apparent viscosity than the neat polymer resulting in lower die pressure losses. Supporting evidence of this hypothesis is presented by Blyler and Kwei (1971). Blyler and Kwei report 20 to 22% apparent viscosity reductions in capillary rheometer flows of HDPE and LDPE containing dissolved gas from a chemical blowing agent.

Another important aspect of the microcellular extrusion system is the stabilization of the solution formation system which was a particular problem with the near-net shape nucleation experiments due to the higher flow rates used in these experiments. The general issue is as follows. When pressure fluctuations (namely low pressure cycles) occur in the first extrusion screw stage, the constant high pressure gas injection flow increases. This results in backflow of the molten polymer through the screw channels driven by the higher pressure gas flow. Pressurized gas pockets then escape through the extruder hopper. The high temperature gas tends to fuse the polymer pellets and clog the hopper causing further pressure fluctuations in the extruder flow and resulting in a cascading instability of the solution formation system. As discussed in chapter 7, the process variable controlling the pumping requirement was the length of the first metering zone of the venting screw. By increasing the metering zone length, the barrel pressure at the gas injection port becomes less sensitive to flow rate fluctuations, which would tend to minimize the instabilities associated with the solution formation system. Due to limited resources, venting screws having longer metering zones were not utilized during the experimental trials. However, the secondary process variable suggested in chapter 7, the barrel temperature in the melting zone, was adjusted to aid solution formation system stabilization. Lowering the melting zone barrel temperature by 20 to 50 °C, once a foamed extrudate formed, helped to stabilize the solution formation system.

8.3.2 Tubular Film Case

A second near-net shape nucleation strategy was investigated for the continuous production of microcellular films. The ability to produce foamed films is one of the major advantages of microcellular technology over conventional foam technology which produces large cell structures and precludes film processing. The near-net shape nucleation strategy developed to produce microcellular films implemented a tubular film nucleation die. The use of a tubular film die configuration promotes uniform flow rates and therefore uniform nucleation across the circumference of the film. In contrast, planar film dies have non-uniform flow rates across the width of the sheet due to the longer flow paths at the edges of the die. The longer flow paths can lead to non-uniform cell nucleation over the film width.

In an analogous manner to the planar sheet case, the design of a continuous microcellular nucleation device must accommodate the production of large, rapid pressure losses on the order of 20.68 to 34.46 MPa (3000 to 5000 psi). To estimate the necessary dimensions for an annular flow geometry, it is appropriate to begin with momentum equation of (8-9). However, the flow geometry expected for producing such high pressure losses will likely have $L/B >> 1$. Therefore, a simplifying assumption in deriving the pressure loss relation is to model the flow as a thin tubular slit which follows equation (8-19). In this case, the sheet width, W, is taken as the circumference of the tube annulus, $W = \pi D_t$ where D_t is the diameter of the annulus. Thus, the pressure loss in a steady, incompressible, non-Newtonian fluid through a tubular slit of length L and height 2·B is given by equation (8-20).

$$\Delta P = \frac{m\,L}{B}\left[\frac{(1/n)+2}{2\,\pi\,D_t\,B^2}\right]^n Q^n \qquad (8\text{-}20)$$

To design the microcellular film nucleation device, the flow of PS at 230 °C through an annulus slit of diameter 26.1 mm and length 12.7 mm was used in conjunction with equation (8-20). The estimated pressure losses for a flow rate of 31 cm^3/min in slits of height 0.127 and 0.254 mm are 41.79 and 14.17 MPa (6100 and 2100 psi), respectively. Notice again the extreme sensitivity of the pressure loss to the slit height, 2·B. Based on this type of first order analysis, the tubular film nucleation die sketched in Figure 8.11 was manufactured. The tubular film die was then calibrated without gas injection. The calibration experiments indicated a pressure drop of 33.46 MPa (4900 psi) at a flow rate of 31 cm^3/min. Notice that this value is considerably lower than the predicted pressure loss of 41.79 MPa (6100 psi); this is attributed to (1) the viscous heating in the slit flow which tends to decrease the viscosity and (2) the out-of-round tolerance on the tubular die (i.e., about ± 0.0254 mm) which can increase the effective slit height.

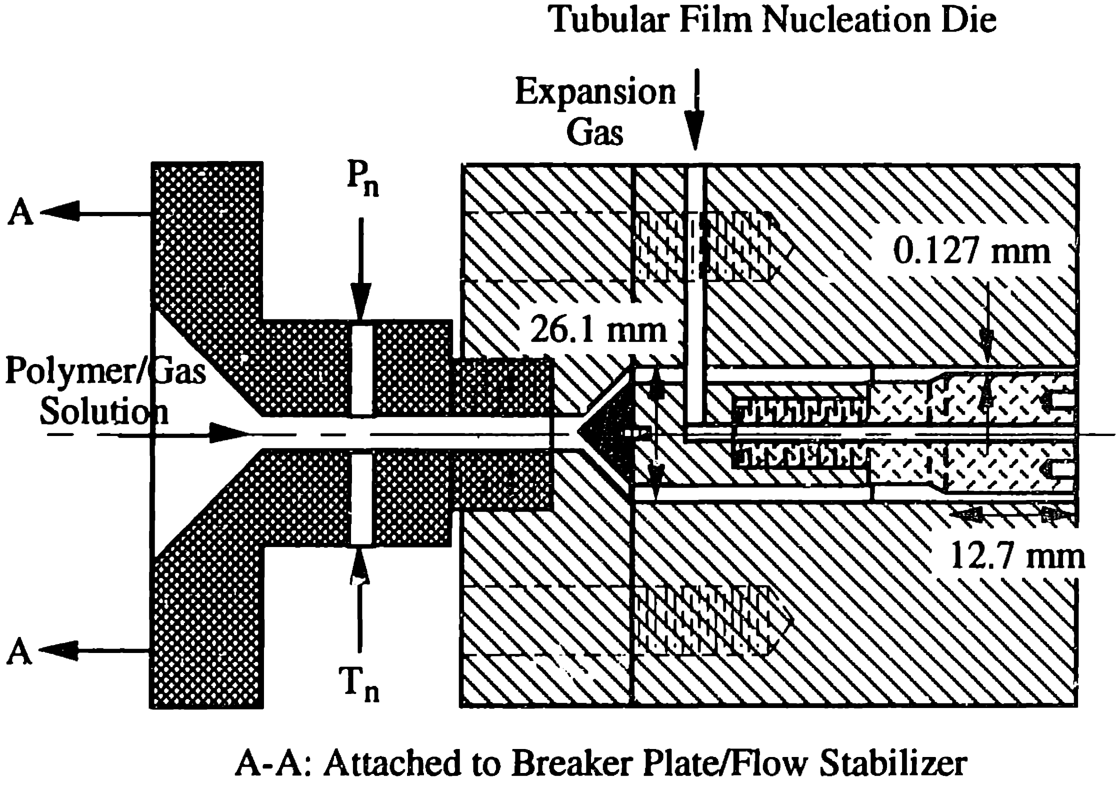

Figure 8.11: Tubular film nucleation die design used for extrusion of microcellular films and to verify concept of near-net shape nucleation.

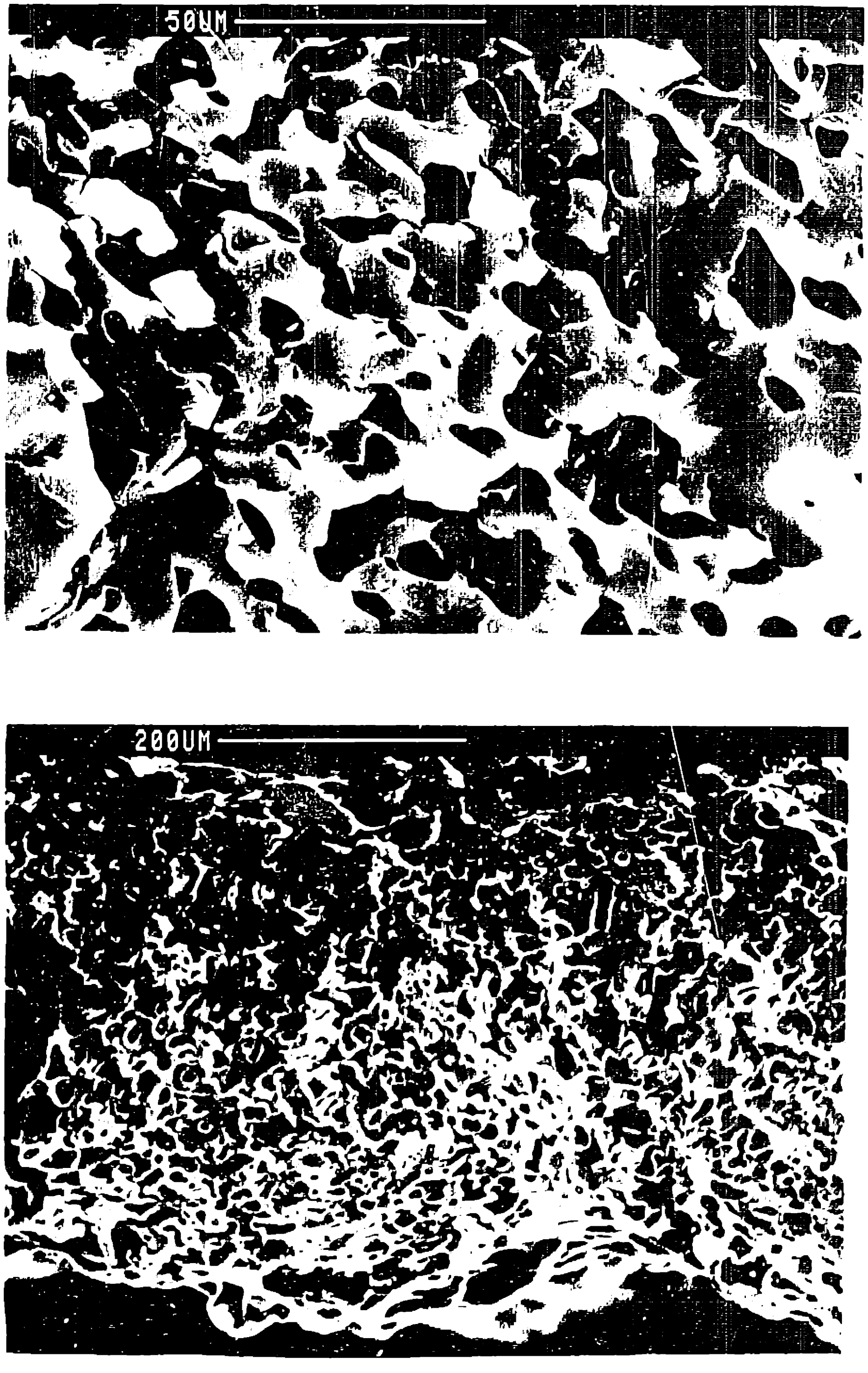

Figure 8.12: Scanning electron microscope micrograph of extruded microcellular polystyrene film.

Next a critical experiment was run to verify the near-net shape nucleation concept using the extrusion system configuration of Figure 8.6 with the tubular film nucleation die of Figure 8.11 in place of the nozzle. The process parameters for the experiment were: material = Novacor 103 PS, slit height = 0.127 mm, annulus diameter = 26.1 mm, slit length = 12.7 mm, flow rate = 15 g/min, die temperature = 199 °C, estimated gas concentration = 4 %, nucleation pressure = 31.71 MPa (4600 psi). The critical experiment was successful in demonstrating the feasibility of continuous near-net shape nucleation. Moreover, this experiment demonstrated feasibility of continuous microcellular film extrusion. A typical scanning electron microscope micrograph of the microcellular polystyrene sheet is shown in Figure 8.12 exhibiting an average cell size of 7 μm and an average cell density of 2×10^9 cells/cm^3.

8.3.3 Limitations on Nucleating Thick Cross-Sections

The basic concept of near-net shape nucleation is to instigate a pressure driven instability in a shaped form which is as close as possible to the final desired sheet dimension. However, when using frictional pressure losses to generate the solubility change and microcell nucleation, there is a limitation in the feasible size of the near-net shape sheet. This limitation can be seen for a planar slit flow by rearranging equation (8-19), yielding equation (8-21). Taking a typical power law coefficient of n = 0.25, and the criteria of producing equal pressure losses over a constant width, W, equation (8-21) reduces to equation (8-22). In order to generate equal pressure losses for a factor of two increase in the slit height and in the land length, a factor of four increase in the flow rate is required. A factor of four increase in the height and a factor of two increase in the length requires a flow rate increase of a factor of 256. The latter flow rate requirement is beyond plasticating extrusion capability. The former flow rate increase can be achieved by extrusion, however such increases require significant redesign of the solution formation system.

$$\frac{Q\,L^{1/n}}{B^{2+1/n}} = \frac{2\,W}{2+1/n}\left(\frac{\Delta P}{m}\right)^{1/n} \tag{8-21}$$

$$\frac{Q\,L^{4}}{B^{6}} = \frac{W}{3}\left(\frac{\Delta P}{m}\right)^{4} = \text{Constant} \tag{8-22}$$

It is clear then that the near-net shape nucleation of film geometries is feasible. However, the near-net shape nucleation of thick cross-sections has only limited feasibility due to the sensitivity of the frictional pressure loss to the slit height. It is recommended that future research explore new nucleation methods which are not as dimensionally sensitive.

8.4 Additional Nucleation Device Design Criteria

Additional design criteria which must be considered in the design of nucleation devices center around the flow instabilities that are inherent to high viscosity frictional pressure loss flows. Four such design considerations/criteria are discussed in this section.

The first design criteria centers around the fact that rapid pressure loss flows can result in very high shear rates leading to shear work, viscous heating, and decomposition of the polymer. In polymer processing, it is desirable to limit shear rates to 10^4 (1/s). High shear rates, on the order of 10^3 to 10^4 (1/s), are characteristic of injection molding, and fall in the upper processing limit for polymers. In the design of continuous nucleation devices, it is necessary to consider the shear rates experienced in the rapid pressure loss flows. The maximum shear rate in nozzle flow, as shown in Figure 8.3, occurs at the wall, r = R, and is given by:

$$\dot{\gamma}_w = \left.\frac{dv_z}{dr}\right|_R = -\left(\frac{\Delta P}{4\,m\,(L/D)}\right)^{1/n} . \tag{8-21}$$

For processing conditions typical of microcellular PS filament extrusion, 230 °C, $\Delta P = 24.81$ MPa, $L/D = 11.9$ and 230 °C, $\Delta P = 34.46$ MPa, $L/D = 25$, the shear rates are $\dot{\gamma}_w = -1 \times 10^5$ (1/s) and $\dot{\gamma}_w = -2 \times 10^4$ (1/s), respectfully. These high shear rates are at the limiting values for polymer processing.

Likewise for thin slit flows, the maximum shear rate is given by:

$$\dot{\gamma}_w = \left.\frac{dv_z}{dx}\right|_B = -\left(\frac{\Delta P}{m\,(L/B)}\right)^{1/n} . \tag{8-22}$$

For processing conditions typical of microcellular PS thin sheet nucleation, 230 °C, $\Delta P = 22.75$ MPa, $L/B = 160$, the shear rates are $\dot{\gamma}_w = -1100$ (1/s). For processing conditions typical of microcellular PS tubular film nucleation, 230 °C, $\Delta P = 31.71$ MPa, $L/B = 200$, the shear rates are $\dot{\gamma}_w = -1600$ (1/s). Notice that while both the nozzle and near-net shape nucleation devices produce comparable nucleation cell densities, the near-net shape nucleation configurations are much less susceptible to viscous heating and polymer decomposition, which is very advantageous.

Another design consideration is the possibility of turbulent "jet" flow emerging from the rapid pressure loss devices used for nucleation (nozzle or near-net shape devices). If a microcellular extrusion system is configured such that a nucleated flow is to be shaped in a secondary foaming die, then a turbulent jet flow, as shown in Figure 8.13, can lead to the loss of stable nuclei through cell coalescence in the eddy flow regions (i.e., through turbulent mixing). Since cell coalescence leads to a decrease in the nucleation cell density, turbulent jet flows couple cell nucleation, shaping, and cell growth.

The transition from a laminar to a turbulent jet occurs for Reynolds numbers greater than 30, Re > 30 (Andrade, 1939). Using the Reynolds number suggested by Dodge and Metzner (1959) for non-Newtonian, power law flows (equation 8-23), the Reynolds number for nozzle flow (equation 8-24) can be used to determine whether the laminar to turbulent transition occurs in typical nozzle nucleation flows. Using the experimental data of run C in Table 8.1 for PS having a pre-nozzle melt temperature of 230 °C, $\mathrm{Re}_n = 0.1$.

$$\mathrm{Re}_n = \frac{2^{3-n}\rho_p}{m}\left(\frac{D}{3+1/n}\right)^n \bar{v}_z^{\,2-n} \tag{8-23}$$

$$\mathrm{Re}_n = \frac{2^{3-n}\rho_p}{m}\left(\frac{D}{3+1/n}\right)^n \left(\frac{4\,Q}{\pi D^2}\right)^{2-n} \tag{8-24}$$

In equations (8-23) and (8-24), ρ_p is the polymer density and $\bar{v}_z$ is the average axial flow velocity.

For slit flow, the Reynolds number is given by equation (8-25). The Reynolds number of the planar sheet nucleation die is $\mathrm{Re}_n \sim 10^{-7}$, and the Reynolds number for the tubular film nucleation die is $\mathrm{Re}_n \sim 10^{-8}$, both well within the laminar flow regime. While turbulent jets did not occur with the decompression flows implemented in this study, it is important to acknowledge the possibility of such flows when scaling-up the microcellular extrusion process to higher flow rates typical of industrial processing, particularly for nozzle nucleation devices. Such a jetting phenomenon could result in poor cell densities due to the mixing effect of the eddy flow even if the proper solution formation and pressure drop instabilities have been designed into the system.

$$\mathrm{Re}_n = \frac{2^{3-n}\rho_p}{m}\left(\frac{2\,B}{3+1/n}\right)^n \left(\frac{Q}{2\,W\,B}\right)^{2-n} \tag{8-25}$$

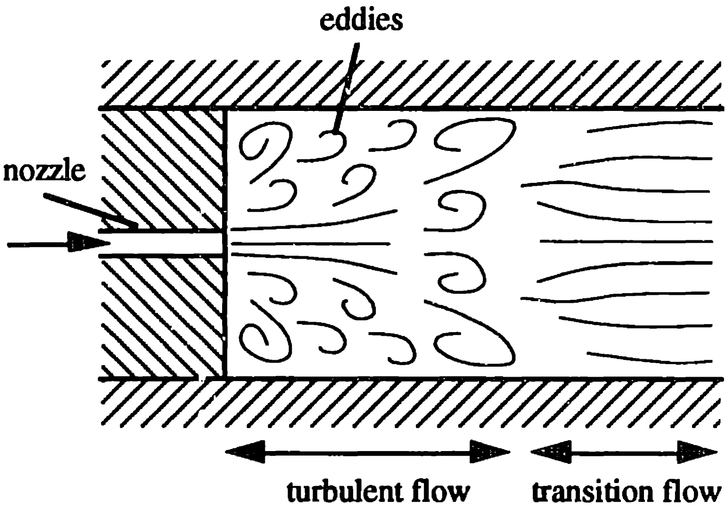

Figure 8.13: Turbulent jet flow emerging from a rapid decompression flow with Re > 30.

A third design consideration of rapid pressure loss flows is the entrance effects characteristic of polymer flow through a contraction. Typical streamlines for polymer entrance flows are shown in Figure 8.14. The vortex flows at the large entrance angles, α, entrap polymer particles which can lead to thermal degradation over time. Solid degradation particles can reduce the mechanical performance of the final product. More importantly, in the case of nozzle flows, the solid particles can clog the nozzle resulting in large back-pressures necessitating system shut-down. Streamlining the rapid contraction regions can reduce vortex formation. In general, the entrance pressure loss through a contraction is a strong function of the total entrance angle, α. Han (1973) has shown for high density polyethylene flows that the entrance flow head loss and vortex scale is constant for entrance angles from 180° to 60°. For $\alpha < 60°$, the head loss and vortex size decrease with entrance angle. Although it is necessary, streamlining the entrance regions can significantly increase the effective pressure loss length of the nucleation device leading to longer nucleation times and promoting greater competition between cell nucleation and growth (as illustrated by equation 8-8 for longer characteristic times, t). Such effects must be accounted for in the design of nucleation devices.

To reduce the entrance flow effects in the nozzle designs presented above, entrance angles of 118° were used. In the case of the planar sheet die and tubular film die designs, entrance angles of 90° and 45°, respectively, were used to reduce the formation of vortex flow patterns in the entrance regions and reduce the entrance losses.

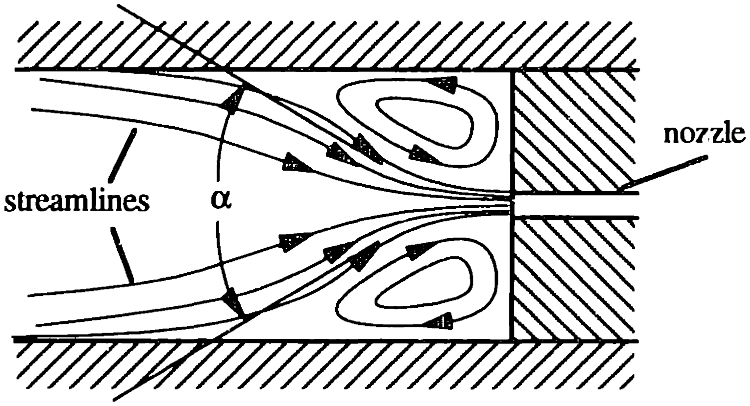

Figure 8.14: Entrance flow patterns in molten polymers.

A final consideration in the design of rapid pressure loss flow devices is the potential of instigating the flow instabilities of "melt fracture". Typically, melt fracture occurs once a critical shear stress value of 10^5 N/m^2 is reached in a polymer flow field (Tadmor and Gogos, 1979). The melt fracture phenomenon of particular interest in the design of nucleation devices results from the destabilization of entrance region vortex flows. Above the critical shear stress level, the entrance vortex flows, characteristic of these high shear stresses, become unstable and are entrained into the nozzle flow. The emerging nozzle flow then contains secondary vortex flow patterns creating an unstable/turbulent flow region at the nozzle exit. In such a flow field, the stabilization of nucleated cells is hampered and the potential of cell coalescence is greatly increase due to the inherent mixing promoted by the vortex motions. The resulting situation is similar to that of turbulent jet flow; however, the characteristic size of the vortex flow in the case of melt fracture is considerably larger than that for a turbulent jet flow.

To determine the potential for melt fracture in nucleation flows, the maximum shear stress must be estimated. The maximum shear stress for nozzle flow can be derived from equation (8-10) and is given by equation (8-26). At conditions common to microcellular nozzle nucleation, $\Delta P = 24.81$ MPa, L/D = 11.9 and $\Delta P = 34.46$ MPa, L/D = 25, the wall shear stresses are 5×10^5 N/m^2 and 3×10^5 N/m^2, respectively. These shear stresses are in the critical range for melt fracture. Melt fracture was experimentally observed during the nozzle calibration experiments of PS without gas injection. However, during the microcellular nucleation experiments (runs A through E), melt fracture was observed only when low gas concentrations were dissolved into the polymer matrix (i.e., on the order of 1% CO_2). The use of higher flow rates and higher gas concentrations appeared to suppress the melt fracture phenomenon. It is interesting to note that Blyler and Kwei (1971) also report suppression of melt fracture in capillary flows of HDPE containing dissolved gases produced by a chemical blowing agent.

$$\tau_w = \tau_{rz}(R) = \frac{\Delta P}{4\,(L/D)} \tag{8-26}$$

In the case of slit flows like the planar sheet nucleation die and the tubular film nucleation die, the wall shear stress is given by equation (8-27). In these systems, the flow length to height ratio is typically one order of magnitude larger than for nozzles producing comparable pressure drops. At conditions common to near-net shape nucleation, the processing conditions for planar sheet case and tubular film case are $\Delta P = 22.75$ MPa, $L/B = 160$ and $\Delta P = 31.71$ MPa, $L/B = 200$, respectively. The respective wall shear stresses are 1.4×10^5 N/m^2 and 1.6×10^5 N/m^2. The characteristically lower shear stresses involved with slit flow, help to minimize melt fracture during nucleation. No melt fracture was observed in the neat polystyrene calibration experiments of the planar sheet nucleation die and the tubular film nucleation die. Moreover, melt fracture was not observed in the critical experiments used to verify near-net shape microcellular nucleation. This result is not surprising since Vlachopoulos and Chan (1979) have shown that the critical shear stress for melt fracture instabilities in slit flows is typically larger than that for nozzle flows.

$$\tau_w = \tau_{xz}(B) = \frac{\Delta P}{L/B} \tag{8-27}$$

8.5 Summary

A critical element of the microcellular sheet extrusion system is the design of a continuous microcellular nucleation system. The principle of the nucleation system is to continuously nucleate a high pressure polymer/gas solution flow. In this chapter, two design strategies for satisfying this requirement were presented. The first design used nozzle configurations to rapidly decrease the solution pressure. Based on the critical experiments presented, this design configuration is very effective for continuously nucleating homopolymer/gas solutions. However, nozzle nucleation designs suffer from a number of drawbacks including high shear rates, potential turbulent jet flow, entrance vortex flow, and the flow instabilities associated with melt fracture. Furthermore, the final filament shape of the nozzle flow has very limited uses as a final product and is not readily shaped into a desired geometry using standard extrusion dies. Such shaping operations result in serious degradation of the cell morphology.

For this reason, a second design concept for continuous nucleation was developed: near-net shape nucleation. The basic principle of near-net shape nucleation is to simultaneously shape and nucleate a polymer/gas solution flow having dimensions as close as possible to the final product. Two near-net shape nucleation designs were presented in this chapter: a thin sheet nucleation die and a tubular film nucleation die. The critical experiments presented verified the near-net shape nucleation concept. Both the thin sheet and tubular film experiments produced continuous microcellular polystyrene having cell densities on the order of 10^9 cells/cm^3 and cell sizes on the order of 10 μm. Moreover, the results of the tubular film nucleation experiments demonstrated for the first time a technology for continuously manufacturing microcellular films. This represents a significant advancement in microcellular processing technology and paves the way for microcellular product applications requiring thin, lightweight insulation or barrier components. It is important to note that the near-net shape nucleation concepts did not suffer from the same drawbacks as the nozzle nucleation configurations. The near-net shape nucleation dies had substantially lower shear rates, Reynolds numbers, and shear stresses.

Finally, this chapter presented a series of criteria by which nucleation device designs can be evaluated on a relative basis. Such criteria will prove to be instrumental in scaling up the prototype microcellular extrusion system to industrial levels.

CHAPTER 9

CONTINUOUS SHAPING AND CELL GROWTH CONTROL

9.0 Introduction

In the previous chapter, the concept of near-net shape nucleation was introduced and experimentally verified using the microcellular extrusion system. Near-net shape nucleation is an initial step towards continuous microcellular sheet processing, although as the name implies, the limiting dimensions of the technology may not produce net shapes meeting specifications (see section 8.3.3). Therefore, in this chapter, the potential of shaping and controlling cell growth of a nucleated polymer/gas solution is investigated with the goal of designing a device (or devices) to accomplish the task. To this end, the design of a shaping and cell growth control device is discussed in the context of the overall system design with particular emphasis in the system level functional requirements of cell nucleation, cell growth, and shaping. Next, the basic design concepts and strategy underlying the shaping and cell growth control device are presented. These concepts are then used to develop a process model which provides reasonable estimates ot the critical design parameters based on the system process variables. Finally, two shaping/cell growth control devices (or dies) are presented along with critical experiments which verify the feasibility of shaping a nucleated polymer/gas solution flow.

9.1 Basic Concepts and Design Strategy

The basic premise of the shaping and cell growth control die (also called the foaming die) design is to devise a way of handling and shaping a nucleated polymer/gas solution using cell growth control such that the nucleated cell density is not diminished. In other words, the design must maintain the functional independence of cell nucleation, cell growth, and shaping. The design strategy utilized in this work was to use close temperature control and staged pressure changes, as shown in Figure 9.1. Since cell nucleation, cell growth, and shaping are so integrated in continuous microcellular processing, it is helpful to consider these functional requirements in a single design equation, even though they span different hierarchy levels and functional branches.

Looking at these requirements in a single design matrix provides a useful frame of reference for the design of a shaping and cell growth control device. Based on the developments of chapters 6 and 7, the overall design equation for these requirements is given by

$$\begin{Bmatrix}\text{Cell Nucleation}\\ \text{Cell Growth}\\ \text{Geometry/Shaping}\end{Bmatrix} = \begin{bmatrix} X & X & X\\ 0 & X & X\\ 0 & 0 & X\end{bmatrix}\begin{Bmatrix}\text{Rapid Pressure Loss}\\ \text{Staged Expansion Pressure}\\ \text{Shaping Elements}\end{Bmatrix} \tag{9-1}$$

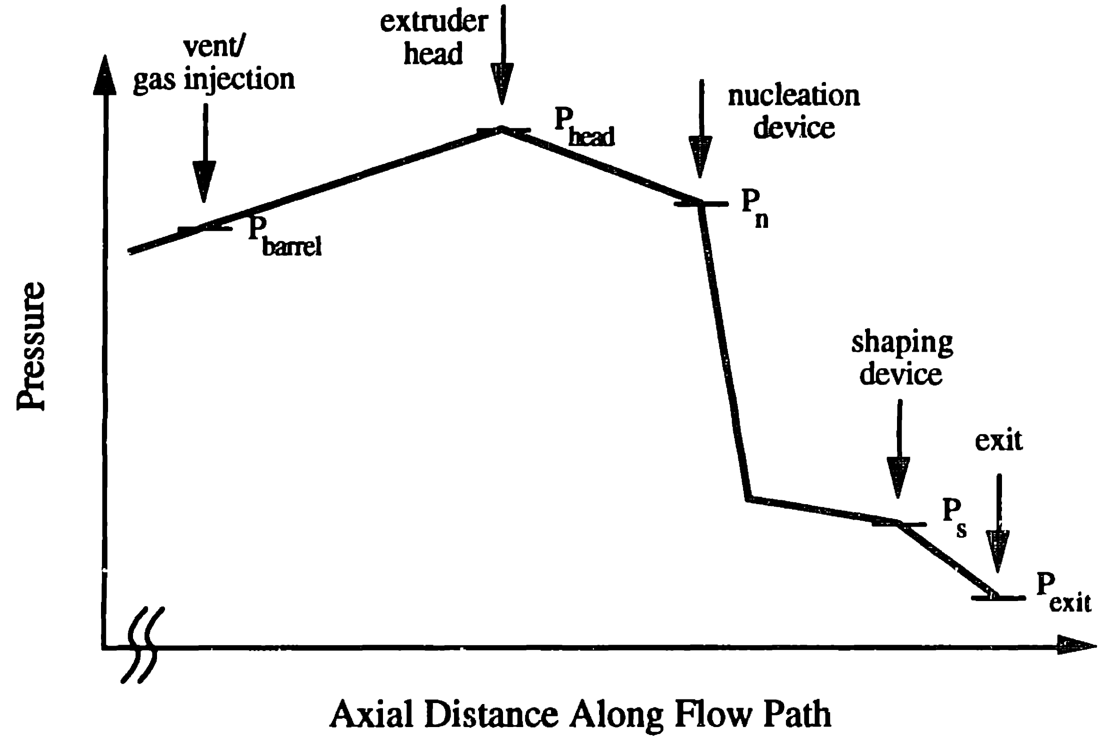

Figure 9.1: Representative pressure profile along the polymer flow field.

The decoupled nature of equation (9-1) follows from the physical link of these functions by the polymer/gas solution flow which allows pressure changes to be transmitted throughout the flow. In general, the solution pressure links shaping to cell growth and cell growth to nucleation. In order to satisfy the functional independence of equation (9-1), the shaping elements must be specified first, followed by the staged expansion pressure, and finally specification of the rapid pressure loss. The physical coupling of equation (9-1) can be interpreted as follows. Specification changes in the shaping die can change the flow resistance which alters the inlet pressure of the shaping die. This in turn influences cell nucleation and cell growth by changing the upstream pressures. To achieve the proper the cell growth, the expansion pressure can be adjusted independently of the shaping operation. Similarly, changes in the expansion pressure will influence cell nucleation by changing the upstream nucleation pressure, $\Delta P_{nuc} \approx P_n - P_s$. The cell nucleation requirement can then be satisfied by adjusting the rapid pressure loss parameter, P_n, without influencing the cell growth or shaping requirements.

To maintain functional independence from cell nucleation and shaping, the cell growth requirement is expanded into three subordinate requirements. These functional requirements include controlling cell growth prior to shaping, controlling cell growth after shaping, and stabilizing the growing cells. The design parameters chosen to satisfy these requirements are the nucleated solution pressure during shaping, P_s, a mechanical constraint, and the die temperature, T_{die}. The basic concept is sketched in Figure 9.2 and the design equations are presented in equations (9-2) and (9-3).

$$\begin{Bmatrix} \text{Pre–Shaping Growth} \\ \text{Post–Die Shaping Growth} \\ \text{Stabilize Cell Growth} \end{Bmatrix} = \begin{bmatrix} X & 0 & X \\ 0 & X & X \\ 0 & 0 & X \end{bmatrix} \begin{Bmatrix} \text{Shaping Pressure} \\ \text{Mechanical Constraint} \\ \text{Die Temperature} \end{Bmatrix} \tag{9-2}$$

$$\begin{Bmatrix} \text{Shaping Pressure} \\ \text{Mechanical Constraint} \\ \text{Die Temperature} \end{Bmatrix} = \begin{bmatrix} X & 0 & X \\ 0 & X & 0 \\ 0 & 0 & X \end{bmatrix} \begin{Bmatrix} \text{Die Lip Length} \\ \text{Surface Temperature} \\ \text{Die Lip Cooling} \end{Bmatrix} \tag{9-3}$$

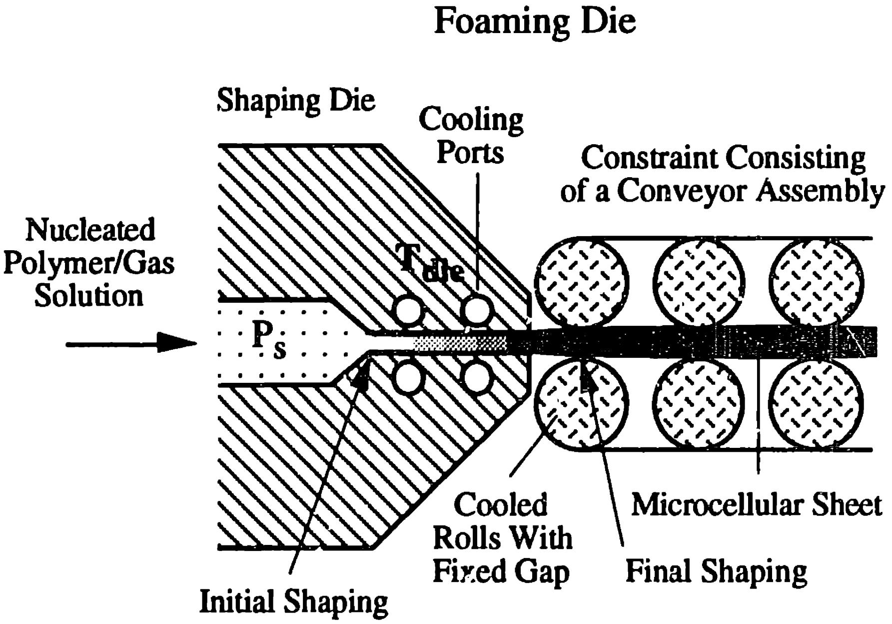

Figure 9.2: Foaming die concept for shaping and controlling cell growth of nucleated polymer/gas solutions.

As implied in Figure 9.2, the geometry/shaping functional requirement is expanded into two subordinate functional requirements. The design equations (9-4) and (9-5) present the basic strategy for satisfying the shaping requirement. Notice that the shaping requirement is satisfied in two stages. The initial shaping is performed by the die, while the final dimensions are fixed by a physical constraint. In Figure 9.2, the constraint is shown as a conveyor assembly. The cross-sectional dimensions of the conveyor fix the final dimension of the sheet while the cooled rolls control the surface temperature and provides for the post-shaping cell growth control.

$$\begin{Bmatrix} \text{Initial Cross-Section} \\ \text{Final Cross-Section} \end{Bmatrix} = \begin{bmatrix} X & 0 \\ X & X \end{bmatrix} \begin{Bmatrix} \text{Shaping Die} \\ \text{Shape Constraint} \end{Bmatrix} \tag{9-4}$$

$$\begin{Bmatrix} \text{Shaping Die} \\ \text{Shape Constraint} \end{Bmatrix} = \begin{bmatrix} X & 0 \\ X & X \end{bmatrix} \begin{Bmatrix} \text{Die Cross–Sectional Dimensions} \\ \text{Constraint Cross–Sectional Dimensions} \end{Bmatrix} \tag{9-5}$$

Perhaps the most important aspect of the designs presented in equations (9-1) through (9-5) is the ability to control the shaping and cell growth functions independently of cell nucleation. The ability to achieve functional independence centers around three functional requirements: the control of pre-shaping cell growth, the stabilization of the growing cells, and the initial shaping requirement. These three functional requirements will be the focus of the remainder of the chapter.

The need for pre-shaping cell growth control stems from the affinity of nucleated cells to agglomerate and coalesce during shaping operations. This follows since the agglomeration of cells is promoted by the compression, extension, and shear flow associated with shaping operations. The coalescence of cells leads to a deterioration of the nucleated cell density and couples cell nucleation, cell growth, and shaping. Cell coalescence occurs when adjacent cells agglomerate, at which point the cells merge into a single cell. The coalescence of cells is driven by the system free energy which must decrease for this spontaneous process. For coalescing cells of similar size, the free energy decreases due to surface energy contributions (i.e., a decrease in the surface area). If the agglomerated cells are of sufficiently different sizes, then coalescence is driven by a rupture of the membrane common to both cells. The rupture of the cell membrane occurs due to the differential gas pressure between cells of different size. To minimize the effects of coalescence, the agglomeration of the cells must be minimized, which can be achieved by increasing the mean interfacial distance between adjacent cells.

The pre-shaping cell growth control is also important in reducing the effects of shear on the nucleated polymer/gas solution flow. In general, viscous, non-Newtonian flow generates large shear stresses and shear rates near the boundary walls. The shear thinning behavior of the non-Newtonian flow localizes the shear effects to the wall (i.e., much like boundary layer flow) while the core regions experience relatively little shear effects (i.e., plug flow). Cells within the shear field are elongated, forming needle-like structures. The elongation of the cells near the boundary can lead to dispersive mixing which is discussed in section 3.1.2. When a cell is highly stretched, its surface becomes unstable resulting in the formation of one or more new cells and increasing the number of cells in a given volume (i.e., the cell density). However, the shear flow at the boundary can also lead to the coalescence of cells. The shear deformation of the cells increases the surface to volume ratio of each cell. This decreases the interfacial distance between cells (i.e., the striation thickness as given by equation 3.1-12) promoting agglomeration and cell coalescence. It is clear that the shear field generates competing mechanisms which can affect the cell density: dispersive mixing which increases the number of cells and cell coalescence which decreases the number of cells. In the design that follows, no attempt is made to reduce the dispersive mixing aspects of the shear flow. Instead, the design provides for minimization of cell coalescence so as to decouple cell nucleation, cell growth, and shaping. Ultimately, the critical experiments will give some indication whether the dispersive mixing aspects of shear flows must be addressed in the design of foaming dies. In general, dispersive mixing effects will influence the cell morphology along the surface of the extrudate.

To understand the rationale underlying the shaping pressure design parameter which satisfies the pre-shaping cell growth requirement, consider the following. Specifying relatively large shaping pressures, P_s, maintains relatively small cells in the nucleated polymer/gas solution. Provided that the cells are small enough during shaping (i.e., die flow), the cells will not tend to agglomerate, and the effects of cell coalescence and boundary shear flow will be minimized. For nucleated solutions having equal cell densities, smaller cell sizes imply larger interfacial distances between adjacent cells (striation thickness). This reduces the probability that adjacent cells will come in contact leading to coalescence and cell density deterioration. Note however, that the smaller cell size at high shaping pressures does not necessarily reduce the effects of dispersive mixing in the boundary shear field.

The use of the shaping pressure to maintain relatively small cells in the nucleated solution can be understood with the aid of Figure 9.3. In equilibrium, the gas phase pressure in the cells, P_g, is a function of the solution pressure surrounding the cells, P, and the surface energy, γ_{bp}, where from Laplace's equation, $P_g = P + 2\gamma_{bp}/R$. Likewise, the specific volume of the gas, v_g, varies inversely with the gas phase pressure based on the ideal gas law (see Figure 9.3). Therefore, as the solution pressure or shaping pressure is increased, the specific volume of the gas decreases leading to smaller cell sizes.

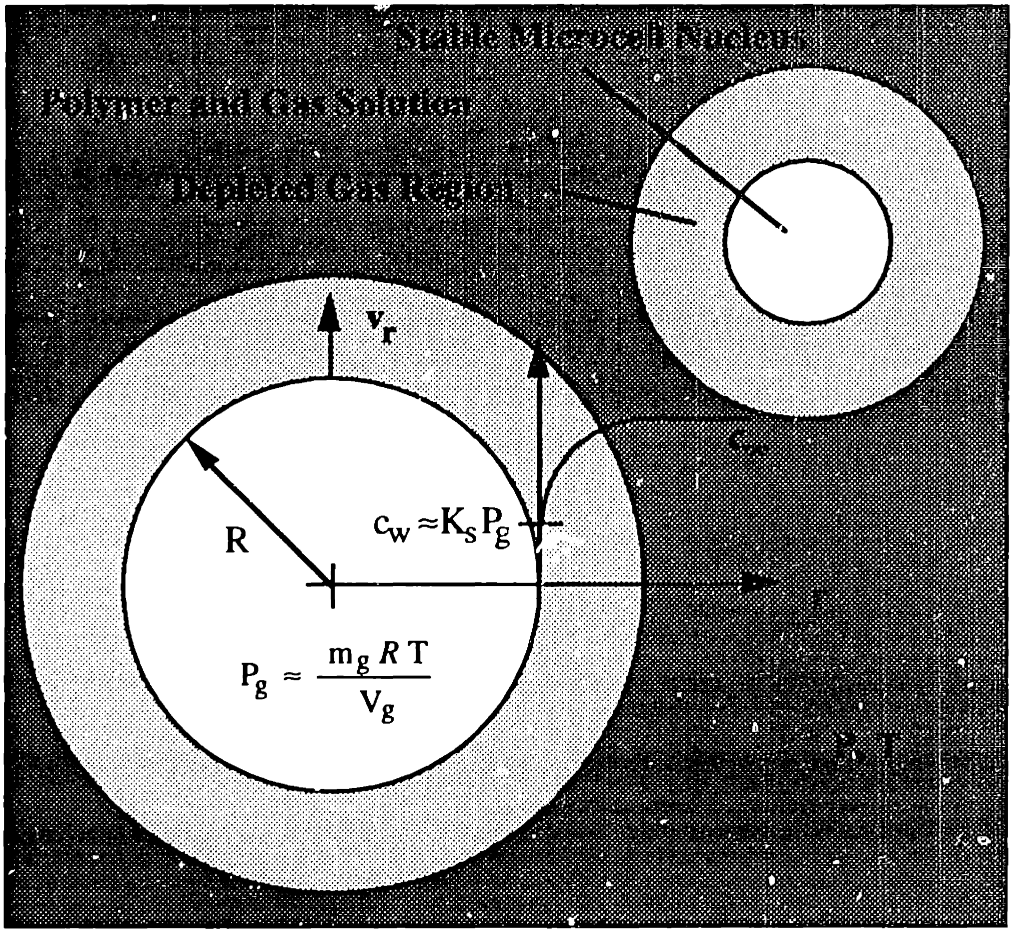

Figure 9.3: Schematic of growing microcells in a polymer/gas solution.

A final cell growth control requirement that deserves mention is that of cell growth stabilization. The importance of cell growth stabilization follows from the tendency of the nucleated solution flow to experience unstable cell growth and over-expansion of the cells, particularly when exiting the foaming die. When cell growth occurs without constraint, it becomes unstable and can lead to cell wall rupture and a deterioration of the cell density. This problem is pronounced at the elevated temperatures of melt processing due to the low melt strength of the polymer matrix, the relatively high specific volume of the gas phase, and the low surface tension of the polymer/cell interface. One might expect that the over-expansion of cells is pronounced at the surfaces of the foaming sheet, which is typically the case in microcellular sheet extrusion. In order to minimize the over-expansion of cells, lower temperatures can be employed (see equations 9-2 and 9-3) which increase the melt strength or stiffness of the viscoelastic matrix, decrease the specific volume of the gas phase, and increase the surface tension.

9.2 Analysis of a Nucleated Solution Flow During Shaping

To satisfy the pre-shaping cell growth control requirement, it is necessary to design a shaping and cell growth control die which can maintain the required shaping pressures. Therefore, the design of a shaping and cell growth die requires knowledge of the pressure loss effects of nucleated polymer/gas solutions. In general, the flow of a nucleated polymer/gas solution is complex and involves a heterogeneous system consisting of a polymer melt with dispersed cells having relatively large center-to-center spacing compared with the average cell diameters (see Figure 9.4). The pressure loss in the flow results from frictional effects at the die walls. As the pressure decreases along the die channel, the nucleated cells grow resulting in an increase in (1) the specific volume (or the decrease of density) of the two-phase system and (2) the volumetric flow rate. Cell growth is driven by the pressure within the cells and diffusion of solution gas into the cells. Gas diffusion into the cells results from the decrease in solubility as the solution pressure decreases along the die channel. As the heterogeneous system expands, there is less polymer across any given area of the flow channel to support the shear stresses generated by the wall friction. This implies that the expanding solution has a lower apparent viscosity. The apparent viscosity also tends to decrease due to shear thinning as the volumetric flow rate increases.

The flow of a nucleated polymer/gas solution in a slit of height $2 \cdot B$ is sketched in Figure 9.4 where P_s is the nucleated solution pressure entering the die slit, P_{exit} is the system pressure at the die exit, and L is the die slit length. Figure 9.4 also illustrates the influence of the high shear regions near the die walls which tend to elongate the expanding cells near the walls. The shear thinning nature of the polymer flow leads to relatively flat velocity profiles in the center characteristic of plug flow. Similar two-phase flow morphologies are presented by Han and Villamizar (1978) for HDPE and PS flows blown with chemical agents.

For the purposes of designing foaming dies to satisfy the shaping and cell growth control requirements, it is necessary to develop models to estimate the pressure loss and flow rate of a nucleated polymer/gas solution during die flow. The problem can be divided into four limiting cases which span the range of possible flow configurations. The first case accounts for the fact that gas diffuses into the cells as the solution pressure decreases such that cell growth during the die flow is driven by both the gas pressure in the cells and the diffusion of gas into the cells. The second case assumes that negligible gas diffuses into the cells after nucleation such that cell growth during the die flow is driven by the gas pressure in the cells post-nucleation. This case represents an upper limit on the pressure loss during die flow. The third case assumes that all of the available solution gas diffuses into the cells prior to flowing into the die slit such that cell growth is driven by the gas pressure in the cells. This case represents a lower limit on the pressure loss in the die flow. The fourth case is similar to case two but accounts for the diffusion of gas into the cells prior to entering the foaming die and neglects gas diffusion during die flow.

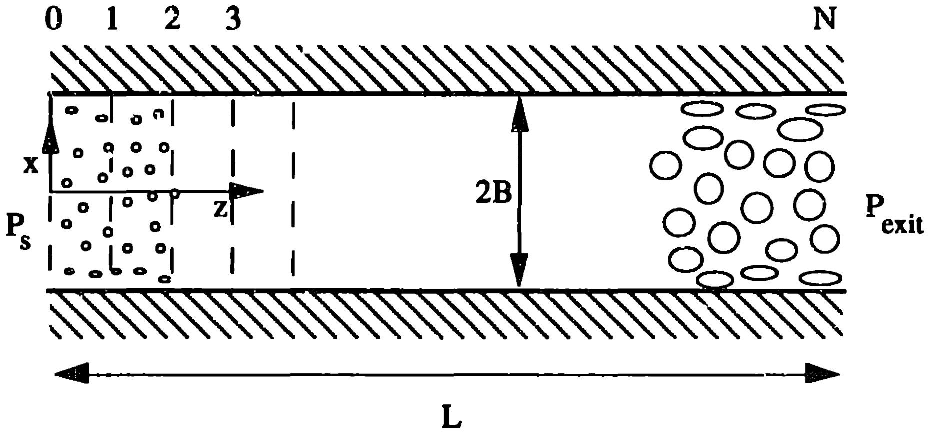

Figure 9.4: Representative view of the cell morphology during the flow of a nucleated polymer/gas solution in a slit.

While the following analysis incorporates a number of simplifying assumptions, it is important to keep in mind the intent of the analysis which is to develop an approximate design model for predicting the pressure loss and flow rates of nucleated polymer/gas solutions. In this analysis, the model is kept as simple as possible while capturing the major physics of the complex two-phase flow. Such a model has great utility in the design of prototype shaping and cell growth control devices, and more importantly provides a reasonable guide to the basic interactions of the major processing variables involved in continuous shaping and cell growth control operations.

9.2.1 Nucleated Flow With Concurrent Gas Diffusion

For case one where the gas diffuses into the cells as the pressure decreases (i.e., the concurrent diffusion case), the pressure loss and volumetric flow rate of a nucleated polymer/gas solution can be estimated based on the frictional losses at the die walls. This is accomplished by treating the nucleated solution as a non-Newtonian fluid having a bulk viscosity and flow rate which are dependent on the volume fraction of cells (voids) in the polymer matrix (given by equations 9-6 and 9-7 , respectively, where Φ_v is the volume fraction of voids).

$$\eta_f \approx \eta(\Phi_v) \tag{9-6}$$

$$Q \approx Q(\Phi_v) \tag{9-7}$$

Based on the apparent viscosity measurements of Oyanagi and White (1979), the rheological behavior of polymeric foams follows similar shear thinning behavior to the neat polymer. Moreover, Oyanagi and White's results indicate that the presence of a blowing agent tends to decrease the apparent viscosity by a multiplicative constant (i.e., showing equivalent power law factors, n). The developments of Kraynik (1981) in polymer foam rheology also indicate decreases in apparent viscosity for many thermoplastic foam flow fields. Therefore, as a first order approximation, the non-Newtonian viscosity of the nucleation solution, η_f, will be given by the modified power law relation of equation (9-8) where m_f is the power law constant of the foam.

$$\eta_f \approx m_f \dot{\gamma}^{n-1} \tag{9-8}$$

The ability of the nucleated solution to resist shear forces is a strong function of the solution void fraction where the presence of cells or voids reduces the effective area of polymer resisting shear. Moreover, the viscosity of the gas within the voids is negligible compared with the viscosity of the polymer matrix. Therefore, the non-Newtonian viscosity of the nucleated solution can be approximated by equation (9-9). For the case where the mass fraction of gas is relatively small, equation (9-9) simplifies to equation (9-10) where ρ_p is the polymer density and $v_{g/p}$ is the specific volume of the gas phase relative to the polymer mass. In this analysis, the possible decrease in the apparent viscosity due to the presence of dissolved gas in the polymer matrix has been neglected since reliable estimates for polystyrene/CO_2 systems are not available. However, Blyler and Kwei (1971) have reported viscosity decreases of 20% and 22% in low and high density polyethylene containing 0.32% dissolved gas from the decomposition of a chemical blowing agent.

$$m_f \approx m(1 - \Phi_v) \tag{9-9}$$

$$m_f \approx m\left(1 - \frac{1}{1 + \frac{1}{\rho_p v_{g/p}}}\right) \tag{9-10}$$

Using the power law approximation of equations (9-8) and (9-10), the bulk flow of a nucleated polymer/gas solution can be described by equation (9-11) for steady, fully-developed, non-Newtonian flow through a constant cross-section slit of height 2·B and width W. ‡

$$-\frac{dp}{dz} = \left[\frac{2 + 1/n}{2\,W\,B^2}\,Q\right]^n \frac{m_f}{B} \qquad (9\text{-}11)$$

The total pressure loss can then be obtained by integrating equation (9-11) over the slit length, L, where P_s is the solution pressure at the slit entrance and P_{exit} is the solution pressure at the slit exit. In equation (9-12), the volumetric flow rate, Q, and the power law coefficient, m_f, are both functions of the local pressure, p.

$$\int_{P_{exit}}^{P_s} dp = \int_0^L \left[\frac{2 + 1/n}{2\,W\,B^2}\,Q(p)\right]^n \frac{m_f(p)}{B}\,dz \qquad (9\text{-}12)$$

In order to integrate equation (9-12), the pressure dependence of the volumetric flow rate and power law factor must be determined. The volumetric flow rate of the nucleated solution can be determined by accounting for the specific volume of the polymer/gas system, v_m, which is a strong function of the local pressure. In the case of relatively low gas concentrations, the volumetric flow rate is given by equation (9-13), where $\dot{m}_p$ is the polymer mass flow rate.

$$Q = \dot{m}\, v_m \approx \dot{m}_p\, v_m \qquad (9\text{-}13)$$

Again using the approximation that the gas concentration is relatively low, the specific volume of the polymer/gas system is given by the sum of the specific volume of the gas phase relative to the polymer mass, $v_{g/p}$, plus the specific volume of the polymer matrix. Neglecting any swelling of the polymer matrix due to the dissolved gas, the specific volume of the polymer is given by the inverse of the neat polymer density, ρ_p. In this case, the volumetric flow rate is given by

$$Q \approx \dot{m}_p \left(v_{g/p} + 1/\rho_p\right) \quad . \qquad (9\text{-}14)$$

---

‡ Although using the lubrication approximation, this analysis can be modified to accommodate gradual tapers in cross-sectional area where W = W(z) and B = B(z).

To determine $v_{g/p}$, the gas within the cells can be treated as being in quasi-static equilibrium and approximated as a perfect gas such that the total volume of the gas phase, V_g, is given by

$$V_g = m_g \frac{R\,T}{P_g} \tag{9-15}$$

where m_g is the mass of gas phase, R is the gas constant (equal to the universal gas constant divided by the molecular weight of the gas), T is the absolute temperature, and P_g is the pressure of the gas phase. Here the gas phase in each cell is treated uniformly throughout the polymer/gas system. Mass conservation of the gas maintains that the mass of gas phase must equal the mass of the total gas initially dissolved into the polymer, m_T less the mass of gas remaining in solution, m_s. Equation (9-15) then becomes

$$V_g = (m_T - m_s)\frac{R\,T}{P_g} \tag{9-16}$$

The initial mass of dissolved gas is given by the initial gas concentration times the polymer mass. The mass of the remaining dissolved gas can be approximated using Henry's law (equation 3.1-21) assuming at any given instant the solution gas concentration is uniform and the system is in quasi-static equilibrium. Normalizing equation (9-16) relative to the polymer mass then yields

$$v_{g/p} = \frac{V_g}{m_p} = (c_\infty - K_s(T)\,P_g)\frac{R\,T}{P_g} \tag{9-17}$$

where c_∞ is the initial gas concentration and K_s is Henry's law constant. Inherent to equation (9-17) is the assumption that at any given instant., a sufficient amount of gas has diffused into the cells to establish a quasi-static equilibrium. Such a state is typified by uniform solution gas concentrations (i.e., no gas depleted regions around the cells). Strictly speaking, this assumption does not hold, although it provides a useful approximation in obtaining an estimate of the pressure loss and flow rates in the nucleation solution flows.

Based on the quasi-static approximation, the pressure of the gas phase can be related to the local solution pressure using Laplace's equation (9-18) where the cells are treated as having a uniform radius R, P is the solution pressure, and γ_{bp} is the surface tension of the gas/polymer interface. Note that the uniform cell radius is typically a reasonable assumption in microcellular processing due to the narrow cell size distributions achieved with this technology. Inherent to equation (9-18) is the assumption that the cell growth dynamics (as described by equations 3.3-8 through 3.3-11) are sufficiently rapid to allow near-equilibrium conditions to be achieved at any given instant. In addition, it should be noted that equation (9-18) treats the flow field as a viscous medium and neglects the elastic energy of the polymer matrix. At higher melt temperatures, this is a reasonable approximation for many polymers. An alternate to equation (9-18) would be to treat the expanding matrix as neo-Hookean and use the developments of Denecour and Gent (1968) and Gent and Tompkins (1969ab). †

$$P_g = \frac{2\,\gamma_{bp}}{R} + P \tag{9-18}$$

Next, it is necessary to relate the radius of the cells back to the specific volume of the gas phase. This can be achieved using equation (9-19) for a known density of nucleated cells, ρ_c (Remember that the cell density is determined by an independent processing step.). Rearranging equation (9-19) yields the average cell radius given by equation (9-20).

$$V_g = \rho_c \frac{m_p}{\rho_p}\left(\frac{4}{3}\pi R^3\right) \tag{9-19}$$

$$R = \left[\frac{3\,\rho_p}{4\,\pi\,\rho_c} v_{g/p}\right]^{1/3} \tag{9-20}$$

By combining equations (9-17), (9-18), and (9-20), an expression relating the gas phase pressure and the solution pressure is derived and given by equation (9-21).

$$P_g = P + 2\,\gamma_{bp}\left[\frac{3\,\rho_p}{4\,\pi\,\rho_c}\frac{R\,T}{P_g}\left(c_\infty - K_s(T)\,P_g\right)\right]^{-1/3} \tag{9-21}$$

Calculating the gas phase pressure for a given solution pressure, requires equation (9-21) to be solved iteratively, precluding a closed form solution of equation (9-12).

---

† If the expanding cells are treated as having thin shells of thickness, t_o, supporting the extensional stresses, then the relationship between the cell pressure and radius is given by (where G is the shear modulus and R_o is the initial cell radius)

$$P_g/G = (2\,t_o/R_o)\left((R_o/R) - (R_o/R)^7\right) .$$

If the expanding cells are approximated as having thick or infinite walls, then the cell pressure is given by

$$P_g/G = 5/2 - 2\,(R_o/R) - (1/2)\,(R_o/R)^4 .$$

See Gent and Tompkins (1969ab) for similar expressions accounting for the pressure surrounding the cells.

Therefore, a finite difference technique can be used to solve equation (9-12). Using Figure 9.4 as a reference, the slit flow can be divided into N elements of length Δz. The incremental pressure drop ΔP over element i+1 is then given by

$$\Delta P_{i+1} \approx \left[\frac{2+1/n}{2\,W\,B^2}\,Q_i\right]^n \frac{m_{fi}}{B}\,\Delta z \tag{9-22}$$

and the total pressure at i+1 is given by

$$P_{i+1} \approx P_i + \Delta P_{i+1} \tag{9-23}$$

Equations (9-22) and (9-23) can be solved using the boundary condition that at the slit exit, the solution pressure is given by $P(x = L) = P_{exit} = P_N$. The solution to equations (9-22) and (9-23) is accomplished by determining the local gas phase pressure, P_g at the solution pressure P_i via equation (9-21). Equations (9-10), (9-14), and (9-17) can then be used to calculate the local power law coefficient, m_{fi}, and the local flow rate, Q_i. The values of m_{fi} and Q_i are then used to calculate the local pressure drop, ΔP_{i+1}, and the local pressure, P_{i+1}, using equations (9-22) and (9-23). This iterative solution proceeds until i equals N-1.

Pressure loss and flow rate estimates typical of nucleated solution flows during shaping and cell growth operations are presented in Figure 9.5. The model parameters used where for a polystyrene/CO_2 system having $T = 150$ °C, $\rho_p = 1.04$ g/cm^3, $\gamma_{bp} = 0.0314$ N/m (Wu, 1982), $\rho_c = 1.5 \times 10^9$ cells/cm^3, $K_s = 0.003986$ kg(CO_2)/kg(PS)MPa (Park, 1993), $c_\infty = 0.05$, $\dot{m}_p = 26$ g/min, $n = 0.29$, and $m = 40750$ Pa s^n. The slit dimensions used were $B = 0.3175$ mm, $W = 25.4$ mm, $L = 20.32$ mm, and $N = 20$ (i.e., $\Delta z = 1.02$ mm). The boundary condition used was $P_{exit} = 0.965$ MPa (140 psi). This boundary condition is based on the findings of Han et al. (1976) and Han and Villamizar (1978). Han and coworkers measured pressure profiles of polymer foam flows through various die geometries. These measurements revealed exit pressure losses equal to nearly 10% of the die entrance pressures.

Figure 9.5 demonstrates some of the important aspects of nucleated solution flows during shaping and cell growth operations. Notice that the volumetric flow rate increases parabolically along the slit length, and the solution pressure decreases non-linearly along the slit length. In contrast, the neat polymer flow demonstrates a constant flow rate and a linear decrease in pressure over the slit length. The pressure loss trends of Figure 9.5 can be understood by looking back at equation (9-11). The decrease in pressure gradient along the slit length results from the decrease in the effective viscosity of the heterogeneous polymer/gas matrix along the slit length. The viscosity decrease follows from the expansion of the nucleated solution which reduces the effective area supporting the shear stresses. In this case, the viscosity decrease is sufficiently large to overcome the contributions of the increasing flow rate along the slit length. Notice from equation (9-11) that an increasing flow rate tends to increase the pressure loss. The non-linear pressure profiles predicted by this macroscopic treatment of nucleated solution flow are supported by the experimental findings of Han et al. (1976) and Han and Villamizar (1978). Han and coworkers present pressure profile measurements in polymer foam flows indicating non-linear trends similar to those of Figure 9.5 with the exception of the pressure profiles near the exit reported by Han et al. (1976) which show increased pressure gradients near the die exit.

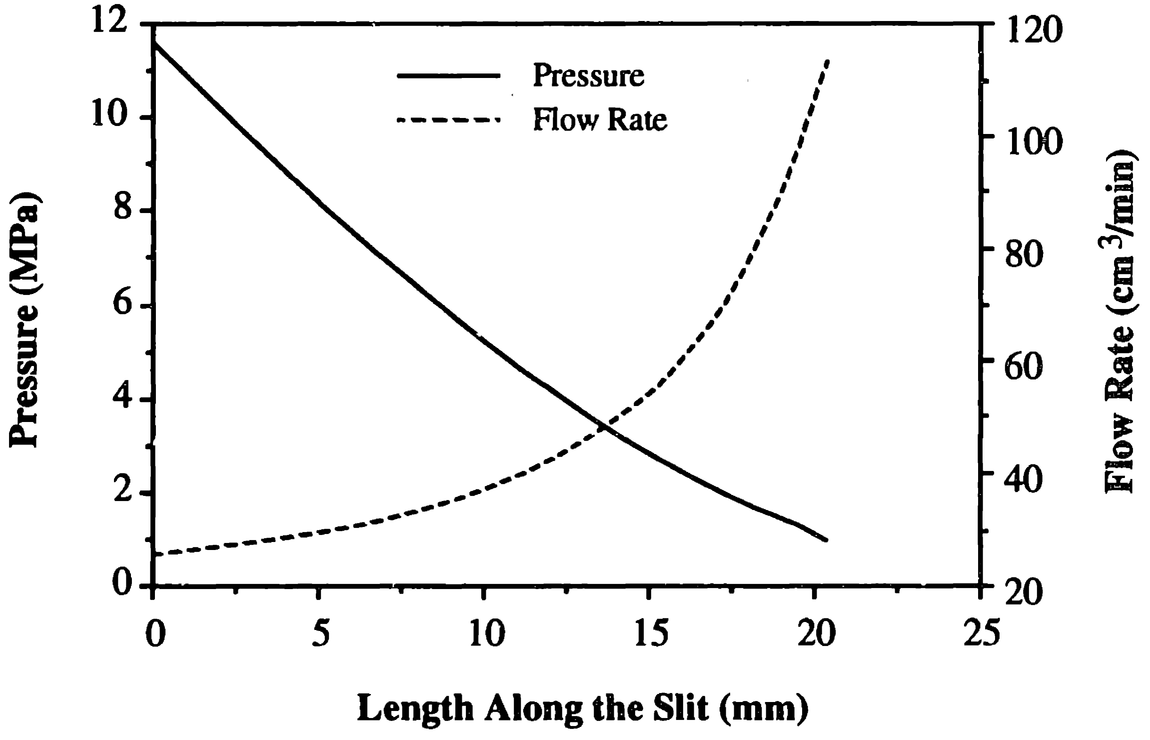

Figure 9.5: Pressure loss and flow rate estimates for the flow of a nucleated polymer/gas solution through a slit.

9.2.2 Nucleated Flow With Post Gas Diffusion

In addition to the concurrent diffusion case presented above, it is important to understand the limiting cases for the flow of nucleation polymer/gas solutions. Predicting the limiting cases will provide a useful comparison for the intermediate models and will further illustrate the critical processing characteristics that need to be addressed in the design of shaping and cell growth control devices.

As a limiting case, consider the flow of a nucleated polymer/gas system in which only the gas present in the stable nuclei is available for expanding the cells (i.e., the post-diffusion case). In this case, gas diffusion into the cells is treated as being very slow compared with the flow rate during shaping operations. All of the appreciable gas diffusion occurs post-shaping. The analysis follows the same lines and is restricted by the same assumptions of section 9.2.1. Again, the flow field of interest is a planar slit flow of a nucleated polymer/gas solution as shown in Figure 9.4.

The gas phase present in the stable nuclei can be determined based on classical nucleation theory (equations 3.2-4 and 3.2-5). For spherical nuclei, the critical radius size, R_o, is given by

$$R_o = r^* = \frac{2\gamma_{bp}}{\Delta P_{nuc}} \tag{9-24}$$

where ΔP_{nuc} is the pressure change used to instigate the thermodynamic instability for nucleation. The mass of the gas phase can then be determined by equating equations (9-15) and (9-19) and substituting equation (9-24) for the solution conditions post-nucleation. Immediately after nucleation, the solution temperature is T_n and the pressure of the gas phase in the cells is $P_{go} \approx \Delta P_{nuc}$. The mass of the gas phase immediately after nucleation is then given by

$$m_g = \frac{4\pi\rho_c}{3\rho_c}\frac{\Delta P_{nuc}}{R\ T_n}\left[\frac{2\gamma_{bp}}{\Delta P_{nuc}}\right]^3 m_p \ . \tag{9-25}$$

Substituting equation (9-25) into equation (9-15) yields the specific volume of the gas phase relative to the polymer mass given by equation (9-26). The specific gas volume applies at any point along the flow field under the assumption that the gas amount is fixed at the nucleation stage.

$$v_{g/p} = \frac{4\pi\rho_c}{3\rho_c}\frac{T}{T_n}\frac{\Delta P_{nuc}}{P_g}\left[\frac{2\gamma_{bp}}{\Delta P_{nuc}}\right]^3 \tag{9-26}$$

In equation (9-26), T is the solution temperature during the slit flow which can be different from the solution temperature at nucleation.

Finally, an expression for the gas phase pressure as a function of the solution pressure can be obtained by substituting equation (9-20) and (9-26) into equation (9-18).

$$P_g = P + \Delta P_{nuc}\left[\frac{T}{T_n}\frac{\Delta P_{nuc}}{P_g}\right]^{-1/3} \tag{9-27}$$

Equation (9-27) can then be used to evaluate the pressure of the gas phase as a function of the local solution pressure. In order to determine the local pressure change and the local solution pressure via equations (9-22) and (9-23), equation (9-27) can be used to evaluate the local gas phase pressure, P_g. Equation (9-26) can then be used to calculate the local specific volume of the gas. The local volumetric flow rate and the local power law coefficient can then be determined from equations (9-14) and (9-10). Finally, the pressure loss and the volumetric flow rate profiles along the slit can be determined using the finite difference technique discussed in section 9.2.1.

9.2.3 Nucleated Solution Flow With Complete Gas Diffusion

As a second limiting case, consider the flow of a nucleated polymer/gas system in which all of the available gas has diffused into the cells prior to shaping or cell growth operations (i.e., the pre-diffusion case). In this case, gas diffusion into the cells is treated as being very rapid compared with the flow rate such that all of the available gas diffuses into the cells prior to shaping. The analysis follows the same lines and restrictions of section 9.2.1. Again, the flow field of interest is a planar slit flow of a nucleated polymer/gas solution as shown in Figure 9.4.

By assumption, all of the available gas has diffused into the cells prior to the slit flow. Therefore, the mass of the gas phase is constant throughout the shaping process. In this case, the initial gas concentration is determined independently by the solution formation system, such that the mass of the gas is given by

$$m_g = c_\infty m_p \ . \tag{9-28}$$

The specific volume of the gas phase relative to the polymer mass is obtained by substituting equation (9-28) into equation (9-15).

$$v_{g/p} = c_\infty \frac{\mathcal{R}\,T}{P_g} \tag{9-29}$$

In the case of complete gas diffusion, the local gas phase pressure can be obtained by substituting equation (9-29) and (9-20) into equation (9-18) yielding

$$P_g = P + 2\,\gamma_{bp}\left[\frac{3\,\rho_p}{4\,\pi\,\rho_c}\,\frac{R\,T}{P_g}\,c_\infty\right]^{-1/3} . \qquad (9\text{-}30)$$

Equation (9-31) can then be used to evaluate the pressure of the gas phase as a function of the local solution pressure. In order to determine the local pressure change and the local solution pressure via equations (9-22) and (9-23), equation (9-30) can be used to evaluate the local gas phase pressure, P_g. Equation (9-29) can then be used to calculate the local specific volume of the gas. The local volumetric flow rate and the local power law coefficient can then be determined from equations (9-14) and (9-10). Finally, the pressure loss and the volumetric flow rate profiles along the slit can be determined using the finite difference technique discussed in section 9.2.1.

9.2.4 Nucleated Solution Flow With Partial Gas Diffusion

A final case to consider for the flow of a nucleated polymer/gas solution is a variation of that presented in section 9.2.2. In this case, the gas is assumed to diffuse into the cells prior to slit flow creating a quasi-static equilibrium state where the gas concentrations are uniform and the mass of gas in the cells is uniquely determined by the solution pressure at the inlet to the slit, P_s (i.e., the partial pre-diffusion case).

First, the gas mass available prior to entering the slit flow must be determined. To accomplish this, it is assumed that a quasi-static equilibrium condition is reached just upstream of the slit where and equilibrium mass of gas has diffused into the cells and uniform gas concentrations have been achieved in the solution. Using Henry's law and an initial gas phase pressure, P_{go}, just upstream of the slit, the constant mass of the gas phase is given by

$$m_g = \left(c_\infty - K_s(T)\,P_{go}\right) m_p \ . \qquad (9\text{-}31)$$

Substituting equation (9-31) into equation (9-15) gives the specific volume of the gas phase.

$$v_{g/p} = \frac{V_g}{m_p} = \left(c_\infty - K_s(T)\,P_{go}\right)\frac{R\,T}{P_g} \qquad (9\text{-}32)$$

Using an analogous derivation of the gas phase pressure presented in section 9.2.1, the initial gas phase pressure just upstream of the slit is given by equation (9-33) where P_s is the solution pressure just upstream of the slit. Equation (9-33) can be used to determine the gas phase pressure when the inlet solution pressure, P_s, is known.

$$P_{go} = P_s + 2\,\gamma_{bp}\left[\frac{3\,\rho_p}{4\,\pi\,\rho_c}\,\frac{\mathcal{R}\,T}{P_{go}}\left(c_\infty - K_s(T)\,P_{go}\right)\right]^{-1/3} \tag{9-33}$$

Similarly, the gas phase pressure at any point in the slit flow field is given by equation (9-34).

$$P_g = P + 2\,\gamma_{bp}\left[\frac{3\,\rho_p}{4\,\pi\,\rho_c}\,\frac{\mathcal{R}\,T}{P_g}\left(c_\infty - K_s(T)\,P_{go}\right)\right]^{-1/3} \tag{9-34}$$

Equation (9-33) can be used to evaluate the initial pressure of the gas phase at the slit inlet using an estimated solution pressure at the slit inlet. Equation (9-34) can then be used to evaluate the pressure of the gas phase as a function of the local solution pressure. In order to determine the local pressure change and the local solution pressure via equations (9-22) and (9-23), equation (9-34) can be used to evaluate the local gas phase pressure, P_g. Equation (9-32) can then be used to calculate the local specific volume of the gas. The local volumetric flow rate and the local power law coefficient can then be determined from equations (9-14) and (9-10). Finally, the pressure loss and the volumetric flow rate profiles along the die slit can be determined using the finite difference technique discussed in section 9.2.1.

9.2.5 Comparison of Nucleated Solution Flow Models

In order to compare these four models, the parameters given in Table 9.1 for a polystyrene/CO_2 system typical of microcellular polymer sheet extrusion were used. The pressure profile results from the concurrent diffusion model (section 9.2.1), the post-diffusion model (section 9.2.2), the pre-diffusion model (section 9.2.3), and the partial pre-diffusion model (section 9.2.4) are plotted in Figure 9.6. Notice first that the post-diffusion case (i.e., where only the nucleated gas phase is present during slit flow) and the pre-diffusion case (i.e., where all of the solution gas is present in the gas phase) give the upper and lower pressure loss limits for the nucleated solution flow. The total pressure losses predicted by these limiting cases differ by 63%. The post-diffusion case is interesting in that it has a constant pressure gradient similar to the neat polymer flow. From closer inspection of this case, it is found that the post-diffusion case and the neat polymer flow are identical. This results from the assumption that the only the nucleated gas phase is available for expanding the cells during slit flow. Since the nucleated gas phase has very little volume, the initial cell size is quite small, which leads to large surface tension contributions and negligible cell growth as the solution pressure decreases.

Table 9.1: Parameters used in the nucleated solution flow models.

ρ_p	1.04 g/cm^3
γ_{bp}	0.0314 N/m
K_s	0.004 kg(CO$_2$)/kg(PS) MPa
n	0.29
m	40750 Pa s^n
ρ_c	1.5 x 10^9 cells/cm^3
$\dot{m}_p$	26 g/min
P_{exit}	0.965 MPa (140 psi)
T	150 °C
T_n	200 °C
ΔP_{nuc}	22.75 MPa (3300 psi)
P_s	9.65 MPa (1400 psi)
c_∞	0.05 kg(CO$_2$)/kg(PS)
B	0.3175 mm
W	25.4 mm
L	20.32 mm
Δz	1.02 mm

A similar situation holds for the partial pre-diffusion case where it is assumed equilibrium concentrations exist prior to slit flow and gas diffusion during slit flow is negligible. This case also demonstrates a nearly constant pressure gradient. In addition, notice that the pressure gradient is less than that of the post-diffusion case (the neat polymer flow). The lower pressure gradient results from the finite cell size and specific volume of gas phase existing upstream of the slit. The presence of these cells tends to lower the bulk viscosity of the nucleated solution flow, which decreases the effective pressure gradient over the slit. Notice further that initial signs of non-linearity are shown near the slit exit where the pressure is low and cells expand quickly.

The pressure loss results for the concurrent diffusion and pre-diffusion cases both show non-linear behavior with decreasing pressure gradients along the slit length. The decreasing pressure gradients are indicative of the fact that the viscosity changes dominate the pressure loss despite the fact that the flow rates increase along the slit length.

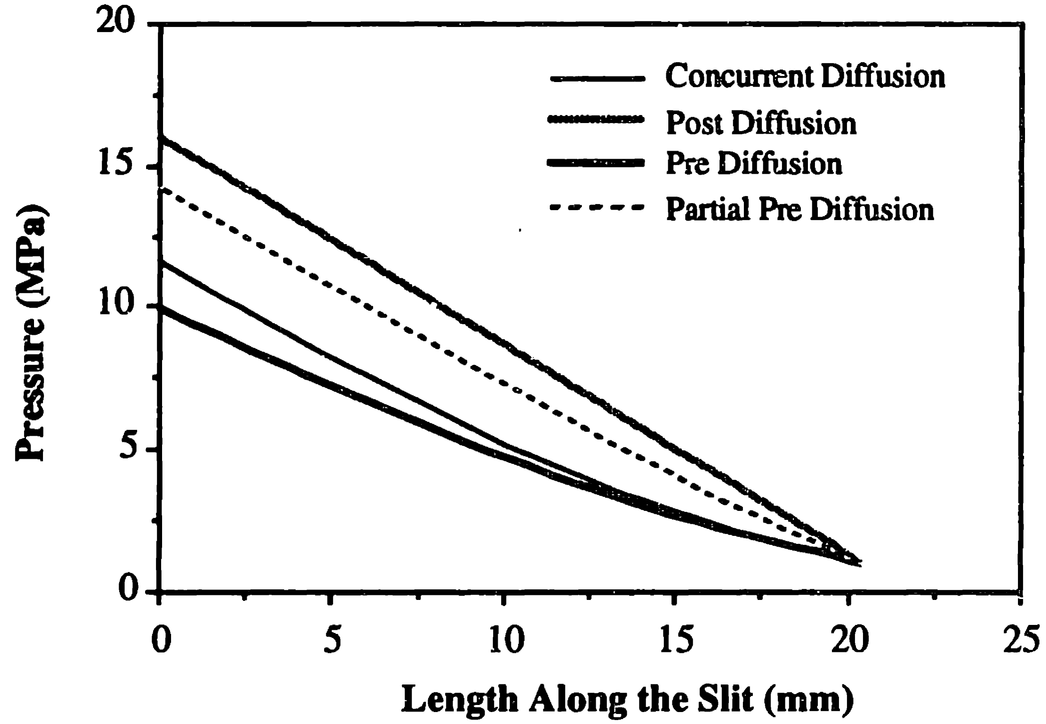

Figure 9.6: Pressure loss profiles for a planar slit predicted by the four nucleated solution flow models.

Since the rationale of designing the die is to maintain small cell sizes during shaping operations, it is important to compare the estimated average cell sizes for the four models. The post-diffusion model estimates an average cell radius at the slit inlet of 0.0021 μm. At the other limit, the pre-diffusion case estimates a cell radius of 4.0 μm. The current diffusion and partial pre-diffusion cases estimate entrance cell radii of 1.9 μm and 2.2 μm, respectively. Since the final cell size range for microcellular polymers is 10 to 20 μm, initial shaping cell sizes around 2 μm should be sufficient to prevent degradation of the cell density and therefore satisfy the pre-shaping cell growth control functional requirement.

The volumetric flow rate results for the four the nucleated polymer/gas solution flow models are shown in Figure 9.7. Notice first, the limiting flow rates given by the post-diffusion case and the pre-diffusion case. The post-diffusion case demonstrates a constant flow rate equal to the neat polymer flow which results form the negligible expansion of the nucleated gas phase during slit flow. In contrast, the pre-diffusion case shows a rapid increase in flow rate over the slit length resulting from the expanding cells which contain all the available gas. Notice further that the pre-diffusion case has an initial flow rate which is twice that of the neat polymer due to the larger initial cell size at the slit entrance. The intermediate case of concurrent diffusion shows flow rate trends similar to the pre-diffusion case with slightly larger gradients near the slit exit due to the larger expansion rates occurring for simultaneous gas diffusion. The other intermediate case of partial pre-diffusion, where equilibrium conditions are reached prior to entering the slit and no diffusion occurs in the slit, shows a more gradual change in the flow rate over the slit length since the gas available to expand thc cells is limited.

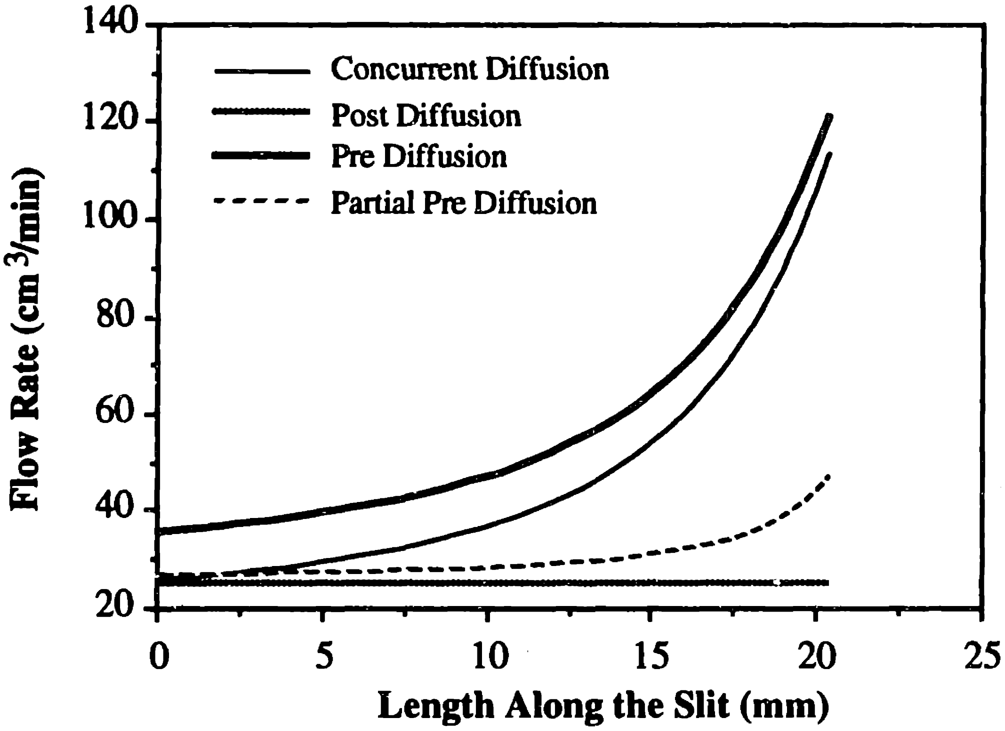

Figure 9.7: Volumetric flow rate profiles for a planar slit predicted by the four nucleated solution flow models.

The estimates of Figure 9.6 and 9.7 have a number of implications on the design of shaping and cell growth control devices. In general, each of these cases can be associated with a particular type of die design and system flow depending on a dimensionless parameter consisting of the characteristic flow rate and the characteristic gas diffusion rate. The characteristic flow rate of a fluid particle is given by

$$\frac{\bar{v}}{L} \approx \frac{Q}{L\,A} \tag{9-35}$$

where L is the channel length and A is the channel cross-sectional area. The characteristic diffusion rate is given by

$$\frac{1}{\tau} \approx \frac{D}{l^2} \approx \frac{D}{\rho_c^{-2/3}} \tag{9-36}$$

where the characteristic diffusion distance is approximated by the center-to-center distance between cells, $\rho_c^{-2/3}$.

In general, one can associate the different flow cases with a particular foaming die configuration as summarized in Table 9.2. Notice, at very high processing rates, the nucleated solution flow would tend to behave more like the post-diffusion flow of Figures 9.6 and 9.7. This follows since at very high processing rates, the die flow occurs over a much shorter time frame then that of gas diffusion into the cells. For foaming die designs having large post-nucleation channel volumes (L_{pn} A_{pn}) and relatively small shaping channel volumes (L_s A_s), the nucleated solution flow would tend to behave like the partial pre-diffusion case. In this case, enough time is allowed for gas diffusion to equilibrate prior to slit flow. However, during slit flow, velocities are sufficiently large to inhibit appreciable gas diffusion. If the flow rates and diffusion rates are on the same order, then the concurrent diffusion case would tend to estimate the correct pressure loss and flow rates. Finally, under conditions where the flow rates are low and the flow channel volumes (L A) are high, the-pre diffusion case would tend to estimate the correct pressure losses and flow rates of nucleated polymer/gas solutions.

Table 9.2: Characterization of nucleated polymer/gas solution flows for various foaming die configurations. (L_{pn} and A_{pn} are the post-nucleation flow length and area. L_s and A_s are the post-shaping flow length and area.)

$\dfrac{\text{Characteristic Flow Rate}}{\text{Characteristic Diffusion Rate}}$	Nucleated Solution Flow Case
$\dfrac{Q}{L\,A\,D\,\rho_c^{2/3}} >> 1$	Post-Diffusion Case
$\dfrac{Q}{L_{pn}\,A_{pn}\,D\,\rho_c^{2/3}} << 1$ and $\dfrac{Q}{L_s\,A_s\,D\,\rho_c^{2/3}} >> 1$	Partial Pre-Diffusion Case
$\dfrac{Q}{L\,A\,D\,\rho_c^{2/3}} \sim 1$	Concurrent Diffusion Case
$\dfrac{Q}{L\,A\,D\,\rho_c^{2/3}} << 1$	Pre-Diffusion Case

Finally, it should be mentioned that the analysis of sections 9.2.1 through 9.2.4 applies equally well for tube flows. In this case, equation (9-37) is substituted for (9-11) where D is the diameter of the tube. The solution to equation (9-37) proceeds in a similar manner to the slit flow case where a finite difference technique is used to locally solve the relative pressure loss and solution pressure.

$$-\frac{dp}{dz}=\left[\frac{8\,(3+1/n)}{\pi\,D^3}\,Q\right]^n\frac{4\,m_f}{D} \tag{9-37}$$

9.2.7 Potential Cooling During Cell Growth

A final consideration in modeling the shaping and cell growth of nucleated polymer/gas solution flows is the potential of adiabatic cooling of the gas phase during free expansion. The emerging polymer/gas solution flow from the die slit maintains a finite exit pressure, P_{exit}, due to the stored elastic energy of the polymer matrix. Once outside the die, the polymer matrix can relax allowing the pressure of the system to approach atmospheric. These relatively small pressure changes lead to significant specific volume increases and can lead to adiabatic cooling of the gas phase. In order to estimate the maximum cooling effect of the gas, this expansion process can be modeled as reversible and adiabatic. For an ideal gas, this yields equation (9-38) where T is the absolute temperature, v is the specific volume of the gas at the exit and final states, and $k = c_p/c_v$ and is the specific heat ratio of the gas. Based on the model estimates of section 9.2.5 for the pre-diffusion and concurrent diffusion cases (with k = 1.29 for CO_2), the adiabatic gas phase temperatures are -58 °C and -63 °C for an exit melt temperature of 150 °C. For an exit temperature of 200 °C, the adiabatic gas phase temperatures are -32 °C and -38 °C for the pre-diffusion and concurrent diffusion cases. Since the actual expansion process is not reversible and is not likely to be adiabatic, these rough estimates represent lower limits and serve only to demonstrate that some internal cooling can result from the final expansion process which helps to constrain the post-shaping cell growth.

$$\frac{T_{final}}{T_{exit}}=\left(\frac{v_{exit}}{v_{final}}\right)^{k-1} \tag{9-38}$$

9.3 Shaping and Cell Growth of a Thick Filament

In order to verify the concept of shaping a nucleated polymer/gas solution flow, a relatively simple geometry was selected capable of producing large diameter filaments. The predictions of the previous section indicate that shaping pressures on the order of 6.9 to 14 MPa (1000 to 2000 psi) are required to satisfy the pre-shaping cell growth control requirement. Using this pressure range as an acceptable design parameter range, a nucleated flow analysis was performed for tube flow following the same lines as that of section 9.2. Based on this analysis, the shaping and cell growth control die design of Figure 9.8 was manufactured. This design consists of a nozzle nucleation device and a filament shaping die. This staged nozzle configuration provides for the necessary staged pressure losses to maintain functional independence of the nucleation, cell growth, and shaping requirements.

Next a critical experiment was run to verify the concept of shaping a nucleated solution flow using the extrusion system configuration of Figure 9.9 and the foaming die of Figure 9.8. The process parameters for the experiment were: material = Novacor 101 PS, nozzle diameter = 0.533 mm, nozzle length = 6.35 mm, filament die diameter = 1.04 mm, filament die length = 12.7 mm, flow rate = 23 g/min, die temperature = 149 °C, estimated gas concentration = 6 %, nucleation pressure = 28.28 MPa (4100 psi), shaping pressure = 6.89 MPa (1000 psi). The critical experiment was successful in demonstrating the feasibility of continuous shaping of a nucleated polymer/gas solution. A typical scanning electron microscope micrograph of the microcellular polystyrene thick filament is shown in Figure 9.10 exhibiting an average cell size of 10 μm and an average cell density of 1 x 10^9 cells/cm^3. The repeatability of these results was also experimentally verified.

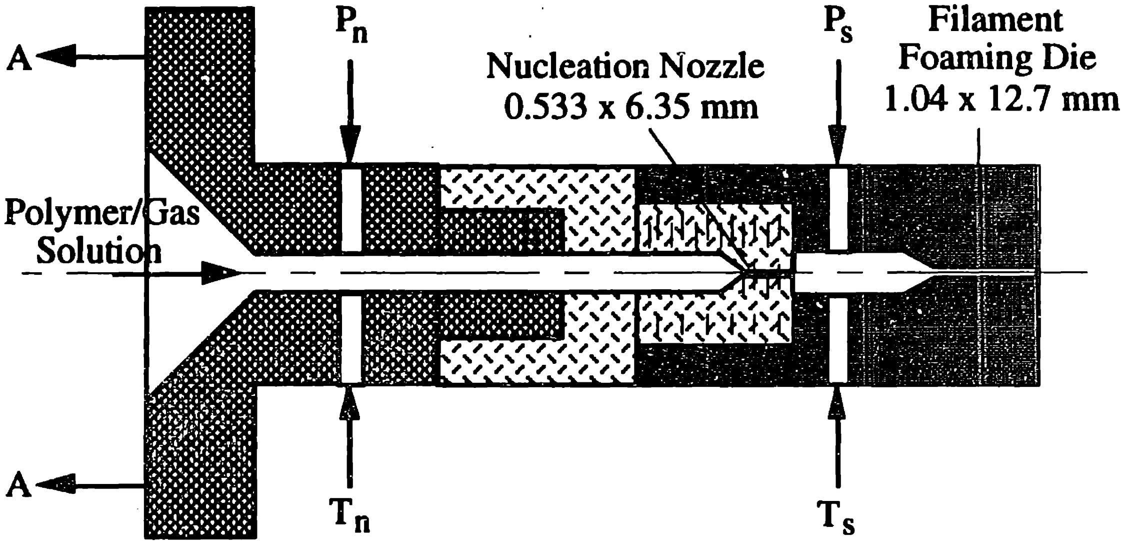

A-A: Attached to Breaker Plate/Flow Stabilizer

Figure 9.8: Filament die and nozzle design configuration used to verify the feasibility of shaping a nucleated polymer/gas solution.

Finally for better understanding, the filament die result was categorized based on Table 9.2. The thick filament flow had a characteristic flow rate to diffusion rate ratio equal to 9 (during shaping). Therefore, this die flow configuration tended to follow the post-diffusion or the partial pre-diffusion case. Since the post-nucleation channel volume is relatively large in this case, it is likely that the nucleated solution flow followed the partial pre-diffusion case.

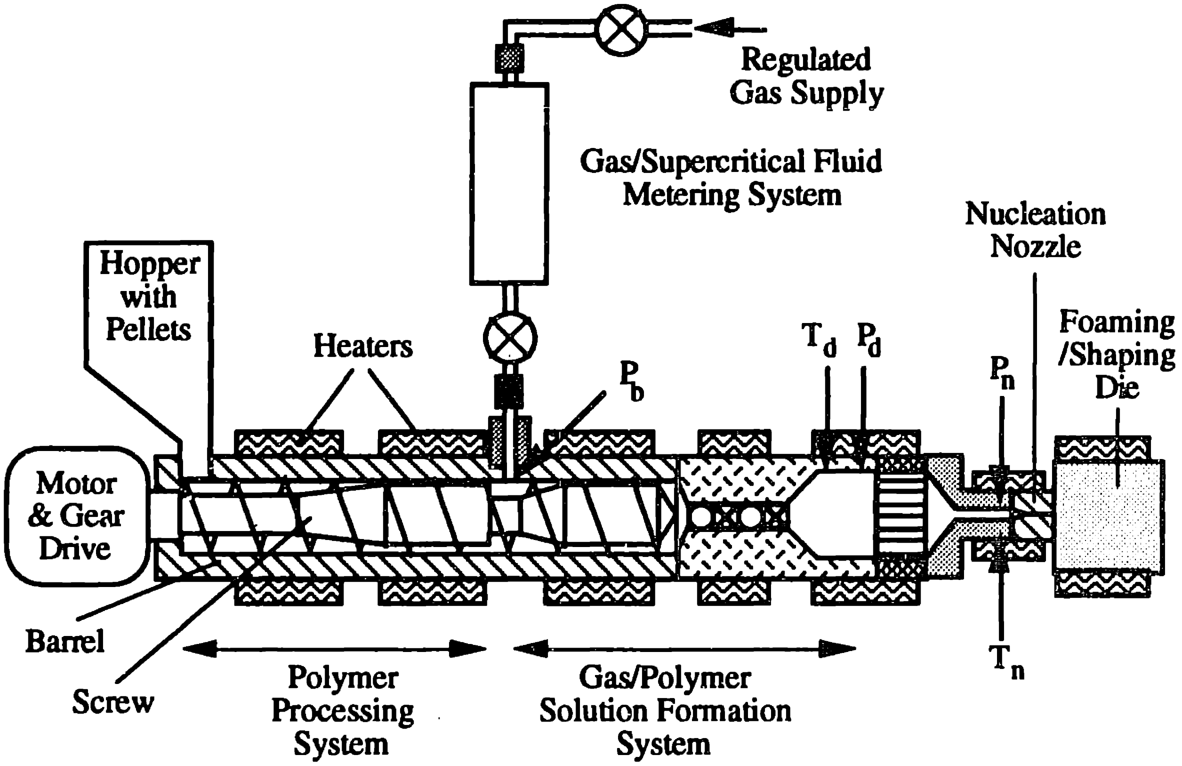

Figure 9.9: Schematic of the microcellular extrusion system used for the shaping and cell growth control experiments.

9.4 Shaping and Cell Growth of a Planar Sheet

To further verify the concept of shaping a nucleated polymer/gas solution flow and to demonstrate continuous microcellular sheet extrusion, a planer sheet foaming die was used. The die design was based on the analysis if section 9.2 which resulted in the configuration shown in Figure 9.11. This design consisted of a nozzle nucleation device and a planar sheet foaming die. In this case, the nozzle provided the rapid pressure loss for controlling cell nucleation and the die provided the initial sheet shaping and the shaping pressure control. The foaming die design of Figure 9.11 also included a technique for stabilizing cell growth. Cell growth stabilization is satisfied by maintaining close temperature control of the die lips using the cooling ports located near the upper and lower die lips.

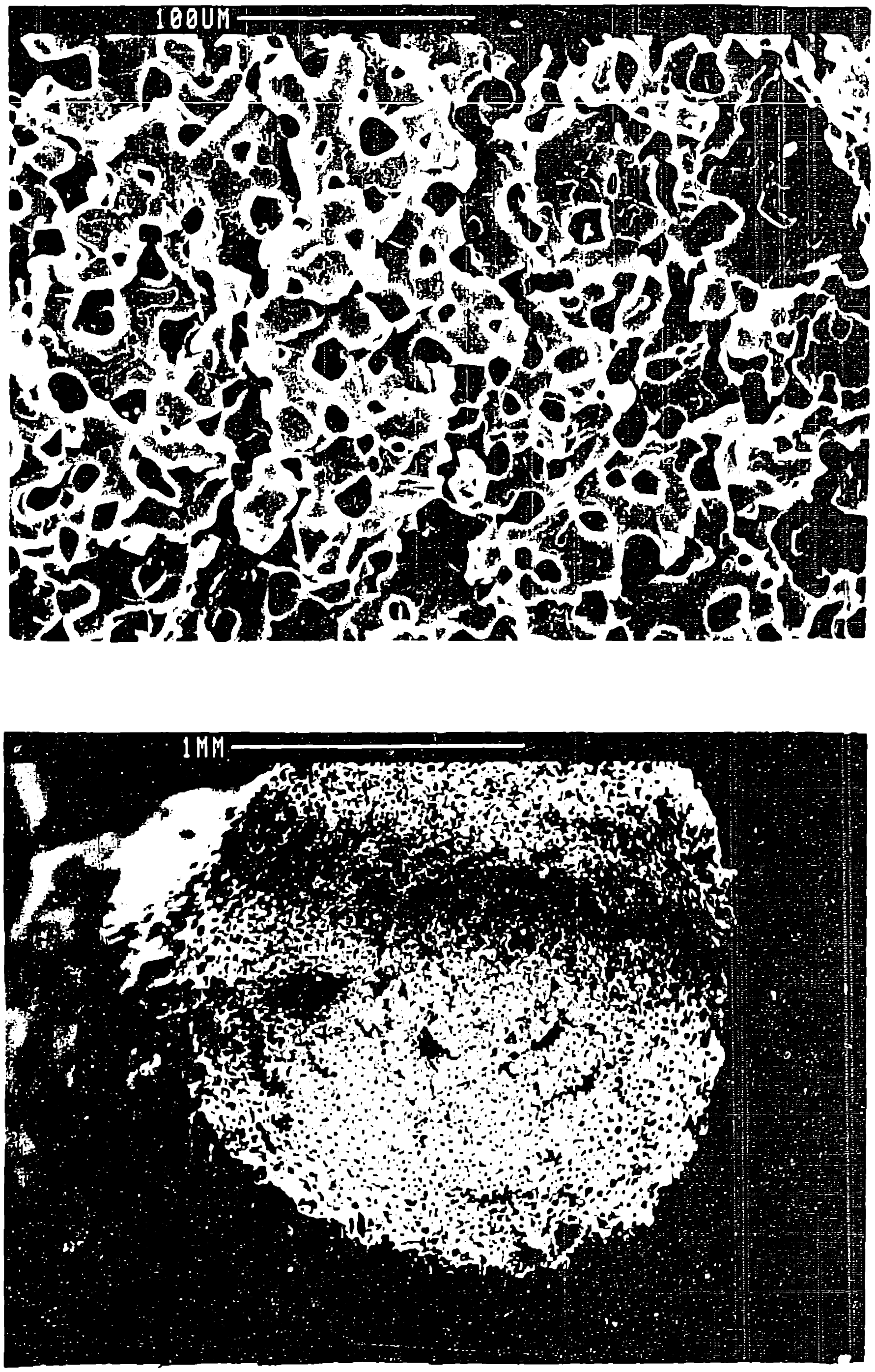

Figure 9.10: Scanning electron microscope micrographs of the extruded microcellular polystyrene thick filament.

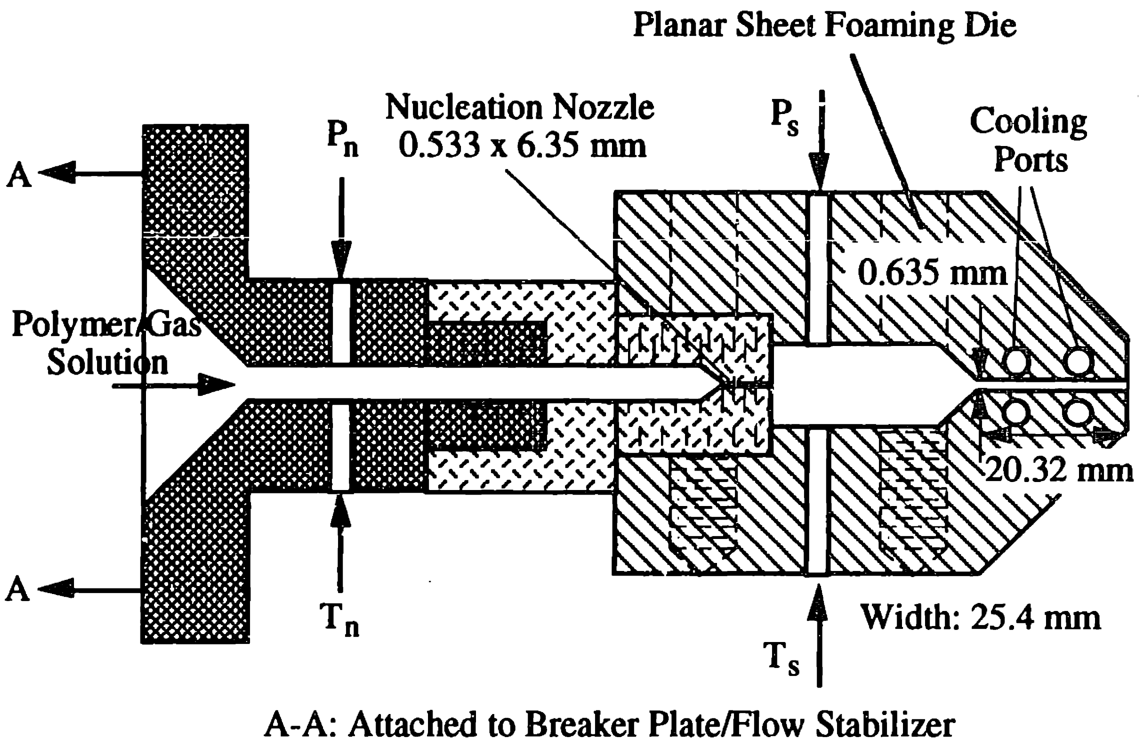

Figure 9.11: Planar sheet die and nozzle design configuration used to produce microcellular sheets.

Next a critical experiment was run to verify the planar sheet processing system using the extrusion system configuration of Figure 9.9 with the foaming sheet die of Figure 9.11. The process parameters for the experiment were: material = Novacor 103 PS, nozzle diameter = 0.533 mm, nozzle length = 6.35 mm, slit height = 0.635 mm, slit length = 20.32 mm, slit width = 25.4 mm, flow rate = 26 g/min, die temperature = 150 °C, estimated gas concentration = 5 %, nucleation pressure = 32.40 MPa (4700 psi), shaping pressure = 9.65 MPa (1400 psi). The cooling medium used was a low pressure carbon dioxide. The critical experiment was successful in demonstrating the feasibility of continuous shaping of a nucleated polymer/gas solution. A typical scanning electron microscope micrograph of the microcellular polystyrene sheet is shown in Figure 9.12 exhibiting an average cell size of 11 μm and an average cell density of 1.5 x 10^9 cells/cm^3. The repeatability of these results was also experimentally verified.

Finally, it was interesting to compare the flow rate results of this foaming die configuration with the analysis results of section 9.2. Figures 9.5 through 9.7 corresponding to the same flow parameters as the planar sheet extrusion experiments presented above. The comparison was made with the aid of Table 9.2. For the microcellular sheet extrusion configuration,

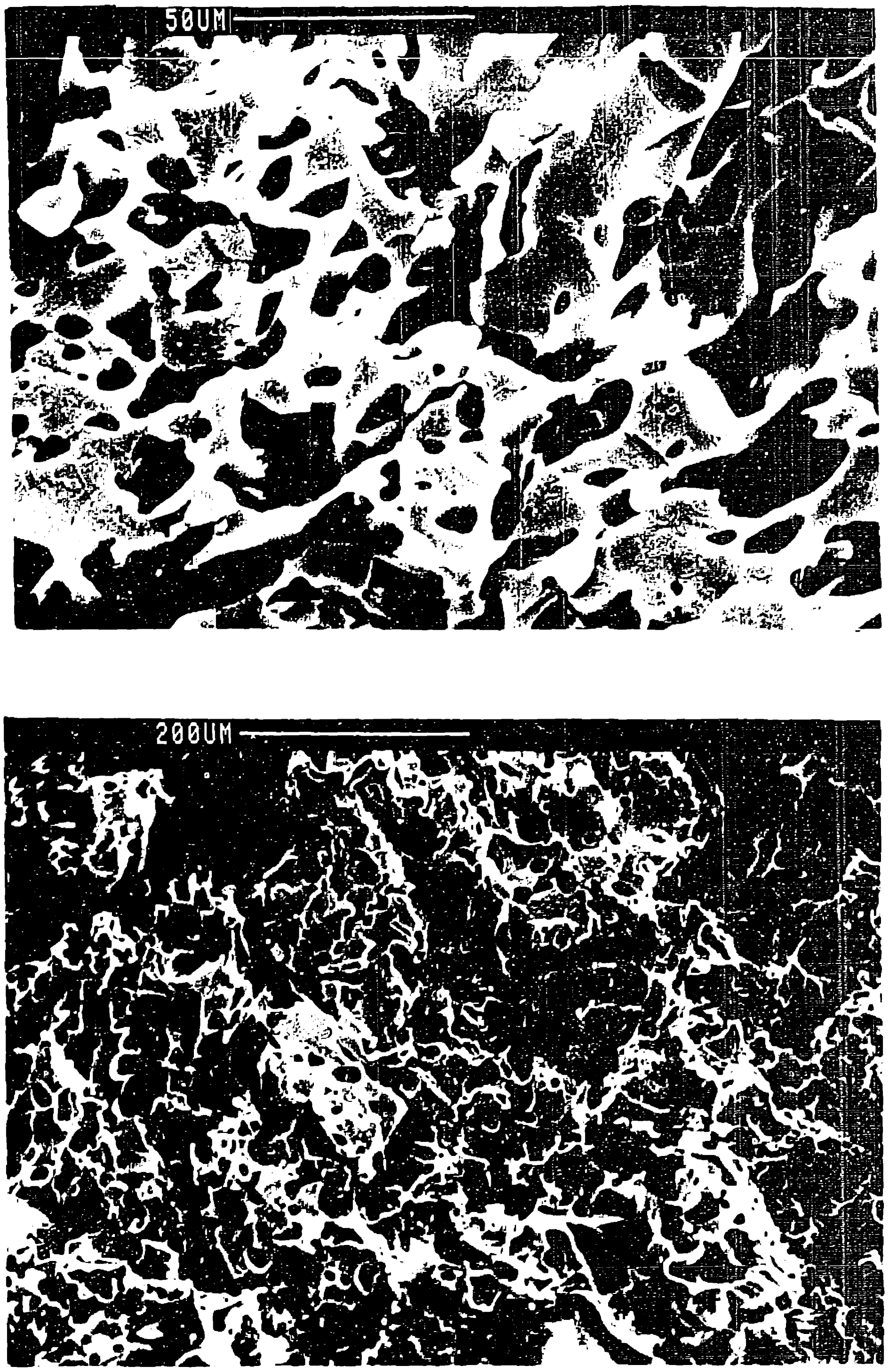

Figure 9.12: Scanning electron microscope micrographs of the extruded microcellular polystyrene planar sheet.

$$\frac{Q}{L\,A\,D\,\rho_c^{2/3}} \sim 0.2$$

Therefore, the nucleated sheet die flow fell between the concurrent diffusion case and the pre-diffusion case. Furthermore, notice that the shaping pressure achieved by the foaming die, $P_S = 9.65$ MPa (1400 psi), was in reasonable agreement with the predicted values of 10 MPa and 11.5 MPa (1450 psi and 1670 psi) for the pre-diffusion and concurrent diffusion flow configurations. Also, notice the predictions based on the neat polymer flow over-predicted the actual pressure loss by 66%. Thus, the pressure loss estimates from the nucleated solution flow models appeared to capture the major physics of the shaping and cell growth processes to provide reasonable estimates for foaming die designs.

9.5 Summary

In this chapter, the shaping and cell growth control functions of the microcellular sheet extrusion system design of chapter 7 were addressed. The principle of the basic design was to shape a nucleated polymer/gas solution flow under pressure and close temperature control. In this way, the initial cell growth was controlled so as to prevent degradation of the nucleated cell density during shaping. Two foaming die designs for satisfying the initial shaping and cell growth requirements were presented. Critical experiments were then performed which verified the concept of shaping a nucleated polymer/gas solution. Moreover, these experiments demonstrated the feasibility of the overall microcellular polymer sheet extrusion system design.

The feasibility of shaping a nucleated polymer/gas solution represents a significant advancement for microcellular plastics process technology. Through proper design of the foaming die, nucleated solution flows can be shaped to arbitrary dimensions while maintaining the functional independence of cell nucleation, cell growth and shaping. To maintain functional independence, stringent pressure and temperature design specifications, which supersede those of conventional foam processing, must be met by the foaming die design. As a means of aiding the design process, a series of models were developed for predicting pressure losses and flow rates of nucleated polymer/gas solutions. A comparison of the model predictions and the actual foaming die design performance showed good agreement for limited data. Moreover, these relatively simple models capture the major physics of the complicated two-phase flow field and provide a sound base from which scale-up of the foaming die concept to industrial levels can be achieved.

CHAPTER 10
CONCLUSIONS

The goal of this work has been the design and development of a prototype microcellular sheet extrusion system. As a first step, a comprehensive microcellular processing characterization of amorphous and semi-crystalline polymers was performed using a batch processing technique. This study demonstrated a new process technology for semi-crystalline polymers which utilized processing temperatures below the melting point. In the first phase of this process characterization, the formation of a gas and semi-crystalline polymer solution was studied in the presence of a crystallizing matrix with particular emphasis on the effects of viscoelasticity and crystallinity on microcellular processing.

Based on the experimental characterization of gas dissolution with induced crystallization, it appears that the degree of crystallinity can be controlled by the gas saturation time and the gas concentration. Furthermore, it was revealed that the gas-induced crystallization process occurs within the microcellular processing window once a critical gas concentration is reached. For the PET/CO_2 systems studied, the critical gas concentration was approximately 0.045 kg(CO_2)/kg(PET) at 20 °C. Therefore, during microcellular processing, it is important to consider the effects of gas-induced crystallization if the gas concentrations achieved during saturation are in excess of a critical concentration.

The viscoelastic behavior characterization of polymer/gas solutions showed that solutions of crystalline polymer and gas tend to have higher storage moduli compared with their amorphous counterparts. In the transition region at 50 °C, solutions of crystalline PET and CO_2 had a storage modulus twice that of comparable solutions of amorphous PET and CO_2. Moreover, it was found that for the PET/CO_2 systems the glass transition temperature decreases linearly with gas concentration.

The gas-induced crystallization and the resulting change in viscoelastic behavior played a major role in microcellular processing. This study showed that crystallization influences microcellular processing through its effects on (1) cell nucleation mechanisms resulting in larger cell densities and (2) cell growth mechanisms resulting in smaller cell sizes. In general, polymer crystallization increases the number of microvoids nucleated which is attributed to heterogeneous nucleation contributions at the amorphous/crystal interfaces. The semi-crystalline PET/CO_2 systems studied showed an increase in cell density of two orders-of-magnitude compared with the amorphous systems while the semi-crystalline CPET/CO_2 systems showed an order-of-magnitude larger cell density. Additionally, it is shown that the cell growth process of the semi-crystalline PET systems tends to be dominated by the viscoelastic behavior of the PET/CO_2 solution due to the relatively large matrix stiffness associated with the semi-crystalline systems. Moreover, the large matrix stiffness appeared to be a major contributor to the smaller cell sizes observed in the semi-crystalline PET resins. In contrast, the amorphous PET foams appeared to have cell growth processes that are dominated by the gas diffusion rate due to the lower matrix stiffness associated with these systems.

In the second phase of this batch processing characterization, the influence of the major microcellular processing variables was studied for amorphous and semi-crystalline polymers. These results illustrated significant differences in the microcellular processing characteristics of amorphous and semi-crystalline polymers. Moreover, these differences in processing characteristics required the specification of independent process design strategies. The amorphous polyesters studied revealed three narrow processing windows and process design strategies. In contrast, the semi-crystalline polymers showed a broad processing window suggesting a single process design strategy.

Specifically, it was found that both the amorphous PET and CPET exhibited similar nucleation characteristics and therefore nucleation mechanisms. At low saturation pressures, these materials appeared to experience heterogeneous nucleation due to inherent flaws. At higher pressures, both the amorphous PET and CPET showed a strong cell density dependence indicating the activation of additional nucleation sites and/or homogeneous nucleation contributions. The semi-crystalline polymers also showed similar nucleation mechanisms; however, the cell density dependence on the saturation pressure was considerably less for the amorphous materials. In general, the semi-crystalline polymers exhibited considerably higher cell densities than the amorphous polymers over the range of saturation pressures studied.

Finally, it was found for the amorphous polymers that foaming temperatures near the glass transition influenced the cell density, indicating thermally activated nucleation. In contrast, the semi-crystalline polymers exhibited a strong cell size dependence on foaming temperature and a relatively independent cell density. The foaming temperature dependence on the cell size is attributed to the viscoelastic behavior of the semi-crystalline polymers.

Using this batch processing characterization as a guide, a microcellular polymer sheet processing system was synthesized based on a plasticating extrusion technique. In this work, the axiomatic design principles were utilized to facilitate the design process. These principles provided an effective framework for synthesizing the system and identifying the critical process functions. The microcellular sheet extrusion system represents one of the first reported applications of the axiomatic design principles to larger scale physical systems (i.e., which span multiple hierarchy levels). In addition, this work has identified some of the complexities involved in the design of large scale physical systems such as inadvertent coupling of functional requirements and transient functional requirements (i.e., the complexities associated with system start-up).

The hierarchical design of the microcellular sheet extrusion system was structured such that each major process function was independently satisfied by a unique design parameter or process variable. During the overall system design, three major process functions were identified and considered in detail: (1) microcellular nucleation, (2) cell growth control, and (3) shaping.

The principle of the microcellular nucleation system was to continuously nucleate a high-pressure polymer/gas solution flow using a rapid pressure drop. Two design strategies for satisfying this process requirement were presented. The first design used nozzle configurations to rapidly decrease the solution pressure (first implemented by Park, 1993). Based on the critical experiments presented, this design configuration was very effective for continuously nucleating homopolymer/gas solutions. However, designs incorporating nozzle nucleation can suffer from a number of drawbacks including high shear rates, potential turbulent jet flow, entrance vortex flow, and the flow instabilities associated with melt fracture. Furthermore, the final shape of the nozzle flow (a filament) has limited use as a final product and is not readily shaped into a desired geometry using standard extrusion dies. The application of such conventional shaping operations can result in serious degradation of the cell morphology.

For this reason, a new nucleation technique was developed called near-net shape nucleation. The basic principle was to simultaneously shape and nucleate a polymer/gas solution flow having dimensions as close as possible to the final product. Two near-net shape nucleation designs were developed including a thin sheet nucleation die and a tubular film nucleation die. In addition, critical experiments were preformed which verified the concept of near-net shape nucleation. Both the thin sheet and tubular film experiments produced continuous microcellular polystyrene having cell densities on the order of 10^9 cells/cm^3 and cell sizes on the order of 10 μm. Moreover, the results of the tubular film nucleation experiments demonstrated for the first time a technology for continuously manufacturing microcellular films. The continuous production of films represents a significant advancement in microcellular processing technology and paves the way for product applications requiring thin, lightweight insulation or barrier components. It is also important to note that the near-net shape nucleation concepts did not suffer from the same flow instabilities associated with nozzle designs.

To aid in the design of a continuous nucleation system, two dimensionless groups were derived. These dimensionless groups compare the kinetics of cell nucleation and cell growth and provide a means for determining the relative importance of these competing mechanisms. In continuous melt processing, competition between cell nucleation and growth can be significant, resulting in a decrease in the nucleated cell density. The dimensionless groups derived serve as useful design criteria indicating that nucleation rates should be maximized and diffusivities should be minimized. From a physical design standpoint, these criteria translate into the use of rapid pressure losses and low nucleation temperatures. Moreover, these dimensionless groups illustrate the significant physical and technological differences between microcellular processing and conventional foam processing, clearly demonstrating that conventional processing systems cannot be used for producing microcellular structures.

Lastly, the critical microcellular foam processing functions of shaping and cell growth control were addressed. The design of foaming dies was based on the principle of shaping a nucleated polymer/gas solution flow under pressure and close temperature control so as to minimize initial cell growth and prevent degradation of the nucleated cell density. Secondary mechanical constraints, such as a conveyor assembly, can then be used to impart post-shaping cell growth control and dimensional stability. Two foaming die designs were presented including a filament shaping die and a planar sheet die. Critical experiments were performed which verify the concept of shaping a nucleated polymer/gas solution using a staged pressure drop for cell growth control. Moreover, these experiments demonstrated the feasibility of the overall microcellular polymer sheet extrusion system design.

The feasibility of shaping a nucleated polymer/gas solution represents a significant advancement for microcellular plastics process technology. Through proper design of the foaming die, nucleated solution flows can be shaped to arbitrary dimensions while maintaining the functional independence of cell nucleation, cell growth, and shaping. To maintain functional independence, stringent pressure and temperature design specifications must be met by the foaming die design. As a means of aiding the design process, a series of models were developed for predicting pressure losses and flow rates of nucleated polymer/gas solutions. A comparison of the model predictions and the actual foaming die design performance showed good agreement for limited data.

The importance of the design criteria and process models developed during the course of this work should be emphasized. Although relatively simple, they capture the critical physics which dominate nucleation, cell growth, and shaping operations in continuous melt processing. Therefore, these models and criteria provide a means of scaling the prototype process to industrial levels. Moreover, these criteria and models provide considerable insight into the effects of the major design parameters and process variables. Thus, they provide the necessary foundation for further design refinements, analysis, and innovation.

In conclusion, the design and development of the prototype microcellular sheet extrusion system represents a significant advancement in microcellular plastics technology and may lead to the industrial production and commercialization of these innovative materials in the near future. Moreover, this extrusion system provides a flexible technology platform from which new microcellular processing technologies can be developed.

CHAPTER 11

RECOMMENDATIONS

Based on the developments of this research, four areas for future work are recommended. The first concerns extending existing microcellular nucleation theories to achieve more accurate predictions of commonly observed in microcellular processing characteristics. Secondly, the design and development of a system for controlling post-die cell growth and final sheet dimensions should be undertaken. Thirdly, the ability to scale the microcellular extrusion system needs to be verified. Finally, it is recommended that the microcellular extrusion technology platform, presented in this work, be extended to include other polymer processing techniques.

While existing microcellular nucleation theories, based on the classical approach, provide a reasonable qualitative understanding of the effects of the major microcellular processing variables, these theories do not yield reliable quantitative predictions nor do they necessarily predict the trends shown by experimental results. For example, chapter five illustrates that the current theories do not reflect the actual functional relationships between the cell density, pressure, and temperature. In particular, for varying saturation pressure, the experimental results show a linear trend while the theory predicts non-linear behavior. It is clear that further contributions could be made in this area.

Some of the issues that must be addressed are that existing nucleation theories assume the thermodynamic state change driving nucleation is isothermal. However, it is not uncommon to change both the temperature and pressure to promote nucleation. This should be reflected in microcellular nucleation theories. Moreover, existing theories assume the polymer/gas system is saturated at nucleation. However, in continuous processing, gas concentrations below the solubility limit can be injected into the flow. Therefore, microcellular nucleation theories should be extended to better reflect the gas solubility or gas concentration dependence on nucleation. Finally, it is necessary to address the kinetics of nucleation with the understanding that nucleation is not instantaneous as is typically assumed. In contrast, nucleation can take place over a finite time period which is closely related to the time over which the solubility change occurs. Moreover, the transient nucleation kinetics must be addressed where the number of stable nuclei formed may differ from the number of detectable nuclei. For example, Shi and Seinfeld (1991) have presented a theoretical treatment of this subject which relates the number of stable nuclei formed to the number of nuclei that grow to detectable sizes.

Next, to complete the overall microcellular sheet extrusion system, it is recommended that the functional requirements of post-die cell growth control and final cross-sectional dimension control be addressed. To satisfy these requirements, the used of a conveyer assembly was suggested in chapter 9. The principle here is to use a mechanical constraint to stabilize the final cell growth and to impart the required dimensions on the sheet.

Figure 11.1 demonstrates the need for post-die cell growth control and final cross-sectional dimension control. These micrographs demonstrate a characteristic buckling which occurred for all of the microcellular sheets produced in this work. The buckling creates a sinusoidal curving in the sheet over the width and results in a rippling of the sheet surface. This structure is created when the sheet exits the die and expands in width (as well as in thickness) generating transverse stresses in the polymer matrix. These stresses exceed the local buckling limit. Using a mechanical constraint such as a conveyor assembly would prevent this problem by constraining dimensional changes to the sheet plane. By using cooling rolls, the stiffness of the polymer matrix can be increased and the sheet dimensions stabilized.

Figure 11.1 also shows some evidence of over-expansion of the surface cells resulting from the lack of post-die cell growth control. Again, a mechanical constraint can be used to limit the expansion of surface cells by applying a surface pressure and by rapidly cooling the sheet as it emerges from the foaming die.

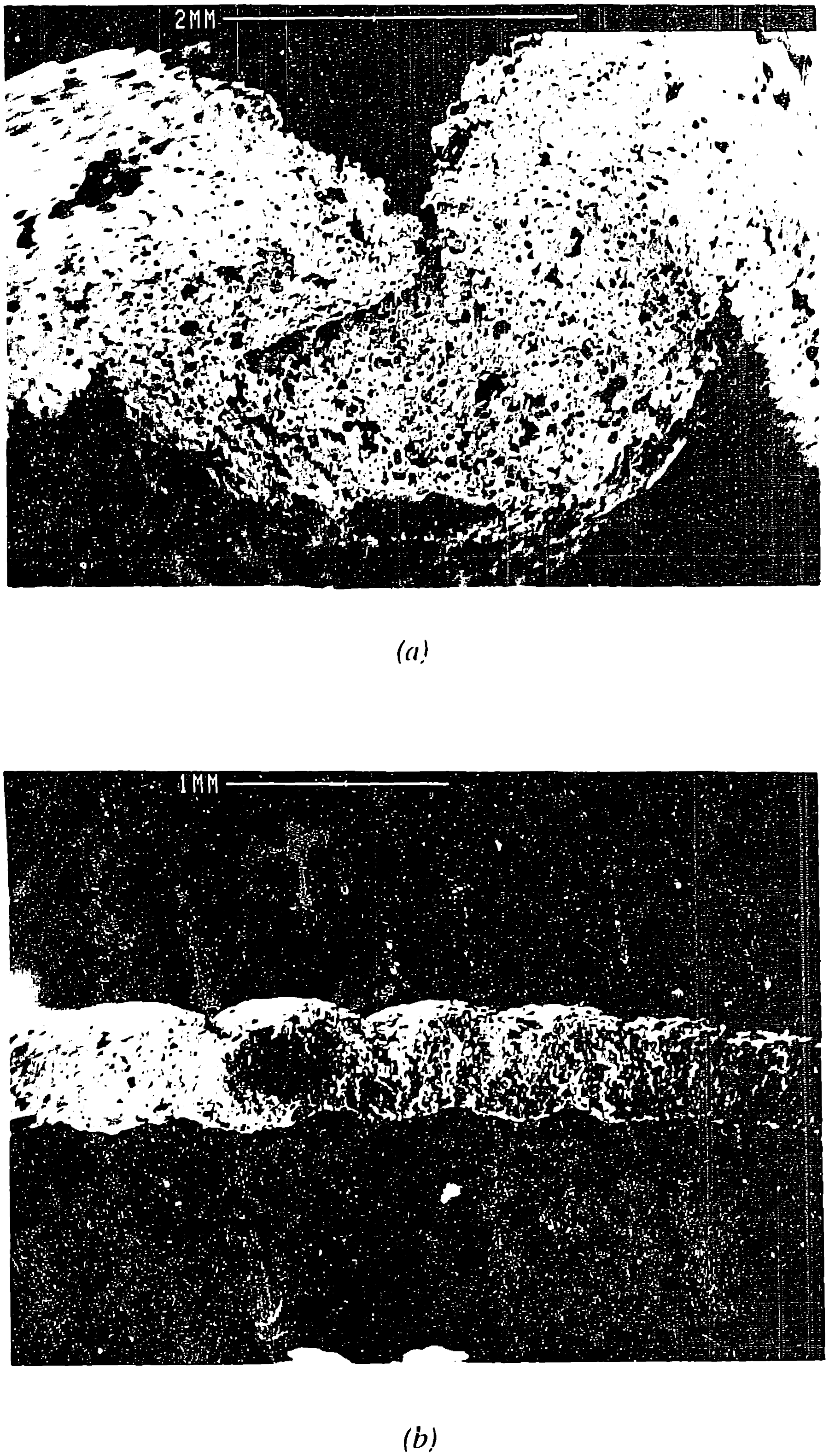

Figure 11.1: Scanning electron micrographs of the cross sections of near-net shape (a) sheet and (b) film.

Another important aspect of the sheet extrusion system that deserves serious attention is the scaling of this technology to industrial levels. While current microcellular technologies might be sufficient for some low-volume, high-value-added applications such as specialty wire coatings, they do not meet the production requirements of high-volume, low-value-added products. It is the authors opinion that significant contributions can be made by addressing the complexities involved in scaling microcellular technologies to industrial levels. For example, scale-up of the microcellular extrusion process requires knowledge of the major processing functions and their relation to the critical process variables and design parameters. It was the deliberate attempt in this work to develop process models and design criteria which can be used as a foundation from which the design of larger scale microcellular processing systems can be developed.

Finally, it is recommended that the microcellular process technology platform be extended to other widely used commercial polymer processing techniques. In this thesis, a number of critical process variables and design parameters have been identified for microcellular processing of polymer melts. This basic knowledge along with the process models and design criteria form a knowledge base which can be used to extend the microcellular processing platform to include molding, injection molding, and blow molding to name just a few.

REFERENCES

Aklonis, J.J., MacKnight, W. J., and Shen, M., 1972, Introduction to Polymer Viscoelasticity, Wiley-Interscience, New York.

Alderson, W.L., 1945, "Process for obtaining Cork-Like Products From Polymers of Ethylene," *U.S. Patent* 2387730.

Amon, M. and Denson, C.D., 1984, "A Study of the Dynamics of Foam Growth: Analysis of the Growth of Closely Spaced Spherical Bubbles," *Polymer Engineering and Science*, Vol. 24, pp. 1026-1034.

Andrade, E.N., 1939, *Proceedings of the Physics Society*, London, Vol. 51, p. 784.

Andrew, G.D. and Smith, N.K., 1987, "Optimized Processing of Microcellular Polyurethane Systems Through Catalyst and Surfactant Technology," *Journal of Elastomers and Plastics*, Vol. 19, pp. 204-218.

Arefmanesh, A., Advani, S.G., and Michaelides, E.E., 1990, "A Numerical Study of Bubble Growth During Low Pressure Structural Foam Molding Process," *Polymer Engineering and Science*, Vol. 30, pp. 1330-1337.

Aubert, J.H., 1988, "An Objective Characterization of the Cell Size of Microcellular Foams," *Journal of Cellular Plastics*, Vol. 24, pp. 132-145.

Aubert, J.H. and Clough, R.L., 1985, "Low-Density, Microcellular Polystyrene Foams," *Polymer*, Vol. 26, pp. 2047-2054.

Aubert, J.H. and Sylwester, A.P., 1991, "Morphological Characterization of Microcellular Carbon Foams," *Journal of Materials Science*, Vol. 26, pp. 5741-5752.

Baldwin, D.F., Shimbo, M., and Suh, N.P., 1994, "The Role of Gas Dissolution and Induced Crystallization During Microcellular Polymer Processing: A Study of Poly(ethylene terephthalate) and Carbon Dioxide Systems," to be published in the Transactions of the ASME *Journal of Engineering Materials and Technology*.

Baldwin, D.F., Gustafson, D.E., Shimbo, M. , and Suh, N.P., 1993, "Viscoelastic Behavior of Gas/Polymer Solutions: Glass Transition Temperature Depression at High Gas Concentrations," *Society of Plastics Engineers Technical Papers*, Vol. 39, pp. 1840-1843.

Baldwin, D.F., Suh, N.P., and Shimbo, M., 1992, "Gas Dissolution and Crystallization in Microcellular Thermoplastic Polyesters," *Cellular Polymers*, MD-Vol. 38, ASME, pp. 109-127.

Baldwin, D.F. and Suh, N.P., 1992, "Microcellular Poly(ethylene terephthalate) and Crystallizable Poly(ethylene terephthalate)," *Society of Plastics Engineers Technical Papers*, Vol. 38, pp. 1503-1507.

Baldwin, D.F. and Suh, N.P., 1991, "Modeling Gas Sorption in Semi-Crystalline Polymers," *Society of Plastics Engineers Technical Papers,* Vol. 37, pp. 1300-1303.

Becker, R. and Döring, W., 1935, *Ann. Physik*, Vol. 24, p. 719.

Berins, M.L. ed., 1991, SPI Plastics Engineering Handbook, Van Nosrand Reinhold, New York.

Bird, R.B., Armstrong, R.C., and Hassager, O., 1987, Dynamics of Polymeric Liquids: Volume 1 Fluid Mechanics, John Wiley & Sons, New York.

Blyler, L.L. and Kwei, T.K., 1971, "Flow Behavior of Polyethylene Melts Containing Dissolved Gases," *Journal of Polymer Science: Part C*, No. 35, pp. 165-176.

Byon, S.K. and Youn, J.R., 1990, "Ultrasonic Processing of Thermoplastic Foam," *Polymer Engineering and Science*, Vol. 30, pp. 147-152.

Cha, S.W., Suh, N.P., Baldwin, D.F., and Park, C.B., 1992, "Microcellular Thermoplastic Foamed with Supercritical Fluid," *U.S. Patent* 5158986.

Cha, S.W. and Suh, N.P., 1992, "Room-Temperature Microcellular Foaming," *Society of Plastics Engineers Technical Papers*, Vol. 38, pp. 1527-1531.

Cheung, T.M., Davis, C.L., and Prince, J.E., 1991, "Process for Making Lightweight Polyester Articles," *U.S. Patent* 4981631.

Chiou, J.S., Barlow, J.W., and Paul, D.R., 1985, "Polymer Crystallization Induced by Sorption of CO_2 Gas," *Journal of Applied Polymer Science*, Vol. 30, pp. 3911-3924.

Cho, W.J., Park, H., and Youn, J.R., 1992, "Ultrasonic Bubble Nucleation in Polyurethane for RIM Applications," *Cellular Polymer*, MD-Vol. 38, ASME, pp. 15-24.

Chow, T.S., 1980, "Molecular Interpretation of the Glass Transition Temperature of Polymer-Diluent Systems," *Macromolecules*, Vol. 13, p. 362.

Clark, M.-H.N. and Seeler, K.A., 1991, "Sintering Microcellular Foam Parts," *Society of Plastics Engineers Technical Papers*, Vol. 37, pp. 1411-1413.

Clausing, D., 1988, Dept. of Electrical Engineering, Bernard M. Gordon Adjunct Processor of Engineering Innovation and Practice, *personal communications.*

Collias, D.I. and Baird, D.G., 1992, "Does a Microcellular Structure Improve the Modulus of Toughness of a Polymer Matrix," *Society of Plastics Engineers Technical Papers,* Vol. 38, pp. 1532-1535.

Colombo, E.A., 1977, "Controlling the Properties of Extruded Polystyrene Foam Sheet," Science and Technology of Polymer Processing, N.P. Suh and N.H. Sung eds., MIT Press, Cambridge, pp. 394-413

Colton, J.S., 1989, "The Nucleation of Microcellular Foams in Semi-Crystalline Thermoplastics," *Material and Manufacturing Processes*, Vol. 4, pp. 253-262.

Colton, J.S., 1985, "The Nucleation of Microcellular Thermoplastic Foam," *Ph.D. Thesis in Mechanical Engineering*, Massachusetts Institute of Technology, September.

Colton, J.S. and Suh, N.P., 1992, "Microcellular Semi-Crystalline Thermoplastics," *U.S. Patent* 5160674.

Colton, J.S. and Suh, N.P., 1987a, "Nucleation of Microcellular Foam: Theory and Practice," *Polymer Engineering and Science*, Vol. 27, pp. 500-503.

Colton, J.S. and Suh, N.P., 1987b, "The Nucleation of Microcellular Thermoplastic Foam with Additives: Part 1: Theoretical Considerations," *Polymer Engineering and Science*, Vol. 27, pp. 485-492.

Colton, J.S. and Suh, N.P., 1987c, "The Nucleation of Microcellular Thermoplastic Foam with Additives: Part 2: Experimental Results and Discussion," *Polymer Engineering and Science*, Vol. 27, pp. 493-499.

Comyn, J. ed., 1985, Polymer Permeability, Elsevier, New York.

Condo, P.D., Sanchez, I.C., Panayiotou, C.G. and Johnston, K.P., 1992, "Glass Transition Behavior Including Retrograde Vitrification of Polymers with Compressed Fluid Diluents," *Macromolecules*, in press.

Cook, N.H. and Suh, N.P. eds., 1990, "Manufacturing Engineering: Part II Analysis and Synthesis of Manufacturing Processes, Systems, and Related Issues," MIT, Cambridge, MA.

Crank, J., 1975, The Mathematics of Diffusion, Clarendon Press, Oxford, pp. 203-253.

Denecour, R.L. and Gent, A.N., 1968, "Bubble Formation in Vulcanized Rubbers," *Journal of Polymer Science: Part A-2*, Vol. 6, pp. 1853-1861.

Desai, A.B. and Wilkes, G.L., 1974, "Morphology Studies on Solvent Induced Crystallization of Polyethylene Terephthalate," *Journal of Applied Polymer Science: Polymer Letters Edition.*, Vol. 12, pp. 113-119.

Dodge, D.W. and Metzner, A.B., 1958, *AIChE Journal*, Vol. 5, pp. 189-204.

Dunning, W.J., 1969, "General and Theoretical Introduction," Nucleation, Marcel Dekker, New York, pp. 1-67.

Durning, C.J. and Russel, W.B., 1985, "A Mathematical Model for Diffusion With Induced Crystallization 1 & 2," *Polymer*, Vol. 26, pp. 119-130 and pp. 131-140.

Durning, C.J., Rebenfeld, L., Russel, W.B., and Weigmann, H. D., 1986, "Solvent Induced Crystallization: I. Crystallization Kinetics and II. Morphology," *Journal of Polymer Science: Polymer Physics Edition*, Vol. 24, pp. 1321-1340 and pp. 1341-1360.

Durril, P.L. and Griskey, R.G., 1966, "Diffusion and Solution of Gases in Thermally Softened or Molten Polymers: Part I," *A.I.Ch.E. Journal*, Vol. 12, pp. 1147-1151.

Durril, P.L. and Griskey, R.G., 1969, "Diffusion and Solution of Gases in Thermally Softened or Molten Polymers: Part II," *A.I.Ch.E. Journal*, Vol. 15, pp. 106-110.

Epstein, P.S. and Plesset, 1950, "On the Stability of Gas Bubbles in Liquid-Gas Solutions," *Journal of Chemical Physics*, Vol. 18, pp. 1505-1509.

Flory, P.J., 1953, Principles of Polymer Chemistry, Cornell University Press.

Garbini, J.L., Holl, M.R., Kumar, V., Murry, W.R., and Jorgensen, J.E., 1992, "Non-Destructive Characterization of Microcellular Foam Structure: Error Analysis of a Proposed Sensor," *Society of Plastics Engineers Technical Papers*, Vol. 38, pp. 1519-1526.

Gaspari, J. D., 1993, "Microcellular Foams," *Plastics Technology*, February, pp. 63-65.

Gent, A.N. and Tompkins, D.A., 1969a, "Nucleation and Growth of Gas Bubbles in Elastomers," *Journal of Applied Physics*, Vol. 40, pp. 2520-2525.

Gent, A.N. and Tompkins, D.A., 1969b, "Surface Energy Effects for Small Holes or Particles in Elastomers," *Journal of Polymer Science: Part A-2*, Vol. 7, pp. 1483-1488.

Gibson, L.J. and Ashby, M.F., 1982, "The Mechanics of Three-dimensional Cellular Materials," *Proceedings of the Royal Society, London,* Vol. A241, pp. 376-396.

Gibson, L.J. and Ashby, M.F., 1988, Cellular Solids: Structure and Properties, Pergamon Press, New York.

Goel, S.K. and Beckman, E.J., 1992, "Generation of Microcellular Polymeric Foams Using Supercritical Carbon Dioxide," *Polymeric Materials Science and Engineering*, Vol. 67, Proceedings of the ACS Conference, August, pp. 506-507.

Gore, R.W., 1980, "Porous Products and Process Therefor," *U.S. Patent* 4187390.

Gutowski, T.G. and Suh, N.P., 1982, "Polymer Solution Thermodynamics and Engineering Applications," Polymer Processing: Analysis and Innovation, ASME, Vol. PED-5, pp. 145-163.

Gyftopoulos, E.P. and Beretta, G.P., 1991, Thermodynamics: Foundations and Applications, Macmillan, New York.

Hall, C., 1989, Polymer Materials, Wiley, New York.

Han, C.D., 1973, "Influence of the Die Entry Angle in Entrance Pressure Drop, Recoverable Elastic Energy and Onset of Flow Instability in Polymer Melt Flow," *Journal of Applied Polymer Science*, Vol. 17, p. 1403.

Han, C.D., Kim, Y.W. and Malhotra, K.D., 1976, "A Study of Foam Extrusion Using a Chemical Blowing Agent," *Journal of Applied Polymer Science*, Vol. 20, pp. 1583-1595.

Han, C.D. and Villamizar, C.A., 1978, "Studies of Structural Foam Processing I. The Rheology of Foam Extrusion," *Polymer Engineering and Science*, Vol. 18, pp. 687-698.

Hansen, R.H. and Martin, W.M., 1965, "Novel Methods for the Production of Foamed Polymers II. Nucleation of Dissolved Gas by Finely-Divided Metals," *Polymer Letters*, Vol. 3, pp. 325-330.

Harasin, S.J., 1985, "Introduction to RIM," *Proceedings of the S.P.I. Annual Structural Foam Conference*, SPI, New York, NY, p. 1-6.

Hardenbrook, S.B., Harasta, L.P., Faulkenberry, S.T., and Bomba, R.D., 1988, "Method for Producing Microcellular Foamed Plastic Material With Smooth Integral Skin," *U.S. Patent* 4761256.

Hauser, J.R. and Clausing, D., 1988, "The House of Quality," *Harvard Business Review*, pp. 63-73, May-June.

Hilyard, N.C., ed., 1982, Mechanics of Cellular Plastics, Macmillan, New York.

Hobbs, S.Y., 1976, "Bubble Growth in Thermoplastic Structural Foams," *Polymer Engineering and Science*, Vol. 16, pp. 270-275.

Holman, J.P., 1981, Heat Transfer, McGraw Hill, New York.

Jackson, C.L. and Shaw, M.T., 1990, "Phase Behavior and Geletion of a Rod-Like Polymer in Solution and Implications for Microcellular Foam Morphology," *Polymer*, Vol. 31, pp. 1070-1084.

Jameel, H., Waldman, J., and Rebenfeld, L., 1981, "The Effects of Orientation and Crystallinity on the Solvent-Induced Crystallization of Poly(ethylene terephthalate): I. Sorption-Diffusion-Related Phenomena," *Journal of Applied Polymer Science*, Vol. 26, pp. 1795-1811.

Johnson, J.E., 1959, "X-Ray Diffraction Studies of the Crystallinity of Polyethylene Terephthalate," *Journal of Applied Polymer Science*, Vol. 2, pp. 205-209.

Kline, D.E., and Hansen, D., 1970, "Thermal Conductivity of Polymers," Techniques and Methods of Polymer Evaluation, Vol. IV, Slade, P.E. and Jenkins, L.T., eds., Dekker, New York.

Kogelnik, H-J., Adam, N., Prolingheuer, E.C., and Henrichs, P., 1992, "Microcellular Polyurethane Elastomers as Damping Components in Various Applications," *Cellular Polymers*, MD-Vol. 38, ASME, pp. 41-54.

Koros, W.J. and Paul, D.R., 1980, "Sorption and Transport of CO_2 Above and Below the Glass Transition of Poly(ethylene terephthalate)," *Polymer Engineering and Science*, Vol. 20, pp. 14-19.

Kumar, V., 1991, "Synthesis and Processing of Microcellular Plastics: A Review," *Processing and Manufacturing of Composite Materials*, ASME, pp. 185-195.

Kumar, V., 1988, "Process Synthesis for Manufacturing Microcellular Thermoplastic Parts: A Case Study in Axiomatic Design," *Ph.D. Thesis in Mechanical Engineering*, Massachusetts Institute of Technology, May.

Kumar, V. and Gebizlioglu, O.S., 1992, "Thermal and Microscopy Studies of CO_2-Induced Morphology in Crystalline PET Foams," *Society of Plastics Engineers Technical Papers*, Vol. 38, pp. 1536-1540.

Kumar, V. and Gebizlioglu, O.S., 1991, "Carbon Dioxide-Induced Crystallization in PET Foams," *Society of Plastics Engineers Technical Papers*, Vol. 37, pp. 1297-1299.

Kumar, V. and Suh, N.P., 1990, "A Process for Making Microcellular Thermoplastic Parts," *Polymer Engineering and Science*, Vol. 30, pp. 1323-1329.

Kumar, V and Vander Wel, M.M., 1991, "Microcellular Polycarbonate-Part II: Characterization of Tensile Modulus," *Society of Plastics Engineers Technical Papers*, Vol. 37, pp. 1406-1410.

Kumar, V. and Weller, J.E., 1992, "Bubble Nucleation in Microcellular Polycarbonate Foams," *Polymeric Materials Science and Engineering*, Vol. 67, Proceedings of the ACS Conference, August, pp. 501-502.

Kumar, V., Weller, J.E., and Montecillo, R, 1992, "Microcellular PVC," *Journal of Vinyl Technology*, Vol. 14, pp. 191-197.

Kumar, V and Weller, J.E., 1991a, "Microcellular Polycarbonate-Part I: Bubble Nucleation and Growth," *Society of Plastics Engineers Technical Papers*, Vol. 37, pp. 1401-1405.

Kumar, V. and Weller, J.E., 1991b, "Model for Skin Thickness of Microcellular Plastics," *Heat and Mass Transfer in Solidification Processing*, HTD-Vol. 175, ASME, pp. 157-162.

Kumar, V., Wing, G., Pasricha, A., and Tuttle, M., 1993, "Linear and Nonlinear Viscoelastic Behavior of Polycarbonate and Microcellular Polycarbonate Foam," *Society of Plastics Engineers Technical Papers*, Vol. 39, pp. 1832-1839.

Kraynik, A.M., 1981, "Rheological Aspects of Thermoplastic Foam Extrusion," *Polymer Engineering and Science*, Vol. 21, pp. 80-85.

Kweeder, J.A., Ramesh, N.S., Campbell, G.A., and Rasmussen, D.H., 1991, "The Nucleation of Microcellular Polystyrene Foam," *Society of Plastics Engineers Technical Papers*, Vol. 37, pp. 1398-1400.

Lee, E.H., 1960, "Viscoelastic Stress Analysis," *Proceedings of the 1st Symposium on Naval Structural Mechanics*, p. 456.

LeMay, J.D., Hopper, R.W., Hrubesh, L.W., and Pekala, R.W., 1990, "Low-Density Microcellular Materials," *MRS Bulletin*, Vol. 15, pp. 19-45.

Lin, S.B. and Koenig, J.L., 1983, "Spectroscopic Characterization of Solvent-Induced Crystallization of PET," *Journal of Polymer Science: Polymer Physics Edition*, Vol. 21, pp. 1539-1558.

Lundberg, J.L., Wilk, M.B., and Huyett, M.J., 1966, *Journal of Applied Physics*, Vol. 31, p. 1131.

Martini, J.E., 1981, "The Production and Analysis of Microcellular Foam," *S.M. Thesis in Mechanical Engineering*, Massachusetts Institute of Technology, January.

Martini-Vvedensky, J.E.,. Suh, N.P., and Waldman, F.A, 1984, "Microcellular Closed Cell Foams and Their Method of Manufacture," *U.S. Patent* 4473665.

Martini, J., Waldman, F.A., and Suh, N.P., 1982, "The Production and Analysis of Microcellular Thermoplastic Foam," *Society of Plastics Engineers Technical Papers*, Vol. 28, pp. 674-676.

Mizoguchi, K., Hirose, T., Naito, Y., and Kamiya, Y., 1987, "CO_2-Induced Crystallization of Poly(ethylene terephthalate)," *Polymer*, Vol. 28, pp. 1298-1302.

Moore, W.R. and Sheldon, R.P, 1961, "The Crystallization of Polyethylene Terephthalate by Organic Liquids," *Polymer*, Vol. 2, pp. 315-321.

Nevins, J.L. and Whitney, D.E., eds., 1989, Concurrent Design of Products and Processes - A Strategy for the Next Generation in Manufacturing, McGraw-Hill, New York.

Newitt, D.M., and Weale, K.E., 1948, "Solution and Diffusion of Gases in Polystyrene at High Pressures," *Journal of Chemical Science*, Part II, pp. 1541-1549.

Ostwald, W., 1925, *Kolloid-Z.*, Vol. 36, pp. 99-117.

Oyanagi, Y. and White, J.L., 1979, "Basic Study of Extrusion of Polyethylene and Polystyrene Foams," *Journal of Applied Polymer Science*, Vol. 23, pp. 1013-1026.

Park, C.B., 1993, "The Role of Polymer/Gas Solutions in Continuous Processing of Microcellular Polymers," *Ph.D. Thesis in Mechanical Engineering*, Massachusetts Institute of Technology, May.

Park, C.B., Baldwin, D.F., and Suh, N.P., 1993, "Cell Nucleation by Rapid Pressure Drop in Continuous Processing of Microcellular Plastics," to be published in the proceedings of the Winter Annual Meeting of ASME, *Symposium on the Mechanics of Plastics and Plastic Composites*, November, New Orleans, LA.

Park, C.B. and Suh, N.P., 1993, "Extrusion of Microcellular Polymers Using a Rapid Pressure Drop Device," *Society of Plastic Engineers Technical Papers*, Vol. 39, pp. 1818-1822.

Park, C.B and Suh, N.P., 1992a, "Extrusion of Microcellular Filament: a Case of Axiomatic Design," *Cellular Polymers*, MD-Vol. 38, ASME, pp. 69-91.

Park, C.B. and Suh, N.P., 1992b, "Rapid Heating for Microcellular Nucleation in a Polymer Melt," *Society of Plastics Engineers Technical Papers*, Vol. 38, pp. 1513-1518.

Park, H. and Youn, J.R., 1993, "Processing of Cellular Polyurethane by Ultrasonic Excitation," *ASME Journal of Engineering for Industry*, to be published.

Pekala, R.W., Alviso, C.T., Hulsey, S.S, and Kong, F.-M., 1992, "Aerogels, Emulsions, and Composites: Controlling Structure With Organic Sol-Gel Chemistry," *Cellular Polymers*, MD-Vol. 38, ASME, pp. 129-135.

Potter, M.C. and Foss J.F., 1982, Fluid Mechanics, Great Lakes Press, Okemos, MI.

Pugh, S., 1991, Total Design: Integrated Methods for Successful Product Engineering, Addison-Wesley, Reading, MA.

Ramesh, N.S., Rasmussen, D.H., and Campbell, G.A., 1993, "The Nucleation of Microcellular Foams in Polystyrene Containing Low Glass Transition Particles," *Society of Plastics Engineers Technical Papers*, Vol. 39, pp. 1828-1831.

Ramesh, N.S., Kweeder, J.A., Rasmussen, D.H., and Campbell, G.A., 1992, "An Experimental Study on the Nucleation of Microcellular Foams in High Impact Polystyrene," *Society of Plastics Engineers Technical Papers*, Vol. 38, pp. 1078-1081.

Ramesh, N.S., Rasmussen, D.H., and Campbell, G.A., 1991, "Numerical and Experimental Studies of Bubble Growth During the Microcellular Foaming Process, *Polymer Engineering and Science*, Vol. 31, pp. 1657-1664.

Seeler, K.A., and Kumar, V., 1993, "Tension-Tension Fatigue of Microcellular Polycarbonate: Initial Results," *Journal of Reinforced Plastics and Composites*, Vol. 12, pp. 359-376.

Seeler, K.A., and Kumar, V., 1992, "Fatigue of Notched Microcellular Polycarbonate," *Cellular Polymers*, MD-Vol. 38, ASME, pp. 93-108.

Sepe, M.P., 1992, "Dynamic Mechanical Analysis," *Advanced Materials and Processes*, p. 32, April.

Shafi, M.A. and Flumerfelt, R.W., 1992, "Analysis of Free Expansion Polymer Foaming Process," to be published in *Polymer Engineering and Science*.

Shi, G. and Seinfeld, J.H., 1991, "Transient kinetics of nucleation and crystallization: Part I: Nucleation," *Journal of Materials Research*, Vol. 6, pp. 2091-2096.

Shimbo, M., Baldwin, D.F., and Suh, N.P., 1993a, "Viscoelastic and Mechanical Behavior of Microcellular Plastics with Varying Cell Size," *Proceedings of the ATEM'93 Conference on Advanced Technology in Experimental Mechanics '93*, JSME, pp. 309-313.

Shimbo, M., Baldwin, D.F., and Suh, N.P., 1993b, "Investigation of the Cell Size Effect in the Viscoelastic Behavior of Microcellular Plastics," *Society of Plastics Engineers Technical Papers*, Vol. 39, pp. 1844-1848.

Shimbo, M., Baldwin, D.F., and Suh, N.P., 1992, "Viscoelastic Studies of Microcellular Plastics," *Polymeric Materials Science and Engineering*, Vol. 67, Proceedings of the ACS Conference, August, pp. 512-513.

Stannett, V., 1968, "Simple Gases," Diffusion in Polymers, Crank, J and Park, G.S., eds., Academic Press, New York, pp. 41-73.

Stone, H., Lichvar, S., Bredbenner, C.W., Rupp, R., and Minnich, E., 1990, "Blowing Agents for Polyurethane Foam," *U.S. Patent 4906672*.

Suh, K.W. and Webb, D.D., 1985, "Cellular Materials," Encyclopedia of Polymer Science and Engineering, Vol. 3, John Wiley & Sons, New York, pp. 1-59.

Suh, N.P., 1990, The Principles of Design, Oxford, New York.

Suh, N.P., 1986, Tribophysics, Prentice-Hall, Englewood Cliffs, NJ, Appendix 8.A.

Suh, N.P., Baldwin, D.F., Cha, S.W., Park, C.B., Ota, T., Yang, J., and Shimbo, M., 1993, "Synthesis and Analysis of Gas/Polymer Solutions for Ultra-Microcellular Plastics Production," *Proceedings of the 1993 NSF Design and Manufacturing Systems Grantees Conference*, Charlotte, N.C., January, pp. 315-326.

Suh, N.P., Baldwin, D.F., Park, C.B., and Cha, S.W., 1994, "Processing of Microcellular Thermoplastics Foamed with Supercritical Fluid," *U.S. Patent Pending*.

Tadmor, Z., 1966, "Fundamentals of Plasticating Extrusion I. A Theoretical Model for Melting," *Polymer Engineering and Science*, Vol. 6, pp. 185-190.

Tadmor, Z. and Gogos, C.G., 1979, Principles of Polymer Processing, Wiley, New York.

Tadmor, Z. and Klein, I., 1970, Engineering Principles of Plasticating Extrusion, Van Nostrand Reinhold, New York.

Taguchi, G., 1987, System of Experimental Design: Engineering Methods to Optimize Quality and Minimize Cost, American Supply Institute.

Taguchi, G. and Phadke, M.S., 1984, "Quality Engineering Through Design Optimization," *Proceedings of the IEEE GLOBECOM-84 Conference*, Atlanta, GA, pp. 1106-1113.

Tang, C. and Kong, Y., 1991, "Amorphous Microcellular Polytetrafluoroethylene (PTFE) Foam Film," *Vacuum*, Vol. 42, p, 1066.

Throne, J.L., 1977, "Principles of Thermoplastic Structural Foam Molding: A Review," Science and Technology of Polymer Processing, N.P. Suh and N.H. Sung eds., MIT Press, Cambridge, pp. 77-131.

Van Krevelen, D.W., 1976, Properties of Polymers, Elsevier, New York.

Veith, W.R., Tam, P.M., and Michaels, A.S., 1966, *Journal of Colloid and Interface Science*, Vol. 22, pp. 360-370.

Vlachopoulos, J. and Chan, T.W., 1979, "A Comparison of Melt Fracture Initiation Conditions in Capillaries and Slits," *Journal of Applied Polymer Science*.

Waekem, A., 1923, *Oil and Color Chemical Association Journal*, Vol. 6, pp. 33-88.

Waldman, F.A., 1982, "The Processing of Microcellular Foam," *S.M. Thesis in Mechanical Engineering*, Massachusetts Institute of Technology, January.

Wang, W-C. V., Kramer, E.J., and Sachse, W.H., 1982, "Effects of High-Pressure CO_2 on the Glass Transition Temperature on Mechanical Properties of Polystyrene," *Journal of Polymer Science: Polymer Physics Edition*, Vol. 20, pp. 1371-1384.

Weinkauf, D.H. and Paul, D.R., 1990, "Effects of Structural Order on Barrier Properties," Barrier Polymers and Structures, W.J. Koros ed., American Chemical Society, pp. 60-89.

Weller, J.E. and Kumar, V., 1992, "Application of Effective Medium Theories for Predicting the Tensile Modulus of Microcellular Foams," *Cellular Polymers*, MD-Vol. 38, ASME, pp. 55-67.

White, S.A., Gotsis, A.D., and Baird, D.G., 1987, "Review of the Entry Flow Problem: Experimental and Numerical," *Journal of Non-Newtonian Fluid Mechanics*, Vol. 24, pp. 121-160.

Williams, J.M. and Wilkerson, M.H., 1990, "High-Density Foams Prepared With the Styrene-Divinylbenzene Copolymer/Heptane System," *Polymer*, Vol. 31, 2162-2170.

Wissinger, R.G. and Paulaitis, M.E., 1991, "Molecular Thermodynamic Model for Sorption and Swelling in Glassy Polymer-CO_2 Systems at Elevated Pressures," *Ind. Eng. Chem. Res.*, Vol. 30, p. 842.

Wissinger, R.G. and Paulaitis, M.E., 1987, "Swelling and Sorption in Polymer-CO_2 Mixtures at Elevated Pressures," *Journal of Polymer Science Part B Polymer Physics*, Vol. 25, p. 2497.

Wu, S., 1982, Polymer Interface and Adhesion, Marcel Dekker, New York, pp. 67-132.

Yoo, H.J. and Han, C.D., 1981, "Studies of Structural Foam Processing III. Bubble Dynamics in Foam Extrusion through a Converging Die," *Polymer Engineering and Science*, Vol. 21, pp. 69-75.

Youn, J. and Suh, N.P, 1985, "Processing of Microcellular Polyester Composites," *Polymer Composites*, Vol. 6, pp. 175-180.

Youn, J., 1984, "Lightweight Polyester Composites," *Ph.D. Thesis in Mechanical Engineering*, Massachusetts Institute of Technology, January.

Young, A.T., 1987, "Polymer-Solvent Phase Separation as a Route to Low Density, Microcellular Plastic Foams," *Journal of Cellular Plastics*, Vol. 23, pp. 55-72.

Young, R.J. and Lovell, P.A., 1991, Introduction to Polymers, Chapman & Hill, New York.

Zeldovich, J.B., 1943, *Acta physicochimia*, U.R.S.S., Vol. 18, p. 1.

Zettlemoyer, A.C., ed., 1969, Nucleation, M. Dekker, New York.

APPENDIX A
EXPERIMENTAL CONFIGURATION OF THE MICROCELLULAR EXTRUSION SYSTEM

The following page presents an itemized description of the microcellular extrusion system which was use used for the critical experiments of chapters 8 and 9.

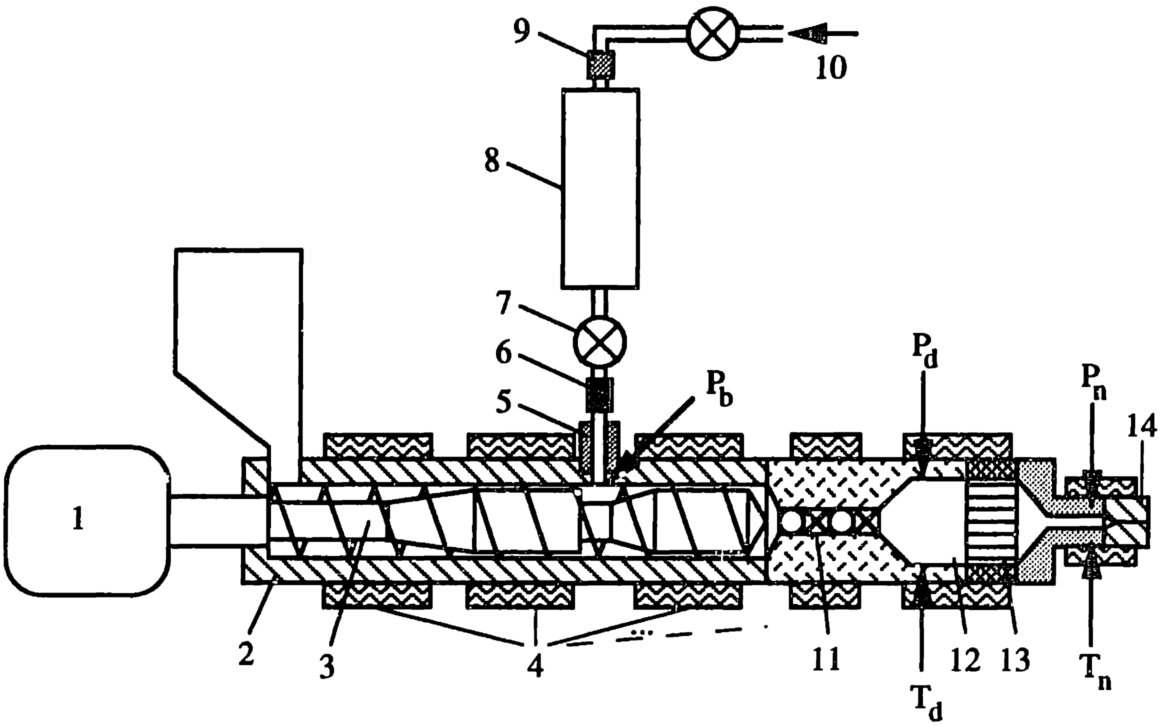

Item	Description
1	Dayton Variable Speed DC Motor (1hp), Drive (208 rpm max.) and Gears (~2:1 output to input)
2	C.W. Brabender 3/4 in., 25:1 L/D, Model 2523, Vented Extruder with 3 Barrel Zones
3	C.W. Brabender Venting Screw Model 05-00-048A or Mixing Screw Model 05-00-051
4	Heaters with Temperature Controllers
5	Standard Barrel Vent (see item 2)
6	Porous Metal Flow Resistance Assembly Using a Mott Metallurgical Encapsulated Restrictor # 5000032
7	High Pressure Stainless Steal Shut-Off Valve
8	Chilled Stainless Steal Pressure Chamber (see Park, 1993)
9	Nupro Model SS-4TF-0.5 In-Line Gas Filter
10	Regulated Supply of Carbon Dioxide or Nitrogen
11	Omega Model FMX8441S Stainless Steel Static Mixer
12	Diffusion Chamber (see Park, 1993)
13	Flow Stabilizer Element/Breaker Plate
14	Nozzle
P_b	Barrel Pressure Tap
P_d	Diffusion Chamber Pressure Tap
T_d	Diffusion Chamber Melt Temperature
P_n	Inlet Nozzle Pressure
T_n	Nozzle Melt Temperature

APPENDIX B
DIMENSIONAL ANALYSIS OF CELL NUCLEATION AND GROWTH KINETICS

B.1 Competition Between Cell Nucleation and Growth

In this analysis, we are interested in determining the characteristic time for nucleating additional cells subject to the competition for available gas while previously nucleated cells grow, Δt_n. It is expected that the characteristic nucleation time is uniquely determined by:

$$\Delta t_n = f\,(l\,, N, D) \tag{B-1}$$

where l is a characteristic distance over which adjacent nuclei compete for available gas, N is the cell nucleation rate, and D is the gas diffusivity.

Next taking the units of time, t, and length, L, as a fundamental set, equations (B-2) and (B-3) are obtained where the symbol [ ] is used to indicate the units of the quantity enclosed. Equation (B-3) indicates that l and N have independent unites.

$$[\Delta t_n] = t \tag{B-2}$$

$$[l\,] = L\,,\ [N] = \frac{1}{L^3\,t}\,,\ [D] = \frac{L^2}{t} \tag{B-3}$$

The units of the remaining variable D can be expressed as a combination of the independent set and is given by equation (B-4). Similarly, the units of the characteristic nucleation time are given by equation (B-5).

$$[D] = \frac{L^2}{t} = \frac{1}{L^3\,t}(L)^5 = [N]\,[l\,]^5 \tag{B-4}$$

$$[\Delta t_n] = t = L^3\, t \frac{1}{(L)^3} = [N]^{-1}[l]^{-3} \tag{B-5}$$

Based on equations (B-4) and (B-5), the dimensionless forms of the diffusivity and characteristic nucleation time are given by equations (B-6) and (B-7), respectively. It follows that the characteristic nucleation time is function of a single dimensionless quantity of D/Nl^5.

$$D^* = \frac{D}{N\, l^{\,5}} \tag{B-6}$$

$$\Delta t_n^* = \Delta t_n\, N\, l^{\,3} = f\left(\frac{D}{N\, l^{\,5}}\right) \tag{B-7}$$

A physical interpretation of the dimensionless quantity, D/Nl^5, can be obtained by looking at two characteristic time factors. For nucleation, a characteristic time factor is derived from equation (B-7) and given by equation (B-8).

$$\Delta t_n \sim \frac{1}{N\, l^{\,3}} \tag{B-8}$$

The second characteristic time is for gas diffusion over the length l and is given by equation (B-9).

$$\Delta t_d \sim \frac{l^{\,2}}{D} \tag{B-9}$$

Taking the ratio of these time factors yields the relation of (B-10) for the situation where this is negligible competition between cell nucleation and growth.

$$\frac{D}{N\, l^{\,5}} << 1 \tag{B-10}$$

It follows then that the physical interpretation of the functional dependence of Δt_n (equation B-7) is given by:

$$\frac{\text{Characteristic Nucleation Time}}{\text{Characteristic Diffusion Time}} << 1 \;. \tag{B-11}$$

BIOGRAPHICAL NOTE

Daniel F. Baldwin was born in Fort Collins, Colorado in 1965. He received the B.S.E. degree in Mechanical Engineering from Arizona State University in 1988 and the S.M. degree in Mechanical Engineering from the Massachusetts Institute of Technology in 1990. His master's research dealt with the development of algorithms and software tools for the generation of mechanical assembly sequences. He began his doctoral studies in Mechanical Engineering at MIT in 1990 with a minor in computer science.

He has worked as a software analyst for Colorado State University critiquing educational software packages and as a research assistant at Colorado State University on robotic assembly systems. In 1987, he worked as an engineering intern for Mitsubishi Electric, Yokohama Japan, on Japan's fifth generation computer project. In addition, he served as the research manager for the MIT-Industry Microcellular Plastics Consortium and Research Group during his doctoral studies.

After completing his doctoral studies, Daniel Baldwin will be joining the faculty of The George W. Woodruff School of Mechanical Engineering at the Georgia Institute of Technology. In 1994, prior to joining the Georgia Tech faculty, he will be on the technical staff of AT&T Bell Laboratories in Princeton, New Jersey working in the area of microelectronics miniaturization and assembly.

Daniel Baldwin is a member of Tau Beta Pi, Pi Tau Sigma, Phi Kappa Phi, Sigma Xi, SME, SPE, IEEE, ASEE, and ASME, and he is a registered engineer-in-training in Arizona. He is also holds one patent and has three pending patents.